C.A.R.S. Temperature Measurements and Chemical Kinetic Modelling of Autoignition in a Methanol-fuelled Internal Combustion Engine

R.D. Lockett

November 19, 1992

This thesis is submitted in fulfilment of the requirements of the degree of Doctor of Philosophy.

Department of Physics, University of Cape Town

JST 530 Lock

93/9933

Abstract

The temperature inside the cylinder of a methanol-fuelled single-cylinder Ricardo E6 research engine running under knocking conditions, is measured by means of Coherent Anti-Stokes Raman Spectroscopy (CARS), and the pressure is measured with a pressure transducer. In order to obviate any errors arising from deficiencies in the spectral scaling laws which are commonly used to represent nitrogen Q-branch spectra at high pressure, a purely experimental technique is employed to derive temperatures from CARS spectra by cross-correlation with a reference library of spectra recorded in an accurately calibrated high-pressure high-temperature optical cell.

The temperature and pressure profiles obtained from the engine running under knocking conditions, are then used as input data for chemical kinetic modelling of end-gas autoignition. Five published mechanisms (Grotheer et al 1992, Grotheer and Kelm 1989, Norton and Dryer 1989, Dove and Warnatz 1983, and Esser and Warnatz 1987) are used in the autoignition study, and the results for the different mechanisms are compared. A good qualitative understanding of the mechanism underlying end-gas autoignition in the engine is obtained, although the calculated autoignition points occur slightly earlier than the observed point.

A sensitivity analysis of the methanol autoignition system is undertaken, and the importance of the decomposition of hydrogen peroxide and the hydroperoxyl chemistry is demonstrated. The discrepancies between the predicted results of the different mechanisms is shown to be caused by a small number of sensitive reactions for which there are conflicting data.

Finally, a linear mode analysis from the geometric qualitative theory of differential equations is performed on the non-linear chemical rate equations. The

equilibrium points in the generalised phase space of the non-linear chemical system are shown to be defined in terms of three regions. The equilibrium points are unstable improper nodes in the first region (T< 1100K), unstable focii in the second region (1100K<T<1170K), and stable focii in the third region (T>1170K).

Acknowledgements

I would like to thank Prof. G. Robertson for suggesting the project, guiding me, and organising financial support for the past five years. I am grateful also to Dr. S. Driver and Dr. R. Hutcheon, the former for the rigour and care that he took during experiments, discussions and reading this thesis, and the latter for help with the technical aspects of the experiments. I also thank Dr. A. Yates and Mr. R. Nates for the detailed discussions on the engineering aspects of engine knock and the Ricardo E6 engine, and Dr. G. Hendricks for his contribution to the engine experiment.

I am grateful to Fiona McKay, Mike Auret, and Gerard Drennan for their assistance in proofreading, and Jonathon Knight, for many stimulating discussions. I must also thank John Dixon, for keeping me fit on the squash court while I was writing this thesis.

Finally, this thesis would not have been possible without financial assistance from the Foundation for Research Development, and the National Energy Council.

Contents

List of Figures

List of Tables

Chapter 1

Introduction

1.1 Motivation

In the years following the 1973 Middle East oil crisis, there was widespread international concern over access to stable sources of petroleum in the short and medium term, and over the continued availability of petroleum and related hydrocarbon products in the long term. Predictions that a worldwide shortage of petroleum would develop early in the Twenty-first Century stimulated governments and oil companies to support research into the development of alternative fuels that might eventually replace petroleum based fuels.

Following these early pessimistic predictions, a more realistic picture of the state of international petroleum resources has emerged. Presently, there are larger known reserves of crude oil than at any other time during the Twentieth Century, and these reserves are considered sufficient to last until the middle of the Twenty-first Century. While this has reduced the immediate urgency of alternative fuel development, environmental concerns have clarified

the potential hazards of continued fossil fuel combustion and the desirability of developing renewable fuel sources.

Methanol (wood alcohol), and ethanol (grain alcohol) have both been suggested as possible alternatives to conventional hydrocarbon fuels, for use in reciprocating spark ignition engines, and in diesel engines. Alcohols are already in use in pure or blended form in Brazil, the Republic of South Africa, Cuba and Zimbabwe. Methanol is widely used as a fuel for racing cars with specially designed high performance engines, as its volumetric energy density is about 13% greater than conventional gasoline in the same engine [58]. Methanol can be derived from lignite or coal, municipal solid wastes, waste biomass, or specifically grown biomass. It is advantageous to use biomass for producing methanol as the process is carbon dioxide neutral, and so no extra CO_2 is added to the atmosphere, while deriving methanol from lignite or coal would release considerable amounts of excess CO_2.

Methanol has many desirable properties as an engine fuel. It has a high degree of knock resistance (a high octane number), a high energy density, and its combustion chain produces no soot. Pollutant emission levels from engines fuelled with methanol are lower than emission levels from engines fuelled with conventional hydrocarbon fuels. The fact that the fuel in combustion produces no soot makes it a good candidate for use in diesel engines, despite its low cetane number, and it has, in fact, been successfully tested and used as a diesel fuel substitute [107].

In addition to the interest in methanol as an alternative automotive fuel, there is considerable interest in its ignition chemistry. Methanol is a simple fuel, and its combustion in air is described by only a few reaction steps. Therefore it offers a unique opportunity to understand the overlap of fluid dynamical processes and chemical processes in a fluid combustion system. Furthermore,

important kinetic features of methanol oxidation also apply to more complex hydrocarbon fuels, and therefore it serves as an important reference fuel for purposes of comparison with other fuels.

It was thus surprising to find that few fundamental chemical studies had been done on the abnormal combustion (engine knock) of methanol in a firing engine. The most comprehensive chemical kinetic modelling of abnormal methanol combustion in an engine was performed by Dimpelfeld and Foster [30], and even this study was fairly rudimentary. Therefore it was felt that a more comprehensive study of methanol autoignition should be undertaken, in order to illuminate the chemical processes in methanol combustion around the explosion limits at high pressure, and contribute to the understanding and development of appropriate combustion mechanisms.

1.2 Methanol as an Engine Fuel

1.2.1 Basic Physical and Chemical Properties of Methanol

Methanol is the simplest of the aliphatic alcohols. Its combustion properties are similar to other small-molecule hydrocarbon fuels. The oxygen atom constitutes 50 % of its mass, and is bonded to a hydrogen atom, forming a hydroxyl group. The molecule has a large dipole moment, and hydrogen bonding dominates its thermodynamic behaviour in the liquid state, and the liquid-vapour phase transition. Compared with hydrocarbon fuels, methanol has a low vapour pressure, a large specific heat, a high boiling point, and a large latent heat of vaporisation. Since methanol is partially oxidised, it has only 45 % to 48 % of the heat of combustion (per kg) of reference iso-octane (2,2,4 trimethyl-pentane). The thermodynamic, chemical and combustion properties

of methanol are presented in Appendix (1).

The stoichiometric combustion of methanol and iso-octane is described by the following reactions:

$$CH_3OH + 3/2O_2 \rightarrow CO_2 + 2H_2O,\ \Delta H^0 = -638.11\text{kJ.mol}^{-1} \qquad (1.1)$$

$$C_8H_{18} + 12.5O_2 \rightarrow 8CO_2 + 9H_2O,\ \Delta H^0 = -5069.3\text{kJ.mol}^{-1}. \qquad (1.2)$$

These stoichiometric heats of combustion give rise to specific heats of combustion of $\Delta H^0 = -19.925\text{MJ.kg}^{-1}$ and $\Delta H^0 = -44.381\text{MJ.kg}^{-1}$ for methanol and iso-octane respectively [58].

Methanol is miscible in all proportions with water, but it retains sufficient hydrocarbon nature to be readily soluble in dry gasoline. However, small amounts of water ($> 0.1\%$) cause phase separation. Mixtures of methanol and gasoline produce a non-linear increase in vapour pressure, and thus deviate from Raoult's law.

The reactive hydroxyl group in methanol causes severe corrosion in zinc, lead, and magnesium, and moderate corrosion in aluminium and copper. Furthermore, methanol is a strong solvent, and swells or softens many of the plastics and rubbers used as gaskets or floats in conventional fuel systems.

1.2.2 Methanol Combustion and Autoignition

"Engine knock" is the term given to the audible knocking sound from a spark ignition engine run with a compression ratio set too high, or with too lean

a fuel/air mixture, or with a very advanced spark ignition. Engine knock is caused by ignition of the unburned fuel/air mixture ahead of the advancing flame front, and if prolonged, can damage the engine. The compression ratio of an engine is an important determining factor in whether a given fuel will knock. Therefore the need to prevent knock in an engine imposes an upper limit on the compression ratio of the engine for a given fuel.

Two principal theories of the ignition of the unburned fuel/air charge (otherwise called the end-gas or the core gas) have been developed. The first holds that engine knock is the result of a detonation wave developing in the end-gas, originating either from the flame front, or from within the end-gas itself [85] [82]. The second holds that engine knock is the result of a global homogeneous explosion of the end-gas (otherwise called autoignition or self-ignition), caused by the near isentropic compression of the end-gas to its explosion limit, by the expansion of the burnt gases and the advancing flame front [96] [105] [42]. Evidence obtained in recent years suggests strongly that engine knock is a consequence of autoignition of the end-gas [105] [63].

Conventional paraffin fuels exhibit a two-stage autoignition in the unburned portion of the end-gas when an engine is run with a high compression ratio. The first stage of autoignition is observed as a cool flame process, and lasts for a few milliseconds, while the second stage is a high temperature process [33]. Methanol does not exhibit the first (cool flame) stage of autoignition, and only ignites at high temperature.

The combination of the high latent heat of vaporisation of methanol and the high temperature of methanol ignition in air causes methanol to be highly resistant to autoignition when compared with conventional hydrocarbon fuels [127]. This resistance to autoignition permits considerably higher compression ratios in an engine running on methanol, than in an engine running on

conventional gasoline, thus permitting greater efficiency and power [51]. The maximum thermodynamic efficiency η of an idealised spark ignition engine cycle is related to the compression ratio r in the following way:

$$\eta = 1 - \frac{1}{r^{\gamma-1}}, \tag{1.3}$$

where γ is the ratio of the specific heats of the fuel/air mixture [42]. Thus increasing the compression ratio increases the thermodynamic efficiency of the engine. Conventional gasoline engines usually run with compression ratios between 8:1 and 10:1, while methanol engines have been run with compression ratios of as much as 16:1 [58].

If an engine is designed to perform at maximum thermodynamic efficiency, then engine knock (end gas autoignition) will determine the upper limit of that efficiency. Engine knock is primarily a chemical process, with fluid flow processes being of secondary importance, even though modern engines use flow processes to promote complete combustion. (Modern engines running on gasoline are designed to swirl and squish the gases in the combustion chamber to increase the speed of combustion by inducing greater levels of turbulence. This is intended to secure complete combustion before the unburned fuel/air charge in the end gas reaches autoignition conditions.)

1.3 Engine Diagnostics

1.3.1 Conventional Techniques

The analysis of spark ignition engine cycles requires the use of a number of standard diagnostics. The following discussion on conventional diagnostics

comes mainly from Ferguson's book, "Internal Combustion Engines - Applied Thermosciences" [42], and the review paper "A Perspective of Reciprocating-Engine Diagnostics without Lasers", by C. Amann [5].

Applying load and controlling engine speed, measurement of fuel flow rate, air flow rate, cylinder pressure versus volume, in-cylinder temperature, spark ignition timing, oil and coolant temperature and residual fraction are all relevant to the determination of engine behaviour.

Dynamometers are used in engine research to load a firing engine in order to maintain constant engine speed, and for the determination of engine power under different running conditions. Electric dynamometers can also be used to motor an engine at constant speed.

An old technique of measuring fuel flow rate was to weigh the quantity of fuel delivered to the engine over a few minutes. This gives an average fuel mass flow rate. More modern methods of measuring fuel flow rate involve the use of small positive displacement turbines installed in the fuel line, or the use of an electronic transducer to measure mass flow rate. These more modern techniques facilitate instantaneous measurement of fuel flow rate.

Air flow rates cannot be measured with the same precision as fuel flow rate. Air flow meters are usable only in steady flows, while air flow to an engine is typically unsteady. Some of the air-flow meters in use are the laminar flow meter, the critical flow nozzle, the turbine meter, and the hot wire meter. The laminar flow meter usually consists of a bundle of tubes sized so that the Reynold's number in each is well within the laminar regime, and so flow rate depends linearly on the pressure drop across the meter. The critical flow nozzle is a venturi in which the flow is choked, and thus flow rate depends linearly upon the delivery pressure. The turbine meter rotates with an angular velocity

linearly dependent on the air-flow velocity. The hot wire meter is a hot wire anemometer inserted into the flow to measure the centre-line velocity. Hot wire anemometers have also been used to measure instantaneous velocities inside motored and firing engines in order to determine turbulence intensity.

Cylinder pressure is usually measured using a continuous measurement piezo-electric sensor, coupled to a charge amplifier. There are difficulties though in obtaining the correct cylinder pressure using this method, as piezoelectric sensors tend to drift.

In-cylinder temperatures are usually calculated from the ideal gas law, based on knowledge of the cylinder volume and cylinder pressure prior to spark ignition. Infra-red pyrometers and electro-optical hot gas pyrometers have been used to measure cylinder temperature during the compression cycle.

A non-optical technique of measuring in-cylinder temperatures was developed at M.I.T., and relies on the temperature dependence of the velocity of sound in a gas. An acoustic impulse is transmitted through a gas path of known length in the cylinder, and its transit time is measured. This measurement determines an average in-cylinder temperature.

Flame propagation through the fuel/air mixture has been observed and photographed using engines with optical access, and engines with transparent cylinder heads. The use of Schlieren methods for studying the propagation of the flame front has also been widely used.

Fast gas sampling valves are used to sample in-cylinder gases over a brief crank-angle interval. Most sampling valves involve intermittent flow, using a reciprocating needle or pintle.

Unburned hydrocarbons from the engine are usually measured with a flame

ionisation detector, while carbon dioxide and carbon monoxide concentrations are measured using a non-dispersive infra-red analyser. A chemiluminescent analyser is now usually used to measure oxides of nitrogen, while oxygen concentration is measured either by a polarographic analyser or a paramagnetic analyser.

1.3.2 Non-intrusive Laser Diagnostics for Temperature Measurement in Engines

There are a number of laser techniques in use to measure temperature in internal combustion engines. Examples are Spontaneous Raman Scattering [22] [105], Coherent Anti-Stokes Raman Scattering (CARS) [78], and more recently, Laser Induced Fluorescence (LIF) techniques [12].

Spontaneous Raman scattering is an inelastic scattering process whereby monochromatic light of frequency ω incident on a target vapour medium of a given molecular species produces scattered light of frequency $\omega \pm \Delta\omega$, where the frequency shifts correspond to transition frequencies between rotational, vibrational and electronic energy levels in the target species. Normally, the incident light is scattered to lower frequencies (Stokes scattering).

For a given incident frequency, the energy levels of a given species produce a unique Raman spectrum, which depends strongly on the rotational and vibrational energy level structure of the molecule. The relative intensities of these Raman lines are temperature dependent, and so thermometry using Raman scattering is feasible. Indeed, Raman scattering in nitrogen has been used as a means of measuring combustion temperatures in flames, rocket engines, shock tubes, electric discharge tubes and internal combustion engines. The disadvantages of spontaneous Raman scattering are that the scattering is

isotropic, with low intensity, and the scattering is to longer wavelengths, often experiencing interference from fluorescence.

Laser induced fluorescence (LIF) occurs with the promotion of an atom or molecule to an excited electronic state, resulting in the spontaneous emission of light as the atom or molecule decays back to a lower energy state. LIF thermometry is performed mainly through the use of two line atomic fluorescence. Trace atoms are introduced to the system, and the relative population of two low energy levels are measured via a common excited state. The main disadvantage in using LIF is that quenching of the LIF signal occurs at high pressures. Very recently, pre-dissociated LIF has been devised to overcome quenching problems, and two-dimensional measurements of temperature and radical species concentrations have been successfully performed in a diesel engine [12].

CARS has become the most widely used laser diagnostic technique for temperature measurement, as a consequence of its high signal strength, good spatial and temporal resolution, and relative immunity from interference. CARS has been successfully applied as a means of measuring temperatures in spark ignition engines, diesel engines, jet combustors, industrial burners, and furnaces [98] [107] [37].

CARS is a coherent molecular scattering process in which two laser beams of frequency ω_p and ω_s are focussed down to a focal waist in the combustion medium, and through a third order process involving the non-linear susceptibility of the target medium, generate a coherent beam at the frequency $2\omega_p - \omega_s$. The frequencies ω_p and ω_s are chosen in such a way that $\omega_p - \omega_s$ matches the frequency difference between the ground state and the first vibrational state of the target molecule. The most standard CARS technique for thermometry uses a narrow band Nd:YAG laser with a broadband dye laser

which together probe the Raman vibrational Q-branch transition in molecular nitrogen ($\Delta v = 1, \Delta J = 0$).

The CARS susceptibility and thus the CARS signal spectrum depends on the non-linear polarisability of the target molecules, which exhibits a resonant structure associated with vibrational and rotational transitions in the molecule. Thus CARS spectra are dependent on the molecular structure of the target species, and reflect the rotational state and vibrational state population distributions as a function of temperature. This means that if sufficient Raman spectroscopic data on a given type of molecule exists, it is possible in principle to calculate theoretically the form of the CARS spectrum for a gas constituted of that molecular species as a function of temperature and pressure.

Indeed, this is how nitrogen Q-branch thermometry is usually performed. A library of theoretical CARS Q-branch spectra is calculated for a specified range of pressures and temperatures. A set of experimentally obtained CARS spectra at a given temperature and pressure is then compared with the library of theoretical spectra, and the temperature of the combustion system is deduced by means of fitting the experimental spectra to the theoretical spectra.

CARS was the laser diagnostic technique of choice in this study, for the above reasons. Furthermore, the Ricardo E6 research engine available required little modification for CARS optical access. The engine was fitted with a spacer between the cylinder head and engine block, which housed two diametrically opposed windows to give optical access to the engine for CARS measurements.

1.4 Survey of CARS Thermometry in Internal Combustion Engines

CARS has been used fairly widely as a method of determining temperatures in internal combustion engines. The first published report of the use of CARS in this way was by Stenhouse et al [106] in 1979. In this paper, the authors reported CARS temperature measurements in a Ricardo E6 research engine, run on propane and gasoline. They used a J.K. series 2000 Nd:YAG laser to pump a narrow band tunable Molectron DL 200 dye laser for the Stokes beam. The pump and dye laser were then brought together in a co-linear geometry. Since they employed a narrow band dye laser, they had to use scanning CARS to acquire the full CARS signal. The resultant spectra were then analysed by comparing the spectra with theoretical spectra generated by code developed by Taran's research group at ONERA.

The Shell-Harwell team found problems with window fouling when motoring the engine, and when running with a rich mixture of gasoline, but not when the engine was running on propane. They also found occasional beam defocussing, and suggested that this could be caused by dielectric breakdown, or refraction effects due to very large density gradients in the flame front.

In 1981, Klick et al [71] published a paper on broadband single-pulse CARS spectra in a fired internal combustion engine. They used a modified Megatech Mark III single cylinder engine, operating with a compression ration of 3:1, with an Nd:YAG laser and a broadband dye laser producing broadband CARS spectra of molecular nitrogen, carbon monoxide, and molecular hydrogen. They ran the engine using propane and methanol.

They concluded that the nitrogen data could be used for temperature determination, and the data in the CO spectral region could be used for concentration

determination, relative to the concentration of nitrogen. They suggested the use of a variable rate laser system, capable of pulsing synchronously with the engine at repetition rates of up to 20 Hz, and simultaneous referencing for proper normalisation of the CARS spectra.

In 1983, Kataoka et al [69] reported the results of a study for nitrogen CARS thermometry at high pressure. They obtained nitrogen CARS spectra from inside a diesel engine over a pressure range of one to fifty atmospheres. They fitted experimentally obtained CARS spectra against a library of CARS spectra generated using Hall's EGL model of collisional narrowing. This paper is discussed in some detail in chapter 3, in the review of pressure narrowing in nitrogen CARS spectra.

In the same year, Alessandretti and Violino [4] published a paper on nitrogen thermometry using broadband CARS in an automobile engine. They obtained temperatures from the combustion chamber of one cylinder in a 2-litre production model four-stroke reciprocating engine. The compression ratio of the cylinder with optical access was 9:1. The engine was coupled to a d.c electric motor in order to run at constant speed (within 1 %) in motored and firing conditions, and was run with iso-octane, premium gasoline, using normal lubricating oil.

They used a pulsed Nd:YAG laser to pump a Rhodamine 640 dye laser, and aligned the two beams using a co-linear geometry. They brought the beams to a focal waist inside the combustion chamber using 100mm focal length lenses. They assumed the laser lineshapes to be Gaussian, and used Hall's EGL model for the calculation of collisionally narrowed linewidths.

They showed that the effect of the non-resonant third order susceptibility was small at high density, and that it was therefore not necessary to eliminate the

non-resonant background. They argued that co-linear CARS provided sufficient spatial resolution to obtain data suitable for combustion modelling. They reported an accuracy of $\pm 80K$ for their temperatures, and found considerable cycle to cycle temperature fluctuation for small crankshaft angles ($\sim 300K$) which decreased as the crankshaft angle increased.

In 1985, Marie et al [83] reported the results of CARS thermometry in a spark ignition engine fueled with liquid hydrocarbon fuel. They used a commercial four-stroke four-cylinder P.S.A./R.N.U.R. engine model 829, coupled to a d.c. electric motor, and adapted to enable optical access, running on iso-octane for the engine experiment. They used a monomode Nd:YAG laser to pump a broadband dye laser, and aligned the beams in a co-linear geometry without background suppression. They performed simultaneous referencing through the use of a high pressure argon reference cell.

They found that there was considerable cycle to cycle temperature variation at the same measurement point in the combustion chamber, which gave rise to a maximum temperature uncertainty of about 100 K. They found some difficulties with pressure narrowing effects in the fitting of the experimental spectra, but argued that deduced temperatues would improve with improvements in the model. Finally, they concluded that accuracy limits reached elsewhere in CARS measurements should also be obtainable in a running engine.

In 1987, Lucht et al [78] reported CARS temperature measurements of unburned gas temperatures in an internal combustion engine. They used the SANDIA optical engine (described in chapter 3), fuelled with n-butane. They operated the engine using skip firing under both normal and knocking conditions. (Skip firing reduces cycle to cycle fluctations.) They used a multimode Quanta-Ray Nd:YAG laser to pump a broadband dye laser, and the beams were aligned and focussed inside the engine using a three dimensional phase

matching geometry.

They analysed the experimentally obtained CARS spectra using the method developed by Koszykowski et al [73], Hall's EGL model, and Gordon's rotational diffusion model for calculating collisional linewidths. This method is discussed in some detail in chapter 3, in the review of collisional narrowing in CARS. They found that the non-resonant susceptibility of n-butane in the unburnt gas significantly affected the deduced temperatures. Consequently, they used polarisation methods to suppress the non-resonant background.

They found temperature fluctuations in the skip-fired engine of the order of 20 K to 30 K, and argued that the most significant factor affecting accurate determination of average temperature is long term drift in the dye laser spectrum. They estimated a systematic uncertainty of approximately 40 K in the presentation of the engine temperature histories.

Finally, in 1989, Brüggeman et al [19] reported temperature measurements in a knocking spark ignition engine by CARS spectroscopy. They used an air-cooled single cylinder ROTAX engine, fuelled with unleaded gasoline. The cylinder head contained nearly 100 holes with optical fibres, a pressure transducer for engine pressure measurement, and quartz windows for CARS optical access. In the course of their CARS studies, they performed CARS calibration measurements in a heated high pressure vessel, and reported that deduced CARS temperatures differed from thermocouple measurements by less than 25 K over the measurement range of 300 K to 1300 K, and 1 bar to 50 bar.

They reported standard deviations in the CARS temperature measurements in the engine of between 20 K and 35 K. The CARS temperature measurements for the firing engine and motored engine were compared with a simple polytropic compression model and gave good agreement. They found that knocking

cycles experienced higher pressure histories than normal cycles, which resulted in higher end gas temperatures, and that the flame front occupied a greater area at comparable time for knock cycles than for normal cycles. They suggested that it was necessary to establish the extent of cycle to cycle variations in pressure and temperature at the spark ignition point, and the consequences on the evolution of the flame, and that quantitative studies on the connection between the shape and structure of the flame front and its propagation needed to be undertaken.

1.5 Analysis of CARS Spectra

Normally, experimental CARS spectra are fitted against theoretical CARS spectra using a non-linear least squares fitting method. The non-linear least squares method is justified for fitting discrete data functions, if each data point is normally distributed about the mean, and uncorrelated with other data points. Problems can arise with convergence of the sum of least squares to the correct minimum if the discrete data functions are too noisy. Non-linear least squares methods are also computationally complex, as non-linear equations need to be solved by iteration, and this raises the question of termination criteria.

CARS spectral data do not satisfy these demands. Data points are correlated through cross-talk between pixels, and noise levels in the data are correlated with the CARS signal intensity for a given pixel. Furthermore, CARS data noise is fairly high, as a result of the unstable mode behaviour in the dye laser, and this often gives rise to numerical convergence difficulties.

In this thesis, an alternative method is employed to fit experimentally obtained CARS spectra against reference CARS spectra, based on cross-correlation and

auto-correlation techniques. The method is very closely related to the non-linear least squares method, but it is linear. It is computationally simple, and provides an unambiguous measure of goodness of fit. The method involves the calculation of normalised cross-covariances for the discrete data functions, and then finding the maximum of the cross-covariances. The temperature for which the cross-covariance is maximum is then selected as the desired temperature.

Rather than apply imperfect scaling laws for the calculation of pressure narrowing effects in theoretical CARS spectra, experimental CARS spectra obtained from a calibrated high pressure high temperature cell have been used to deduce temperatures from the CARS spectra recorded in the Ricardo E6 research engine. The cross-covariances obtained by comparing sets of experimental spectra against each other are shown to be consistently higher then those obtained using theoretical models. Furthermore, systematic errors associated with this method are small and are easily identified, in contrast to the unknown, and possibly large systematic errors using theoretical models.

1.6 The CARS Engine Experiment

1.6.1 The Ricardo E6 Research Engine

The Ricardo E6 research engine used for the methanol knock experiment is a variable compression ratio engine, equipped with a Lawrence Scott dynamometer. The engine can be motored at constant speed, or run at constant speed while firing. As mentioned earlier, the engine was fitted with a spacer between the engine block and the cylinder head. The spacer contained two spectrosil windows (8mm diameter, 10mm thick) for optical access to the combustion chamber. The engine was run with a compression ratio of 9.5:1 with the spacer

in place, sufficient for a lean preheated methanol/air mixture to knock.

The combustion chamber is almost perfectly cylindrical, with the spark plug positioned slightly off centre. Diagonally across from the spark plug was a piezoelectric pressure transducer for end-gas pressure measurement. The engine was naturally aspirated, and the fuel/air consumption continuously monitored. The spark ignition timing could be varied manually.

The engine was equipped with a fuel flow meter, an air flow meter, an air pre-heater, and an oil temperature gauge. The engine was run on methanol for a variety of speeds, fuel/air mixtures, spark ignition timing, and inlet air heating in order to study methanol knock.

1.6.2 The U.C.T. CARS System

The U.C.T. CARS laser research group operates a single longitudinal mode (s.l.m.) Nd:YAG laser and a tunable broadband dye laser for CARS thermometry experiments. The lasers were focussed down to a focal waist in the centre of the combustion chamber 6mm below the cylinder head using a co-linear CARS geometry. The co-linear CARS signal was split off from the pump and Stokes beams using a dichroic filter, and then directed onto an intensified diode array using a concave holographic grating spectrometer.

Five groups of thirty single shot nitrogen CARS spectra were obtained from the centre of the combustion chamber for each crankshaft angle chosen. Engine pressure traces were simultaneously obtained using the pressure transducer coupled to a personal computer. The engine gas temperatures for the different crankshaft angles were then deduced by comparing the single shot spectra with spectra obtained from a calibrated high pressure high temperature (HPHT) cell, using the method of cross-covariance mentioned above.

1.7 Chemical Kinetic Modelling of Methanol Autoignition

1.7.1 Description

The chemical model of methanol autoignition developed in this thesis is zero-dimensional, a consequence of deliberate separation of fluid processes from the chemistry. For a chemical kinetic study of this kind, with the intention of illuminating the essential chemistry, including flow processes in the model would just add more complexity to an already complex system, and would serve to obscure rather than clarify. Research in this area is not yet at the stage where the fluid flow processes can be integrated with the chemical processes.

The zero-dimensional model of autoignition developed here, was justified through the use of a variable compression Ricardo E6 research engine running at low speeds for the methanol knock tests. The Ricardo E6 research engine is a low swirl, low turbulence engine, and the use of this engine made it possible to ignore flow processes, and concentrate more carefully on the chemistry. These issues are discussed in Chapter 4 and Chapter 6.

The methanol autoignition model treats the unburned methanol/air charge as a homogeneous mixture, such as that obtained in a static or well stirred reactor. The fuel/air mixture is considered to be compressed isentropically by the piston, and by the flame front and burnt gases once the spark has fired. Thus the unburned part of the end gas experiences an evolving temperature-pressure history which ultimately leads to autoignition.

Once the temperature and pressure histories have been determined, they are used in the equation of state for the methanol/air mixture. The evolving chem-

istry of methanol autoignition is modelled using five major published methanol oxidation mechanisms, and the results of the modelling are compared.

A detailed discussion of the evolution of the chemical system is given, focussing on the different temperature regimes through which the system passes, and the essential chemistry involved in each regime. The chemistry of autoignition is established qualitatively, but it is shown that autoignition is predicted to occur earlier than it is observed to occur experimentally, with all five methanol oxidation mechanisms.

A local sensitivity analysis of the reaction system is performed for the most modern mechanism, in order to establish which reactions dominate the autoignition chemistry, and thus which reaction rates need to be most accurately known for a successful quantitative analysis of autoignition.

1.7.2 Sensitivity Analysis in Chemical Kinetic Modelling

Reaction rate coefficients in detailed reaction mechanisms are usually deduced indirectly from simple reaction experiments. Sensitivity studies have been adapted to chemical kinetic modelling as a result of the uncertainties involved in the reaction rate coefficients. Sensitivity coefficients are developed in order to establish which parameters in the system have the most important effect on the system.

Sensitivity coefficients in chemical reaction systems usually reflect the sensitivity of a particular property of the system to the mechanism's reaction rate coefficients. For example, in flame studies, one might calculate the sensitivity of laminar flame speed to reaction rate coefficients. In two-stage autoignition studies, one might calculate the sensitivity of the induction time to reaction rate coefficients.

In this thesis, a first order local sensitivity analysis is performed on the temperature evolution, and the species concentration evolution, as a function of reaction rate coefficients, in order to establish which reactions the system is most sensitive to. Four key reactions in the methanol oxidation system are identified, and a critical discussion of the uncertainties in literature values is presented. It is reported that the most important rate coefficient in the chemical mechanism has never been directly measured.

1.7.3 Dynamical Methods in Chemical Kinetic Modelling

The temporal evolution of a complex chemical reaction system is non-linearly dependent on the species concentrations, and the variables of state. The non-linear system of equations defining the temporal evolution of the system are 'stiff', in a technical mathematical sense. 'Stiffness' reflects the very different time scales that define the evolution of the system. Stiff evolution equations imposes constraints on the type of numerical method of solution of these equations. Normal numerical methods of solution applied to stiff systems are susceptible to catastrophic rounding and truncation errors, unless very small integration step sizes are used, and usually diverge from the true solution. Therefore special numerical techniques need to be used to solve stiff systems of equations. Deuflhard's stiff differential equation solver LIMEX is used in Warnatz's zero-dimensional homogeneous chemical kinetics program HOMCHEM, which was used here for the calculation of the methanol/air kinetics.

A standard method of analysing the local properties of non-linear systems is by solving the easier linearised system, concentrating on the qualitative analytic structure of the linear solutions. Interestingly, this method has not been widely used in studying chemical reaction systems, even though this application is a good example of the potential use of linearised methods.

The method involves linearising the set of chemical rate equations, and then solving the resultant linear system in terms of the eigenvector and eigenvalue decomposition of the system. The system evolves in terms of exponential eigenmodes in time, with the eigenvalues determining the rate of the evolution of the eigenmodes. This method of analysing the methanol/air oxidation system is presented here, and the three most modern mechanisms are used in this context. The eigenmode decomposition of the system is analysed with reference to the three mechanisms, and the results are compared and discussed.

This method is not intended as a substitute for normal numerical integration of systems of stiff differential equations; rather it is intended as an aid to the understanding of the mathematical structure of the solution once it has been obtained, and it aids chemical interpretation.

Chapter 2

The Cross-covariance Method of Fitting CARS Spectra

2.1 The Basic Theory of CARS

Coherent Anti-Stokes Raman Spectroscopy (CARS) is a coherent molecular scattering process whereby two laser beams of frequency ω_p and ω_s, called the pump beam and the Stokes beam respectively, are focussed down to a focal waist in a target medium, and through a third order process involving the non-linear susceptibility of the target medium, generate a coherent beam of frequency $2\omega_p - \omega_s$.

The pump and Stokes beams serve to polarise the medium through an electric dipole interaction with the target molecules. The vector components of the polarisation density can be written

$$P_i = \sum_j \chi^{(1)}_{ij} E_j + \sum_{jk} \chi^{(2)}_{ijk} E_j E_k + \sum_{jkl} \chi^{(3)}_{ijkl} E_j E_k E_l + \cdots, \qquad (2.1)$$

where E_i are the vector components of the electric fields. For isotropic media, $\chi^{(1)}$, the linear response of the medium, is a scalar quantity, and $\chi^{(2)} = 0$. Therefore $\chi^{(3)}$ is the highest non-linear term in the above expression for the polarisation density. The polarising electric fields have frequencies specified above, ω_p and ω_s, giving rise to polarisation densities at frequencies specified by the sums and differences of ω_p and ω_s. For $\omega_p - \omega_s$ matching the Raman vibrational Q-branch transition, the polarisation density term involving the frequency $2\omega_p - \omega_s$ is resonantly enhanced. The polarisation density in turn drives a coherent field of frequency $\omega = 2\omega_p - \omega_s$ which obeys the equation

$$(\nabla^2 - \frac{n^2(\omega)}{c^2}\frac{\partial^2}{\partial t^2})\vec{E}(\vec{r},t) = \mu_0 \frac{\partial^2 \vec{P}(\vec{r},t,\omega)}{\partial t^2}. \qquad (2.2)$$

$\chi^{(3)}$ can be theoretically calculated using a quantum-mechanical density matrix formalism. The method is described in Druet and Taran's review article [35] in 1981, and is outlined briefly below.

The quantum state of the scattering molecules at point $\vec{r}$ is represented by the density operator $\rho(\vec{r},t)$. In gases of normal temperature and pressure, classical trajectories are good approximations to the complicated motion of molecules. Thus $\rho(\vec{r},t)$ can be expressed as

$$\rho(\vec{r},t) = \int \rho(\vec{v},\vec{r},t) F(\vec{v}) d^3\vec{v}, \qquad (2.3)$$

where $F(\vec{v})$ is the velocity distribution function, and $\rho(\vec{v},\vec{r},t)$ is the solution of the density operator evolution equation

$$\frac{\partial \rho}{\partial t} + \vec{v} \cdot \vec{\nabla} \rho + (\frac{\partial \rho}{\partial t})_{damping} = \frac{-i}{\hbar}[H_0 + V(t), \rho], \tag{2.4}$$

for a class of molecules with velocity $\vec{v}$. H_0 is the Hamiltonian for an unperturbed isolated molecule, and $V(t) = -\vec{\mu} \cdot \vec{E}(\vec{r}, t)$ is the dipole moment interaction potential. The damping term is determined by stochastic processes such as spontaneous emission of light and collisions between molecules, and can be expressed in terms of a relaxation matrix. This is a key subject of the review of pressure broadening and collisional narrowing in CARS in chapter 3.

The solution for $\rho(\vec{v}, \vec{r}, t)$ is expressed in terms of a perturbation series in the perturbation potential $V(t)$. This series can be represented by a set of diagrams, called Feynman diagrams, which facilitate calculating the transition matrix elements for the density matrix. Because we are dealing with the density matrix operator, defined as

$$\rho = \frac{1}{Z} \sum_{states} |\psi > e^{-\beta H} < \psi|, \tag{2.5}$$

the diagram representation for ρ is in the form of two-sided Feynman diagrams. In CARS, we are dealing with a four level system, and it turns out that calculation of 384 diagrammatic terms are necessary for the full calculation of the non-linear susceptibility. The most important terms in this calculation are those containing the Raman resonance $\omega_{ab} - (\omega_p - \omega_s)$, where ω_{ab} refers to the frequency difference between vibrational states a and b. There are a total of 32 such terms, and they dominate the other terms in the calculation. For a four level system, 8 of the 32 Raman resonant terms are distinct, and the other 24 terms can be deduced using appropriate permutation symmetry.

$\chi^{(3)}_{CARS}$ can also be expressed as

$$\chi^{(3)}_{CARS}(-\omega,\omega_p,\omega_p,-\omega_s) = \chi^{NR} + \chi^{RES}, \tag{2.6}$$

where χ^{NR} is the non-resonant part of the non-linear susceptibility, and χ^{RES} is the resonant part of the non-linear susceptibility, and has the form

$$\chi^{RES} = \frac{a}{(\omega_{ab} - \omega_p + \omega_s) + i\Gamma}. \tag{2.7}$$

χ^{RES} can be expressed more fully in the form [38]

$$\chi^{RES} = \frac{4\pi^2\epsilon_0 c^4 N}{\hbar} \sum_{a,b} \frac{\Delta\rho^0_{ab}}{\omega_s^4} (\frac{d\sigma}{d\Omega})_{ab} \frac{1}{\omega_{ab} - \omega_p + \omega_s + i\Gamma_{ba}}. \tag{2.8}$$

$\Delta\rho^0_{ab}$ refers to the fractional population difference between vibrational states a and b, and N is the number of scattering molecules in the system. $(\frac{d\sigma}{d\Omega})_{ab}$ refers to the differential cross section for spontaneous Raman scattering between states a and b, and ω_{ab} corresponds to the frequency difference between the above states. It can be shown that the CARS signal intensity for plane pump and Stokes waves at frequency $\omega = 2\omega_p - \omega_s$, driven by the polarisation density in a slab medium of length l, according to equation 2.2, has the form [38]

$$I(\omega) = K_1 I^2(\omega_p) I(\omega_s) |\chi^{(3)}_{CARS}|^2 l^2 \frac{\sin^2(\frac{1}{2}\Delta k_l l)}{(\frac{1}{2}\Delta k_l l)^2}. \tag{2.9}$$

K_1 is a constant, $I(\omega_p)$ and $I(\omega_s)$ are the intensities of the pump laser and Stokes laser beams respectively, $\chi^{(3)}_{CARS}$ is the non-linear CARS susceptibility

of the medium, and $\Delta k_l = \Delta\vec{k} \cdot \vec{l}$. The $\frac{\sin^2 x}{x^2}$ term expresses the directional nature of the CARS signal.

Equation 2.9 can be specialised to the case of diffraction-limited laser beams with Gaussian-shaped spatial density profiles. This yields an expression for the CARS signal power in terms of the powers of the pump and Stokes beams with no explicit length dependence. In this instance, the interaction volume is assumed cylindrical with a diameter specified by the focal spot diameter of a Gaussian beam $d = 2f\lambda/D$ (f is the focal length of the lens, and D is the $1/e^2$ beam diameter incident on the lens), and length specified by twice the confocal parameter $L_R = \frac{\pi d^2}{4\lambda}$. Assuming the interaction length equals the confocal parameter, and converting to beam power, the CARS signal power becomes [38]

$$P(\omega) = K_2 P^2(\omega_p) P(\omega_s) |\chi^{(3)}_{CARS}|^2. \tag{2.10}$$

For a single Raman resonance, the CARS non-linear susceptibility has the form

$$\chi^{(3)}_{CARS} = \chi_1^{RES} + i\chi_2^{RES} + \chi^{NR}, \tag{2.11}$$

and therefore the anti-Stokes output has a spectrum given by

$$|\chi^{(3)}_{CARS}|^2 = (\chi_1^{RES} + \chi^{NR})^2 + (\chi_2^{RES})^2. \tag{2.12}$$

Because of the presence of the non-resonant susceptibility in $|\chi^{(3)}_{CARS}|^2$, the spectrum appears asymmetric with respect to the resonant frequency term

$\omega_{ab} - \omega_p + \omega_s$, and has a peak and a dip at [105],

$$(\omega_p - \omega_s)_{\pm} = \omega_{ab} + \frac{1}{2}[-\frac{a}{\chi^{NR}} \pm ([\frac{a}{\chi^{NR}}]^2 + 4\Gamma^2)^{1/2}]. \qquad (2.13)$$

CARS is therefore very sensitive to the relative strengths of the Raman resonance on the one hand, and the non-resonant background on the other. The non-resonant background is proportional to the density of the gas, and so CARS experiments in high pressure media must take account of the effects of the non-resonant background in the experimental CARS spectra. Polarisation techniques involving relative polarisations of the pump and Stokes beams have been developed in order to suppress the non-resonant background, but the intensity of the resultant CARS spectra is considerably reduced.

The CARS susceptibility and thus the CARS signal spectrum depends on the non-linear polarisability of the target molecules, which exhibits a resonant structure associated with vibrational and rotational transitions in the molecule. Thus CARS spectra are dependent on the molecular structure of the target species, and reflect the rotational state and vibrational state population distributions as a function of temperature. This means that if sufficient Raman spectroscopic data on a given type of molecule exists, it is in principle possible to calculate theoretically the form of the CARS spectrum for a gas constituted of that molecular species as a function of temperature and pressure.

Indeed, this is how nitrogen Q-branch thermometry is normally undertaken. A library of theoretical CARS Q-branch spectra are calculated for a specified range of pressures and temperatures. A set of experimentally obtained CARS spectra at a given temperature and pressure are then compared with the library of theoretical spectra, and the temperature of the combustion sys-

tem is deduced by means of fitting the experimental spectra to the theoretical spectra.

In order to calculate the theoretical CARS spectrum for a given temperature and pressure for comparison with an experimentally obtained spectrum, the pump and Stokes laser lineshapes, and the detector response function have to be taken into account. The intensity of the CARS signal at a given frequency ω on a diode array detector is given by [78]

$$I(\omega) = \int d\omega_{as} d^2\omega_p d\omega_s |\chi^{(3)}_{CARS}|^2 g(\omega - \omega_{as}) S_p^2(\omega_p) S_s(\omega_s) \delta(\omega_{as} - 2\omega_p + \omega_s). \tag{2.14}$$

The $S_i(\omega_i)$ are the normalised spectral density functions for the lasers, ω_{as} is the anti-Stokes frequency, and $g(\omega - \omega_{as})$ is the normalised response function of the intensified diode array. Usually the normalised spectral density function of the pump laser is modelled by a delta function or a narrow Gaussian, while in the early stages of the development of CARS, the diode array response function was usually modelled by a Gaussian or a Lorentzian function. More modern CARS experiments usually use a Voigt profile to model the diode array response function.

2.2 Conventional Methods of Fitting CARS Spectra

The conventional way of comparing experimental spectra with a library of theoretical spectra involves finding the minimum of the sum of squares of the residuals, i.e.

$$\alpha_{min} = \min [\sum_{j=1}^{N} (f_j^{exp} - f_j^{th})^2].$$

There are some theoretical objections and practical limitations to this method of finding the minimum. Least squares minimisation is valid only if the errors of observation are normally distributed and are uncorrelated. The practical limitations are encountered when the experimental data has a high noise level. There is the question of how to normalise the spectra f^{exp} and f^{th} before finding α_{min}. The normal equations are non-linear. Therefore, calculating α_{min} is computationally time-consuming, and there are often convergence difficulties. Furthermore, if the data are noisy, the convergence criteria are difficult to satisfy. Finally, the two sets of data being compared have to be shifted relative to each other repeatedly in order to find the appropriate minimum.

This chapter presents a simpler numerical method of comparing experimental spectra against a library of theoretical spectra. The method uses a cross-correlation technique, and appears to be less sensitive to experimental noise, enabling the comparison of two sets of experimental spectra. Indeed, Chapter 4 presents the use of this method in the analysis of CARS spectra from a running engine, compared directly with a set of spectra taken from a calibrated high pressure high temperature (HPHT) cell.

2.3 Definition and Properties of the Cross-Covariance Function

The cross-covariance or cross-correlation function is defined for two general functions $f(t)$ and $g(t)$ to be

$$i(t) = \int_{-\infty}^{\infty} f(\tau)g(\tau - t)d\tau. \tag{2.15}$$

The functions $f(t)$ and $g(t)$ must be $\mathcal{L}^2$ integrable. The normalised cross-covariance function $I(t)$ can be defined by

$$I(t) = \frac{\int_{-\infty}^{\infty} f(\tau)g(\tau - t)d\tau}{\sqrt{\int_{-\infty}^{\infty} \mid f(t) \mid^2 dt \int_{-\infty}^{\infty} \mid g(t) \mid^2 dt}}. \tag{2.16}$$

$i(t)$ is very closely related to the Fourier convolution function $[f \otimes g](t)$ which is defined as

$$[f \otimes g](t) = \int_{-\infty}^{\infty} f(\tau)g(t - \tau)d\tau.$$

The convolution function has the property that when Fourier transformed,

$$\mathcal{F}[f \otimes g](\omega) = F(\omega)G(\omega).$$

The Fourier transform of $I(t)$ is given by

$$\mathcal{F}I(\omega) = \frac{-F(\omega)G^*(\omega)}{\sqrt{\int_{-\infty}^{\infty} \mid f(t) \mid^2 dt \int_{-\infty}^{\infty} \mid g(t) \mid^2 dt}} \tag{2.17}$$

$$= \frac{-2\pi F(\omega)G^*(\omega)}{\sqrt{\int_{-\infty}^{\infty} \mid F(\omega) \mid^2 d\omega \int_{-\infty}^{\infty} \mid G(\omega) \mid^2 d\omega}}. \tag{2.18}$$

where F(ω) and G(ω) are the Fourier transforms of $f(t)$ and $g(t)$ respectively, and are defined as

$$F(\omega) = \int_{-\infty}^{\infty} f(t)e^{-i\omega t}dt$$

and

$$f(t) = \frac{1}{2\pi}\int_{-\infty}^{\infty} F(\omega)e^{i\omega t}d\omega.$$

The normalised cross-covariance function can be used directly to compare mathematical functions. For $f(t) = g(t)$, the cross-covariance function becomes the auto-correlation function.

The normalised cross-covariance function $I(t)$ is really a fitting function of the function $g(\tau)$ against the function $f(\tau)$, where t serves as a shifting parameter. The maximum of the function $I(t)$ occurs at the point t where the functions $f(\tau)$ and $g(\tau - t)$ are maximally overlapped with each other. Furthermore, as $g(\tau - t)$ approaches $f(\tau)$ in functional form, $I(t)$ approaches the value 1.

2.4 The Discrete Cross-covariance Function

When the functions that are to be compared with each other exist in the form of discrete real data F_i and G_i, then the normalised cross-covariance function must be converted to a summation over the data in the form

$$I_i = \frac{\sum_{j=i+1}^{N} F_j G_{j-i}}{\sqrt{\sum_{j=i+1}^{N} F_j^2 \sum_{j=1}^{N-i} G_j^2}} \tag{2.19}$$

for $i \geq 0$, and for $i < 0$,

$$I_i = \frac{\sum_{j=1}^{N+i} F_j G_{j-i}}{\sqrt{\sum_{j=1}^{N+i} F_j^2 \sum_{j=1-i}^{N} G_j^2}}. \tag{2.20}$$

This form of the cross-covariance function is very simple to calculate numerically. I_i will have its maximum value when the two functions F_i and G_i are maximally overlapped. For functions with a single prominent maximum, such as CARS spectra, the numerical calculation can be significantly shortened. Instead of calculating I_i for all i, one can initially shift G_{j-i} so that its maximum coincides with that of F_j, and then calculate I_i for a limited set of values around this coincidence point. There must, of course, be a procedure for checking that I_i converges to its maximum value.

The normalised cross-covariance method of fitting discrete data functions is equivalent to the non-linear least squares fitting method with appropriate normalisation. This can be seen from the following: If we are dealing with two discrete dat functions F_i and G_i, then the normalised non-linear least squares minimisation criterion can be written

$$\alpha_{min}^{j} = \min \left[\sum_{i=1}^{N-j} \left(\frac{F_i}{\sqrt{\sum_{k=1}^{N-j} F_k^2}} - \frac{G_{i+j}}{\sqrt{\sum_{k=j}^{N} G_k^2}}\right)^2\right]. \tag{2.21}$$

In the expression above, a shifting parameter j has been put in explicitly to facilitate the minimisation of α, and both functions F_i and G_i have been mean square normalised. Now, by multiplying the argument of the summation out, equation 2.21 can be written in the form

$$\alpha_{min}^{j} = \min \left(2 - 2\frac{\sum_{i=1}^{N-j} F_j G_{j+i}}{\sqrt{\sum_{i=j}^{N-j} F_j^2 \sum_{i=j}^{N} G_j^2}}\right). \tag{2.22}$$

The minimum of α occurs when the term

$$\beta = \frac{\sum_{i=1}^{N-j} F_j G_{j+i}}{\sqrt{\sum_{i=j}^{N-j} F_j^2 \sum_{i=j}^{N} G_j^2}} \tag{2.23}$$

is maximum. The expression above for β is just the discrete normalised cross-covariance function defined in equation 2.19. β reaches its maximum value when $F_i = G_i$, and then $\beta_{max} = 1$. Clearly, when $\beta_{max} = 1$, $\alpha_{min} = 0$.

Therefore the minimisation of the normalised sum of squares of differences is transformed to a simpler, linear, and more systematic method of maximising the normalised cross-covariances. Convergence of the normalised cross-covariances is straightforward.

Multi-parameter non-linear least squares fitting techniques are valid if the off-diagonal elements in the variance-covariance matrix of parameter estimates is small. However, because of uncertain averaging (due to shot-to-shot instability of the dye laser), and correlated CARS data, data point variances cannot be accurately estimated. Therefore in CARS, non-linear least squares fitting techniques are acceptable only if one parameter (temperature) is being estimated. In such circumstances, the method of cross-covariance may also be used.

2.5 Fitting CARS Spectra

Usually CARS spectra are fitted by comparing a set of experimental spectra taken at the same temperature, against a library of theoretical spectra. The set of experimental spectra usually contains some mode noise, usually originating from the instability of the dye laser, or inhomogeneities in the target region.

The form of the normalised cross-covariance function is stable to random noise, as a result of the simple product of the spectral data points in I_i. The effects of random noise in I_i tend to be cancelled out when one takes the sum of the product terms in I_i.

Consequently, the advantage of using the normalised cross-covariance function for fitting CARS spectra is that the function is robust to random signal noise, it is easy to calculate numerically, it has desirable Fourier transform properties, the convergence criteria of the function are straightforward, and it provides an objective measure of goodness of fit.

2.5.1 Methods of Fitting CARS Spectra

There are two simple ways in which one would approach fitting CARS spectra using the normalised discrete cross-covariance function. These are determined by whether the analysis is done in the time domain, or the frequency domain.

The calculation of the non-linear susceptibility $\chi^{(3)}$ can be performed both in the frequency domain and the time domain.

The Time Domain

The instrument function of a spectrometer can usually be well represented by a Voigt function

$$H(\omega - \omega_0) = \frac{e^{-c(\omega-\omega_0)^2}}{(\omega-\omega_0)^2 + a^2}.$$

This can be Fourier transformed to the time domain giving

$$h(t) = e^{-at-\frac{1}{2}bt^2}.$$

If $\chi^{(3)}$ is calculated in the time domain, then the corresponding theoretical CARS spectrum $f(t)$ is given by the product $f(t) = \chi^{(3)}(t)h(t)$. The experimental CARS signal G_i is then also Fourier transformed from the frequency domain to the time domain. Following this, the Fourier transformed discrete cross-covariance function must be calculated, i.e.

$$\mathcal{F}^{-1}I_i(t) = \frac{-2\pi f_i g_i^*}{\sqrt{\sum_{j=i+1}^{N}|f_j|^2 \sum_{j=1}^{N-i}|g_j|^2}} \tag{2.24}$$

$I(t)$ is then Fourier transformed back to the frequency domain, where it now has the familiar form,

$$I_i(\omega) = \frac{\sum_{j=i+1}^{N} F_j G_{j-i}}{\sqrt{\sum_{j=i+1}^{N} F_j^2 \sum_{j=1}^{N-i} G_j^2}}. \tag{2.25}$$

I_i is now a function of frequency, and it is simple to find the maximum value of I_i. This maximum is just the best fit cross-covariance coefficient for the two spectra F_i and G_i.

If one has a library of theoretical spectra f_i^k for different temperatures defined by k, then it is simple to find the time domain discrete cross-covariance functions. They are just

$$\mathcal{F}^{-1}I_i^k(t) = \frac{-2\pi f_i^k g_i^*}{\sqrt{\sum_{j=i+1}^{N}|f_j^k|^2 \sum_{j=1}^{N-i}|g_j|^2}}. \tag{2.26}$$

These are then Fourier transformed back to the frequency domain,

$$I_i^k(\omega) = \frac{\sum_{j=i+1}^{N} F_j^k G_{j-i}}{\sqrt{\sum_{j=i+1}^{N}(F_j^k)^2 \sum_{j=1}^{N-i} G_j^2}}. \tag{2.27}$$

The maximum value of I_i^k for the shift parameter i, and for the temperatures k, then gives the best fit temperature of the experimental CARS spectrum against the library of theoretical CARS spectra at discrete temperatures. Following this, one can interpolate theoretical spectra for temperatures of smaller interval, and calculate cross-covariances from the comparison of the experimental CARS spectrum with the interpolated theoretical spectra. The maximum cross-covariance found in this way indicates the temperature of the system that the experimental CARS spectrum was obtained from.

Clearly, this is a more powerful method of fitting spectra than using the familiar non-linear least squares fit. The Fourier properties of the cross-covariance function are being exploited fully, and the relevant numerical code is more efficient when utilised in this way. The principal computational burden in doing these calculations comes from the need to perform multiple Fourier transforms. This burden can be offset by the development of hardware Fast Fourier Transforms, but this was not used here.

The Frequency Domain

If the library of theoretical spectra is calculated in the frequency domain, then it is a rather simple matter to deduce the temperature of the experimental spectrum under examination. If the experimental spectrum under examination is G^i, and the library of theoretical spectra are given by F_i^k, then the cross-covariance function is given by equations 2.19 and 2.20.

It is not necessary to calculate the entire cross-covariance function for all the data points. Only the discrete values of the function from the points around the coincidence of the maxima of the two spectra need to be calculated. The maximum of the cross-covariance function occurs within a small neighbourhood of the coincidence of the maxima of the spectra being fitted.

The Program SPECFIT

A program named SPECFIT was written, which reads in either an averaged experimental CARS spectrum, or a set of experimental spectra, defined by the user, and a set of reference spectra from a library. It then calculates the normalised cross-covariance function for ten data points to the right and to the left of the coincidence of the maxima of the two discrete spectra to be compared.

Following this, the program then finds the maximum of the cross-covariance function for these data points, and systematically checks for smooth convergence of the function to the maximum. The calculation is repeated for all of the spectra in the reference library. Then the cross-covariance coefficients are compared, and the maximum cross-covariance coefficient and the corresponding temperature is stored. The program then fits a cubic polynomial to the cross-covariances around the maximum as a function of the corresponding temperature data points, and then finds the maximum of the cubic polynomial, and the corresponding temperature. This temperature, and the corresponding maximum of the cross-covariance is then stored as the data associated with that shot.

This calculation is performed for all of the single-shot spectra, or for the single averaged spectrum, depending on the choice of the user. Therefore, a

maximum cross-covariance coefficient and corresponding temperature is stored for each of the spectra being analysed. Finally, the program calculates the mean temperature from all of the spectrum temperatures, the standard error, and the error in the estimate of the true mean.

2.6 Direct Fitting of Experimental Spectra

As a consequence of the theoretical and computational limits of the ONERA computer code for CARS spectra at high pressures [104] (the theory was not tested at high pressures), alternative methods of deducing the temperatures from spectra taken in high pressure combustion environments had to be found.

The CARS Research Group at U.C.T. had already decided to build the HPHT cell, and generate a database of experimental spectra. It was decided that this database could be used directly for the deduction of temperatures from high pressure combustion environments, as long as these spectra were taken from environments that could be reproduced within the HPHT cell, and that the HPHT cell spectra were sufficiently stable. It was of concern that signal noise within the two sets of experimental spectra would cause serious convergence problems during data analysis. It was with this concern in mind that the cross-covariance technique of fitting spectra was developed, and the particular problem of stability and convergence of best fit criteria carefully studied.

The U.C.T. CARS group experimented with a range of laser dyes, focussing on the problem of dye laser stability [65]. It was found that the most stable dye for shot-to-shot reproducibility that could be used with the SOPRA dye laser was sulpho-rhodamine. The use of this dye sacrifices output power, but for the HPHT cell experiment, and the creation of an experimental spectrum database, shot-to-shot reproducibility from the dye laser was considered to be

more important than output power.

2.6.1 An Example of Fitting Two Sets of Experimental Spectra

In order to judge the advantages of the method of cross-covariance, it is necessary to present a few typical examples of the use of the method. For this purpose, sets of referenced single shot spectra taken during the HPHT cell experiment were compared against a database of different averaged experimental spectra. It is instructive to compare these individual cross-covariances with the cross-covariances attained when using a model database. These examples also serve as a test of the thermal stability of the HPHT cell.

The sets of spectra presented below were fitted against a database of averaged HPHT spectra taken at 7.0 bar at temperatures of around 425^o C. The CARS optical layout was realigned a number of times between the days the two sets of spectra were taken. The focussing conditions could have been different for the two sets of spectra, but as will be seen from the table below, the focussing and alignment for the two data sets was almost identical. These examples therefore serve as a realistic test of the cross-covariance method for comparing the results of one experiment against the results of another experiment.

The tables below show shot-by-shot statistics using the cross-covariance method. The first column specifies the shot number, the second column specifies the interpolated temperature for the specified shot, the third column specifies the interpolated maximum cross-covariance coefficient. The fourth column specifies the discrete experimental temperature for which the calculated cross-covariance coefficient is maximum, and the fifth column specifies the maximum calculated cross-covariance coefficient.

The data presented below was statistically analysed in two different ways. The first way was to use the program SPECFIT as specified above, using a cubic interpolation method for the four largest cross-covariances, in order to find the maximum cross-covariance, and the correponding temperature. The second method, which was not as rigorous as the first, was to define the shot temperature for a specified shot as that experimental temperature for which the calculated cross-covariance was maximum. This method means that the temperatures are put into separate bins of bin interval 25° C. These two methods of analysing the data are then compared.

Figures 2.1 and 2.2 present the averaged spectra fitted against each other for the data presented in Tables 2.1 and 2.2.

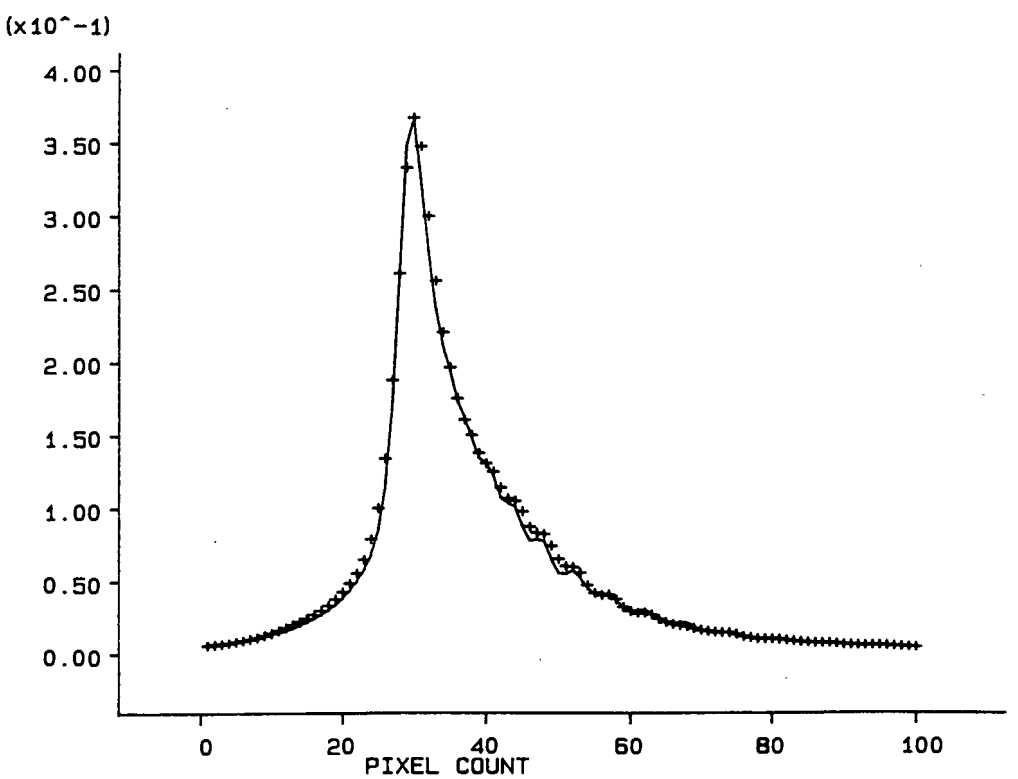

Figure 2.1: Averaged CARS spectra for T = 400°C, P = 7.0bar

Data Set No. 1:- HPHT Cell Temperature = $400^{o}C \pm 15^{o}C$, Pressure = 7.0 bar

The maximum cross-covariance from comparing the averaged spectra taken from the HPHT cell in the same conditions, but on different days, with different alignment was found to be

$\bar{I}_{max} = 0.99878,$

$T^{(1)}_{CARS} = 391.1^{o}C \pm 5.2^{o}C,$

$T^{(2)}_{CARS} = 392.0^{o}C \pm 5.9^{o}C.$

Shot no.	Temp. (Interp.) Celsius	max.c-c. (Interp.)	Temp. (Exp.) Celsius	max.c-c. (Exp.)
1	402	.99831	400	.99829
2	355	.99834	350	.99831
3	368	.99725	375	.99723
4	357	.99835	350	.99832
5	355	.99869	350	.99867
6	353	.99774	350	.99773
7	476	.99738	475	.99738
8	351	.99692	350	.99692
9	354	.99784	350	.99782
10	300	.99795	300	.99795

Shot no.	Temp. (Interp.) Celsius	max.c-c. (Interp.)	Temp. (Exp.) Celsius	max.c-c. (Exp.)
11	395	.99707	400	.99701
12	361	.99737	375	.99730
13	402	.99603	400	.99602
14	352	.99904	350	.99904
15	361	.99889	350	.99881
16	456	.99624	450	.99622
17	353	.99823	350	.99822
18	404	.99865	400	.99861
19	401	.99915	400	.99915
20	403	.99718	400	.99717
21	401	.99837	400	.99837
22	403	.99910	400	.99908
23	356	.99795	350	.99791
24	401	.99768	400	.99768
25	402	.99878	400	.99876
26	394	.99797	400	.99788
27	403	.99610	400	.99608
28	411	.99799	400	.99797
29	396	.99878	400	.99875
30				
31				
32				

Shot no.	Temp. (Interp.) Celsius	max.c-c. (Interp.)	Temp. (Exp.) Celsius	max.c-c. (Exp.)
33	432	.99642	425	.99637
34	405	.99501	400	.99488
35	432	.99833	425	.99828
36	400	.99378	400	.99378
37	467	.99674	475	.99671
38	405	.99679	400	.99672
39	403	.99832	400	.99831
40	474	.99444	475	.99444
41	404	.99573	400	.99571
42	401	.99917	400	.99917
43	351	.99874	350	.99874
44	356	.99903	350	.99901
45	353	.99871	350	.99871
46	353	.99916	350	.99915
47	402	.99805	400	.99804
48	397	.99860	400	.99857
49	396	.99609	400	.99604
50	423	.99830	425	.99829

Table 2.1: Cross-covariances from comparison of CARS spectra at T = $400^{o}C$, P = 7.0bar

Data Set No. 2:- HPHT Cell Temperature = $425^oC \pm 15^oC$, Pressure = 7.0 bar

$\bar{I}_{max} = 0.99880,$

$T^{(1)}_{CARS} = 424.0^oC \pm 8.7^oC,$

$T^{(2)}_{CARS} = 422.4^oC \pm 8.8^oC.$

Shot no.	Temp. (Interp.) Celsius	max.c-c. (Interp.)	Temp. (Exp.) Celsius	max.c-c. (Exp.)
1	300	.99858	300	.99858
2	300	.99790	300	.99790
3	469	.99804	475	.99801
4	432	.99856	425	.99845
5	353	.99952	350	.99951
6	401	.99792	400	.99792
7	300	.99832	300	.99832
8	425	.99852	425	.99852
9	300	.99849	300	.99849
10	300	.99733	300	.99733
11	351	.99863	350	.99863
12	429	.99885	425	.99884

Shot no.	Temp. (Interp.) Celsius	max.c-c. (Interp.)	Temp. (Exp.) Celsius	max.c-c. (Exp.)
13	505	.99805	500	.99803
14	432	.99763	425	.99756
15	403	.99906	400	.99902
16	525	.99719	525	.99719
17	525	.99610	525	.99610
18	464	.99848	450	.99839
19	472	.99778	475	.99778
20	401	.99889	400	.99888
21	432	.99855	425	.99842
22	430	.99629	425	.99921
23	477	.99806	475	.99806
24	468	.99762	475	.99759
25	448	.99779	450	.99779
26	490	.99735	500	.99732
27	403	.99734	400	.99732
28				
29	468	.99879	475	.99876
30	433	.99881	425	.99871
31	434	.99856	425	.99842
32	430	.99888	425	.99883
33	432	.99828	425	.99822
34	470	.99806	475	.99804

Shot no.	Temp. (Interp.) Celsius	max.c-c. (Interp.)	Temp. (Exp.) Celsius	max.c-c. (Exp.)
35	481	.99742	475	.99740
36	468	.99797	475	.99793
37	475	.99783	475	.99783
38	300	.99746	300	.99746
39	427	.99853	425	.99853
40	466	.99822	475	.99818
41	430	.99887	425	.99885
42	433	.99820	425	.99810
43	353	.99902	350	.99901
44	479	.99803	475	.99802
45	348	.99830	350	.99830
46	395	.99795	400	.99782
47	431	.99839	425	.99833
48	434	.99824	425	.99813
49	481	.99696	475	.99694
50	471	.99889	475	.99888

Table 2.2: Cross-covariances from comparison of CARS spectra at T = $425°C$, P = 7.0bar

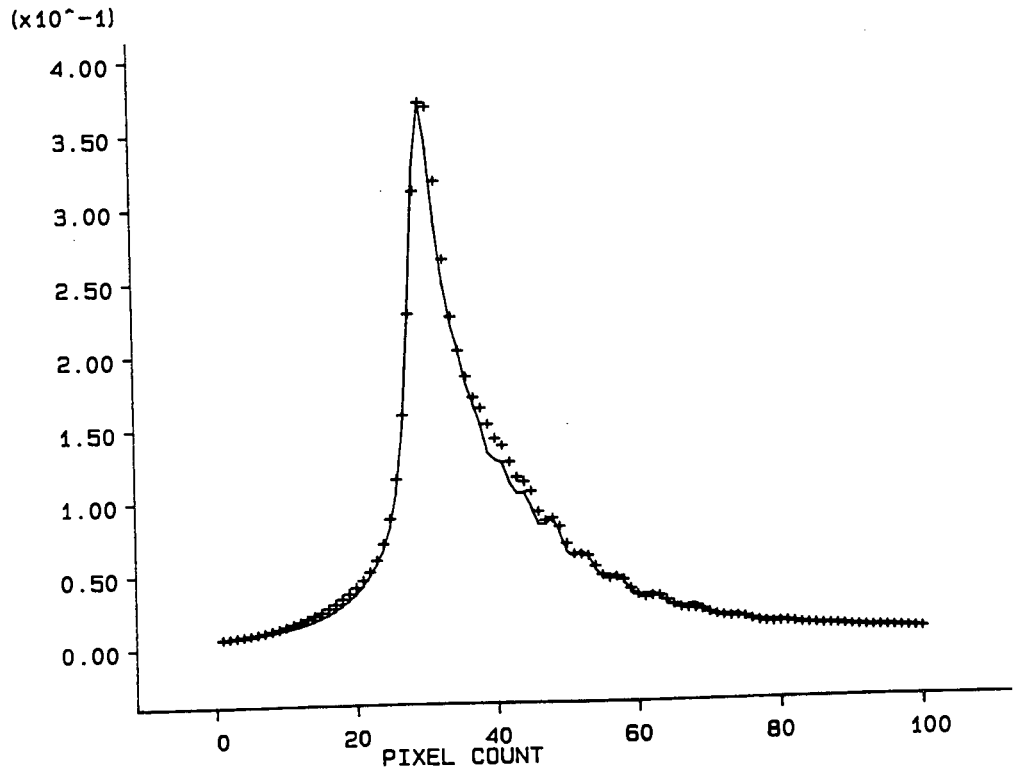

Figure 2.2: Averaged CARS spectra for T = 425°C, P = 7.0bar

Discussion of HPHT Data Statistics

It is clear from the data statistics presented above that putting the data into discrete bins, and deriving statistics from the binned data gives almost identical results when compared with the more rigorous method of finding interpolated temperatures for each shot, and then calculating the group statistic. This was confirmed from an analysis of many data sets similar to those presented above, for a wide range of HPHT temperatures and pressures.

Consider also the interpolated maximum cross-covariances and the discrete maximum cross-covariances, as compared with cross-covariances of the same

data with EGL model spectra presented in Chapter 3. The maximum cross-covariances presented above are consistently higher than those calculated when the HPHT data are compared with the EGL model spectra. Furthermore, the maximum systematic error in the HPHT database is $\pm 15^{o}C$ at all pressures, whereas model spectral calculations can systematically overestimate or underestimate pressure narrowing effects, and thereby generate much greater systematic errors when deducing temperatures (see section 3.5 of chapter 3).

2.6.2 Problems of Focussing

When CARS experiments are performed, the optical alignment is always a delicate procedure. The final test of optimal alignment is the quality of the focussed CARS signal on the optical detector, in this case an intensified diode array. The test of optimal alignment in CARS work is usually the width of the Nd:Yag signal on the OMA, and the width of a room temperature CARS spectrum on the OMA. Every different experiment performed needs a new alignment of the optics, and often alignment needs to be repeated daily for the same experiment.

Repeated alignment during CARS experiments can change the focussing of the CARS signal onto the optical detector from experiment to experiment. Therefore if the CARS results from one experiment are to be compared with the CARS results from another experiment, the possibility of different focussing conditions for the two experiments must be taken into account.

The best way of taking different focussing into account is through the instrument function. Essentially, the instrument function has been changed if the focussing conditions of the experiment were changed. The instrument function is usually modelled by a Voigt function in the frequency domain, which

is Fourier transformed to

$$h(t) = e^{-at-\frac{1}{2}bt^2}$$

in the time domain. Different focussing conditions change the shape of $h(t)$, either broadening it in the case of finely focussed conditions, or narrowing it in the case of coarsely focussed conditions.

In order to match the focussing conditions of two different experiments, the instrument function $h(t)$ needs to be matched for the two experiments. If the two experiments have instrument functions $h_1(t)$ and $h_2(t)$, then they can be matched by broadening or narrowing $h_1(t)$ to fit $h_2(t)$.

2.6.3 Empirical Broadening

Given the instrument functions for two separate experiments $h_1(t)$ and $h_2(t)$ such that

$$h_1(t) = e^{-a_1t-\frac{1}{2}b_1t^2}$$

$$h_2(t) = e^{-a_2t-\frac{1}{2}b_2t^2}$$

Assuming that $b_2 > b_1$, the instrument function for experiment 2 is broader than the instrument function for experiment 1 in the frequency domain. This means that the focussing is finer for experiment 1 than for experiment 2. The consequence of this is that a room temperature CARS spectrum taken during experiment 1 will be observed to have a narrower width than a room

temperature CARS spectrum taken during experiment 2. In order to compare the results from the two experiments directly, it is necessary to broaden the instrument function from experiment 1 to match the instrument function of experiment 2.

This is done in the time domain by multiplying $h_1(t)$ by a Gaussian factor e^{-ct^2}. The narrowing parameter c in the time domain serves to broaden the Gaussian part of the instrument function in the frequency domain to the point where the two instrument functions match. The width of the Voigt profile is dominated by the Gaussian term, and so it is natural to broaden the instrument function by using an appropriate Gaussian narrowing parameter.

Practically this means the following. A room temperature CARS spectrum is taken during the two experiments. The results are contained in the discrete data functions F_i and G_i. The spectral information contained in the two room temperature spectra are identical. The only difference between the two spectra is the focussing, and hence the instrument functions. The spectrum to be broadened, F_i, is Fourier transformed to the time domain to yield f_i. This spectrum is then multiplied by a Gaussian factor to give

$$f_i^c = f_i e^{-ci^2}.$$

f_i^c is then Fourier transformed back to the frequency domain to the data function F_i^c. This data function is then fitted to the data function G_i using the normalised cross-correlation fit. In this way the time domain narrowing parameter c can be optimised to match the room temperature CARS spectra, and hence the focussing conditions of the two experiments.

Following this, the complete set of spectra taken during experiment 1 can be broadened, matching the focussing conditions for the two experiments. This

means that the spectra from the two experiments can finally be compared with each other directly.

The Program COFIT

A program named COFIT was written, which reads in two spectra taken under the same pressure and temperature conditions, but with different focussing conditions. It then Fourier transforms the spectrum to be broadened to the time domain using the Fast Fourier Transform from the HARWELL subroutine library. The spectrum is then represented discretely in the time domain. The discrete data file is then multiplied by the aforementioned Gaussian narrowing term. The altered time domain spectrum is then Fourier transformed back to the Frequency domain, and fitted against the other experimental spectrum.

This procedure is performed for a range of broadening parameters chosen by the user, and in this way the optimal broadening parameter is found.

The Program ALTSP

After finding the optimal broadening parameter, the entire set of spectra from experiment 1 can be broadened to match the focussing conditions of experiment 2.

The program ALTSP was written, which reads in the optimal broadening parameter, and the database of experimental or theoretical spectra to be broadened. The program then Fourier transforms each spectrum from the database, from the frequency domain to the time domain. It then multiplies the time domain spectrum by the appropriate Gaussian narrowing term, and then Fourier transforms the modified spectrum back to the frequency domain. This gives

rise to a whole set of spectra that can now be compared to the spectra in experiment 2 directly.

An Example of Empirical Broadening

Room temperature, atmospheric pressure spectra were taken during the CARS engine experiment, and the HPHT experiment referred to in the last chapter. Focussing conditions for the two experiments were different, as can be deduced from the normalised cross-covariance fit of the averaged spectra against each other. The maximum cross-covariance coefficient for given sets of spectra from the two experiments was found to be $I_{max} = 0.9864$. This is not a good fit for comparable spectra. This can be seen from a comparison of this figure with maximum cross-covariances resulting from fitting averaged spectra taken during the same experiment with the same focussing conditions.

Typical maximum cross-covariances for such spectra are found to exceed 0.999. Furthermore, maximum cross-covariances for fitting model spectra with appropriately averaged experimental spectra typically satisfy $0.990 < I_{max} < 0.999$ [102]. Thus the low coefficient given above reflects the different focussing conditions for the two experiments.

When the averaged HPHT spectrum was empirically broadened, using the programs COFIT and ALTSP, in order to match the focussing of the two experiments, the optimal broadening parameter was found to be $c = 0.00136$ pixel^2, and the corresponding maximum cross-covariance coefficient was $I_{max} = 0.9961$. This is a great improvement over the previous figure of 0.9864, and compares favourably with fully optimised model fitting maximum cross-covariances [102].

Figure 2.3(a) shows the fit of the averaged room temperature, atmospheric

pressure spectra obtained from inside the internal combustion engine, and from the HPHT cell. The two averaged spectra were obtained with different focussing conditions in the two experiments, and this accounts for the poor fit.

Figure 2.3(b) shows the fit of the same two, averaged, room temperature, atmospheric pressure spectra, with the averaged HPHT spectrum empirically broadened to match the focussing conditions of the two experiments, in the way described above. Clearly, the fit is much improved.

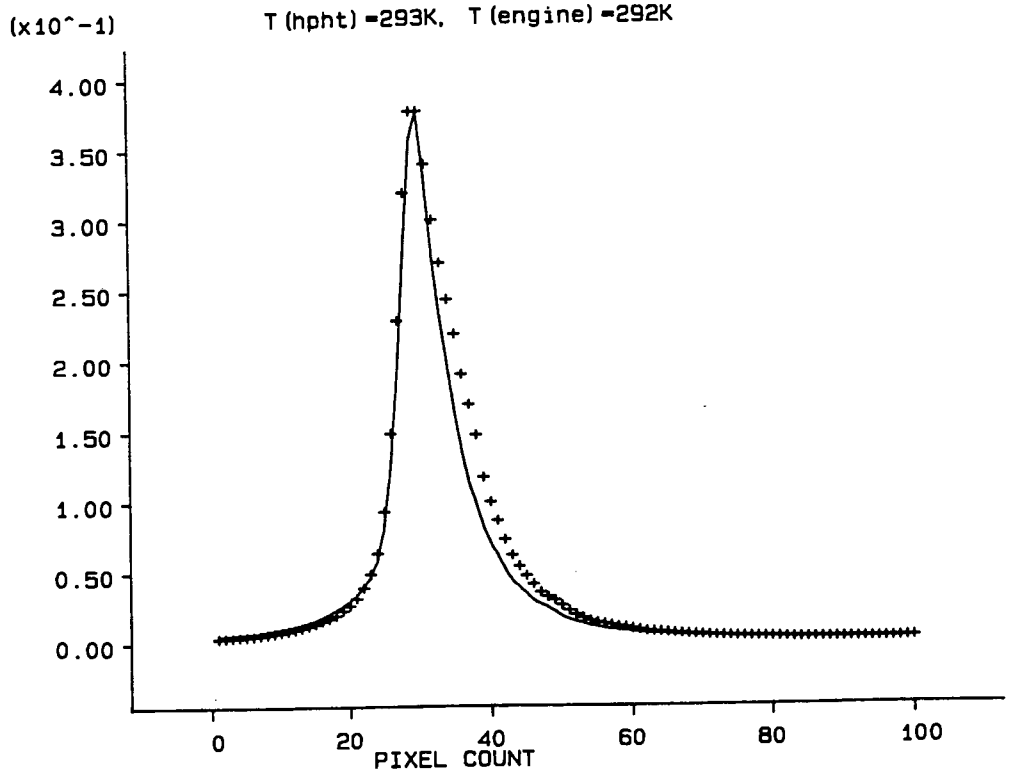

Figure 2.3(a): Averaged spectra obtained from s.i. research engine and HPHT cell at room temperature, atmospheric pressure with different focussing conditions.

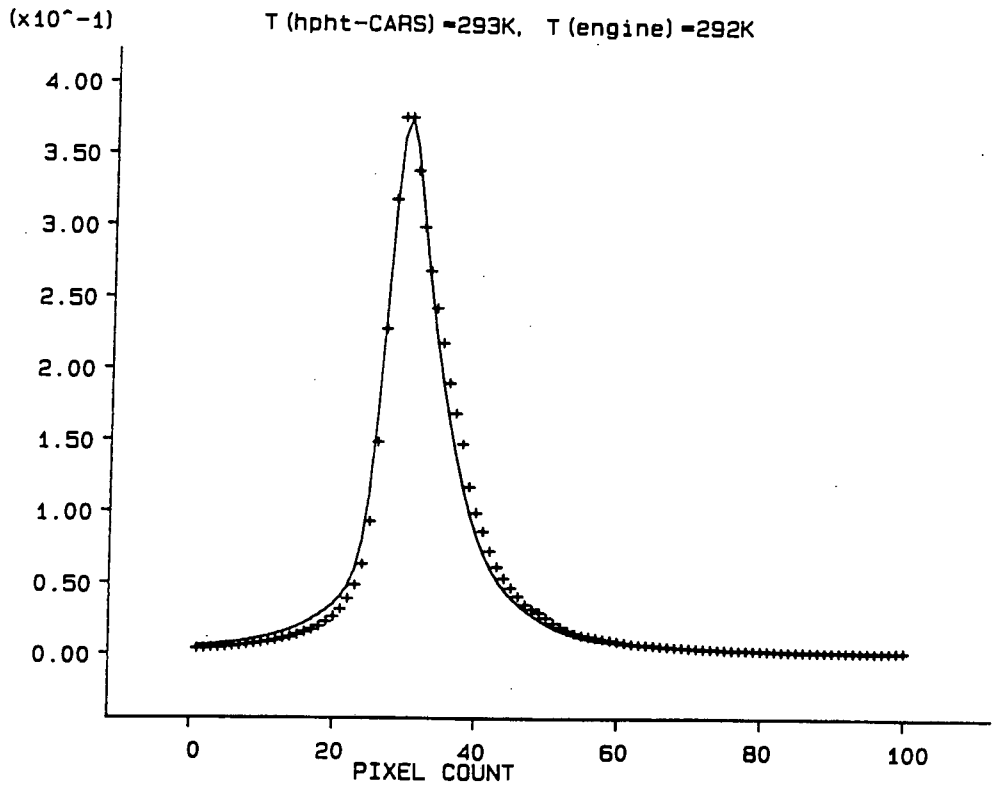

Figure 2.3(b): Averaged spectra obtained from s.i. research engine and HPHT cell at room temperature, atmospheric pressure with matching focussing.

Indeed, The following table shows the shot statistics for a set of referenced spectra taken in the internal combustion engine at known pressure, and compared directly with a library of empirically broadened averaged spectra of known temperatures, at the same pressure. Note the predicted temperatures of the single shot spectra, and the corresponding cross-covariances. Many of the single shot spectra have cross-covariances $I^i_{max} > 0.998$. These cross-covariances are significantly higher than those that occur during fitting of experimental spectra to established model spectra [102].

CARS Engine Data Set: Temperature $= 358.3°C \pm 8.9°C$**, Pressure** $= 7.2 \pm 0.2$ **bar**

Shot no.	Temperature Celsius	max.c-c.	Shot no.	Temperature Celsius	max.c-c.
1	325	.99782	16	400	.99592
2	450	.99754	17	300	.99863
3	375	.99798	18	300	.99825
4	300	.99842	19	350	.99535
5	375	.99850	20	300	.99772
6	375	.99810	21	350	.99878
7	300	.99874	22	400	.99910
8	400	.99839	23	375	.99899
9	300	.99703	24	450	.99813
10	375	.99900	25	450	.99709
11	300	.99824	26	375	.99792
12	325	.99612	27	375	.99883
13	300	.99857	28	400	.99689
14	400	.99750	29	300	.99843
15	400	.99620	30	325	.99892

Table 2.3: Cross-covariance data from comparison of engine spectra with broadened, averaged HPHT spectra at 7.2 ± 0.2 bar

Figure 2.4 shows the best fit of the averaged spectrum obtained from the engine (data presented above) against the broadened, averaged HPHT spectrum

corresponding to the deduced temperature.

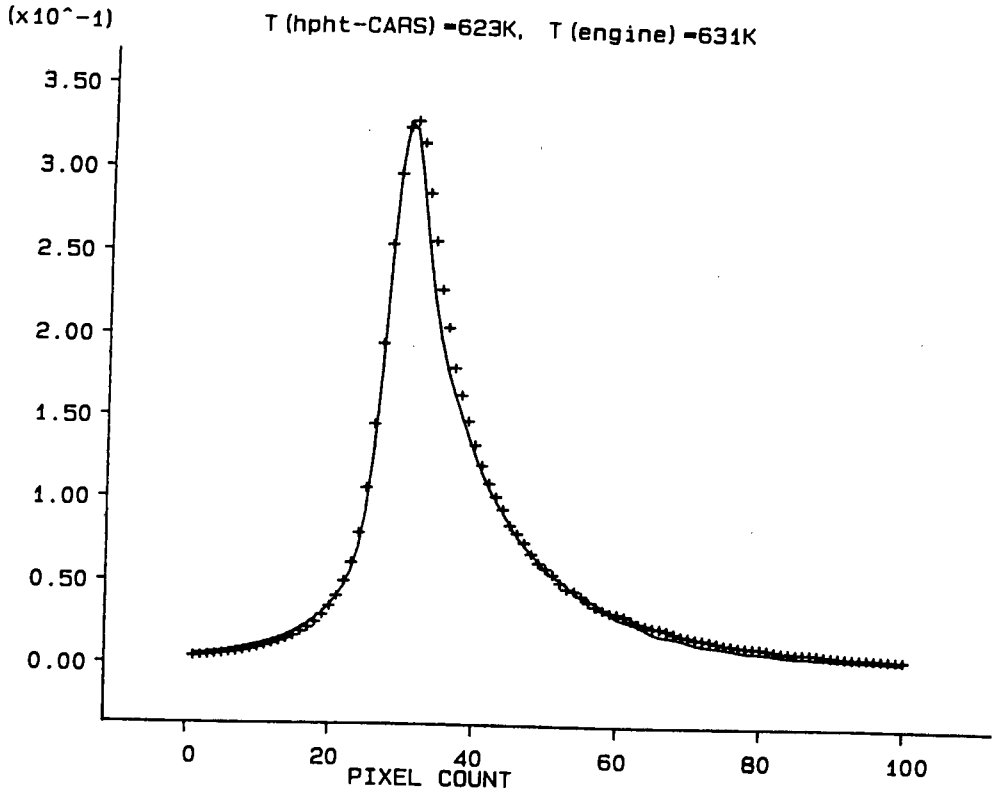

Figure 2.4: Averaged spectra obtained from s.i. research engine and HPHT cell at P = 7.2 ± 0.2bar.

The cross-covariances from the comparison of the engine CARS spectra with the HPHT spectra are larger than the cross-covariances obtained from the comparison between the engine CARS spectra and both EGL and ONERA hard collision model spectra, indicating a better fit for the HPHT data. For comparison, see section 3.5 in chapter 3 on the experimental evaluation of the ONERA hard collision model and the EGL model.

Chapter 3

The High Pressure High Temperature Cell Experiment

3.1 A Review of the Theory of Collision Broadening and Pressure Narrowing in CARS Spectra

This subject is reviewed in some detail by Greenhalgh [53]. This section follows Greenhalgh's review to some extent, but there are some topics that are considered in more detail here.

In 1980, Hall et al published a study of pressure induced narrowing of the CARS spectrum of N_2 [60], where they presented a relatively simple method for calculating Q-branch nitrogen CARS spectra. This method was based on Gordon's semi-classical theory of rotational band contours in microwave, infra-red and Raman spectra [49] [50]. Gordon's theory is a generalisation of

Baranger's impact calculation for atomic spectra, and is non-perturbative in approach.

Gordon defined a normalised spectral intensity $\hat{I}(\omega)$ as the Fourier transform of the correlation function for the direction of the dipole moment,

$$< \vec{u}(0) \cdot \vec{u}(t) >= \int_{-\infty}^{\infty} \hat{I}(\omega) e^{i\omega t} d\omega, \tag{3.1}$$

and

$$\hat{I}(\omega) = \frac{\epsilon(|\omega)|)}{\omega[1 - exp(-\hbar\omega/kT)]} / \int_{-\infty}^{\infty} \frac{\epsilon(|\omega|)}{\omega[1 - exp(-\hbar\omega/kT)]}, \tag{3.2}$$

where $\epsilon(\omega)$ is the absorption coefficient at the frequency ω and kT is the thermal energy.

The motion of the dipole moment for times long compared with the duration of a collision can be considered in terms of the complete collisions that occur in the time interval from 0 to t. In order for the impact theory to be valid, the collision process is considered to occur in a time Δt such that $\Delta t << t$. Therefore the molecule is considered to evolve freely for most of the time interval between collisions. The effect of one of these complete collisions is to transfer a molecule in a specific initial state, to a specific final state after the collision. Impact theory assumes that the velocities of successive collisions are uncorrelated and randomly chosen from a thermal distribution. Gordon showed that the transfer of line strength between the lines is a Markov random process, and that the correlation function $< \vec{u}(0) \cdot \vec{u}(t) >$ has the form

$$< \vec{u}(0) \cdot \vec{u}(t) >= \vec{d} \cdot exp[i(\tilde{\omega}_0 + i\tilde{\Pi})t] \cdot \tilde{P} \cdot \vec{d}. \tag{3.3}$$

$\tilde{\Pi}$ is a transition rate matrix for the amplitudes. The off-diagonal elements

of $\tilde{\Pi}$ give minus the rate at which a unit amplitude in one line is transferred to another line by collisions. The diagonal elements of $\tilde{\Pi}$ gives the rate at which the amplitude in a given line decreases due to transitions to all other lines. $\tilde{\omega}_0$ is a diagonal matrix whose elements are the absorption frequencies minus the emission frequencies of the free molecule. The diagonal matrix $\tilde{P}$ gives the populations of the initial states of the lines. Finally, $\vec{d}$ is a vector whose components are the reduced matrix elements of the dipole moment, corresponding to the various lines.

Gordon then wrote the matrix $\tilde{\Pi}$ in terms of collision cross sections. He defined a collisional transfer matrix $\tilde{S}$, whose *fi*th element gives the transition matrix element for a collisional transition from state i to state f. If the intermolecular collision frequency is τ^{-1}, then the transition rate is

$$\tilde{\Pi} = < \tau^{-1}(\tilde{I} - \tilde{S}) >_{coll} , \tag{3.4}$$

with the average taken over all types of collisions. The collision frequency has the usual value from kinetic theory,

$$\tau^{-1} = \rho v \pi b_0^2, \tag{3.5}$$

where ρ is the number density of perturber molecules, v is the relative velocity between molecules in the collision, and b_0 is an upper limit to the range of the intermolecular potential. Therefore,

$$\tilde{\Pi} = \rho \int_0^{b_0} 2\pi b db < v(\tilde{I} - \tilde{S}) >_{coll} . \tag{3.6}$$

The range b_0 may be taken to be large, and thus

$$\tilde{\Pi} = \rho\bar{v}\tilde{\sigma}, \tag{3.7}$$

where

$$\tilde{\sigma} = \bar{v}^{-1}\int_0^\infty 2\pi b db < v(\tilde{I} - \tilde{S}) >_{coll} . \tag{3.8}$$

The Fourier transform of the dipole correlation function may now be compared with an experimental spectrum in the frequency domain

$$\hat{I}(\omega) = \pi^{-1}\mathrm{Im}\ \vec{d}\cdot(\omega - \omega_0 - i\rho\bar{v}\tilde{\sigma})^{-1}\cdot\tilde{P}\cdot\vec{d}. \tag{3.9}$$

In the paper by Koszykowski et al [73] in 1985, a CARS spectrum probing the third-order susceptibility was expressed as

$$\hat{I}(\omega) = c\vec{d}\cdot\tilde{G}^{-1}\cdot\tilde{P}\cdot\vec{d}, \tag{3.10}$$

where c was defined as some scalar constant, $\vec{d}$ was a vector of dipole moment transition amplitudes, and $\tilde{P}$ was a diagonal matrix of population differences between the initial and final ro-vibrational states. They use what they call the G-matrix method, which is based on Gordon's results presented above, with the matrix $\tilde{G}(\omega)$ defined as

$$\tilde{G}(\omega) = -\omega\tilde{1} + \tilde{\omega}_0 + i\rho < v\sigma > , \tag{3.11}$$

$\tilde{1}$ is the identity matrix, ρ is the gas density, $\tilde{\omega}_0$ is the diagonal matrix of transition frequencies, ω is the spectral frequency being probed, and $< v\tilde{\sigma} >$ is the velocity averaged cross-section matrix. This matrix has a sign difference from the matrix defined in Gordon's method shown earlier. This is due to Koszykowsky's convention of taking emission frequencies as positive.

The G-matrix method was first used in the calculation of theoretical CARS spectra by Hall et al [60], where they presented the following expression for the non-linear susceptibility,

$$\chi^{(3)} = \sum_t \frac{iN\alpha_t}{\hbar} \sum_s \alpha_s \Delta\rho^{(0)} \tilde{G}_{ts}^{-1}, \tag{3.12}$$

where t and s denote the collection of ro-vibrational quantum numbers belonging to particular Q-branch transitions, $\Delta\rho^{(0)}$ is the unperturbed fractional population difference for transition s, and $\tilde{G}_{ts}$ is the G-matrix,

$$\tilde{G}_{ts}(\omega) = i(\omega_1 - \omega_2 - \omega_t)\delta_{ts} + (\Gamma_t/2 - i\Delta_t)\delta_{ts} + \gamma_{ts}(1 - \delta_{ts}). \tag{3.13}$$

ω_t, Γ_t, and Δ_t are the frequency, isolated linewidth, and line shift respectively, of collisional transition t, δ_{ts} is the delta function, and γ_{ts} is an off-diagonal linewidth parameter denoting the collisional transition rates. Γ_t, Δ_t and γ_{ts} are related to the collision (scattering) matrix $\tilde{S}$ in the following way:

$$\frac{1}{2}\Gamma_t - i\Delta_t = \int (1 - \tilde{S}^+_{t_1 t_1} \tilde{S}_{t_2 t_2}) F(g) dg, \tag{3.14}$$

$$\gamma_{ts} = - \int \tilde{S}^+_{t_1 s_1} \tilde{S}_{s_2 t_2} F(g) dg, \tag{3.15}$$

where the subscripts 1 and 2 refer to the initial and final states of the transitions t and s respectively.

For low gas pressures, the off-diagonal linewidths can be omitted from the G-matrix, to yield

$$\tilde{G}_{ts}^{-1} = \frac{\delta_{ts}}{i(\omega_1 - \omega_2 - \omega_t) + \Gamma_t/2}, \tag{3.16}$$

and therefore

$$\chi^{(3)} = \frac{2N}{\hbar} \sum_t \frac{\alpha_t^2 \Delta\rho_t^{(0)}}{2(\Delta\omega_{12} - \omega_t) - i\Gamma_t}. \tag{3.17}$$

This is the low pressure isolated lines approximation. For higher pressures, where lines overlap substantially, the complex G-matrix has to be numerically inverted. The **Exponential Gap Law** (EGL) was proposed as a simple model for the temperature dependence of the off-diagonal linewidth parameters. In this model the rate constant for the collisional transition $J \rightarrow J'$ is assumed to be proportional to the exponential of the rotational energy defect, i.e. for downward transitions,

$$\gamma_{J'J} = d_{J'} A_J exp(-C_J |\Delta E_{JJ'}|/kT), \tag{3.18}$$

where $d_{J'}$ is the rotational energy degeneracy of J', A_J and C_J are parameters, and $\Delta E_{JJ'}$ is the rotational energy defect. For upward transitions, the principle of detailed balance gives

$$\gamma_{JJ'} = d_{J'} A_J exp(-\Delta E_{JJ'}/kT) exp(-C_J|\Delta E_{JJ'}|/kT). \qquad (3.19)$$

The justification of the form of the EGL comes from linewidth measurements and calculations in hydrogen halides.

The theoretical spectra calculated in this way were compared with experimental spectra obtained at a temperature of 300 K from a high pressure vessel, using broadband colinear CARS. Bandwidths were measured with a high resolution monochromator as a function of pressure from one to one hundred atmospheres. They found reasonable agreement between the theoretical CARS widths and the experimental CARS widths, although there was a significant discrepancy for low pressures in the range of one to fifteen atmospheres.

Following Hall's paper [60], the EGL model was widely used in the calculation of spectra for high pressure CARS applications. In 1983, Kataoka et al [69] reported the results of a study for N_2 CARS thermometry at high pressure. They obtained experimental CARS spectra at high pressure and high temperature from the cylinder of a running engine, and fitted them to a library of theoretical spectra. They were able to show that the EGL CARS spectral widths followed the correct trends at high temperatures as a function of pressure. However, this paper does not accurately calibrate EGL spectra as a function of temperature and pressure.

In 1982, Hall and Greenhalgh [59] applied Gordon's rotational diffusion model [49] to the calculation of nitrogen CARS spectral intensities. This model was based on an impact strong collision approximation, which assumes that the rotational state of an optically active molecule is randomly changed after each collision. The approximation made in this model did not allow the rotational energy transfer rates to satisfy the principle of detailed balance. This lim-

its the accuracy of the approximation. However, they found good agreement with 300K nitrogen spectra over the pressure range one to one hundred atmospheres.

The paper of Koszykowski et al [73] discussed above was an important contribution to modelling pressure narrowing in CARS spectra. The authors compared high-resolution experimental CARS spectra with theoretical EGL CARS spectra at temperature 294 K, and at pressures one atmosphere, five atmospheres and ten atmospheres, and reported excellent agreement between the experimental data and the theoretical model. Furthermore, they presented a new computational method for calculating CARS spectral intensities at different temperatures and pressures, that involves only a single G-matrix diagonalisation and inversion per temperature and pressure.

Also in 1985, Greenhalgh et al [54] presented a polynomial energy-gap model for molecular linewidths. The model was intended as an improvement over the Hall et al energy gap law (EGL), and the Rosasco et al statistical power gap law (SGL). Beginning with the general form for the off-diagonal collisional transfer rates,

$$\gamma_{jk}(T,P) = Pg(T)\rho_j(T)f(\xi_{jk}), \tag{3.20}$$

where $\xi_{jk} = |E_j - E_k|^{-1}$, ρ_j is the fractional population of the j'th rotational state, and f and g were to be determined, they suggested the following expression,

$$\gamma_{jk}(T,P) = (P/T^A)\rho_j \sum_{l=0}^{n} c_l \xi_{jk}^l. \tag{3.21}$$

For a given temperature exponent A and polynomial order n, they determined the set of coefficients c_n by least squares fitting the accurate 298 K experimental N_2 isolated linewidth data from Rosasco et al [103]. They then varied A iteratively to give a simultaneous best fit to the high temperature data of Rahn et al [99]. They used the optimised PEG model to generate linewidths around 1000 K for computer modelling of CARS spectra, and compared the calculated spectra against experimental spectra obtained from a furnace of known temperature. They reported agreement between the theoretical and experimental spectra within limits of experimental accuracy.

In 1986, Rahn and Palmer [100] reported the results of studies of nitrogen self-broadening at high temperature with inverse Raman spectroscopy (IRS). They measured nitrogen Q-branch linewidths in pure nitrogen at temperatures up to 1500 K and at pressures from 20 torr to 760 torr using high resolution IRS. Transitions from $J = 0$ to $J = 30$ were measured with a resolution of $1.5 \times 10^{-3}\text{cm}^{-1}$ and a Raman shift accuracy of $1.0 \times 10^{-3}\text{cm}^{-1}$. The experiments were performed using a single mode pulsed pump laser to induce a small absorption in a single mode cw argon-ion probe laser beam through SRS. The pump and probe lasers were focussed in a crossed-beam configuration to a waist diameter of about 100μm inside a windowed furnace. They fitted the data using a Galatry line-shape model in order to provide J-dependent collisional broadening coefficients.

They proposed a new scaling law to describe the dependence of the collisional broadening coefficients on temperature and rotational quantum number. The off-diagonal collisional transition rates for transitions between rotational states i to j, with $i < j$ (upward transition) were presented as

$$\gamma_{ji} = \alpha P(\frac{T_0}{T})^n(\frac{1 + 1.5E_i/kT\delta}{1 + 1.5E_i/kT})^2\exp(-\beta\Delta E_{ij}/kT). \qquad (3.22)$$

This is the **Modified Exponential Gap Law** (MEGL). The rate of downward rotational transitions from state j to state i is determined from microscopic reversibility,

$$\gamma_{ij} = \frac{2J_i + 1}{2J_j + 1}\gamma_{ji}\exp(\Delta E_{ij}/kT). \tag{3.23}$$

The fitting parameters α, β and δ were determined from fits to inverse Raman spectra at 295 K. Comparisons were made between theoretical IRS lineshapes and experimental lineshapes over a range of temperatures, and agreement was considered to be excellent. It was noted that the scaling law discussed in this paper predicts collisional broadening coefficients for nitrogen only, and that models of Raman line shapes in practical combustion environments must ultimately account for broadening due to collisions with other collision partners.

An experimental evaluation of MEGL N_2 CARS spectra was conducted, using spectra obtained from a high pressure, high temperature cell. This evaluation is presented and discussed at the end of this chapter.

Also in 1986, Sala et al [104] reported on the development of a rotational thermalisation model for the calculation of collisionally narrowed isotropic Raman scattering spectra with application to the SRS N_2 Q-branch. This model calculates the rotational transition probabilities within the strong collision approximation, allowing the rotational energy transfer rates to be expressed in terms of the individual Q(J) line broadening coefficients. These transfer rates satisfy the principle of detailed balance, and unitarity of the S-matrix.

This rotational thermalisation model of Sala et al [104] was a more rigorous form of the Gordon rotational diffusion model when compared with earlier models [59], applied to the calculation of CARS or SRS spectra. It generalised

the model of Hall and Greenhalgh [59], satisfying both the principle of detailed balance and unitarity of the scattering matrix.

Further approximations concerning the rotational distribution of the collision frequency were made, enabling simpler expressions for the transfer rates, which did not necessarily satisfy both detailed balance and unitarity. They were able to derive a simple analytical expression for the collisional transfer rates. The argument was developed as follows:

The normalised spontaneous Raman (or SRS) isotropic Q-branch $v = 0 \rightarrow v = 1$ profile can be expressed as

$$F(\omega) = \frac{1}{\pi}|\bar{\alpha}_{01}|^2 \,\mathrm{Re}\,[\sum_{J,J'} p_J \tilde{G}^{-1}_{JJ'}(\omega)], \tag{3.24}$$

where $G_{JJ'}$ is the G-matrix, and is given by

$$\tilde{G}_{JJ'}(\omega) = i(\omega - \omega_{1J',0J'}\delta_{J'J}) + nW_{JJ'}. \tag{3.25}$$

$W_{JJ'}$ is the matrix element of the collisional (scattering) operator S specified earlier, for rotational transitions $J \rightarrow J'$ in both $v = 0$ and $v = 1$ vibrational states.

The strong collision model is a useful and simple model to use to calculate the collisional transfer rates. It assumes that each collision thermalises the rotational state of the Raman active molecule. In other words, the probability of a collision transfer from rotational state $J \rightarrow J'$ is assumed to be independent of J. Therefore, the energy transfer rates are of the form

$$W_{JJ'} = -\tau_J^{-1} f(J'), \tag{3.26}$$

where τ_J^{-1} is the rotational energy dependent collision frequency. The expression for $f(J)$ can be deduced from the normalisation condition

$$\sum_{J'} f(J') = 1, \tag{3.27}$$

and from the principle of detailed balance,

$$p_J W_{JJ'} = p_{J'} W_{J'J}, \tag{3.28}$$

$$f(J) = p_J \tau_J^{-1} / < \tau^{-1} > , \tag{3.29}$$

where the symbol $< \cdots >$ means

$$< \tau^{-1} >= \sum_J p_J \tau_J^{-1}. \tag{3.30}$$

This gives

$$\gamma_J = W_{JJ} = \tau_J^{-1}[1 - \frac{p_J \tau_J^{-1}}{< \tau^{-1} >}], \tag{3.31}$$

$$W_{JJ'} = -\frac{\tau_J^{-1} p_{J'} \tau_{J'}^{-1}}{< \tau^{-1} >}, J \neq J'. \tag{3.32}$$

The isotropic Q-branch profile can now be calculated. The authors went on to make three further approximations based on the above result.

The first approximation consisted of neglecting the dependence of the collision frequencies τ_J^{-1} on the rotational quantum number J. This approximation gives

$$\gamma_J = W_{JJ} = \tau^{-1}(1 - p_J), \tag{3.33}$$

$$W_{JJ'} = -\tau^{-1} p_{J'}, J \neq J'. \tag{3.34}$$

This yielded the final expression

$$F(\omega) = \frac{1}{\pi}|\bar{\alpha}_{01}|^2$$

$$\times \mathrm{Re}\left[\frac{\sum_J p_J[i(\omega - \omega_{1J,0J}) + n\gamma_J/(1-p_J)]^{-1}}{1 - n[\gamma_J/(1-p_J)]\sum_J p_J[i(\omega - \omega_{1J,0J}) + n\gamma_J/(1-p_J)]^{-1}}\right]. \tag{3.35}$$

This model was considered attractive in that it does not require an inversion of the G-matrix. However, the authors pointed out that the approximation is physically unrealistic at moderate temperatures, but that it becomes more realistic at high temperatures.

The second approximation consisted of neglecting the J-dependence of τ_J^{-1} in the $\tau_J^{-1}/ < \tau^{-1} >$ term in equation 3.31. This gives

$$\gamma_J = W_{JJ} = \tau_J^{-1}(1 - p_J), \tag{3.36}$$

$$W_{JJ'} = -\frac{\gamma_J p_{J'} \gamma_{J'}/(1-p_{J'})}{1 - p_J \sum_{J''} p_{J''} \gamma_{J''}/(1-p_{J''})}, J' \neq J. \quad (3.37)$$

This expression for the $W_{JJ'}$ matrix elements rigorously satisfies the principle of detailed balance, but not the sum rule from the unitarity of the S-matrix. Furthermore, the inversion of the G-matrix is required for an expression of the isotropic Q-branch profile.

The third approximation consisted of applying the second approximation

$$\tau_J^{-1} / < \tau^{-1} >= 1$$

to equation 3.32 as well. This gives

$$\gamma_J = W_{JJ} = \tau_J^{-1}(1 - p_J), \quad (3.38)$$

$$W_{JJ'} = -\frac{p_{J'} \gamma_J}{(1-p_J)}, J' \neq J. \quad (3.39)$$

This expression for $W_{JJ'}$ rigorously satisfies unitarity of the S-matrix, but not the principle of detailed balance. The final result is

$$F(\omega) = \frac{1}{\pi} |\bar{\alpha}_{01}|^2$$

$$\times \ \mathrm{Re}\left[\frac{\sum_J p_J [i(\omega - \omega_{1J,0J}) + n\gamma_J/(1-p_J)]^{-1}}{1 - n \sum_J p_J [\gamma_J/(1-p_J)][i(\omega - \omega_{1J,0J}) + n\gamma_J/(1-p_J)]^{-1}}\right]. \quad (3.40)$$

This is an analytic expression that does not require an inversion of the G-matrix. The ONERA hard collision model computer code for the calculation

of isotropic Q-branch N_2 CARS spectra is based on this expression for $F(\omega)$. An experimental evaluation of this code was conducted, using spectra obtained from a high pressure high temperature cell. The results of this evaluation are presented and discussed at the end of this chapter.

The authors performed high resolution measurements of N_2 rotational linewidths using SRS, and compared the experimental data with the predictions resulting from the approximations they developed. They found good agreement for their first two approximation models, but the third approximation model was inaccurate at low temperatures, improving as the temperature increased. They also compared their calculated profiles with profiles calculated from the PEGL model, and found what they considered to be excellent agreement between the two models.

The following year, Koszykowski et al [74] reported the results of theoretical and experimental studies of high-resolution inverse Raman spectra of N_2 at one to ten atmospheres. The experiments were performed at a temperature of 295 K, at pressures one atmosphere, five atmospheres and ten atmospheres, using the same method as that described earlier [100]. The authors compared theoretical spectra, calculated using the MEGL, against the experimental data, and found good agreement. They also compared calculated IRS spectra, using the EGL and PEGL, against the experimental data, and found that the MEGL approximation was much more successful than both the EGL and PEGL approximations in reproducing accurate IRS spectra. Furthermore, the MEGL approximation correctly predicted the temperature dependence of the diagonal elements of the S-matrix calculated from quasi-classical scattering theory, and was found to be in agreement with preliminary experimental data.

The same year, Rahn et al [101] reported the results of comparisons of rotationally inelastic collision models for Q-branch Raman spectra of N_2. They

compared the ability of two fitting laws, an adjusted MEGL model and the PEGL model, to predict inverse Raman spectra of N_2 obtained at 295 K and ten atmospheres, and at 1000 K and twenty atmospheres. They found that both models predict the rotationally inelastic linewidths accurately, but that the adjusted MEGL model was more successful than the PEGL model in calculating collisional narrowing effects. This is because the two models describe the energy gap scaling of the state-to-state rates differently.

In 1989 Bouché et al [15] reported the results of a study of collisional narrowing and spectral shift in CARS spectra of molecular nitrogen up to 2500 bar and 700 K. They used the later MEGL model to calculate theoretical spectra which were compared with the experimental data. They found that measured and calculated spectra agreed for pressures up to 300 bar. At higher pressures differences in the spectra led to a temperature error in excess of 100 K at 700 K, and -150 K at 295 K.

In 1990, Woyde and Stricker [125] published a paper on the application of CARS for temperature measurements in high pressure combustion systems. They recorded averaged broadband CARS spectra from pre-mixed methane/air flames generated from a stabilised high pressure burner which can be operated up to 40 bar. They used an extended MEG law (XMEGL) to model the collisional line narrowing in high pressure CARS spectra, including collisional effects on molecular nitrogen by water vapour and carbon dioxide. They found that the non-resonant background had an increasing influence on deduced temperatures with increasing pressure. In order to achieve agreement between independently obtained temperatures from pure rotational Raman measurements, they had to reduce the non-resonant background susceptibility by 12%.

3.2 The High Pressure High Temperature Cell

The High Pressure High Temperature (HPHT) cell was designed by Dr. D. Ball, and built in the workshop of the Dept. of Physics at U.C.T. [9]. It consists of two hollow concentric stainless steel cylinders, one held in place inside the other with thermal insulation fitted around the inner cylinder, a ceramic frame fitted to the inside of the inner cylinder, and four thin cylindrical, helically wound nichrome elements placed along grooves cut into the inner face of the ceramic frame. The outer cylinder is pressure sealed, designed to hold pressures ranging from atmospheric pressure to 20 bar. Figure 3.1 shows the design of the high pressure high temperature (HPHT) cell.

The four elements were evenly spaced around the inside face of the ceramic holder. A commercial temperature controller was used to maintain a steady temperature in the HPHT cell. The sensing element was a type K thermocouple, and was placed along the inside wall, at the centre of the ceramic frame. The thermocouple was linked to a three phase temperature controller, which controlled a thyristor, which in turn controlled the current for the elements.

The spatial variation of temperature within the HPHT cell was investigated at atmospheric pressure, 5 bar, 10 bar, 15 bar, and 20 bar gauge pressure. The measurements were performed by leaving the control thermocouple placed at the centre along the inside wall of the ceramic holder, while placing two other thermocouples into the central region within the inner cylinder, one radially, and the other along another groove of the ceramic frame, at an azimuthal angle of 30 degrees to the control thermocouple. The radial thermocouple was moved across the space within the inner cylinder, and temperature measurements were made every three millimetres.

All three thermocouples were placed in the centre of the cylinder along the z

axis, corresponding to the point of focus along the z axis of the Stokes and pump beams in the BOXCARS configuration. The temperatures measured from the three thermocouples were then compared with each other, and the systematic differences between the three noted. The results of the temperature measurements are tabulated in Table 3.1. The temperatures presented under the title Probe 1 (Radial) are temperatures measured at the centre of the cylinder, at the point where the CARS temperatures were to be measured.

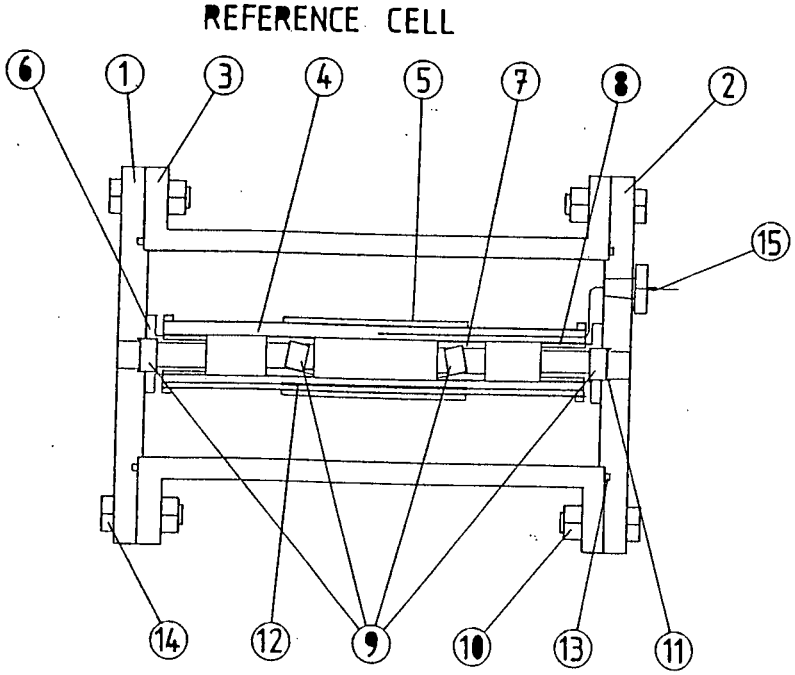

NT	ITEM NAME	MAT.
1	END PLAT L/HAND	SI/Steel 316
2	END PLAT R/HAND	SI/Steel 316
3	PRESSURE CELL	SI/Steel 316
4	CERAMIC TUBE	Ceramic
5	CERAMIC TUBE HOLDER	SI/Steel 316
6	OUTERWINDOW HOLDER	SI/Steel 316
7	INNER WINDOW HOLDER	SI/Steel 316
8	INSULATOR	
9	WINDOWS	Quartz Glass
10	M16 NUT	Mild Steel
11	O-RING	Silicone
12	HEATER ELEMENT	Nichrome
13	O-RING	Neoprene
14	M16 BOLT	Mild Steel
15	THERMOCOUPLE	Nichrome SI/Steel 316

Figure 3.1: High Pressure High Temperature (HPHT) Cell.

Gauge Pressure (bar)	Temperature (Celsius)		
	Probe 1 (Radial)	Probe 2 (Axial)	Probe 3 (Control)
5.0	320 ± 3	334 ± 3	346 ± 3
5.0	690 ± 3	694 ± 3	707 ± 3
10.0	464 ± 3	478 ± 3	499 ± 3
10.0	688 ± 3	703 ± 3	709 ± 3
15.0	570 ± 3	579 ± 3	601 ± 3
15.0	658 ± 3	682 ± 3	700 ± 3
15.0	678 ± 3	690 ± 3	710 ± 3
20.0	782 ± 3	784 ± 3	802 ± 3

Table 3.1: Temperature Calibration of HPHT Cell.

The results of the spatial variation in the temperature measurements can be summarised by the following: the control thermocouple placed along the inside wall of the ceramic holder measured temperatures systematically $20°C$ to $40°C$ too high compared with the temperatures taken from the radial thermocouple at the geometric centre of the HPHT cell. The temperatures of the HPHT cell measured during the CARS experiment were taken from the control thermocouple. Therefore the air temperature at the point of focus of the CARS beams was estimated to be about $30°C$ lower than the temperature measured from the control thermocouple, with a possible systematic error of

$12°C$ in this estimation.

The cell was designed for temperatures ranging from room temperature to $1000°C$. Error estimates for the temperature in the HPHT cell were a possible systematic error of 12 K, and a random error estimate of 3 K, originating from the accuracy of the thermocouple and the transducer. The pressure measurement was made with a WIKA pressure gauge, which had been calibrated using a dead weight tester. The pressure gauge measured pressure over a range of 0 kPa to 2500 kPa. The gauge was measured to be accurate to 0.1% of full scale deflection, with an average error of less than 0.25% throughout the range. The error in the pressure measurement for the HPHT cell experiment was estimated to be 0.05 bar.

3.3 The SOPRA CARS System

The SOPRA CARS system incorporates a single longitudinal mode (s.l.m.) frequency-doubled Nd:YAG laser and a tunable broadband dye laser, which provide up to 200 mJ and 5mJ per pulse respectively. The Nd:YAG laser is passively Q-switched, with a pulse length of 13 ns. The dye laser emission was centered at 607 nm using the laser dye sulphorhodamine. This dye was chosen because it appears to lead to more reproducible shot-to-shot spatial profiles and frequency profiles than Rhodamine-610 (Rh-610) and Rhodamine-640 (Rh-640) dye mixtures. The use of pure Rh-610 dye and pure Rh-640 dye is unsuitable for a transversely pumped dye laser [65].

Figure 3.2 is a diagram of the SOPRA CARS laser table, and includes the optical components for the Nd:YAG laser, and the tunable dye laser. The Nd:YAG laser consists of an oscillator cavity of optical path length 1,2 m, the Nd:YAG rod, two Fabry-Perot etalons, the high powered flash lamps, a

container of saturable absorber in solution, and two single pass amplifier rods. The laser is passively Q-switched by the saturable absorber, which is designed to saturate when the Nd:YAG rod has reached maximum population inversion. The laser pulse which is subsequently generated builds up to maximum power over two to three passes of the laser signal within the oscillator cavity.

Figure 3.2: SOPRA CARS Laser Table: A-Nd:YAG amplifier; B-Fabry-Perot etalon; C-Saturable absorber; D-KDP doubler; E-Dye cell; F-Dichroic mixing plate; G-Parallel plate for BOXCARS

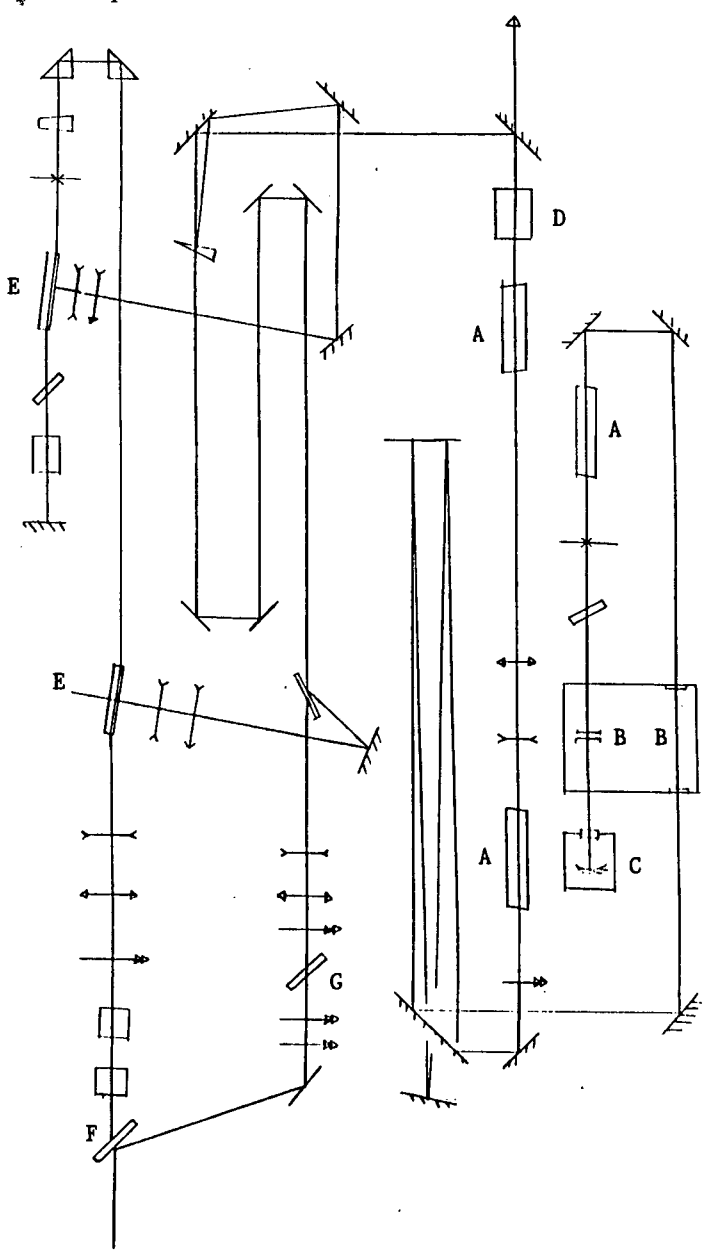

The overlap of the Nd:YAG gain curve, the transmission characteristics of the two Fabry-Perot etalons, and the transmission characteristic of the oscillator cavity, ensure that the cavity oscillates in single longitudinal mode only. The temperature of the Fabry-Perot etalons is carefully controlled to an accuracy of 0.02 degrees celsius. Slight changes in the length of the laser table as a result of temperature changes can cause the Nd:YAG laser to oscillate in two or more modes. This is observed to occur for less then 5% of all shots. Therefore, at least 95% of all the Nd:YAG laser pulses are single longitudinal mode.

The oscillator laser beam is emitted at a wavelength of 1064.4nm, and has a Gaussian beam radius of 0.81 mm. This beam is allowed to diverge naturally from its initial radius to a radius of 2.55 mm, over a path length of 6 m. The beam then passes through two single pass amplifiers. A Galilean telescope placed between the two amplfiers is used to compensate for thermal lensing in the amplifier rods. The beam has an energy of about 1.0J after the amplifiers, and a temporal width of about 13ns (FWHM). The temporal width of the Nd:YAG beam is controlled through the concentration of the saturable absorber in solution.

The amplified beam is then made to pass through a frequency doubling type II KDP crystal, which doubles the frequency of the 1064.4nm infra-red beam to a 532.2nm green beam. The KDP crystal has a frequency doubling efficiency of about 30%. Thus the CARS pump beam comes out at 532.2nm, 13ns width, and about 300mJ of energy. The residual infra-red beam then passes into a beam dump.

Two partially-reflecting mirrors divert energy from the green beam. These diverted beams are used to pump the dye laser oscillator, and a single-pass dye laser amplifier. The dye laser oscillator signal passes through the single pass amplifier, increasing the dye laser output power to about 5mJ. About 30%

of the green beam's power is split off from the main beam in order to pump the dye laser. Therefore the usable energy in the CARS pump laser (green beam) is about 200mJ. The green beam is then delayed by deflecting the beam through longer path length, in order to overlay the dye laser beam and the green beam properly. The two laser beams (pump beam and Stokes beam) are then brought together with a dichroic mixing plate for use in colinear CARS, or the green beam is split into two parallel beams with a beam splitter, and one of the beams is brought together with the dye laser beam (Stokes beam) using the mixing plate, for use in BOXCARS.

Figure 3.3 shows the collection optics for the CARS system. The CARS signal has been generated either by using a colinear CARS geometry, or a BOXCARS geometry. For the colinear geometry, the CARS signal is coincident with the pump and Stokes beams, while for the BOXCARS geometry, the signal is coincident with the pump beam that is not mixed with the Stokes beam. This satisfies the BOXCARS phase relationship: $\vec{k_4}^{CARS} = \vec{k_1^p} + \vec{k_2^p} - \vec{k_3^s}$, where $\vec{k_1^p}$, $\vec{k_2^p}$ are the pump beam wave vectors, $\vec{k_3^s}$ is the Stokes beam wave vector, and $\vec{k_4}^{CARS}$ is the BOXCARS wave vector.

The BOXCARS signal that was generated in the HPHT cell is then directed into a spectrometer. A lens directs the BOXCARS signal through a 50μm slit onto a Jobin-Yvon holographic grating. The Jobin-Yvon holographic grating is a reflective, concave holographic grating with line density 2100 lines per cm. The grating diffracts the incoming BOXCARS signal optimally into the first diffraction order with a focal length of 0.75 meters. The astigmatism of the concave grating causes the diffracted monochromatic light to form a vertical line focus. The signal is then focussed with a 2x zoom telescope, and directed onto a gated intensified optical multichannel analyser (EG&G PARC model 1421 detector, controlled by model 1461 detector controller). The spectrometer and detector dispersion at 474nm is 0.287 cm^{-1} per pixel.

Figure 3.3: SOPRA CARS Collection Optics: A-Dichroic filter; B-High pressure argon reference cell; C-prism; D-Holographic grating; E-2x zoom telescope; F-Optical detector

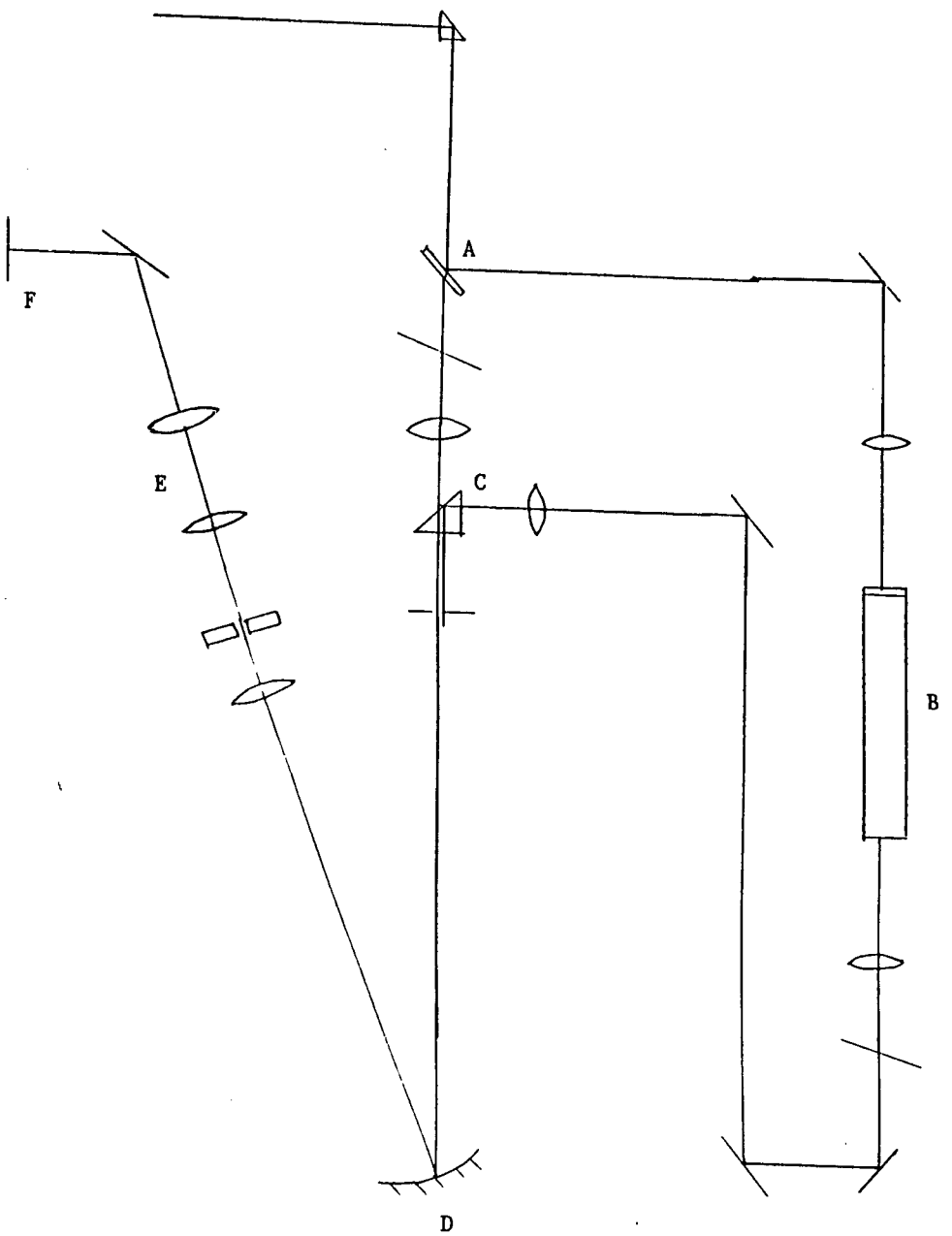

The CARS reference signal was generated in a specially designed high pressure reference cell containing argon at a pressure of 35 bar. The Stokes and pump beams were deflected from their optical path using a dichroic filter, and directed onto a lens system, where they were focussed into the reference cell. The consequent non-resonant CARS reference signal was then directed into the spectrometer and onto the detector, while the pump and Stokes beams were dumped.

The resonant signal and the non-resonant reference signal were directed to the left and right halves of the OMA. This cannot be done if the two signals are at the same height when focussed through the slit. Therefore the slit was slanted at an angle to the vertical, and the two signals were directed and focussed through the slit at different heights and horizontal points. The optical components in the spectrometer maintain this height and horizontal separation to the focii of these signals at the detector, but the astigmatism of the holographic grating ensures line focii of the two signals such that the bottom part of the higher line and the upper part of the lower line can be made to overlap vertically. The OMA has 1024 light sensitive pixels with decreasing sensitivity at the edges. Therefore the resonant signal was offset with respect to the non-resonant reference signal by 512 pixels.

3.4 The HPHT Cell CARS Experiment

The 8 mm diameter pump and Stokes beams were used in a BOXCARS configuration with parallel polarizations, the beams being brought to a focal waist at the midpoint of the HPHT cell with a 500 mm focal length achromat.

The broadband dye lasers used in CARS spectroscopy do not have a perfectly flat spectral profile, and it is necessary to compensate for this by referencing.

Various methods have been used. The most rigorous method, which is only possible when a s.l.m. Nd:YAG is used, involves simultaneous recording of single-shot resonant CARS spectra in the sample and non-resonant CARS spectra in a reference cell [95]. The corrected CARS signal is then found by taking a shot-by-shot quotient of the resonant signal with the non-resonant signal. This has the advantage of taking shot-to-shot variations in the dye laser spectral profile into consideration. Other methods of referencing CARS spectra involve:

(i) Referencing by averaging single shot spectra of non-resonant gases (usually argon) at high pressure, and then taking the quotient of the single shot resonant spectra with the average non-resonant spectrum. This simpler reference technique is in common use, and appears to be only marginally less accurate than shot-to-shot referencing [53].

(ii) Referencing by averaging both resonant and non-resonant spectra, and then taking the quotient of the average resonant spectrum with the average non-resonant spectrum. This method gives rather poor results compared with the above shot-to-shot referencing.

On occasion the resonant spectra are not referenced at all. Obviously this method means that the experimenter has no systematic remedy for including the effects of shot-to-shot fluctuation in the dye laser profile in the resultant CARS spectra. Furthermore, the spectra are subject to biassing as a consequence of ignoring the average structure of the dye laser profile.

In the present experiment referencing was performed by simultaneously taking resonant nitrogen spectra in the HPHT cell, and non-resonant argon spectra from a high pressure argon filled reference cell. The quotients of the resonant single shot spectra were taken against the corresponding single shot

non-resonant argon spectra.

The experiment was controlled from a PDP 11/73 minicomputer, setting the detector controller to fire the laser, and hence take CARS spectra at a rate of 5 Hz.

Five sets of fifty spectra were taken for each temperature and pressure. The database was defined as a set of averaged spectra covering a grid of temperatures and pressures at intervals of 25 K in temperature and 0.5 bar in pressure for the range of pressure 1 bar to 10 bar, and intervals of 40 K in temperature and 1 bar in pressure for the range of pressures 10 bar to 20 bar.

3.5 An Experimental Evaluation of the ONERA Hard Collision Model Calculation of CARS Spectra, and the MEGL Model Calculation of CARS Spectra

3.5.1 The ONERA Hard Collision Model

This evaluation was performed by fitting the HPHT spectra of known temperature and pressure against the ONERA hard collision model theoretical spectra, using the cross-covariance method. The following table shows the results of this analysis. The first column shows the pressure for which the comparison was made, the second column the HPHT temperature, the third column was the ONERA model temperature for which the model spectra most closely fitted the averaged HPHT spectrum at the chosen temperature, and the fourth column shows the corresponding maximum cross-covariance.

The ONERA model spectra were prepared for pressures 1 bar to 10 bar at 1 bar intervals, and at discrete temperatures of interval 20 K. The ONERA model convolves four Gaussian segments of user-determined width with the spectral contributions of the rotational states to achieve the theoretical CARS spectrum at a given temperature and pressure. The parameters for these Gaussian lineshapes was set at 0.7 for all four Gaussians, as this setting generated the best fit at room temperature and atmospheric pressure. Furthermore, the ONERA model spectra were calculated with a spectrometer dispersion at detector, of 0.25 cm^{-1} per pixel for 256 pixels, making a spectrometer-detector width of 64 cm^{-1}.

In order to fit the HPHT spectra directly to the ONERA model theoretical spectra, the different spectrometer dispersions had to be taken into account. The dispersion of the U.C.T. CARS system at 474.4 nm is 0.287 cm^{-1} per pixel. This means that the spectral width of the spectrometer at the detector over 256 pixels is 73.47 cm^{-1}. Thus at first glance, the ONERA theoretical spectra would appear to be narrower than experimental spectra obtained using the U.C.T. spectrometer when the signals are compared pixel by pixel. A simple linear interpolation routine is written into the ONERA code which narrows down the experimental spectra to match the spectral width that the ONERA theoretical model was calculated for.

Pressure (bar)	HPHT Temperature (Kelvin)	ONERA Model Temperature (Kelvin)	max.c-c.
1.0	292 ± 15	280	.99575
1.0	362 ± 15	380	.99810
1.0	523 ± 15	500	.99859

Pressure (bar)	HPHT Temperature (Kelvin)	ONERA Model Temperature (Kelvin)	max.c-c.
2.0	363 ± 15	400	.99713
2.0	473 ± 15	480	.99837
2.0	547 ± 15	600	.99679
3.0	383 ± 15	400	.99685
3.0	473 ± 15	480	.99746
3.0	573 ± 15	600	.99771
4.0	423 ± 15	440	.99444
4.0	523 ± 15	540	.99500
4.0	623 ± 15	620	.99660
5.0	473 ± 15	500	.99803
5.0	573 ± 15	600	.99717
5.0	598 ± 15	620	.99594
5.0	648 ± 15	660	.99745
5.0	673 ± 15	680	.99765
6.0	498 ± 15	520	.99510
6.0	523 ± 15	540	.99543
6.0	623 ± 15	640	.99468
6.0	723 ± 15	720	.99708
7.0	573 ± 15	600	.99661
7.0	698 ± 15	720	.99714
7.0	723 ± 15	740	.99715
7.0	773 ± 15	820	.99650
7.0	798 ± 15	840	.99587

Pressure (bar)	HPHT Temperature (Kelvin)	ONERA Model Temperature (Kelvin)	max.c-c.
8.0	700 ± 15	740	.99675
8.0	776 ± 15	820	.99576
8.0	801 ± 15	840	.99583
9.5	773 ± 15	740	.99856
9.5	848 ± 15	780	.99830
9.5	873 ± 15	840	.99825
11.0	760 ± 15	720	.99658
11.0	799 ± 15	760	.99400
12.0	763 ± 15	760	.99666
12.0	843 ± 15	820	.99726
15.0	803 ± 15	740	.99841
15.0	883 ± 15	820	.99785
15.0	1003 ± 15	900	.99697
18.0	924 ± 15	780	.99811
18.0	963 ± 15	820	.99755

Table 3.2: HPHT Evaluation of ONERA CARS Model

Analysing the trends in the above table reveals that from 1 bar to 7 bar, the comparison between the experimental HPHT spectra and the ONERA model spectra is reasonable. Generally, the theoretical spectrum corresponding to the correct discrete temperature is selected as the best fitting spectrum. However, the mean of the cross-covariances is 0.9969, and the standard deviation is 0.0013, which is significantly lower than the cross-covariances obtained from direct comparison of averaged HPHT spectra.

The ONERA code uses four independent Gaussian lineshapes for the instrument function to describe the response of the detector in the four different frequency regions (the far high frequency, near high frequency, near low frequency, far low frequency). The Gaussian lineshape is unrealistic, since it drops off too rapidly in the wings. This is why there is a deviation of the theoretical spectra at low pressures from the experimental spectra in the high frequency region of the spectra. It may be possible to improve the fit by adding a Lorentzian component to the detector instrument function. However, this approach would lead to an over-parameterisation of the ONERA computer code, with questionable benefits.

At 1 bar, the experimental spectra are well fitted by the theoretical ONERA model spectra, except for the deviation in the high frequency region of the spectra. The experimental spectrum obtained at 292K is about 1 pixel narrower (fwhm) than the theoretical spectrum of temperature 280K, while the widths of the theoretical and experimental spectra at 380K and 362K respectively agree exceptionally well. The widths of the theoretical and experimental spectra at 500K and 523K respectively also agree well, but the rotational bands are under-emphasized in the theoretical spectrum.

At 2 bar, the widths (fwhm) of the experimental spectra are well reproduced by the ONERA model, but again the rotational bands in the experimental spectra are under-emphasized in the theoretical spectra.

Over the pressure range 3 bar to 6 bar, the ONERA model begins to underestimate the pressure narrowing of the width of the CARS spectra, and continues to over-estimate the suppression of the rotational bands in the high temperature spectra. Maximisation of the cross-covariances in these cases is a play-off between these sources of error in the calculation of the theoretical spectra.

At 7 bar and 8 bar, the model systematically predicts temperatures 30K to 50K too high. The ONERA model reproduces the rotational bands in the high temperature CARS spectra very poorly, considerably over-emphasising the suppression of the rotational bands.

Curiously, in the pressure regime of 9.5 bar to 11 bar pressure, the ONERA model begins to predict temperatures systematically 25K to 60K too low. This is because between 8 bar and 9.5 bar, the rotational bands in the high temperature CARS spectra undergo significant suppression. In other words, the rotational bands present in high temperature CARS spectra are particularly sensitive to collisional narrowing in this pressure range. This feature of high temperature CARS spectra in this pressure range is not reproduced by the ONERA model, and it still under-emphasises the narrowing of the spectrum in this pressure range.

At a pressure of 12 bar, the ONERA model spectra again correctly predict CARS temperatures. The theoretical widths (fwhm) are only sightly broader than the corresponding experimental spectra, and the rotational bands are still poorly reproduced. For pressures over the range 14 bar to 18 bar, the ONERA code systematically under-estimates CARS temperatures by 40 K to 100 K. In this pressure range, the ONERA model reproduces the spectral widths and the rotational bands poorly.

Figures 3.4 to 3.10 show the best fits of the ONERA model spectra to averaged HPHT spectra for selected data from Table 3.2. The HPHT temperatures are referred to first, followed by the deduced ONERA model temperatures, followed by the HPHT cell pressures. The solid curves are the averaged HPHT spectra, while the discrete points are the ONERA model spectra.

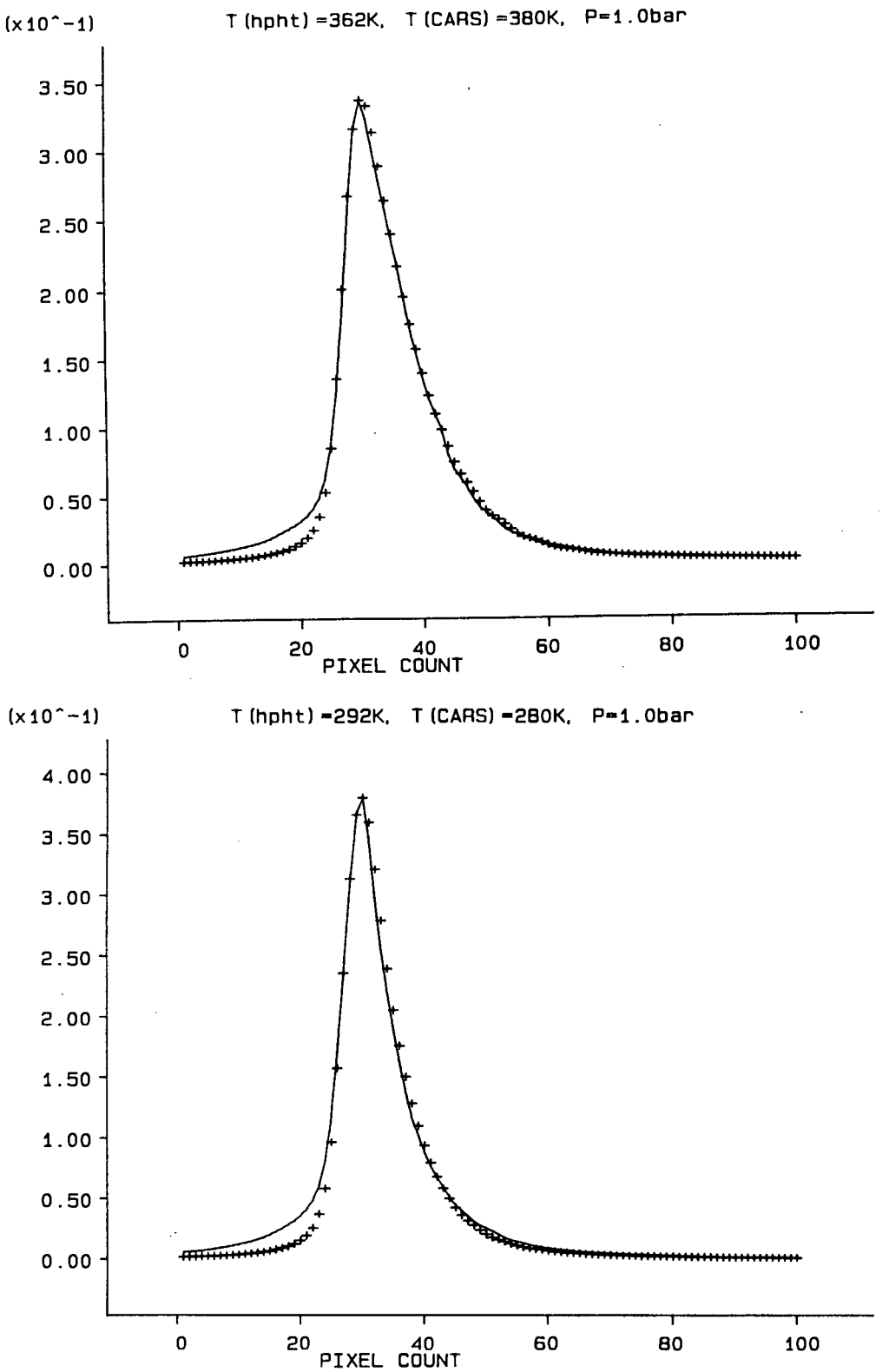

Figure 3.4: HPHT Evaluation of ONERA CARS Model.

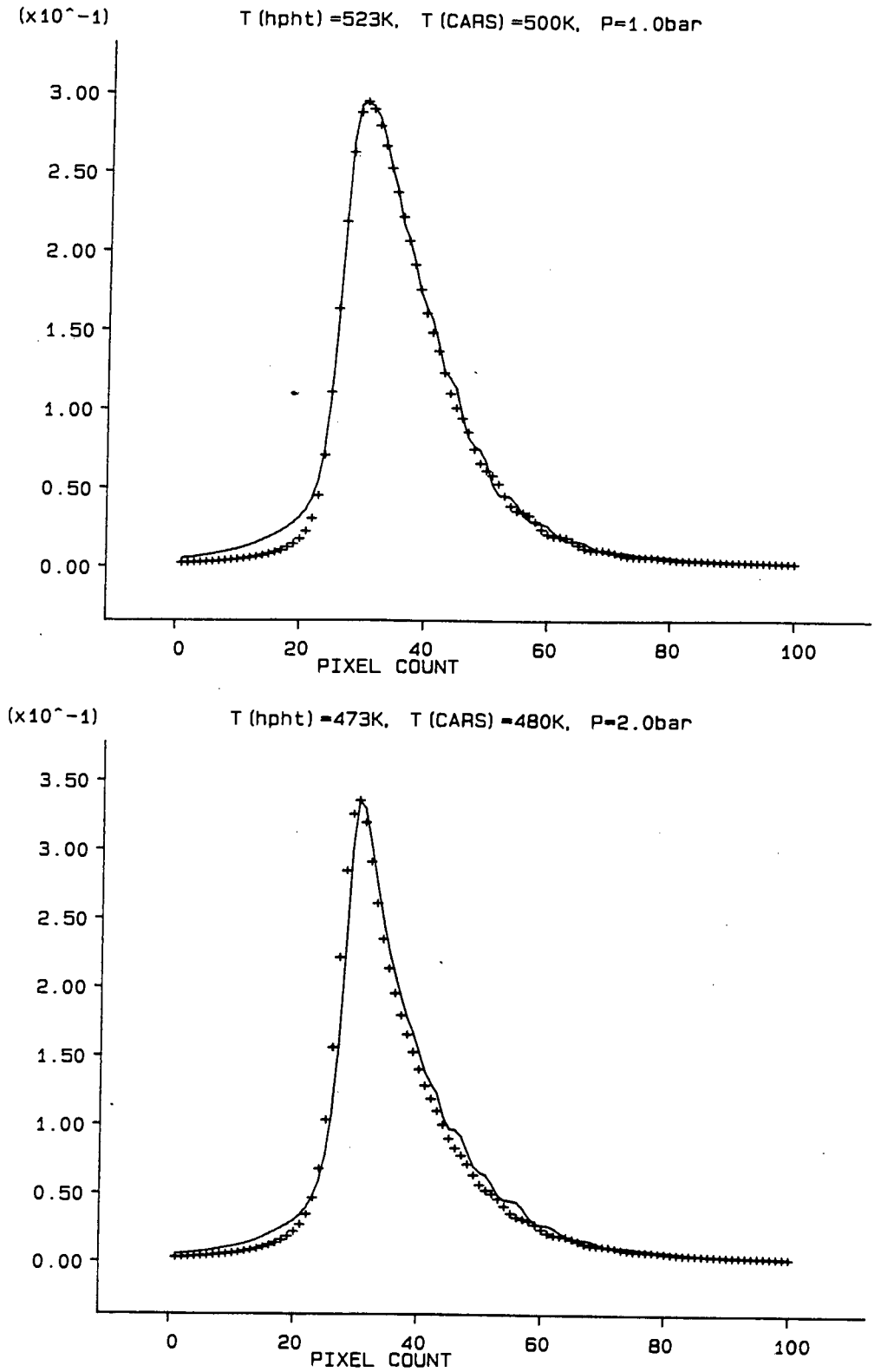

Figure 3.5: HPHT Evaluation of ONERA CARS Model.

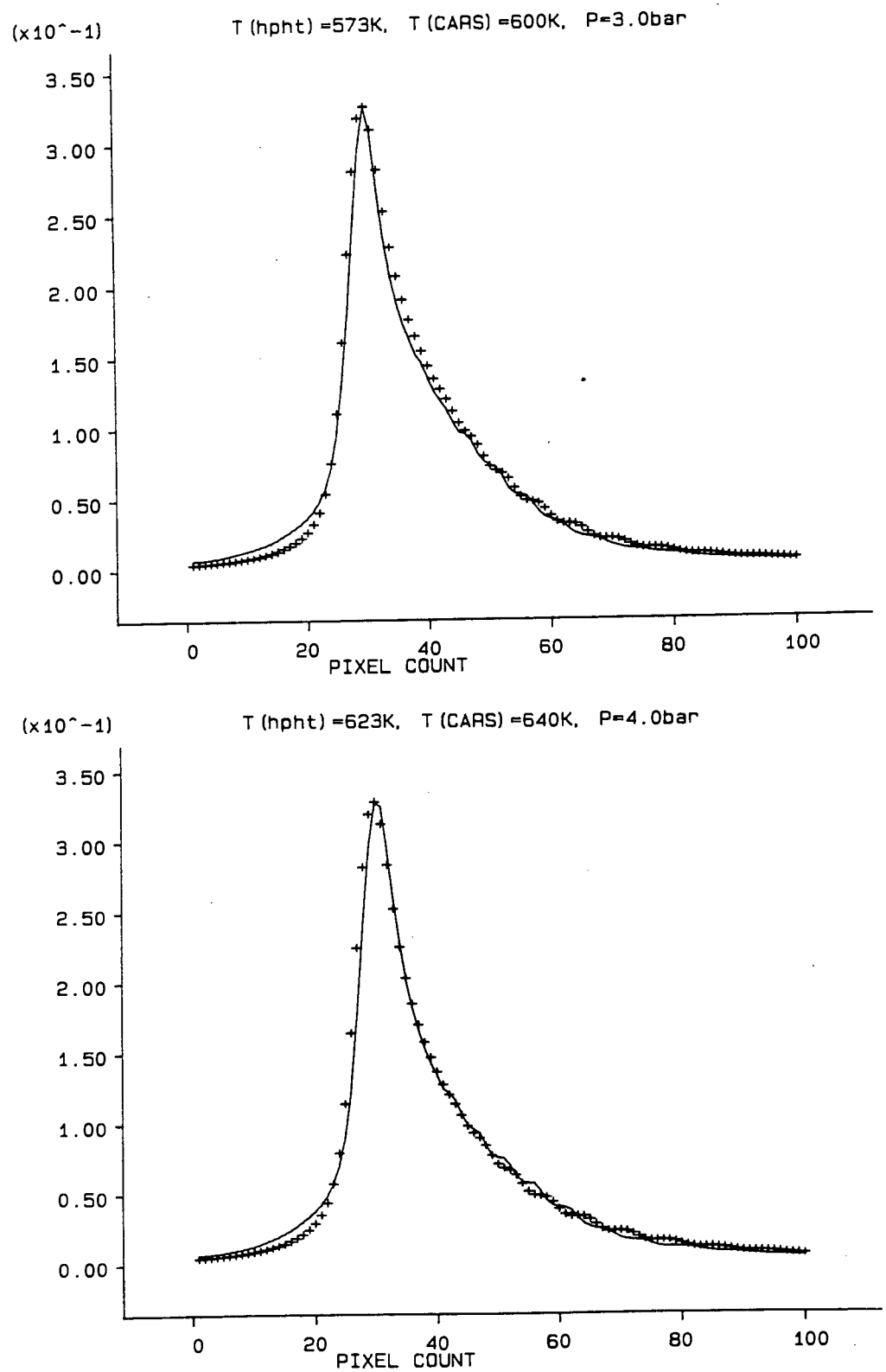

Figure 3.6: HPHT Evaluation of ONERA CARS Model.

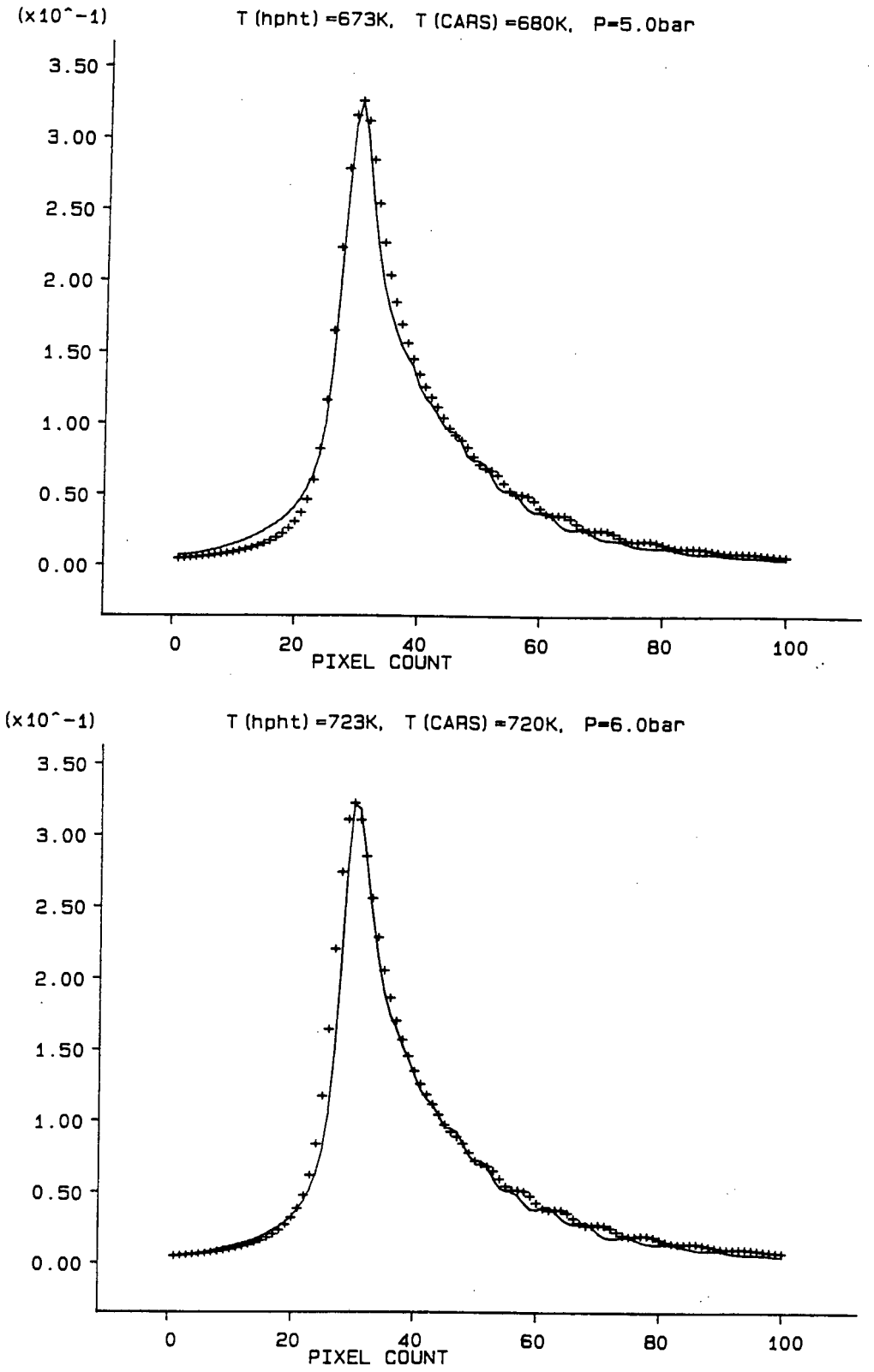

Figure 3.7: HPHT Evaluation of ONERA CARS Model.

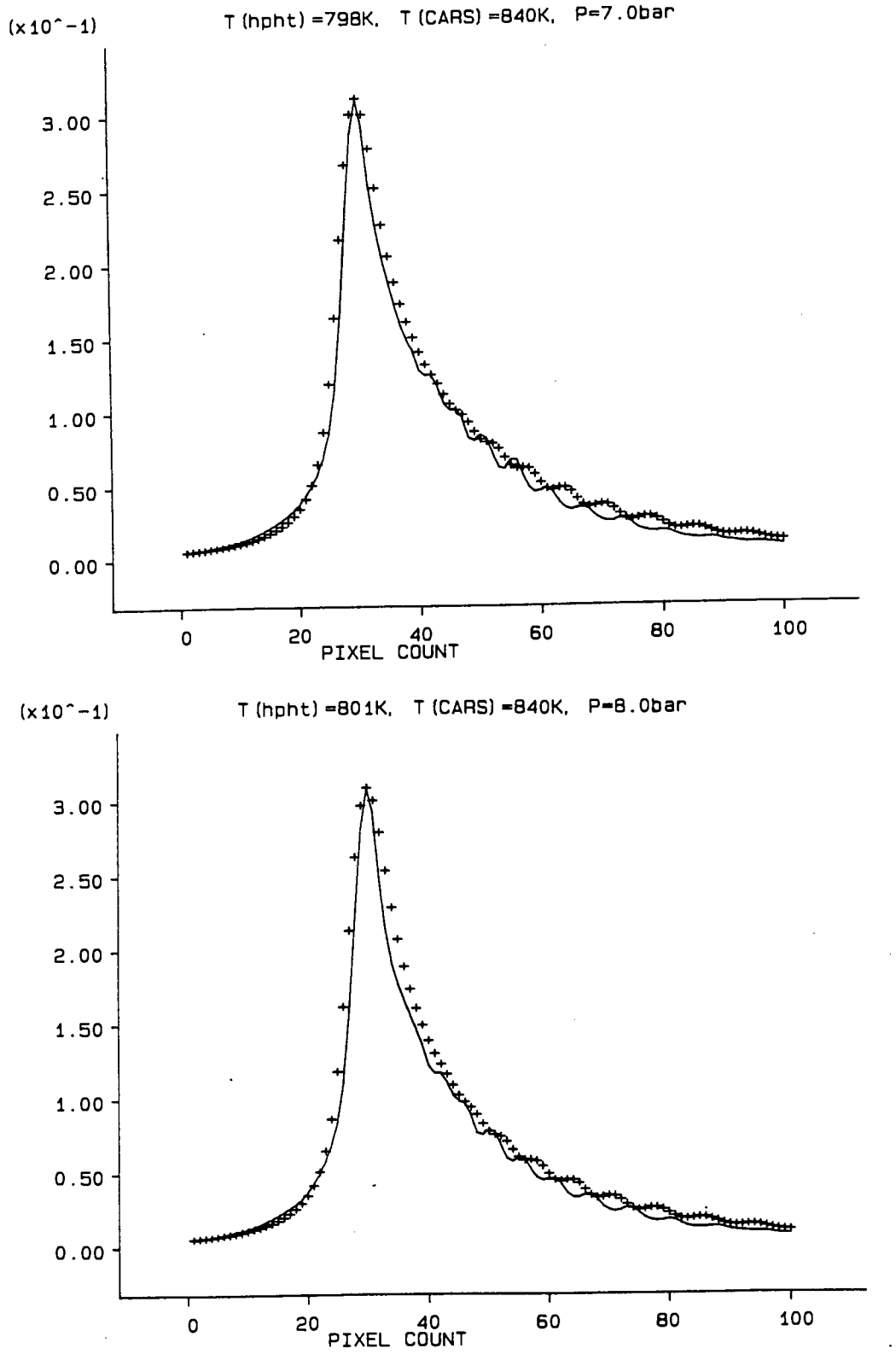

Figure 3.8: HPHT Evaluation of ONERA CARS Model.

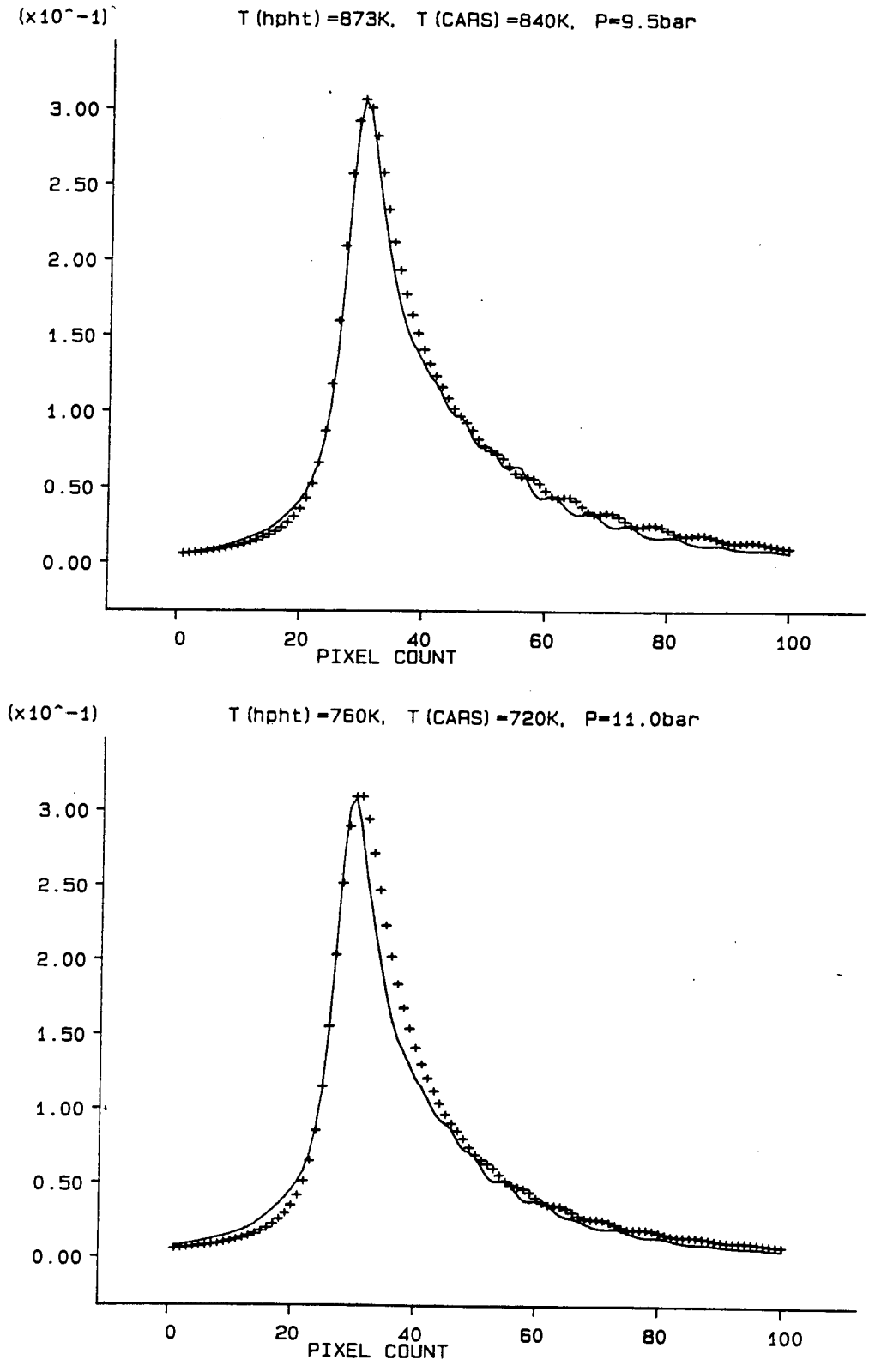

Figure 3.9: HPHT Evaluation of ONERA CARS Model.

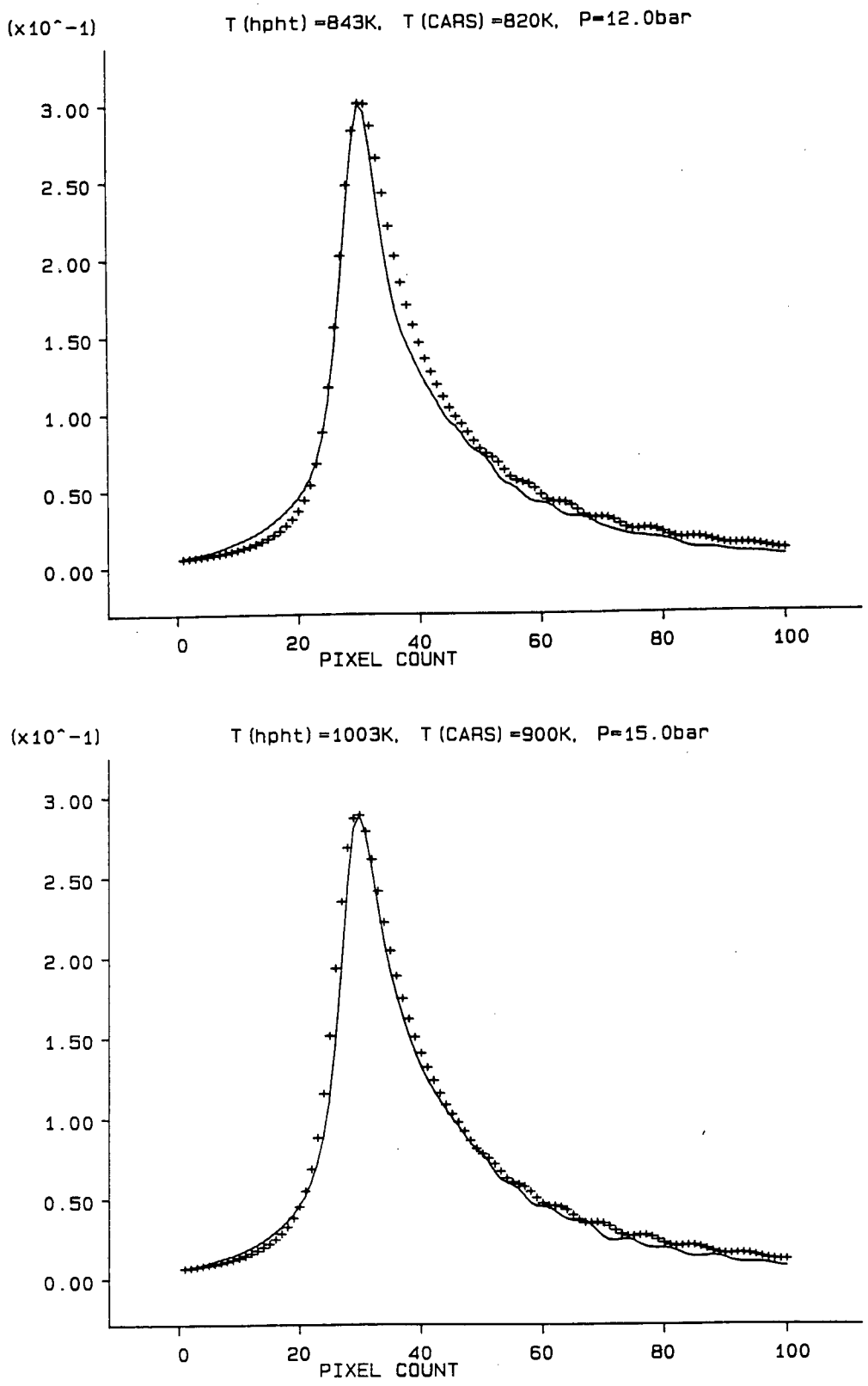

Figure 3.10: HPHT Evaluation of ONERA CARS Model.

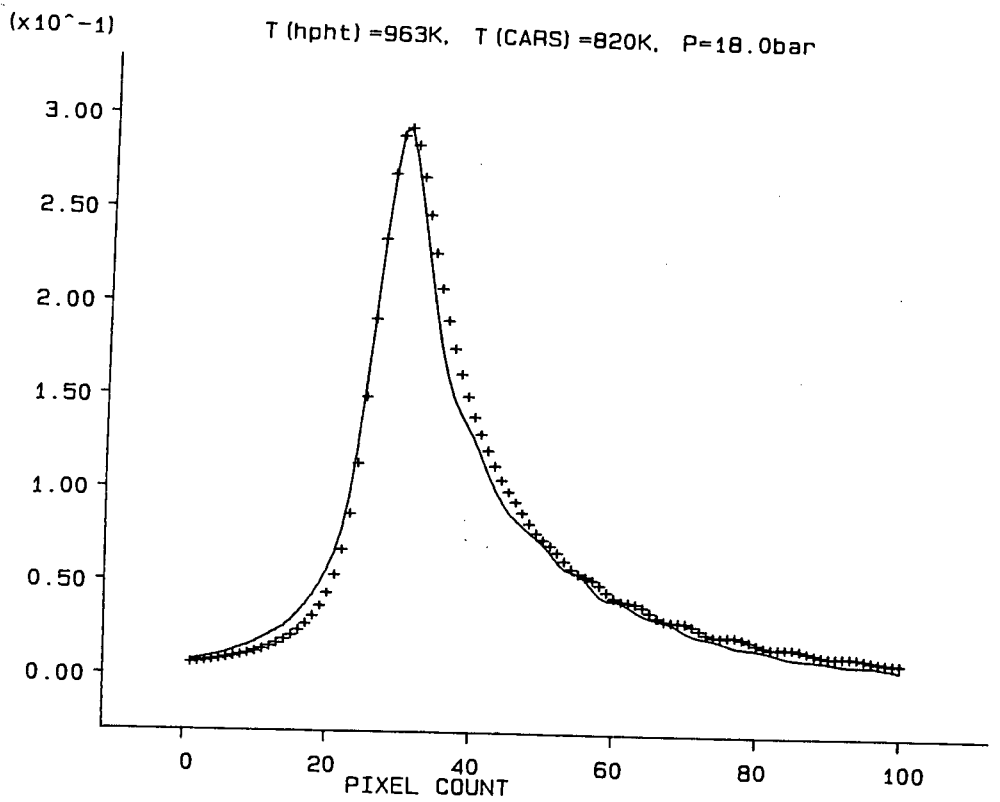

Figure 3.11: HPHT Evaluation of ONERA CARS Model.

3.5.2 The MEGL Model

The theoretical CARS spectra calculated using the MEGL model, which are analysed here, were calculated using the G-matrix method in the time domain, as described in chapter 2. The SOPRA CARS system uses a monomode Nd:YAG laser as the Raman pump beam, and so the normalised spectral density function for the pump beam is just a delta function at 532.2nm. The normalised detector response function was fitted using a Voigt profile, with the width parameters taken from linewidth response measurements made on the detector using the spectral line of mercury.

The following table gives the MEGL model CARS data statistics for a variety of temperatures and pressures, with comparisons performed on HPHT data of known temperature.

Pressure (bar)	HPHT Temperature (Kelvin)	MEGL Model Temperature (Kelvin)	max.c-c.
1.0	407 ± 15	406	.99716
2.0	457 ± 15	501	.99898
3.0	483 ± 15	520	.99959
4.0	523 ± 15	579	.99910
4.0	548 ± 15	630	.99941
5.0	573 ± 15	688	.99905
5.0	598 ± 15	699	.99920
6.0	598 ± 15	675	.99857
6.0	623 ± 15	732	.99843
7.0	673 ± 15	820	.99861
7.0	673 ± 15	827	.99799
7.0	698 ± 15	841	.99812
7.0	698 ± 15	845	.99830
9.5	648 ± 15	741	.99945
9.5	648 ± 15	746	.99947
9.5	673 ± 15	743	.99934
15.0	843 ± 15	1090	.99635
15.0	883 ± 15	1103	.99782
18.0	883 ± 15	1041	.99851
18.0	923 ± 15	1176	.99831

Table 3.3: HPHT Evaluation of MEGL Model.

Analysing the trends in Table 3.3 reveals that the MEGL model works well for predicting temperatures at ambient pressure (about 1 atmosphere), but systematically deteriorates as the pressure increases above 2 bar. In the range of pressures 2 bar to 4 bar, the MEGL model systematically over-estimates temperatures by 40K to 60K. At 5 bar and 6 bar, this over-estimate has worsened to between 100K and 120K. At 7 bar, the MEGL model predicts temperatures about 140K too high.

At 9.5 bar, the MEGL model predicts temperatures about 100K too high. This means that there has been a decrease in the over-estimate of temperature in the pressure range 7 bar to 9.5 bar. This must be compared with the decrease in the predicted temperatures in the same range of pressures, using the ONERA model, and reveals an important change in the structure of the spectrum over these pressures that is not represented in either model.

In the pressure range of 15 bar to 18 bar, the MEGL model has deteriorated again to predicting temperatures 150K to 250K too high.

Author's Note: The comparisons of the HPHT spectra with the MEGL model spectra presented in Table 3.3 were performed by G. Robertson, and are included here for completeness. The MEGL model analysed here is the earlier version of the MEGL model, published by Rahn and Palmer in 1986 [100], and not the later version published in 1987 [101]. The discussion of the comparisons for the different pressures and temperatures is my own.

3.5.3 CARS Data Statistics for Two Representative Data Sets

The following table presents CARS data statistics analysed using the MEGL model and the ONERA hard collision model, for CARS spectra obtained from the HPHT cell at 7.0 bar. The CARS data is the same as that analysed in

chapter 2, in the example of fitting sets of experimental spectra.

Data Set No. 1, Pressure = 7.0 bar, Temperature = $673K \pm 15K$

$\bar{T}_{ONERA} = 709.2K \pm 5.5K$

$\bar{T}_{MEGL} = 812.6K \pm 5.4K$

Shot no.	ONERA Model Temperature (Kelvin)	max.c-c.	MEGL Model Temperature (Kelvin)	max.c-c.
1	700	.99648	823	.99781
2	700	.99763	817	.99773
3	680	.99720	794	.99789
4	680	.99789	799	.99791
5	660	.99745	764	.99873
6	680	.99680	809	.99779
7	760	.99557	888	.99708
8	700	.99657	820	.99724
9	680	.99682	793	.99830
10	680	.99754	796	.99818
11	720	.99653	864	.99670
12	680	.99814	806	.99766
13	760	.99633		

Shot no.	ONERA Model Temperature (Kelvin)	max.c-c.	MEGL Model Temperature (Kelvin)	max.c-c.
14	680	.99706	795	.99827
15	660	.99736		
16	720	.99701		
17	680	.99778	791	.99823
18	720	.99644	828	.99769
19	700	.99642		
20	740	.99644		
21	740	.99636		
22	720	.99684		
23	720	.99691		
24	700	.99354	786	.99832
25	700	.99690	819	.99791
26	660	.99526		
27	740	.99679		
28	720	.99704		
29	680	.99739		
30				
31	760	.99675		
32	780	.99614		
33	760	.99450	863	.99693
34	740	.99510		

Shot no.	ONERA Model Temperature (Kelvin)	max.c-c.	MEGL Model Temperature (Kelvin)	max.c-c.
35	700	.99670	830	.99826
36	680	.99263	785	.99672
37	720	.99398	820	.99662
38	720	.99658		
39	720	.99627		
40	780	.99655		
41	760	.99741	892	.99652
42	700	.99671	819	.99810
43	700	.99600		
44	660	.99619		
45	680	.99724	796	.99874
46	660	.99679	776	.99869
47	720	.99642	847	.99750
48	660	.99642	760	.99857
49	640	.99115	723	.99780
50	720	.99695	861	.99734

Table 3.4: Sample Shot-to-shot HPHT Evaluation of ONERA Model and MEGL Model

Data Set No. 2, Pressure = 7.0bar, Temperature = $698K \pm 15K$

$\bar{T}_{ONERA} = 721.6K \pm 5.2K$

$\bar{T}_{MEGL} = 833.0K \pm 7.4K$

Shot no.	ONERA Model Temperature (Kelvin)	max.c-c.	MEGL Model Temperature (Kelvin)	max.c-c.
1	680	.99592	786	.99876
2	660	.99310	753	.99870
3	720	.99533	828	.99765
4	700	.99550	793	.99738
5	660	.99710	773	.99900
6	720	.99611	848	.99730
7	680	.99576	784	.99803
8	700	.99399	801	.99647
9	640	.99371	738	.99745
10	680	.99677	817	.99747
11	680	.99510	780	.99803
12	760	.99634	868	.99776
13	780	.99565	915	.99732

Shot no.	ONERA Model Temperature (Kelvin)	max.c-c.	MEGL Model Temperature (Kelvin)	max.c-c.
14	720	.99491	832	.99718
15	720	.99557	818	.99798
16	760	.99564	892	.99713
17	820	.99598	959	.99504
18	700	.99560	820	.99809
19	740	.99516		
20	680	.99522		
21	680	.99540	798	.99834
22	760	.99044	847	.99373
23	760	.99594	883	.99736
24	720	.99444	820	.99778
25	700	.99387	816	.99704
26	760	.99398	869	.99590
27	700	.99613		
28	760	.99540		
29	740	.99616		
30	760	.99545		
31	700	.99562		
32	700	.99488		
33	740	.99652		
34	740	.99639	870	.99681
35	780	.99623	906	.99705

Shot no.	ONERA Model Temperature (Kelvin)	max.c-c.	MEGL Model Temperature (Kelvin)	max.c-c.
36	740	.99707	878	.99706
37	760	.99500	867	.99619
38	700	.99395	799	.99707
39	740	.99614		
40	740	.99618		
41	720	.99636		
42	720	.99618		
43	680	.99510		
44	740	.99492		
45	680	.99334		
46	720	.99576		
47	720	.99568		
48	700	.99722		
49	760	.99249		
50	760	.99638		

Table 3.5: Sample Shot-to-shot HPHT Evaluation of ONERA Model and MEGL Model

From Table 3.5, the MEGL model predicts a CARS temperature 133K and 140K too high for the two cases, while the ONERA hard collision model predicts a CARS temperature 23K and 36K too high for the two cases. The

maximum cross-covariances for each shot are found to be systematically larger when the experimental CARS data is fitted against the MEGL model spectra, than when the experimental data is fitted against the ONERA model spectra. However, the MEGL model completely over-emphasizes pressure narowing effects on the spectral width (fwhm), and the rotational bands in the high temperature spectra, and thus consistently over-estimates the temperature of the high pressure system under study.

Comparing the maximum cross-covariances of the fit between the MEGL model spectra and the experimental HPHT CARS spectra, with the maximum cross-covariances of the experimental database fit presented in chapter 2, it is clear that the maximum cross-covariances presented in chapter 2 are generally larger than those presented here. This indicates that the fitting of experimental spectra against each other as presented in chapter 2 is an improvement over fitting experimental spectra against these two sets of model spectra.

Chapter 4

CARS Temperature Measurements in a Knocking Methanol Fuelled Engine

4.1 The Engine Experiment

The engine used for the study was a single-cylinder Ricardo E6 variable compression ratio research engine equipped with a Lawrence Scott dynamometer. The principal details of the engine are:

Bore	75 mm
Stroke	111 mm
Connecting Rod	240 mm

The Ricardo E6 engine is a low-swirl, low turbulence engine. The combustion chamber of the engine is cylindrical in shape, the piston crown and cylinder head being flat. The spark plug is situated 12 mm from the center axis of the cylinder, with the pressure transducer aperture situated 12 mm from the center axis, diametrically opposite the spark plug. The only features of the combustion chamber that break cylindrical symmetry are the spark plug, the pressure transducer, the inlet valve, the exhaust valve, and the recessed windows that provide optical access.

At low engine speeds (less than 2500 rpm) there is so little turbulence in the engine that it takes ten to fifteen crankshaft degrees for the flame front to develop from the spark [128]. In this respect, the Ricardo E6 engine does not reflect modern engineering design: in most modern commercial production engines swirl is deliberately introduced in the cylinder in order to increase turbulence and thereby increase the flame speed, and hence the rate of combustion. Thus modern engines tend to maximise the interaction between the chemical and fluid flow aspects of combustion in order to secure faster flame propagation.

In contrast, the low swirl and low turbulence of the Ricardo E6 engine minimise the interaction between the chemical and fluid flow aspects of combustion. This makes the Ricardo E6 engine an ideal engine for attempting to isolate the specific chemical-kinetic features of engine knock. The special characteristics of the engine allow experimental data to be compared with the results of simplified knock models, which are able to focus on the details of the autoignition chemistry by reducing the dimensionality of the problem to zero.

The engine was fitted with a spacer, 12 mm thick, between the cylinder head and the engine block. The spacer housed two diametrically opposed Spectrosil

B (synthetic fused silica) windows to give optical access to the cylinder. With the spacer in position the maximum compression ratio of the engine was 9.5:1. The engine was naturally aspirated, and provision was made for preheating the inlet air prior to admission to the carburetor. The inlet air was preheated typically to 420 K in order to operate the engine under knocking conditions. Fuel and air intake were monitored with an estimated accuracy of 4% ; and in order to induce knock at a modest compression ratio the timing was advanced and the engine was run lean. Details of the equivalence ratios and other relevant engine parameters are given in Appendix (2).

An AVL water-cooled pressure transducer, type 12QP, was used for pressure measurement. The transducer signal was processed using a Kistler model 568 charge amplifier. A computerized data acquisition system was used to log the cylinder pressure signal. Pressure measurements were taken every half degree of crankshaft angle and written to memory in an IBM XT personal computer fitted with an RC Electronics ISC-16 interface, emulating a digital storage oscilloscope.

The 8 mm diameter pump and Stokes beams were used in a co-linear configuration with parallel polarizations, the beams being brought to a focal waist at the midpoint of the cylinder with a 300 mm focal length achromat. Since this resulted in a 2 mm diameter beam at the windows, the laser had to be operated at reduced pulse energy in order to avoid optical damage. It was nevertheless possible to obtain nitrogen CARS peak signal strengths of the order of ten thousand counts per pixel.

In the present experiment referencing was performed by averaging single-shot spectra of non-resonant argon at high pressure, and then taking the quotient of the single-shot resonant spectra with the average non-resonant argon spectrum. This simpler referencing technique is in common use, and appears to

be only marginally less accurate than shot-to-shot referencing [53].

By using crankshaft and camshaft encoders, a synchronization pulse was generated at top dead center of the exhaust stroke. A time delay was then introduced to fire the laser and gate the OMA at any subsequent crankshaft angle. The engine speed was controlled by manual setting of the dynamometer with an absolute error not exceeding 20 rpm. The experiments were run under the control of a DEC PDP 11/73 computer, which was programmed to sample every tenth compression stroke. Spectra were accumulated in groups of thirty; five groups of thirty shots were recorded at each of the chosen crankshaft angles. Pressure traces from the transducer in the cylinder head were recorded simultaneously. A schematic block diagram of the experiment is presented in figure 4.01.

Spectra were recorded for the engine motoring (i.e. without being fired) at 1000 rpm, in order to provide a check on the accuracy of the pressure and temperature measurements; and for the engine firing at speeds of 800 rpm, 1200 rpm and 1400 rpm under knocking conditions. Spectra were also recorded for the engine running normally at 2000 rpm.

4.2 Analysis of CARS spectra

At the high pressures developed in an internal combustion engine, nitrogen Q-branch CARS spectra are subject to the phenomenon of collisional narrowing, which distorts their shape. The most common method for analyzing high-pressure CARS spectra involves the use of approximate theoretical models derived from spectral scaling laws. Small uncertainties in the theoretical models may lead to significant errors in the temperature. This feature of CARS spectra, and the way in which pressure narrowing is modelled was discussed in

detail in Chapter 3. These errors cannot be tolerated when the temperatures are to be used as input data for chemical kinetic modelling.

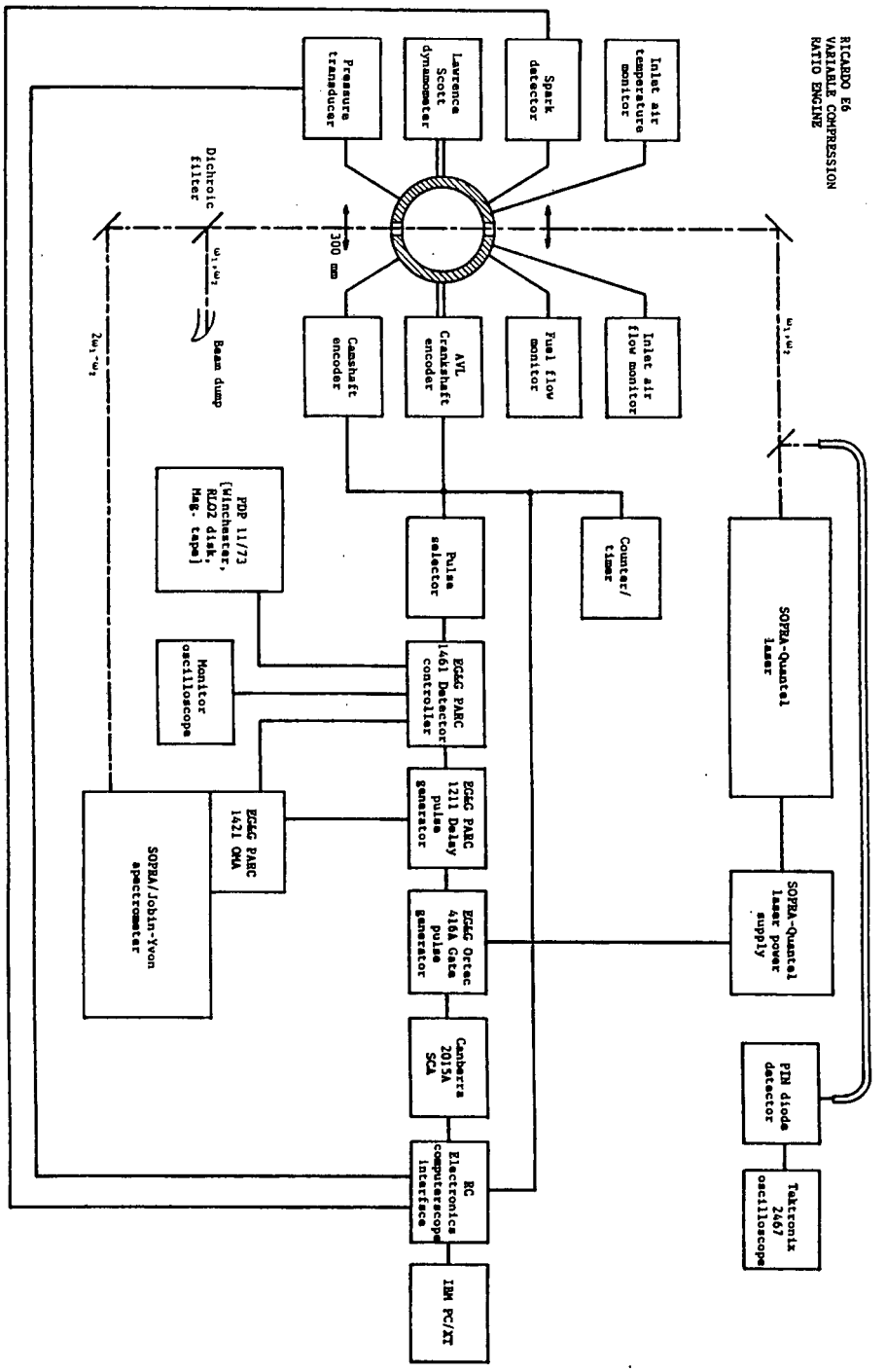

Block Diagram 4.01: Ricardo E6 Engine Diagnostics

This thesis presents a purely experimental method which circumvents these difficulties. Instead of calculating theoretical spectra, we created a database of referenced nitrogen CARS spectra covering the full range of temperatures and pressures relevant to the engine experiment, using a calibrated high-pressure high-temperature (HPHT) cell. The HPHT cell was designed for temperatures ranging from room temperature to 1200 K, and pressures ranging from atmospheric pressure to 20 bar. Error estimates for the temperature in the HPHT cell were a possible systematic error of 12 K, and a random error estimate of 3 K, originating from the accuracy of the thermocouple and transducer. The error in the pressure was estimated to be 0.05 bar. The details of this experiment were discussed in Chapter 3.

Five sets of fifty spectra were taken for each temperature and pressure. The database was defined as a set of averaged spectra covering a grid of temperatures and pressures at intervals of 25 K in temperature and 0.5 bar in pressure for the range of pressure 1 bar to 10 bar, and intervals of 40 K in temperature and 1 bar in pressure for the range of pressures 10 bar to 20 bar.

4.3 Fitting Engine CARS Spectra to HPHT Spectra

The cross-covariance fitting technique discussed in Chapter 3 was used to compare the referenced single-shot engine spectra with the averaged spectra from the HPHT database. Slightly different focusing conditions had been used in the two experiments. This was compensated for by convolving the more finely focused spectra (HPHT cell) with a gaussian function, so as to match the focussing conditions of the more coarsely focused spectra (i.e. engine). The necessary convolution parameters were obtained by comparing the pro-

files of room temperature, atmospheric pressure CARS spectra from the two experiments as described in Chapter 2.

The maximum cross-covariance coefficient from comparing the room temperature, atmospheric pressure spectra directly was $\beta_{max} = 0.99375$. The optimised convolution parameter was found to be $c = 0.00052$, and the maximum cross-covariance coefficient from comparing the averaged internal combustion ambient temperature and pressure CARS spectrum with the broadened HPHT spectrum improved from 0.99375 to $\beta_{max} = 0.99673$.

The subsequent cross-correlations (i.e. the normalized cross- covariances) between the adjusted experimental HPHT spectra, and the engine spectra at higher temperatures and pressures were found to be significantly greater than those between experimental spectra (of either class) and theoretical spectra calculated using the major scaling law models. This suggests that the effect of the differences in non-resonant CARS background under the somewhat different conditions pertaining in the engine (which contained methanol vapor) and in the reference cell (which did not) is less significant than the deficiencies in the theoretical spectral models.

Engine temperatures were deduced by comparing single-shot CARS spectra with database spectra recorded at varying temperatures but at the same pressure as the engine spectrum. Maximum cross-correlation was taken as the goodness-of-fit criterion. For the purpose of data analysis the single-shot temperatures corresponding to the maximum correlation were treated as normally distributed, and the mean, standard error, true mean, and the standard error of the true mean were determined.

The following tables show the shot-to-shot cross-covariance statistics for two representative CARS engine data sets.

CARS Engine Data Set No. 1: Crankshaft Angle = 180.0 degrees BTDC, Engine Pressure = 0.9bar ± 0.1bar

$T_{CARS} = 138.1°C \pm 5.7°C$

Shot no.	Temperature Celsius	max.c-c.	Shot no.	Temperature Celsius	max.c-c.
1	112	.99672	16	112	.99783
2	204	.99773	17	158	.99738
3	112	.99791	18	112	.99801
4	112	.99808	19	89	.99893
5	135	.99854	20	112	.99726
6	135	.99772	21	158	.99784
7	135	.99644	22	181	.99888
8	181	.99660	23	112	.99924
9	135	.99805	24	250	.99617
10	135	.99792	25	112	.99712
11	135	.99781	26	135	.99740
12	135	.99785	27	158	.99808
13	135	.99628	28	112	.99555
14	135	.99561	29	135	.99806
15	135	.99778	30	135	.99673

Table 4.1: Shot-to-shot CARS data statistics for CARS data obtained from the Ricardo E6 research engine at P = 0.9bar.

CARS Engine Data Set No. 2: Crankshaft Angle = 14 degrees BTDC, Engine Pressure = 14.8 ± 0.4 bar

$T_{CARS} = 568.7°C \pm 11.0°C$

Shot no.	Temperature Celsius	max.c-c.	Shot no.	Temperature Celsius	max.c-c.
1	610	.99809	16	610	.99827
2	530	.99818	17	610	.99810
3	650	.99813	18	610	.99811
4	490	.99916	19	730	.99536
5	490	.99603	20	490	.99965
6	570	.99743	21	570	.99868
7	570	.99875	22	570	.99868
8	530	.99695	23	490	.99812
9	690	.99185	24	530	.99455
10	530	.99695	25	530	.99580
11	570	.99744	26	570	.99691
12	570	.99905	27	730	.87143
13	530	.99783	28	570	.99693
14	530	.99562	29	570	.99713
15	530	.99871	30	490	.99824

Table 4.2: Shot-to-shot CARS data statistics for CARS data obtained from the Ricardo E6 research engine at P = 14.8bar.

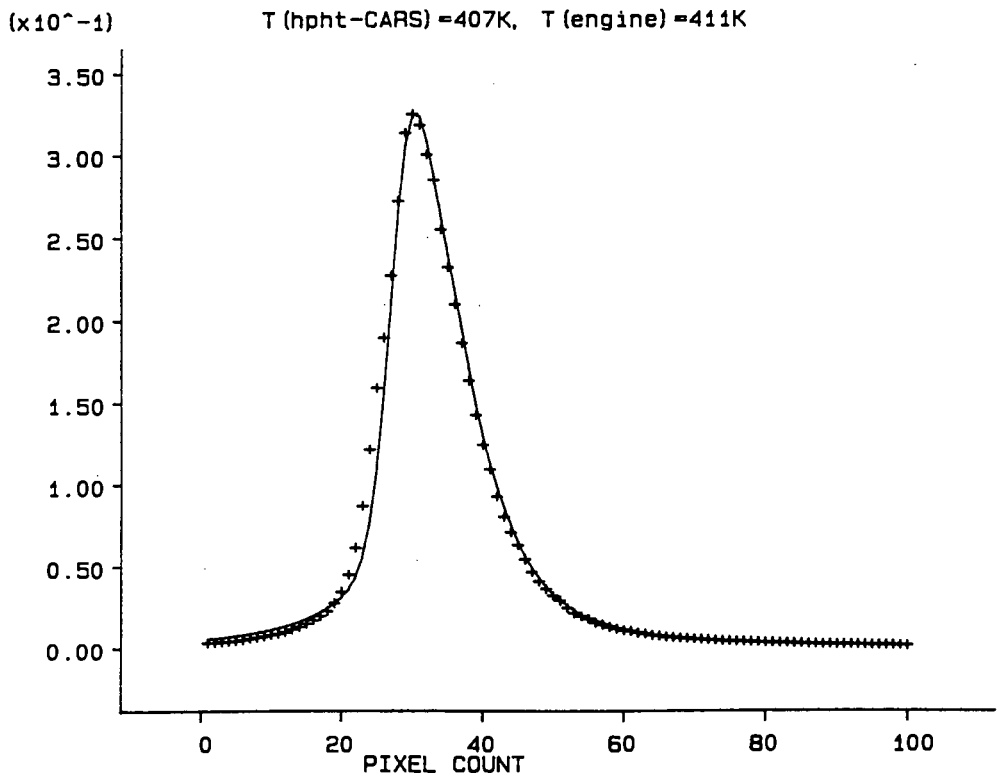

Figure 4.1: Averaged CARS data obtained from the Ricardo E6 research engine at P = 1.0 bar, fitted against a broadened, averaged HPHT spectrum

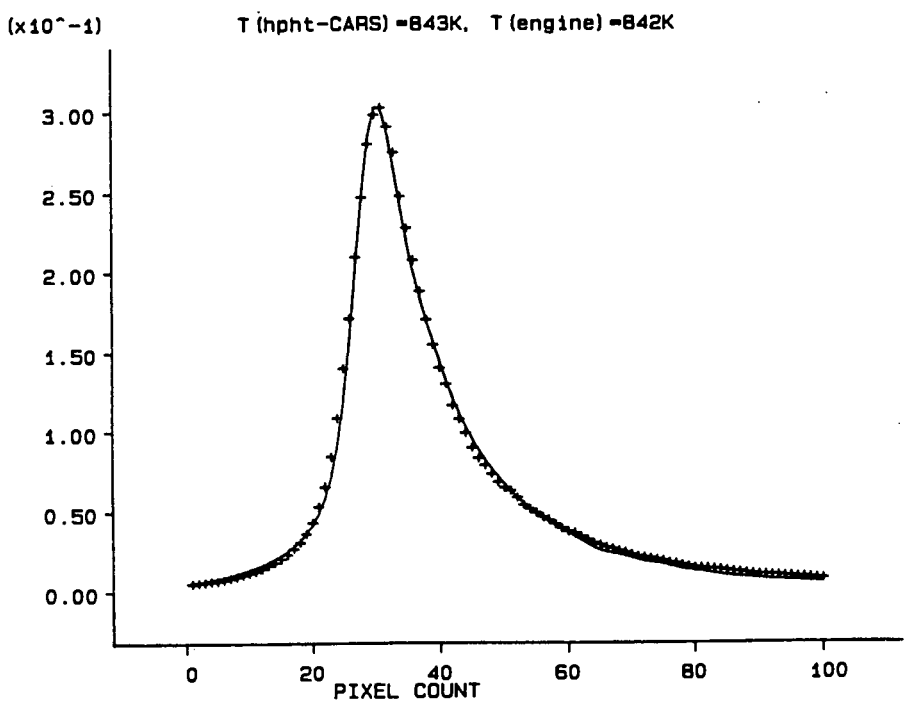

Figure 4.2: Averaged CARS data obtained from the Ricardo E6 research engine at P = 14.8 bar, fitted against a broadened, averaged HPHT spectrum

Figures 4.1 and 4.2 show the best fit of the averaged engine spectra against the broadened, averaged HPHT spectra for the CARS data presented in Tables 4.1 and 4.2

More than two-thirds of the engine CARS spectra have maximum cross-covariances greater than 0.997 when compared against HPHT database spectra. The systematic errors in these deduced temperatures are quantifiable and small ($\pm 15K$). These results must be compared with the results from the ONERA model, and the EGL model. The maximum cross-covariances obtained by comparing HPHT spectra with engine spectra are significantly greater than those obtained by comparing engine spectra with ONERA model spectra, and EGL model spectra. Furthermore, EGL model spectra produce large systematic errors in the predicted temperatures as a result of over-emphasizing pressure narrowing effects. Thus using the experimental HPHT database for deducing engine CARS temperatures is a significant improvement over both the ONERA hard collision model and the EGL model.

4.4 Results

Figures 4.3 and 4.4 show the temperature as a function of crankshaft angle for the engine running under knocking conditions at 1200 r.p.m. and 1400 r.p.m. respectively. The data points are the deduced mean temperatures per data set, and the error bars represent 95 % confidence levels. There are 125 data points in all, of which (as expected) only three are outside the confidence limits.

It is worth commenting on the small local minimum in the temperature observed near 100 degrees before top dead center. This is a consequence of the experimental arrangement. Since the spacer in which the fused silica windows

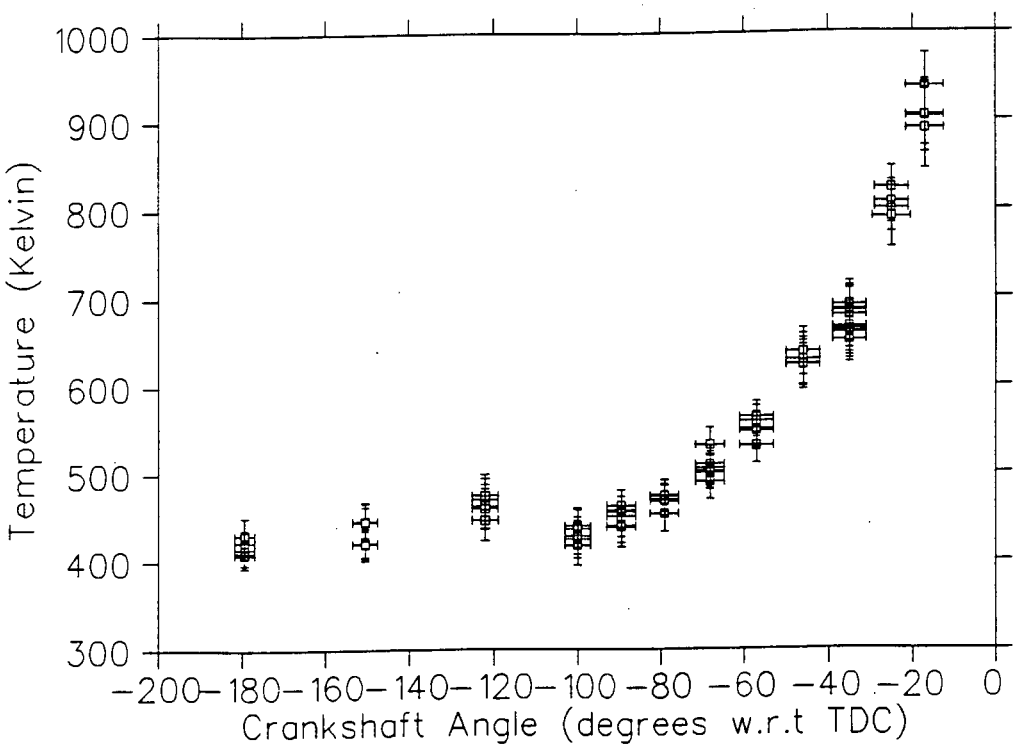

Figure 4.3: Temperature Profile as a function of Crankshaft Angle in the Ricardo E6 Engine running at 1200 rpm.

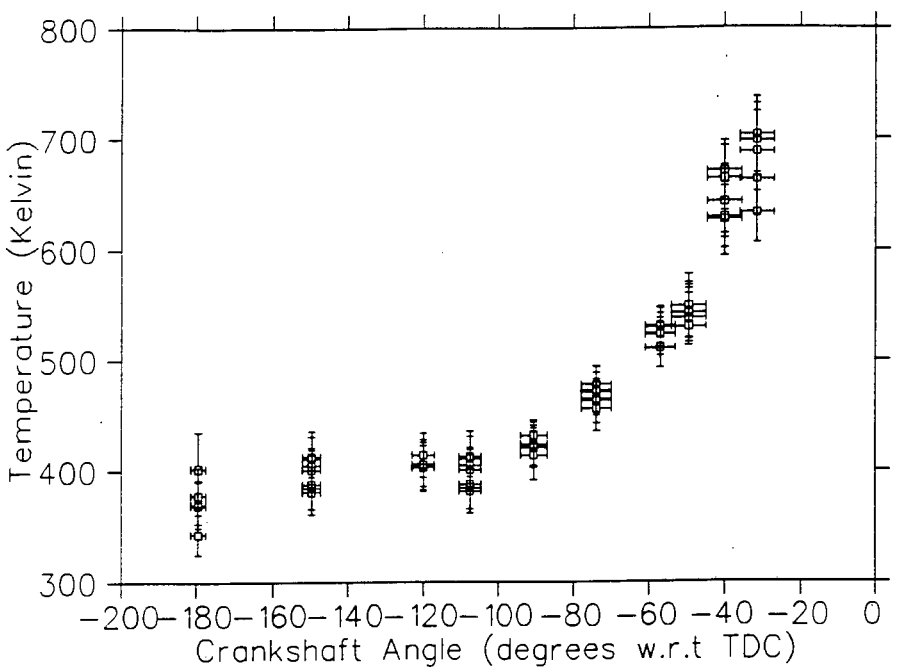

Figure 4.4: Temperature Profile as a function of Crankshaft Angle in the Ricardo E6 Engine running at 1400 rpm.

are mounted is 12 mm thick, the laser beams sample a small volume in the center of the combustion chamber which lies about 6 mm above the top of the cylinder block. At the end of the exhaust stroke some hot gas remains in this region: scavenging is not perfect. The cold charge of air and fuel admitted on the next inlet stroke is not fully mixed with the residual hot gas until halfway through the compression stroke.

Figure 4.5 shows five representative pressure traces for the 1200 r.p.m. data with the engine knocking. The pressure oscillations around the knock point can be seen clearly. These oscillations are produced by the reflections of the autoignition shock wave off the cylinder walls. The knock point occurs about half a degree before the first peak of each pressure trace, with an error estimate of one degree.

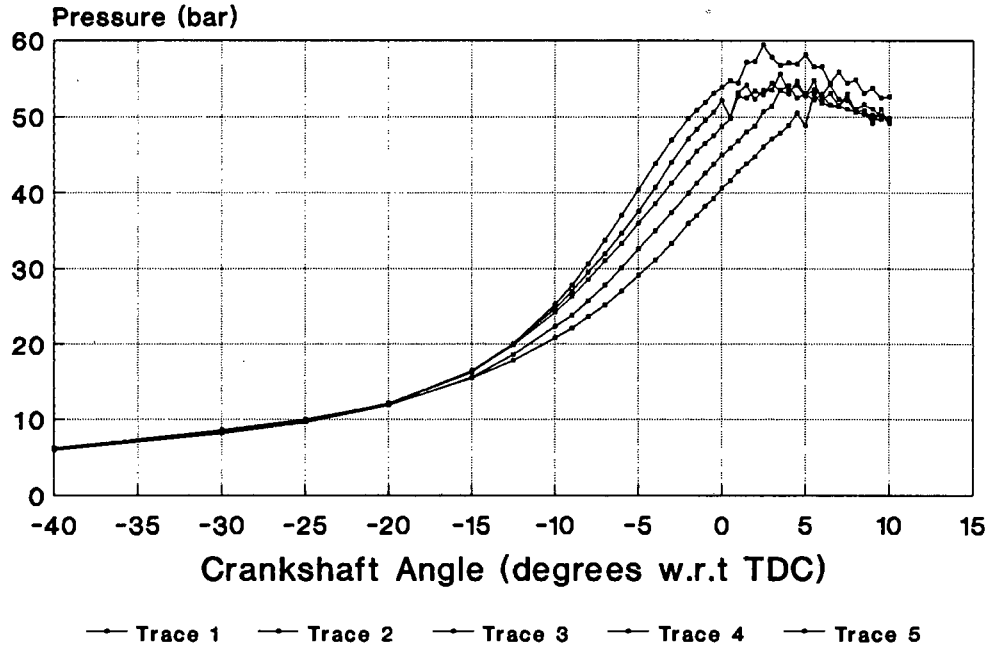

Figure 4.5: Five pressure traces obtained from the Ricardo E6 engine knocking at 1200 rpm.

Successive pressure traces are subject to considerable variation because of cycle-to-cycle fluctuations, which are especially pronounced when the engine knocks. Furthermore, it is difficult to hold the engine speed entirely constant under knocking conditions: the engine tends to run irregularly.

Because of shot-to-shot dye laser spectral fluctuations, it is essential to average the temperatures derived from several comparable CARS spectra (or to average the spectra themselves). Since the laser is fired with a fixed time delay after the crankangle TDC marker pulse, irregularities in engine speed translate into an uncertainty as to the precise value of the crankshaft angle at the moment when a CARS spectrum is recorded: these fluctuations can be as much as 5 degrees. A partial correction for this is made by recording a marker pulse, which is derived from the TTL pulse that fires the laser, on the pressure transducer trace. However, it is inevitable that temperatures derived from CARS spectra recorded at slightly different crank angles are grouped together and averaged. In performing the modelling analysis we have therefore associated pressure traces which have early marker pulses with the lower temperatures in the set, and vice versa. This allows some correction to be made for cycle-to-cycle fluctuations.

The measured temperatures and pressures were then used as input for the chemical kinetic modeling of autoignition without any attempt to correct for imperfect scavenging and mixing. The errors introduced by this are not likely to be significant, since the end-gas reactions are so slow as to be imperceptible at 400 K.

Chapter 5

Review of Chemical Kinetic Modelling of Methanol Combustion and Engine Autoignition

5.1 Methanol Combustion

This review of methanol combustion chemistry begins with the early attempts to develop detailed mechanisms to describe various aspects of methanol combustion. Broadly speaking, there are three temperature regimes for the study of methanol chemistry: the low temperature regime ($T < 900K$), the intermediate temperature regime ($900K < T < 1600K$), and the high temperature regime ($T > 1600K$).

The low temperature regime for methanol combustion occurs in situations

where the conditions are kept nearly isothermal. This occurs when the methanol/oxidant mixture reacts in some kind of chemical reactor or low temperature heat reservoir. The reaction develops slowly, with a low rate of heat release. This regime is useful for studying reaction rates for the creation and consumption of unstable intermediates. Therefore, this low temperature regime is widely used in the careful examination of individual reaction rates. This reaction data is then used in the construction of comprehensive combustion mechanisms.

The intermediate temperature regime occurs in the study of methanol autoignition, stirred and static reactor chemistry, detonation phenomena, inhibited flame chemistry, and flame chemistry of dilute mixtures. This regime is useful for examining reaction rates for the entire system of reactions involved in methanol combustion, and much of the development of the many methanol combustion mechanisms published to date has occurred in this temperature range. Indeed, the temperature-pressure explosion limits for stoichiometric methanol/oxidant mixtures occur in this regime. Explosion limits are widely used as a means of testing combustion mechanisms.

The high temperature regime occurs in the study of shock tube reaction chemistry and near stoichiometric methanol/oxidant flames. Historically, flame chemistry has been the most fruitful area of study for the validation of combustion mechanisms, a consequence of the unique relationship between fuel type and laminar flame speed. A significant test of any comprehensive combustion mechanism is the comparison of the theoretically predicted laminar flame speed with the experimentally measured laminar flame speed. The comparison of the laminar flame speeds is usually performed as a function of mixture fraction and pressure.

The interest in developing a comprehensive mechanism of methanol combus-

tion came about in the mid 1970's, as a consequence of the growing concern regarding pollutant emissions from conventional hydrocarbon fuel, and the perceived need to develop alternative fuels. Consequently, methanol was suggested as an attractive alternative to conventional hydrocarbon fuels. At that stage, very little detailed information on the high temperature oxidation of methanol was known.

In 1975, C. Bowman [16] reported the results of an investigation into the oxidation of methanol behind reflected shock waves. The experiment was performed in the temperature range 1500 K - 2200 K. He reported two distinct combustion phases: an induction phase, where the concentrations of radical species and water increased rapidly with little change in temperature, and an exothermic phase, where the concentrations of radical species and water slowly approached equilibrium, but with a sharp heat release, and consequent rapid increase in temperature. He proposed a 19-reaction mechanism to account for the methanol oxidation chemistry, and reported relatively good agreement between the modelling results and his measurements.

Following Bowman's paper, Adelman et al [2] attempted to use Bowman's 19-reaction mechanism to calculate methanol ignition delays under different low temperature conditions. These calculations were matched against measurements performed by Mullins [87]. The high temperature mechanism of Bowman failed to give comparable results. This led to a modification of the rate coefficients for three key reactions in the Bowman 19-reaction mechanism in order to produce suitable ignition delay results.

It was suggested in a paper by Aronowitz et al [8] that the failure of Bowman' mechanism to reproduce low temperature chemistry results was due to the omission of hydroperoxyl chemistry from his model. This paper went on to model the methanol oxidation rate in an adiabatic, turbulent flow reactor using

semiglobal modelling techniques. They were able to present two correlated semiglobal expressions for the rate of methanol oxidation for lean and rich mixtures respectively. They were able to deduce mechanistic features which were included in a 28 step elementary reaction mechanism.

Aronowitz et al [7] published another paper that year focussing on methanol pyrolysis in an adiabatic turbulent flow reactor in the temperature range 1070K - 1225 K. They proposed a 19-step mechanism to explain the experimental results. Methanol pyrolysis experiments are important in establishing the rates of thermal decomposition of methanol, and the role of hydrogen in pyrolysis reactions. They found that hydrogen promotes pyrolysis, and methane inhibits pyrolysis.

In 1978 Akrich et al [1] published a paper on flame profiles of major species for methanol flames of different equivalence ratios at low pressure. They performed their experiment on a stabilised flat flame burner at a pressure of 80 torr. Major species concentration profiles and flame temperature profile was measured. Using simple mechanistic assumptions, they calculated reaction rates for the major intermediate species. They were able to validate the major features of Bowman's 19-step reaction mechanism for their flame experiment, performed under different experimental conditions to Bowman's experiment.

The following year Westbrook and Dryer [119] proposed a 26 species, 84 elementary reaction mechanism for methanol oxidation. This mechanism was constructed from past studies in methanol combustion chemistry over a range of conditions, and included a detailed study of CH_3OH and CH_2OH reactions taken from a turbulent flow reactor and shock tubes. The proposed reaction mechanism successfully reproduced experimental results from a variety of experiments, covering a temperature range from 1000 K to 2180 K, a pressure range from 1 atmosphere to 5 atmospheres, and equivalence ratios between

0.05 and 3.0. The proposed chemical mechanism was then used to calculate the laminar flame speed of a stoichiometric one-dimensional methanol-air flame. This theoretical value was found to be in good agreement with experimentally measured values.

Westbrook [120] then used this comprehensive mechanism to calculate the laminar flame speeds of a one-dimensional methanol-air flame, for different pressures and equivalence ratios. These values compared favourably with experimentally measured values. He focussed his analysis on the effects of pressure and equivalence ratio on the flame speed and the behaviour of the flame. He found that flame properties changed considerably as a function of pressure at high pressures, and ascribed this behaviour to the competition of the termolecular pressure-dependent reaction

$$H + O_2 + M' \rightarrow HO_2 + M'$$

with the key chain branching reaction,

$$H + O_2 \rightarrow OH + O.$$

Following this paper, Westbrook published a further paper [117] on the inhibition of laminar methane-air and methanol-air flames by hydrogen bromide. The methanol-air flame calculations used the 84 elementary reaction mechanism published earlier [119]. The importance of this paper was that it focussed on the competition for hydrogen atoms within the mechanism through the following reactions,

$$H + HX \rightleftharpoons H_2 + X$$

$$H + X_2 \rightleftharpoons HX + X$$

$$H + O_2 + M' \rightleftharpoons HO_2 + M'$$

$$H + O_2 \rightleftharpoons OH + O$$

$$H + X + M' \rightleftharpoons HX + M'$$

$$X + X + M' \rightleftharpoons X_2 + M'.$$

The computed results were found to agree well with experimental data. It was found that lean flames were inhibited more rapidly than stoichiometric and rich flames. Furthermore, the efficiency of inhibition increased with pressure. This was ascribed to the competition for hydrogen atoms and the pressure dependence in the six above reactions.

Tsuboi and Hashimoto [110] then published a shock tube study on the homogeneous thermal oxidation of methanol highly diluted in argon, performed at temperatures between 1200 K and 1800 K. The equivalence ratio was varied between 0.2 and 2.0. The progress of the methanol oxidation reaction was determined by measuring the infrared emission from the methanol, water, carbon monoxide, carbon dioxide and formaldehyde present behind the shock wave. A reaction induction time was deduced from the infrared signal for the different conditions specified above. A model relating the major species concentrations and the system temperature was fitted to the induction time data. A 57 elementary reaction mechanism was used for comparison with the measured species concentration, and theoretical induction times were calculated. Both calculations agreed well with experimental results.

Tsuboi et al [111] then published a study of the thermal decomposition of methanol behind shock waves. The intention was to establish the temperature and density dependence of the decomposition rate coefficients. This was

done by following the progress of the reactions using uv absorption and infrared emission techniques, and comparing the results of the measurements against the predictions from a chemical kinetic model of methanol decomposition. They found that the rate constants for methanol decomposition were pressure dependent at densities of between 10^{-5} and 2×10^{-4}mol.cm^{-3}, and for temperatures in the range 1300K to 1800K, and determined the Arrhenius parameters for the decomposition reactions.

Natarajan and Bhaskaran [88] performed a similar study to Tsuboi and Hashimoto discussed above, also examining the ignition of methanol-oxygen-argon mixtures behind reflected shock waves. However, this study was performed at pressures of 2.5 bar and 4.5 bar. Ignition was identified by the emission of visible light from the shock tube. The time delay for the reaction was determined to be the time interval between the arrival of the incident shock, and the first visible light emission. An expression relating the ignition delay to the initial concentrations of methanol and oxygen, and the initial temperature was fitted. A 35-step reaction mechanism was proposed to describe the methanol oxidation, and a comparison of the calculated ignition delay times compared well with the experimentally measured delay times.

Now that a comprehensive mechanism had been established for methanol combustion over a range of conditions, the focus of research into methanol combustion switched to modelling emission levels from reaction conditions similar to those found in an internal combustion engine. A number of researchers had identified flame wall quenching, crevice volumes, and surface deposits as possible sources of hydrocarbon emission [28] [3]. Consequently, Westbrook et al [118] undertook a modelling study of laminar flame wall quenching of methane-air and methanol-air flames. This study was performed using a one-dimensional model of a flame incident perpendicular to a wall of temperature 300 K. The flame propagated through a fuel/air mixture of pressure 10 bar.

They were able to show, using the comprehensive mechanisms published in 1979, that differences between the temperature dependence of radical recombination reactions and the conventional chain branching and chain propagating reactions were responsible for quenching the flame at the wall. They calculated that the unburned hydrocarbon content from flame quenching at the walls was considerably smaller than expected.

Following this paper, Ito et al [67] published measurements of unburned methanol and formaldehyde in the exhaust gases from a methanol fuelled Otto engine. They used a derivative spectrophotometer to measure the formaldehyde levels at several distances along the exhaust tube for various equivalence ratios and ignition timings. Measurements were also made of the methanol levels using a gaschromatograph. They found that the emission characteristics of formaldehyde differed considerably from the emission characteristics of the unburned methanol. The unburned methanol concentration was at a minimum for the equivalence ratio satisfying $0.9 < \phi < 1.0$, and increased as the mixture became richer or leaner. The effects of ignition timing were found to be sensitive to rich mixtures. The formaldehyde concentration was found to increase with equivalence ratio in the range of lean mixtures, but varied little for rich mixtures. Oxidation of methanol to formaldehyde was found to occur in the exhaust.

Yano and Ito [126] published modelling studies based on the above measurements, and reported good agreement between their modelling results and the experimental results. Their kinetic mechanism was based on that published by Bowman [16], and Westbrook [119], containing 75 elementary reactions, and included 19 reactions involving NO_X chemistry. The calculation assumed that the exhaust gas flow could be treated as a one-dimensional, steady flow at atmospheric pressure. The temperature of the exhaust gas was considered to remain constant throughout the flow region.

In 1983, Dove and Warnatz [31] published results of a modelling study of methanol-air flames, where they calculated burning velocities as a function of equivalence ratio and pressure. The methanol composition was varied from 8% to 20% at 298 K and 1 bar, and the mixture was set stoichiometric for pressures ranging from 0.0625 bar to 16 bar. A high temperature reaction meachanism, comprising 15 species and 40 reactions was proposed, based on a full survey of high temperature reaction data. They found that the predicted burning velocities decreased with increasing pressure, and concluded that this was because the termolecular reaction

$$H + O_2 + M' \rightarrow HO_2 + M'$$

competed more effectively for hydrogen atoms as a function of pressure compared with the branching reaction

$$H + O_2 \rightarrow OH + O.$$

This result is in agreement with Westbrook's conclusions from his earlier paper on methanol-air flames [120]. Dove and Warnatz also calculated the methanol burning velocities as a function of temperature, and compared their results with experimental data from Gibbs and Calcote [47], Metgalchi and Keck [84], and Gulder [57]. The theoretically calculated dependence agreed well with these experimental results. Finally, Dove and Warnatz performed a normalised sensitivity analysis on the burning velocities as a function of the rate constants, and concluded that the most important reactions for flame calculations were the following:

$$H + O_2 \rightarrow OH + H$$

$$CO + OH \rightarrow CO_2 + H$$

$$CHO + M' \rightarrow CO + H + M'.$$

The importance of this paper has been shown by the wide use of the 40 reaction mechanism published in this paper for other methanol flame studies. Furthermore, this paper points out which reaction rate coefficients must be known with a great deal of accuracy, in order to model methanol flame propagation successfully.

Dimpelfeld and Foster [30] then published results of a modelling study of autoignition in a s.i. engine, using methanol, methane, ethane, ethylene, propane, and n-butane as engine fuels. The experiment was performed on a CFR engine, with experimental pressure data being used to simulate the pressure-temperature history of the end gas. The modelling study of autoignition used comprehensive chemical mechanisms published in the literature. The methanol mechanism used was that published by Westbrook and Dryer [119]. Assuming that the temperature of the end gas followed the same temperature history of the bulk gas, they found that the predicted knock point occurred much later than the observed knock point, and concluded that the core gas must go through a hotter temperature history than the bulk gas.

They then adjusted the temperature history of the end gas, so that the predicted autoignition points for the different fuels coincided with the experimentally determined autoignition points. They then compared the initial temperature differences for the different fuels, and found that methanol was the lowest at about 40 K, while ethylene was the highest with an initial temperature difference of 140 K. They performed a sensitivity analysis on the autoignition of a methane-ethane mixture, and found that only a few reaction equations dominated the rate of oxidation. They noted the importance of peroxide chemistry for this system.

In 1986 Vandooren et al [112] published results of an experimental and modelling study of the kinetics in a lean formaldehyde flame. This study was important, for it provided important rate constant data for formaldehyde oxidation reactions in flames. The experiment was performed using a stabilised Spalding-Botha flat flame burner with operating pressure 22.5 torr. Species concentrations were measured using molecular beam sampling, coupled with mass spectrometry. As a consequence of the simplicity of the formaldehyde oxidation mechanism, the rate coefficients could be accurately determined.

Also in 1986, Olsson et al [91] reported experimental and modelling results of a study of the addition of water to pre-mixed laminar methanol-air flames at low pressure. The experiment was performed with a stabilised water cooled flat flame burner operating at a pressure of 100 torr. The amount of water added to the methanol corresponded to 10% mass of liquid phase. Species profiles were measured by using a modulated molecular beam mass spectrometer. The kinetic mechanism used for the theoretical flame study was based on an updated Westbrook Dryer mechanism [122]; the mechanism was then altered, and the study repeated with rate coefficients of the key reactions replaced by the recommended values from Warnatz [44].

Experimentally, it was found that the presence of water with the methanol left the species profiles more or less unchanged, although it was noted that the rate of thermal decomposition of the CHO radical increased significantly with the presence of water. This was explained by the high chaperon efficiency of water vapour. The flame model was compared with the experimental results, and it was found that the altered mechanism was an improvement over the updated Westbrook Dryer mechanism.

This paper was followed up by another [92] that focussed on lean premixed laminar methanol flames at low pressures. This study was essentially a compar-

ative study between the Dove-Warnatz mechanism [31], and the Westbrook-Dryer-Shugh mechanism [122]. The flame data came from Vandooren et al [113] using a flat flame burner at 40 torr, with modulated molecular beam sampling and mass spectrometry. They found considerable disagreement between the theoretically calculated CH_2OH profile against the experimental CH_2OH profile, and recommended further work in the combustion chemistry of hydrogen, carbon monoxide, formaldehyde, methanol, methane and ethane.

Following Olsson's 1987 paper, Pauwels et al [93] reported on an experimental and numerical study of a low pressure stoichiometric methanol-air flame. They used a stabilised low pressure flat flame burner operating at 80 torr. The species concentrations were measured using gas chromatography coupled with esr detection of oxygen and hydrogen atoms, and hydroxyl radicals. experimental and modelled results were compared both in terms of species mole fraction profiles, and in terms of net reaction rate profiles. The kinetic mechanism used in this study consisted of the Dove-Warnatz mechanism [31], updated by Warnatz [44], except for the termolecular reaction rate coefficient,

$$H + O_2 + M' \rightarrow HO_2 + M'$$

and the formaldehyde-hydroperoxyl reaction rate coefficient,

$$CH_2O + HO_2 \rightarrow CHO + H_2O_2.$$

The rate coefficients for the above reactions were taken from the Lawrence Livermore database revised in 1985. They reported good agreement between the flame modelling results based on the revised Dove-Warnatz mechanism, and the experimentally measured results.

Following this paper, Norton and Dryer [89] reported new kinetic features of methanol oxidation seen in a turbulent flow reactor. They performed their experiments with equivalence ratios in the range of 0.6 - 1.6, initial temperatures between 1025 K and 1090 K at atmospheric pressure. They observed that at an intermediate point during the course of the reaction, a deceleration in the chemical reaction rate occurred, and hence a 'plateau' in the energy release and species concentrations developed. They reported that this effect became more pronounced with increasing equivalence ratio. The earlier comprehensive chemical kinetic mechanism of Westbrook and Dryer failed to explain this effect, and so Norton and Dryer revised the earlier Westbrook-Dryer mechanism. Most of the kinetic data for this revised mechanism came from Tsang's thermochemical database [109] on methanol reactions, plus some adapted rate coefficients. They reported that this revised mechanism gave better agreement with the flow reactor data, and improved understanding of the fundamental reactions involved in methanol oxidation. They emphasised the importance of hydroperoxyl chemistry, and the decreasing role of chain branching reactions during fuel consumption.

Grotheer and Kelm [55] reported the results of a careful study of the elementary reactions involved in high temperature methanol oxidation in flames. They found that there was a significant discrepancy between the experimental flame measurements, and the results of the theoretical calculations based on the existing high temperature oxidation mechanism. Noting that Norton and Dryer [89] had validated the methanol kinetic mechanism at 1000 K, they assumed that the discrepancy between theory and experiment in flame studies was caused by inaccurate rate coefficients at high temperatures. Consequently, they modified the rate coefficients for the CH_2OH and the CH_3O reactions, according to the work of Zaslonko et al [130], and adjusted the rate coefficients of the hydroperoxyl reactions in order to achieve agreement between the laminar flame speed measurements, and the corresponding theoretical calculation

of laminar flame speeds.

In 1990, Norton and Dryer [90] published a comprehensive mechanism for methanol pyrolysis. This mechanism was tested against pyrolysis reactions for a wide range of experiments and conditions. Data was considered from static reactors, flow reactors, and shock tube reactors, covering temperatures of 973K to 2000K, and pressures of 0.3 to 1.0 atmospheres. The model results compared favourably with the experimental results from all three reactors. The pyrolysis system was found to be highly sensitive to the rate of unimolecular fuel decomposition, and rates of chain termination reactions that remove CH_2OH radicals and H atoms from the system.

Following Norton and Dryer's paper, Pauwels et al [94] published a paper on the influence of equivalence ratio on the structure of low-pressure premixed methanol-air flames. They measured species concentration profiles using gas chromatography for the major stable species, and esr for the intermediate species, H atoms, O atoms, and hydroxyl radicals. The modelling calculation was performed using an updated version of the Westbrook-Dryer mechanism [119], with some of the rate coefficients replaced by those suggested by Van Tiggelen [113], and by Dove and Warnatz [31]. They found generally good agreement between the experimental measurements and the modelling, with the exception of the lean flame, where the calculated profiles were displaced further into the flame. They also performed a first order sensitivity analysis for the different species in the flame, and found that the dominant flame reactions were, in order of priority:

$$CHO + M \rightarrow CO + H + M'$$

$$CHO + O_2 \rightarrow CO + HO_2$$

$$CH_2OH + M' \rightarrow CH_2O + H + M'$$

$$CH_2OH + O_2 \rightarrow CH_2O + HO_2$$

$$CO_2 + H \rightarrow CO + OH$$

$$CH_3OH + H \rightarrow CH_2OH + H_2$$

$$CH_3OH + OH \rightarrow CH_2OH + H_2O$$

$$CHO + H \rightarrow CO + H_2$$

$$H + O_2 \rightarrow OH + H$$

$$HO_2 + H \rightarrow OH + OH.$$

Bradley et al [17] then published results of an experimental and theoretical study into laminar flame structure and burning velocities of premixed methanol-air. They used a stabilised flat flame matrix burner, with gas chromatography for the measurement of major species concentration profiles. Measurements were performed of burning velocities as a function of equivalence ratio. The equivalence ratio was varied between 0.7 - 1.3, with the pressure set at 0.089 atmospheres.

The two kinetic mechanisms used for the theoretical flame modelling was a compilation of reaction rate coefficient data from Dixon-Lewis et al [116], optimised Dove-Warnatz rate coefficients, with some rate coefficient data added from Tsuboi and Hashimoto [110], and Norton and Dryer [89]. The two reaction schemes used in the theoretical study were different in the way that they treated the CH_2OH/CH_3O chemistry. The first reaction scheme focussed only on CH_2OH chemistry, while the second reaction scheme treated the chemistry of CH_2OH as distinct from CH_3O. They found that the second reaction scheme reproduced the experimental flame speeds and species profiles with greater accuracy than the first reaction scheme.

Recently, Cribb et al [26] [27] reported the results of a kinetic study of oxidation and pyrolysis of methanol using shock tube and computer simulation

techniques. They employed laser Schlieren densitometry on the reacting gas behind incident shock waves, in order to measure rate of enthalpy change, and hence reaction rate. They also used time-resolved mass spectrometry on the reacting gas behind reflected shock waves, in order to measure absolute concentration profiles of all major reactant and product species, and some intermediate species. The oxidation experiment was performed in a temperature range 1800 K - 2800 K, for five gas mixtures ranging from lean to rich. They found that at high temperatures, the shock wave initiated reaction consisted qualitatively of two steps. The first step consisted of methanol decomposing to form H_2, CO, H_2O, and radicals. The second step consisted of the H_2/O_2 reaction, accompanied by the oxidation of CO.

The pyrolysis experiment was studied in the temperature range 1800 K to 2740 K. They compared experimental results with modelling results, and found a set of seven reactions that the system was particularly sensitive to. They adjusted the rate coefficients of these reactions to fit the experimental data, using the results of the sensitivity analysis and estimated accuracy of existing literature values.

The reaction mechanism developed for oxidation modelling purposes was based on that proposed in 1979 by Westbrook and Dryer [119], but included a number of changes. They did not differentiate between CH_3O and CH_2OH, and introduced some new reactions in the H_2/O_2 scheme for completeness. Some of the reaction rate coefficients were updated from Warnatz's review [44], and from adjusted rate coefficients from the pyrolysis experiment. They performed a sensitivity analysis on the system, and identified seven elementary reactions that the system was particularly sensitive to. These reaction rate coefficents were adjusted in the same way as before, and then compared with rate coefficients from the literature.

Finally, in a paper to be published late in 1992, Grotheer et al [56] comprehensively reviews the current literature on kinetic rate coefficients for the oxidation of methanol/air systems. Based on this review, the authors compile a comprehensive mechanism involving 414 reactions in 44 chemical species for the oxidation of methanol/air systems. They report the results of a modelling study of methanol/air flames, and discuss the comparison of measured flame speeds under a variety of conditions with the modelling results. They found good agreement between the experimentally measured flame speeds and the modelling results, but noted that the margin of error for specific reaction rate coefficients needed to be reduced.

The second paper in this series reports the results of a modelling study of autoignition in a methanol fuelled research engine [34]. The authors present in-cylinder pressure measurements and CARS temperature measurements of the methanol-air charge up to 12^o BTDC, and then assume that the end gas is compressed isentropically by the piston and the advancing flame front. They report that modelled autoignition times precede experimentally determined autoignition times significantly, and point out that rate coefficients for key propagation reactions have large margins of error, or have not even been measured.

5.2 Autoignition in a Spark Ignition Engine

The following summary of developments in autoignition studies prior to 1935 is taken from Egerton's paper, "Estimation of the Combustion Products from the Cylinder of the Petrol Engine and its Relation to 'Knock'" [39]. The summary of developments in the period 1930 to 1963 is taken from the two papers by Downs et al [33] [32], entitled "A Study of the Reactions that lead to 'Knock' in the Spark Ignition Engine", and "Pre-flame Reactions in the Spark

Ignition Engine: The Influence of Tetraethyl Lead and Other Anti-knocks."

Since the discovery of engine knock in 1905, engine researchers have used a variety of experimental and theoretical methods in order to understand the phenomenom. It was quickly understood that engine knock damaged engines. Consequently, engines and fuels had to be designed in such a way that knock was suppressed. This meant that spark ignition internal combustion engines operated with a knock limiting thermodynamic efficiency. Early research into the phenomenon attempted to establish empirically the processes involved in engine knock, and soon the discovery was made that certain chemical additives impeded knock, while other chemical additives aided knock. Ignition of the unburned fuel/air charge was established as a knock related phenomenon in the 1920's. At this time there were competing views regarding the kinetic mechanism causing end-gas ignition. It was argued by Callendar that knock occurred in the end-gas because peroxides were formed and stored, and then suddenly detonated, igniting the whole region simultaneously , while Egerton and others held the view that: quote: "an accumulation and decomposition of the primary products of reaction caused a larger number of chains of reacting molecules to be started in a given time".

It soon became clear that engine knock was predominantly a chemical process, that could be influenced to some degree by fuel/air charge flow processes, and by engine geometry. Consequently, much early research was directed at establishing the presence of, and concentrations of the key chemical species involved in engine knock. Ricardo and Thornicroft reported in 1928 that lead tetraethyl inhibited the formation of aldehydes. Dumanois et al reported in 1932 that when their research engine was knocking, aldehydes and peroxides were present in profusion, but not otherwise. Egerton et al reported estimates of combustion products from a knocking engine, and the relationship of these products to engine knock. They also performed a study of the efficiency of

'anti-knock' chemical agents, including such species as lead tetraethyl, aniline, ethyl iodide, and vapours of lead, thallium, potassium, selenium, and tellurium.

During the ten year period from 1930 to 1940, it was found that engine knock involving the higher paraffinic fuels originated from an ignition process in the 'end-gas' region of the cylinder. It was observed by Townend that this end-gas ignition occurred in two separate, identifiable stages. Later motored engine experiments involving ignition of the fuel/air charge indicated that this two-stage ignition is constituted of a low temperature process, involving the formation and reaction of organic peroxides, and cool flame formation, followed by a high temperature process. It was also established that some fuels (benzene, methane) knock only through a high temperature process, while others knock as a composite of low temperature and high temperature processes [32].

Researchers in the field of engine knock soon began using chemical kinetic methods in order to understand the chemistry of engine knock. Downs et al [33] published a study of the reactions that lead to 'knock' in a spark ignition engine, and concluded that reactions leading to knock with ordinary paraffinic fuels are of the low temperature type, are auto-catalytic, in that they form peroxides, and are catalysed by the addition of organic peroxides; are subject to self-inhibition in that they produce formaldehyde, which had been shown to have an anti-knock effect. They deduced that formaldehyde does not experience cool flame ignition, and that reactions leading to knock with fuels benzene and methane are auto-catalytic via aldehydes, and this was why these fuels experience hot flame ignition.

Downs and collaborators [32] continued to perform detailed studies on the effects of various anti-knock compounds, including tetraethyl lead on pre-flame

reactions in the spark ignition engine. Their experiments involved the measurement of peroxides in the engine using paper and gas chromatography, motoring the engine without spark ignition to measure cool and hot flame limits, and cool flame intensities for a wide range of fuels and fuel mixtures. Finally, they measured the effectiveness of anti-knock additives, individually and in combination, in a fired engine.

They concluded that organic peroxides were important in the first stage of two-stage ignition, and that hydrogen peroxide becomes more important as the second high temperature ignition stage is reached. Tetraethyl lead was believed to have little effect during the first ignition stage, and to lower the concentration of hydrogen peroxide during the second ignition stage, leaving the organic peroxides concentrations unaffected. It was found that increasing the lead concentration lowers the cool flame intensity, and that there was a reciprocal relationship between the temperature sensitivity of a fuel and the cool flame intensity produced under motored engine conditions.

These early studies into pre-flame reactions in the end gas, and the effect of anti-knocks on end gas ignition were very useful in laying the groundwork for later, more rigorous chemical kinetic studies of end gas reactions. Developing models of end gas ignition were and are required to reproduce determined experimental features of engine knock. Two competing models of engine knock developed over the years, although there is common cause amongst combustion researchers that engine knock is an ignition process in the unburned charge ahead of the advancing flame front.

The first model holds that this ignition process is a detonation wave generated in the end-gas from a conversion of the normal combustion wave to a detonation wave, or that it is a detonation wave generated in the end-gas from an autoignition site, with the surrounding region thermally primed to support

a detonation wave [85] [82]. The second model holds that engine knock is a global autoignition of the end-gas, a consequence of the near isentropic compression of the end-gas by the expanding burnt gases and the combustion wave [96] [105] [42]. There was ambiguous experimental evidence supporting both models, although in recent years the evidence has leaned heavily towards the autoignition model [105] [63].

During the 1970's, fuel researchers were performing standard experiments on the primary reference fuels. Barnard and Harwood [10] [11] studied the spontaneous combustion of n-heptane and iso-octane in a static reactor in the temperature range 510 K - 700 K. Pressure and temperature were measured as a function of the progress of the reaction. They determined the slow combustion/cool flame and cool flame/two-stage ignition boundaries for several heptane/oxygen mixtures. They found that the slow combustion reactions and the cool flame reactions were chemically very similar, and that the first stage of a two-stage ignition is identical with cool flame development.

In 1979 Coats and Williams [24] reported the results of an investigation of the ignition and combustion of n-heptane/oxygen mixtures behind incident and reflected shock waves in inert argon. The experiments were performed in a shock tube for equivalence ratios 0.5 to 4.0, and in the temperature range 1300 K to 2000 K. Chemiluminescence emission from OH, CH,C_2 was monitored, together with infra-red emission from CO, CO_2, species containing C-H bonds, and soot emission. They presented information on ignition delay times, and developed a simple kinetic model of n-heptane oxidation. They reported reasonably good agreement between the model results and the experimental data for stoichiometric and lean mixtures, and significant discrepancies for the rich mixtures.

Their kinetic model predicted the following process: the system was initiated

by the reaction

$$n - C_7H_{16} \rightarrow n - C_5H_{11} + C_2H_5.$$

The radical attack on the fuel was specified by the reactions

$$n - C_7H_{16} + X \rightarrow n - C_7H_{15} + XH.$$

The chain branching reaction under all conditions was found to be

$$H + O_2 \rightarrow OH + O.$$

It must be noted that the mechanism presented in this paper represents a preliminary attempt to account for n-heptane oxidation. It does not include alkyl-peroxy isomerisation in any detail and omits hydrogen peroxide thermal decomposition.

During the 1970's there was an attempt to simplify the experimental arrangement associated with knock studies. Previously, fundamental knock studies were performed in research engines or adapted production engines. Flow and ignition processes in such engines were difficult, if not impossible, to model at the time, and detailed flame models had not yet been developed. Therefore, engine knock researchers developed a device that became known as the Rapid Compression Machine (RCM). This device was a combustion chamber with a movable piston, in which fuel and air were premixed at ambient pressure, and then rapidly compressed to a predetermined compression. The fuel/air mixture underwent rapid, near isentropic compression to an intermediate temperature and pressure that could be measured and calculated. Following a

short time delay, depending on the intermediate temperature and pressure, the fuel/air mixture autoignited. Now, depending on the fuel used, the observed ignition was either single stage high temperature ignition, or two stage ignition, where a cool flame was observed to develop in the mixture, followed by a hot flame ignition after another time delay. Much productive autoignition research work was performed using Rapid Compression Machines, and they are still widely used.

During the 1970's and 1980's two strands of theoretical models of end-gas autoignition developed. The first strand is associated with a group of researchers at Shell Research Ltd., Thornton Research Centre, and is widely known as the Shell Knock Model. Halstead et al [61] developed a simple chemical model of autoignition in an RCM that could be computed numerically. The model was based on a Semenov degenerate branched chain mechanism. Their chemical model generalised a class of similar reactions that occur in a complex fuel into a single reaction. In any complex reaction system such as a hydrocarbon/air system there are normally a number of classes of similar reactions. By generalising these reaction classes into single reactions, they were able to simplify the RCM chemical system from one involving hundreds of elementary reactions, to a system only containing ten or so generalised reactions. This simple autoignition model was able to simulate successfully the essential phenomena of two-stage ignition of alkanes in a RCM. It was also able to correctly predict the transition to single stage autoignition, and the variation of the characteristic induction periods as a function of temperature.

The Shell Knock Model has been used widely to study autoignition chemistry in engine knock, the action of anti-knock additives in gasoline engines, the ignition of fuel sprays, and the action of ignition promoters in diesel engines [70]. The following discussions focus solely on the application of the Shell Knock Model to modelling autoignition in rapid compression machines and

gasoline engines.

In 1977, Halstead, Kirsch and Quinn [62] reported results of an experimental study into the autoignition of hydrocarbon fuels at high temperatures and pressures. They carried out systematic studies with a variety of hydrocarbon fuels, emulating engine conditions with a rapid compression machine. They found confirmation of the correlation between performance of the fuels in engines, and their autoignition properties measured in a rapid compression machine. They fitted the Shell Knock Model autoignition mechanism to the experimental results for all the fuels studied, and found that the experimentally observed trends were successfully simulated.

In 1980, Hirst and Kirsch [64] wrote a chapter on the application of a hydrocarbon autoignition model in simulating knock and other engine combustion phenomena, in the book Combustion Modelling in Reciprocating Engines. In this chapter they reviewed the development of the chemical model and its optimisation to give a quantitative prediction of the behaviour of selected fuels, using data obtained from a rapid compression machine. They reported results of an experimental program to characterise engine knock in terms of in-cylinder pressure diagrams under octane rating conditions in a CFR engine. The results were compared with predictions from an optimised form of the knock model, and good agreement was found. The model correctly ranked the various fuels in the study. They found that the computer predictions were sensitive to the accuracy of the basic engine cycle simulation.

In 1985 Kirsch and Quinn [70] published a review of progress towards a comprehensive model of hydrocarbon autoignition. Their discussion of the chemistry of autoignition was based on the findings of several earlier papers using the Shell Knock Model of autoignition. They developed a more complex autoignition model than the original, based on successive trials of different reaction

mechanisms. The model reflected the assumptions and postulates that hydrocarbon oxidation is a radical chain reaction in which self-acceleration occurs through a degenerate branched chain mechanism, that cool flame behaviour reflects self-inhibition which is thermo-kinetic in origin, and that heat release is dominated by fast propagation reactions.

Once the basic model had been developed, they applied the model to the simulation of knock in the gasoline engine, anti-knock activity, modelling of diesel spray ignition, and modelling of autoignition hazards. They concluded further that complex radical termination kinetics were necessary in which participating radicals are removed by processes both first and second order in radical concentration, and that a second route involving reactions of intermediate oxidation products is necessary for the formation of branching agent in the post cool flame reactions. They then discussed the limitations and shortcomings of the chemical model. These were considered to be based on the fact that the model was 'global' in approach.

This was followed by a paper by Cox and Cole [25] which reported the results of a study into the chemical aspects of autoignition of hydrocarbon-air mixtures. The study was performed using data obtained from a RCM, and used a more detailed generalised reaction mechanism of chain propagating steps involving alkylperoxy radical isomerization and oxidation than had been previously used in the Shell Knock Model. They reported that experimental ignition delay times could be satisfactorily described by the model without the need for parameterisation, and that hydrogen peroxide promoted second stage ignition.

In 1987 Hu and Keck [66] reported the results of an experimental and modelling study of autoignition of adiabatically compressed combustible gas mixtures. They used a spherical constant volume combustion bomb to measure the exlosion limits of the various fuels tested. The explosion temperature was

calculated from an experimentally measured pressure trace, assuming isentropic compression of the fuel/air mixture at the centre of the constant volume bomb. The modelling study was performed using Benson's mechanism [14], and is similar in spirit to that of Cox and Cole [25]. This mechanism is a development of the Shell Knock Model idea of generalising classes of reactions into a small set of manageable reactions. They reported good agreement between the experimental data and the results of the modelling study, and concluded that a simple branched chain kinetic model could be used successfully to describe the two-stage ignition process in constant volume bombs. Hydroperoxides are the important branching agents in first stage ignition, and hydrogen peroxide is the important branching agent in the second stage. The adiabatic core temperature controls the autoignition process, and comparison of constant volume bomb data with RCM data shows no observable differences between compression due to a hot flame front as opposed to a cold piston.

The other strand that developed in engine knock modelling through the 1980's was the attempt to construct comprehensive reaction mechanisms, and perform autoignition modelling studies with these large sets of reactions. Difficulties with this approach originate from assembling reliable rate coefficients for all the reactions in the mechanism. There has usually been some uncertainty in the accuracy of the mechanism's rate coefficients, and so researchers adapted the field of sensitivity analysis for such reaction systems. The sensitivity analysis indicates the sensitivity of the reaction system to specific rate coefficients, and therefore indicates which reaction rate coefficients need to be accurately known.

In 1981, Benson [14] began to bridge the gap between generalised reaction modelling and comprehensive mechanism modelling with a paper on the kinetics and thermochemistry of chemical oxidation with application to combustion and flames. He emphasized the chemistry of the cool flame regime (470

K - 670 K), over which the initial chemistry changes from organic peroxide production to hydrogen peroxide production. He shows that the development of cool flames is characterised by a short period of slow radical production yielding RO_2H as product which then autocatalytically accelerates its own production by the reaction

$$RO_2(HO_2) + RH \rightarrow RO_2H(H_2O_2) + R.$$

Chain propagation is eventually taken over by OH, and RO_2H reaches a stationary concentration. In the final approach to stationary state, intermediate aldehydes act as important hydrogen atom donors in competition with fuel molecules, and produce peroxy acids which are faster branching agents than RO_2H. The negative temperature coefficient arises from a turnover in mechanism producing hydrogen peroxide instead of organic peroxide.

In 1984 Westbrook published a review article [121] on chemical kinetic modelling of hydrocarbon combustion. In this paper he reviews the hierarchical approach to modelling hydrocarbon chemistry, beginning with the much studied hydrogen/oxygen system. He emphasizes the importance of systematic validation of successive levels of mechanisms. His discussion of the hierarchical mechanisms moves through H_2/O_2, CO,CH_2O, CH_4,C_2H_6, C_2H_4, C_2H_2, CH_3OH etc. He reviews the current status of modelling studies of detonations, plug flow reactors, stirred reactors, laminar flames, and the application of sensitivity analysis to combustion modelling.

In the same year, Pitz et al [97] published a comprehensive mechanism of hydrocarbon fuel oxidation up to butane. The mechanism consisted of 238 elementary reactions involving 47 species. The mechanism was validated by comparison between computed and experimental results from shock tubes, a turbulent flow reactor, and premixed laminar flames. The model successfully

reproduced n-butane combustion kinetics for wide ranges of pressure, temperature and fuel-air equivalence ratio. The authors described the turbulent flow reactor experiment in some detail, involving temperatures in the range of 990K to 1200K, and equivalence ratios ranging from 0.08 to 1.7, and briefly described the shock tube experiment and the premixed laminar flame experiment.

The authors reported that the modelling results were in good agreement with the measured data from all of the experiments, describing all of the major features of n-butane oxidation. They performed a sensitivity analysis, and found that, despite the large number of species and reactions in the system, the computed results were most sensitive to reactions involving the $H_2 - O_2 - CO$ submechanism. This result is in agreement with other modelling studies of hydrocarbon oxidation.

Also in 1984, Smith et al [105] reported for the first time the results of an experimental and comprehensive modelling study of engine knock using realistic engine fuels, n-butane, isobutane and propane. They used Raman and emission spectroscopy, laser induced fluorescence, Schlieren photography, and gas chromatographic sampling of chemical species from a s.i. single cylinder engine to study preflame conditions and reactions that lead to autoignition. The kinetic model used for the modelling study was taken from a comprehensive mechanism for hydrocarbon oxidation up to butane published by Pitz et al [97]. They found that the detailed kinetic modelling correctly predicted the trends in the autoignition delay times, and that there was little sensitivity of the knock point to low temperature reactions.

Independently that year, Dimpelfeld and Foster [30] published results of a modelling study of autoignition in a spark ignition internal combustion engine, using fuels methane, ethane, propane, ethylene, methanol and n-butane. A short discussion of this paper is presented in the previous section on methanol

combustion.

In 1985, Leppard [76] published results of a detailed chemical kinetics simulation of engine knock, using ethane as the engine fuel. His autoignition model used a comprehensive 84 reaction mechanism obtained from Westbrook, and was based on Westbrook and co-workers mechanism development over the period 1977 to 1982. The autoignition model was tested against the data derived from engine experiments performed by Trumpy et al [108]. He assumed that the end gas formed a closed system that could be modelled as a continuously stirred reactor, and imposed the ideal gas equation of state derived from Trumpy's measurements on the end-gas. He found a two crankshaft angle degree discrepancy between his modelled autoignition point and the experimentally measured autoignition point, was able to identify the elementary reactions leading to knock, and concluded that a current, well validated chemical mechanism was capable of simulating engine knock chemistry.

Also in 1985, Westbrook presented a paper to the International Symposium on Shock Waves and Shock Tubes [123] on chemical kinetic modelling of the influence of molecular structure on shock tube ignition delay. He investigated the influence of molecular size and structure on ignition delay times, focussing on n-paraffin fuels from methane to n-pentane under shock tube conditions. He used the experimental data of Burcat et al [20], for comparison with the results of his modelling study. He found good agreement between the modelled ignition delay times and the experimentally measured ignition delay times for all the fuels studied. He was able to show that the rate of chain branching had a sensitive dependence on the relative rates of hydrogen atom abstraction from the parent fuel molecule at each hydrogen atom site. This paper was published in a separate journal the following year [123].

Esser et al [40] reported results of a modelling study on the chemistry of au-

toignition in hydrocarbon-air mixtures up to octane and its relation to engine knock. This was the first time that a comprehensive chemical kinetic mechanism had been used to model octane autoignition. They used experimental data of ignition delay times of n-heptane oxidation from Coats et al [24] for comparison with the results of their modelling study. They reported agreement between the modelling results and the experimental data within the error limits of the measurements. They found that the reaction sequence

$$RH + HO_2 \rightarrow R + H_2O_2$$

$$H_2O_2 + M' \rightarrow OH + OH + M'$$

and the reaction

$$CH_3 + O_2 \rightarrow CH_2O + O + H$$

to be the chain branching processes responsible for autoignition.

In 1986 Dryer and Brezinsky [36] reported the results of a flow reactor study of the oxidation of n-octane and iso-octane at 1080 K, atmospheric pressure, and equivalence ratio 1.0. It was found that oxidation of iso-octane occurred much slower than the oxidation of n-octane. Iso-octane produced predominantly iso-butylene and propylene as reaction intermediates, while n-octane produced predominantly ethylene as reaction intermediate. They were able to show that the relative rates of oxidation of the two fuels were related to the number of primary, secondary and tertiary hydrogen atoms present in the initial fuel.

Also in 1986 Pitz and Westbrook [96] reported the results of a chemical kinetic modelling study of the high pressure oxidation of n-butane and its relation to engine knock. They combined a validated high temperature mechanism for

n-butane oxidation [97] with a low temperature submechanism added. The low temperature submechanism contained chemical kinetic steps which related primarily to the formation and consumption of alkyl peroxides. The modelling was performed in three different ways: firstly, a sample of fuel/air mixture was constrained to follow temperature-pressure histories as measured by Green et al [105]. This meant that the temperature-pressure history was constrained to begin at 23° BTDC. Secondly, only the pressure history was followed. This meant that a larger portion of the engine cycle was covered. Thirdly, and most simply, constant volume adiabatic combustion was modelled. The adiabatic combustion calculations were performed over a range of initial temperatures (600K - 1000K) at an initial pressure of 30 bar.

They found from the first approach that predicted autoignition occurred 0.4 ms after the experimentally measured knock point, and the predicted end-gas autoignition temperature was about 60K to 100K higher than that measured at knock point. They performed a sensitivity analysis, and identified the following key reactions:

$$C_4H_{10} + HO_2 \rightleftharpoons C_4H_9 + H_2O_2$$

$$H_2O_2 + M' \rightleftharpoons OH + OH + M'$$

$$HO_2 + HO_2 \rightleftharpoons H_2O_2 + M' \text{etc.}$$

The second method of analysis produced a predicted autoignition time 1.18 ms later than the experimentally measured knock point. They concluded that the first method was probably more accurate than the second, because the temperature measurements included the effects of heat transfer to and from the end-gas.

The third method of analysis was considered to be useful for defining characteristic autoignition temperatures and pressures.

The paper concluded with a short discussion of the effects of fuel additives on autoignition. The authors introduced a simple model of the action of tetraethyl lead on the n-butane/air system. They assumed that the lead was oxidised to PbO_2, and then HO_2 and H_2O_2 reacted on the PbO_2 surface to form unreactive products. They found that the predicted autoignition times were significantly affected by this simple model, and suggested that tetraethyl lead inhibits autoignition by removing HO_2 and/or H_2O_2 from the end-gas.

Later in the same year, Cernansky et al [22] reported on the chemistry of fuel oxidation preceding end-gas autoignition. This experiment was similar to the one published earlier in the year, except for a comparison of measured stable species evolution and modelled stable species evolution. They used a high swirl, multi-point s.i. research engine for their autoignition experiments. The design of the engine isolated the end-gas in the centre of the combustion chamber. n-Butane and iso-butane were used as the engine fuels for these experiments. Concentrations of stable species were measured through gas chromatography. The temperature history of the end-gas was measured using spontaneous Raman spectroscopy, while the pressure history was measured using a pressure transducer. The chemical model used in their calculations was the same as that used in their previous paper [96]. They reported good agreement between the modelled results and the experimental data.

Part of this study was intended to clarify why branched chain hydrocarbons are more resistant to autoignition than straight chain hydrocarbons. This is why they studied n-butane and iso-butane in this system. They found that chemical kinetic differences in the oxidation of these two isomers was the consequence of the distribution of radical species resulting from the consumption of the various types of butyl radicals.

In 1987, Morley [86] reported a fundamentally based correlation between

alkane structure and octane number. He argued that the differences in ease of autoignition between alkanes was due to the different rates at which branching agent is formed, and that this process involved two successive internal hydrogen abstractions in peroxy radicals. The rates of these reactions are structure dependent, and he found that they correlate with the RON for most alkanes, with a linear correlation coefficient r=0.94. He concluded that the low temperature oxidation mechanism involving peroxy radical isomerisations provide a possible explanation for autoignition behaviour occurring in the engine during the octane rating test.

In the same year, Ferguson et al [78] [43] published two papers on the evolution of temperature in an engine. The first paper reported the results of CARS temperature measurements of the end-gas in a firing engine. This paper is discussed briefly in the Introduction. The second paper reports the comparison of the CARS temperature measurements of the end-gas with a heat release model of end-gas evolution developed by the authors. The engine used for this study was that described above [22]. Their heat release model is essentially a two zone model, which computes the mass fraction burned and bulk gas temperatures from a measured pressure history. It includes such effects as heat loss, blowby, crevice quenching, short circuiting, and thermal boundary layers. The model defines the thermal boundary layer in terms of the difference between mean gas temperature squared, and the mean squared gas temperature.

They found that the model predicted the bulk gas temperature evolution with great accuracy during the compression stroke, and that the predicted temperatures are systematically slightly lower than the experimentally measured temperatures during combustion, but are within the error bounds. They concluded that due to the success of the heat release model, the role of pressure in autoignition chemistry can now be investigated.

Also in 1987 Green et al [52] reported the results of an autoignition study of iso-butane in a knocking spark ignition engine. The engine used for this study was the same as that mentioned above [22], and the heat release model was that developed by the research group at SANDIA [43], and is briefly discussed above. They measured autoignition times in the end-gas as a function of manifold temperature and engine speed. They carried out end-gas sampling and gas chromatography analysis of major species concentrations. This was compared with the results of a detailed chemical kinetic modelling study of iso-butane oxidation, using the above mentioned heat release model coupled to the chemical heat release calculated from the mechanism.

They found good agreement between the calculated autoignition times compared with those measured experimentally. For only one of six conditions tested (at 300 rpm) was there a significant discrepancy between the calculated and measured autoignition times. They concluded that the preponderance of n-butane to knock in comparison with iso-butane is partially explained by the relative rates of butylperoxy isomerisation, and emphasized the importance of HO_2 as a crucial branching intermediate at temperatures and pressures associated with engine knock, in contrast to the Shell Knock Model, which considered the formation of HO_2 to be a main termination step.

Brezinsky and Dryer [18] published a paper on molecular structure and component blending effects on knock related chemistry. They performed atmospheric pressure flow reactor experiments on the oxidation of n-octane and iso-octane, and the oxidation of n-octane iso-octane blends. They found that even though the rates of fuel decay were about the same, the CO and CO_2 evolution was very different. n-Octane produced CO much more rapidly than iso-octane. Furthermore, n-octane yielded large amounts of ethylene as an intermediate, compared with an order of magnitude lower ethylene levels for iso-octane oxidation.

As a consequence of the different ethylene levels, they added iso-butylene to n-octane and repeated the oxidation experiment. They found that the oxidation time for the mixture was dramatically shortened. They concluded from this study that the difference in knocking tendency of fuels result primarily from the oxidation rates of intermediates, rather than the rate of attack on the initial fuel molecule, and that certain small unsaturated hydrocarbons (like iso-butylene) interfere with the oxidation of intermediates, and may serve as models for octane number enhancements. Furthermore, they argued that flow reactor experiments permit the generation of a correlation between chemical phenomena (such as CO, CO_2 generation) and a macroscopic measurement made in a test engine (such as octane number).

In 1988, Westbrook et al [124] presented a detailed kinetic reaction mechanism for the oxidation of iso-octane and n-heptane over an extended temperature range, and its application to the analysis of engine knock. They combined a high temperature submechanism with reaction paths for the low temperature regime in which the rate and intermediate products of oxidation were controlled by addition of O_2 to alkyl and isomerised alkylperoxy radicals, internal hydrogen atom abstractions, and reactions involving O-heterocyclic species. They validated the mechanism through comparisons of computed results and experimental data from shock tubes, turbulent flow reactor, and low temperature static and stirred reactors. They imposed an empirically determined equation of state on a homogeneous fuel/air mixture, and then computed the chemical, temperature evolution, and ignition delay time of the system.

They were able to reproduce the variations of autoignition delay time with octane number, and interpreted them in terms of detailed differences in the structure of the two primary reference fuels. Most notably, the production of OH radicals decreased with increasing octane number. Structurally, for branched chain hydrocarbons like iso-octane, the isomerisation pathways pro-

ducing OH are inhibited because the steps require the abstraction of primary H atoms with large activation energies, while for straight chain hydrocarbons, the isomerisation pathways involve many secondary H atoms with significantly lower activation energies.

They found that at low temperatures initiation occurred through the reaction

$$RH + O_2 \rightarrow R + HO_2,$$

while the system showed greatest sensitivity to the reactions

$$HO_2 + HO_2 \rightarrow H_2O_2 + O_2$$

$$H_2O_2 + M' \rightarrow OH + OH + M'.$$

High temperature chain branching was found to occur through the usual route,

$$H + O_2 \rightarrow OH + O.$$

In 1990, Maly et al [81] reported the results of a theoretical and experimental investigation of knock induced surface destruction. They measured the propagation speeds of detonation waves in the duct region of the cylinder using very high speed Schlieren diagnostics, and used this data to estimate the wall loading due to instantaneous pressure peaks, and sudden large temperature increases. The surface damage generated in their simulator agreed well with knock induced surface erosion in real engines. They argued that erosion could be caused by excessive surface stresses due to large local heat fluxes and/or high peak pressures in positively interfering shocks.

They performed two-dimensional numerical simulations of shock induced combustion in an L-shaped duct, and found that the sharp convex edge of the duct triggered the formation of Machstem structures in the shock-reaction front, patterns known to be essential for self-sustaining detonation waves.

The above paper was followed by another by König et al [72] reporting the results of a theoretical study on the role of exothermic centres on knock initiation and knock damage. This paper to some extent synthesises the two competing models of 'engine knock', arguing that a detonation wave can be set up in the end-gas as a consequence of an end-gas hot spot ignition. They used microscopic aluminium particles to stimulate exothermic centres in the end-gas, and filmed the knock process using high speed direct light photography, and laser Schlieren filming. They found that chemico-hydrodynamic coupling was especially strong near cylinder walls, as compression heating by reflected pressure waves was most effective. They distinguished three modes of reaction propagation: (1) deflagration (associated with steep temperature gradients), (2) thermal explosion (associated with small temperature gradients), and (3) developing detonation (associated with intermediate temperature gradients). The detonation wave in the end-gas propagates into crevices, where knock damage to the piston is observed to occur.

Recently, Vermeersch et al [114] reported the results of experimental and modelling autoignition chemistry studies of n-butane in a variable pressure flow reactor. They performed their experiments over a pressure range of 3 bar to 8 bar, and a temperature range of 700 K to 1300 K. They used a widely validated comprehensive chemical mechanism of n-butane oxidation for comparison with the experimental data. The model predicted autoignition timescales that were too short at lower temperatures/higher pressures, and too long at higher temperatures/lower pressures. The model seemed to over-emphasize the importance of lower temperature kinetic processes. Worse still, the mechanism failed

to reproduce some of the high temperature atmospheric pressure flow reactor data originally utilised in the initial model development. They suggested a comprehensive hierarchical redevelopment of a mechanism for n-butane oxidation, validated over an appropriate range of pressures and temperatures.

Chapter 6

Chemical Kinetic Modelling of Methanol Autoignition

6.1 Revision of Chemical Kinetic Modelling

Explosive combustion is described in two ways: namely chemical explosion and thermal explosion. A chemical explosion occurs as a result of branching within the chemical system. The net branching factor of a chemically explosive system is defined as the difference in the rate of linear branching and linear termination for a specific radical in the system [25]. Chemical branching causes a rapid increase in the rate of formation of unstable radicals, which in turn react rapidly with major species. A thermal explosion occurs when a chain reaction develops between a fuel and an oxidiser, and the fuel/oxidiser reactions are exothermic.

End-gas autoignition or 'engine knock' is the result of a complex chain branching chemical reaction leading to explosive combustion within the core gas re-

gion of the cylinder. The explosive nature of end-gas autoignition involves heterogeneous chemistry, turbulent fluid motion and non-equilibrium processes. This study attempts to establish the basic chemistry involved in the autoignition of methanol.

A short revision of chemical kinetic modelling, chain branching reactions and the criteria for chemical explosion is appropriate before discussing the details of the methanol autoignition study.

6.1.1 Definitions in Chemical Kinetics

Most of the elementary reactions of importance in combustion are bimolecular reactions of the form

$$A + B \underset{k_{r1}}{\overset{k_{f1}}{\rightleftharpoons}} C + D,$$

where the formation of chemical species C and D via reactive collision of species A and B is the forward reaction, and the formation of species A and B through the reactive collision of species C and D the reverse reaction.

The net rate r of the reaction is then the difference between the forward reaction rate and the reverse reaction rate,

$$\text{r} = \text{forward rate - reverse rate.}$$

The respective reaction rates are given by

$$\text{forward rate} = k_{f1}[A][B],$$

and

$$\text{reverse rate} = k_{r1}[C][D],$$

where k_{f1} and k_{r1} are the forward and reverse reaction rate coefficients respectively, and the notation $[N]$ refers to the concentration of the chemical species inside the brackets, usually in units of mole.m^{-3}. The mass action rate law results in an elementary reaction rate of the form

$$r = k_{f1}[A][B] - k_{r1}[C][D].$$

Hence we may write

$$\frac{d[C]}{dt} = k_{f1}[A][B] - k_{r1}[C][D].$$

Note that there may also occur the unimolecular reaction

$$A \underset{k_{r2}}{\overset{k_{f2}}{\rightleftharpoons}} D + E$$

and the termolecular reaction

$$A + B + C \underset{k_{r3}}{\overset{k_{f3}}{\rightleftharpoons}} E + F$$

yielding reaction rates of the form

$$\frac{d[E]}{dt} = k_{f2}[A] + k_{f3}[A][B][C] - k_{r2}[D][E] - k_{r3}[E][F]$$

and

$$\frac{d[F]}{dt} = k_{f3}[A][B][C] - k_{r3}[E][F].$$

For elementary reactions, the rate coefficients have the Arrhenius form

$$k_i(E_{ai}, T) = C_i e^{\frac{-E_{ai}}{RT}}, \tag{6.1}$$

or the modified Arrhenius form

$$k_i(E_{ai}, T) = C_i T^{b_i} e^{\frac{-E_{ai}}{RT}}, \tag{6.2}$$

where k_i refers to forward or reverse rate coefficients for reaction (i), E_{ai} is the activation energy for the reaction concerned, and T is the temperature of the reaction system. The form of equation 6.1 is theoretically justified from collision theory and kinetic theory. This can be seen from any standard text-book in chemical kinetics or combustion [13] [75] [45]. Usually k_i is specified only for the forward reaction, and k_r has to be calculated from consideration of thermochemical equilibrium. The details of the calculation of the reverse reaction rate coefficient will be discussed later in the chapter.

6.1.2 Modelling of Explosive Systems

A chemical or thermal explosion occurs when the fuel/oxidant temperature rises above a critical value, called the explosion limit. The explosion limit defines the point in pressure and temperature where the chemical system undergoes chain branching, leading to a net increase in the radicals present. As the system branches, it becomes explosively reactive. This is described quantitatively by the following simple example [13] [70] [48].

A general branched chain reaction system can be described by the following set of generalised reactions.

$$M \xrightarrow{k_1} R \text{ initiation}$$

$$R + M \xrightarrow{k_2} \alpha R + M' \text{ chain branching step}$$

$$R + M \xrightarrow{k_3} R + P \text{ propagating step, product formation}$$

$$R + M \underset{gas}{\xrightarrow{k_4}} P' \text{ gas phase termination}$$

$$R \underset{wall}{\xrightarrow{k_5}} P'' \text{ destruction}$$

M and M' are reactant molecules in the system, R represents all the chain carriers, and P, P', P'' are stable products. The system becomes explosive for some value of α. The explosion condition is determined by the rate of formation of the major product P,

$$\frac{d[P]}{dt} = k_3[R][M]. \tag{6.3}$$

Using the steady state condition for the chain carriers,

$$\frac{d[R]}{dt} = k_1[M] + k_2(\alpha - 1)[R][M] - -k_4[M][R] - k_5[R] = 0. \tag{6.4}$$

Therefore,

$$[R] = \frac{k_1[M]}{k_4[M] + k_5 - k_2(\alpha - 1)[M]}. \tag{6.5}$$

Substituting equation 6.5 for [R] into equation 6.4 yields

$$\frac{d[P]}{dt} = \frac{k_1 k_3[M]^2}{k_4[M] + k_5 - k_2(\alpha - 1)[M]}. \tag{6.6}$$

The rate of formation of the product P becomes infinite when the denominator of equation 6.6 equals zero. This defines the point at which the system explodes. Solving for α when the denominator is zero gives the critical branching value for explosion; namely

$$\alpha_{crit} = 1 + \frac{k_4[M] + k_5}{k_2[M]}. \tag{6.7}$$

For a reaction system where $\alpha > \alpha_{crit}$, the system will explode, and for $\alpha < \alpha_{crit}$ the system will react slowly.

6.1.3 Thermochemical Equilibrium and the Reverse Reaction Rate Coefficients

The calculation of the reverse reaction rate coefficient is done through consideration of thermochemical equilibrium. The parameters C_i, b_i and E_{ai} are usually determined empirically for the forward reaction. Now, for a general reaction of the form

$$aA + bB + cC + dD + \ldots \rightleftharpoons eE + fF + gG + \ldots, \tag{6.8}$$

the equilibrium constant K_{eq} is defined for the above reaction as

$$K_{eq} = \left(\frac{[A^a][B^b][C^c][D^d]\ldots}{[E^e][F^f][G^g]\ldots}\right)_{eq}. \tag{6.9}$$

If reaction 6.8 is an elementary reaction with forward and reverse rate coefficients k_f and k_r respectively, then equilibrium demands

$$K_{eq} = \frac{k_f}{k_r}. \tag{6.10}$$

This relation is an example of the principle of detailed balance, and it allows the calculation of k_r from k_f and K_{eq}. If chemical equilibrium is expressed in the form of partial pressures of reactants and products, then we can define a new equilibrium constant, the pressure equilibrium constant K_P by

$$K_P = (\frac{P_A^a P_B^b P_C^c \cdots}{P_E^e P_F^f P_G^g \cdots})_{eq}. \tag{6.11}$$

Substituting expressions from the ideal gas law for the partial pressures in equation 6.11 leads to

$$K_P = [\frac{[A^a][B^b][C^c][D^d]\cdots}{[E^e][F^f][G^g]\cdots}]_{eq}(RT)^{e+f+g+\cdots-a-b-c-\cdots}. \tag{6.12}$$

This is more simply written

$$K_P = (\frac{[A^a][B^b][C^c][D^d]\cdots}{[E^e][F^f][G^g]\cdots})_{eq}(RT)^{\sum \nu_i}, \tag{6.13}$$

where $\sum \nu_i$ is the sum of the stoichiometric coefficients of reaction equation 6.8. Therefore

$$K_P = K_{eq}(RT)^{\sum \nu_i}. \tag{6.14}$$

In order to find k_r in terms of K_{eq} and k_f, we use the van't Hoff isochore

$$\frac{d \log K_P}{d(1/T)} = -\Delta H/R, \tag{6.15}$$

where ΔH is the change in enthalpy for the elementary reaction. The integrated form of this equation is

$$\log K_P = -\Delta G/RT = \Delta S/R - \Delta H/RT, \tag{6.16}$$

where ΔG and ΔS are the changes in the Gibbs free energy and the entropy, respectively, for the elementary reaction. Therefore

$$\log K_{eq} = \log k_f - \log k_r = \log K_P - \sum \nu_i \log RT$$

$$= \Delta S/R - \Delta H/RT - \sum \nu_i \log RT. \tag{6.17}$$

The right-hand side of the above expression can be calculated at any temperature from spectroscopic information and measured heats of formation. Therefore the value of k_r can be calculated. From the above equation we can also identify the relation $\Delta H = E_{af} - E_{ar}$. As ΔH and E_{af} are known, E_{ar} can be calculated. The pre-exponential factor A_r can then be deduced from the relation

$$A_r = k_r e^{E_{ar}/RT}. \tag{6.18}$$

6.1.4 The Chemical Kinetics Program HOMCHEM

The method in Warnatz's HOMCHEM program used in this analysis to calculate the reverse reaction rate coefficients is similar to that described above, but there is a subtle difference in the calculation of the reverse reaction activation energy.

HOMCHEM uses the NASA polynomials for constant pressure specific heats, and standard enthalpies and entropies of formation for the chemical species specified in the forward reaction mechanism. The reverse reaction activation

energy is derived from an expression which is related to the van't Hoff isochore. This is

$$\frac{d \log K_{eq}}{dT} = \frac{\Delta U}{RT^2}, \tag{6.19}$$

where ΔU is the change in internal energy of the reaction system. This expression can be integrated from temperature T_l to temperature T_h to give

$$\log \frac{K_{eq}^{(T_h)}}{K_{eq}^{(T_l)}} = -\frac{\Delta H}{R}(1/T_h - 1/T_l) - \Delta n \log T_h/T_l. \tag{6.20}$$

Gathering terms for the forward and reverse reaction rate coefficients gives

$$\log \frac{A_f^{(h)}}{A_f^{(l)}} + \log \frac{k_r^{(l)}}{k_r^{(h)}} - \frac{E_{af}}{R}(1/T_h - 1/T_l) = -\frac{\Delta H}{R}(1/T_h - 1/T_l) - \Delta n \log \frac{T_h}{T_l}. \tag{6.21}$$

Gathering the linear terms finally gives

$$E_{ar} = \frac{R \log k_r^{(l)}/k_r^{(h)}}{(1/T_h - 1/T_l)}. \tag{6.22}$$

HOMCHEM uses this above expression to calculate E_{ar} for the reverse reaction. Following this, the pre-exponential term is easily calculated from

$$A_r = k_r e^{E_{ar}/RT}. \tag{6.23}$$

The temperature term in the modified Arrhenius form of the rate coefficient

remains unchanged from the forward reaction rate coefficient to the corresponding reverse reaction rate coefficient.

The entire sequence of reactions, and the rate of consumption and formation of reactants and products can be solved numerically. The evolution of the chemical system is treated mathematically as a system of first order coupled non-linear differential equations in the species concentrations as functions of time. The problem is defined as an initial value problem, with the initial concentrations given.

Non-linear rate equations of this kind have solutions with a complicated exponential time dependence. The solutions can be approximated locally by exponential modes of the form

$$y_i = a_i e^{\gamma_i t} + b_i e^{-\gamma_i t}.$$

Often the initial value specification of the problem demands that some of the coefficients $a_i = 0$. Numerical round-off errors may produce a solution in which $a_i \neq 0$. Thus the numerical solution may have incorrect terms developing over large time scales, originating from the product $a_i e^{\gamma_i t}$.

Differential equations producing solutions with this numerical behaviour are called stiff differential equations, and special numerical techniques are necessary to solve them. Gear published the subroutine DIFSUB which was designed to solve systems of stiff differential equations [46]. Deuflhard and coworkers developed an efficient stiff integrator called LIMEX [29] which serves as the core integrator in Warnatz's HOMCHEM program.

6.2 Preliminary Discussion of the Methanol/Air Autoignition Analysis

Abnormal combustion in an Otto engine is, in general, the consequence of the interplay between three-dimensional flow processes, core gas compression, and heat transfer to and from the end-gas. The phenomenon may be complicated by inhomogeneities resulting from squish and swirl, and by the development of hot spots in the end-gas which will undergo more rapid chemical reaction than the bulk. It may be argued that the use of a zero-dimensional chemical kinetic model constitutes an excessive abstraction, which omits important features of the problem. For commercial production engines that reflect modern design practice the criticism is incontrovertible.

Rather than embark on a multidimensional chemical kinetic study of autoignition (with all its attendant uncertainties), an experimental arrangement which minimises the interaction between fluid flow and chemical kinetics has been adopted, by employing a low swirl, low turbulence research engine with a particularly simple shape of combustion chamber. The special characteristics of the Ricardo E6 engine justify the use of a zero dimensional kinetic model which focusses solely on the autoignition chemistry (see chapter 4).

This approach is similar in spirit to the so-called Shell Knock Model [61][64][25], which represents the earliest attempt to model autoignition in rapid compression machines and in Otto engines; and to the subsequent engine modelling studies with exhaustive chemical kinetic mechanisms undertaken at Lawrence Livermore Laboratory [105] [96], and at Heidelberg and Stuttgart Universities [40]. All these models treat the chemical kinetics as homogeneous. It is only very recently that chemical kinetic modelling techniques have become sufficiently refined to enable two-dimensional autoignition phenomena to be

addressed: at present this seems only to be practicable with very simple fuels [80].

The chemical kinetic modelling studies were performed using Warnatz's zero-dimensional chemical kinetics code HOMCHEM with Deuflhard's integrator LIMEX [29]. The computations were done on a VAX 6330 computer, an i-386 personal computer and an i-486 personal computer. The chemical kinetic modelling studies were performed (using the same engine pressure and temperature data) with a variety of published mechanisms and sets of rate constant data for methanol combustion. These are: Dove and Warnatz (1983) [31], Warnatz and Esser (1987) [41], Norton and Dryer (1989) [89], Grotheer and Kelm (1989) [55], and Grotheer et al (1992) [56].

The mechanisms of Norton and Dryer (1989) [89], Grotheer and Kelm (1989) [55], Grotheer et al (1992) [56] (hereafter referred to as ND89, Gr89 and Gr92 mechanisms respectively), are the most closely examined, as they are the most modern contenders for methanol combustion chemistry. In the case of the 1987 Warnatz-Esser (WE87) mechanism, the Gr89 mechanism, and the Gr92 mechanism, the rate constant data is provided in the form of forward rate coefficients, and the program HOMCHEM calculates the reverse rate coefficients from equilibrium, as discussed earlier.

The methanol autoignition calculation was performed by imposing the ideal gas equation of state on the chemistry, using the measured temperatures and pressures up to the last point for which CARS spectra could be recorded. After this point isentropic conditions were assumed, and only the measured pressure profile was used. There are several precedents for this type of approach: a number of authors have reported near isentropic conditions in the end-gas just prior to autoignition [96] [30] [52].

It is worth remarking that with the engine running at 1200 rpm the time interval between the last CARS temperature measurement ($15^o \pm 4^o$ BTDC) and autoignition (at approximately top dead centre) is about 2.5 ms, and during this period the clearance between the cylinder head and piston crown is always greater than 12 mm [127]. This is to be compared with the results of experiments measuring surface temperatures with rapid response thermocouples, where the end-gas thermal boundary layer at the time of arrival of the flame front is estimated to be less than 1 mm thick. Yates has constructed and validated an empirical heat-loss model for a low speed, low turbulence methanol-fuelled engine, and has concluded that heat-loss from the end-gas to the cylinder head and piston at engine speeds exceeding 1000 rpm has very little effect on the core gas temperature [127].

Oscillations in the pressure trace lead to an ambiguity of about one crankshaft angle degree in the measured knock point. In all cases, except one, autoignition was calculated to occur significantly in advance of the measured knock point.

Figures 6.1 and 6.2 illustrate the chemical modelling of the methanol combustion system, using the Gr92 mechanism, while figure 6.3 shows the modelled temperature evolution of the system for the first pressure trace amongst the set presented in Figure 4.5. Figures 6.4 and 6.5 illustrate the chemical modelling of the methanol combustion system, using the ND89 mechanism, with the same pressure data as before, while figure 6.6 shows the modelled temperature evolution of the system, using the ND89 mechanism.

The knock point is predicted to occur 5 degrees before the experimentally measured peak in the pressure trace (Gr92 mechanism), marking the point at which the shock wave reaches the pressure transducer. The experimental knock point occurs about 1.0 degree before the peak of the pressure trace. There is thus a discrepancy of about 4.0 crankshaft angle degrees between

the theoretically predicted knock point and the measured knock point (Gr92 mechanism). Similar results were obtained with other pressure traces, the discrepancy between the observed and calculated knock point never exceeding 7 degrees. This comparison is reasonably satisfactory, though it does suggest that there may still be problems with the published reaction rate constant data in the context of autoignition, notwithstanding the success which can now be achieved in flame speed calculations.

Of the modern mechanisms, the relatively simple 1989 scheme of Grotheer and Kelm [55] (20 species and 171 reactions) gave virtually the same predicted knock point as the greatly extended scheme (43 species, 414 reactions) used for the flame velocity calculations in section 4 above. The mechanism of Norton and Dryer [89] leads to slightly greater discrepancies: for each pressure trace autoignition was predicted to occur 0.3 crank angle degrees earlier than with either Grotheer-Kelm mechanism. However, this apparently good agreement may well be fortuitous, as is shown by the sensitivity analysis presented later in this chapter.

The 1987 scheme of Esser and Warnatz [41] designed to model the ignition of methanol under shock tube conditions (with initiation at ca. 1700 K), gave significantly worse results: autoignition in the engine was systematically predicted to occur three degrees earlier than with the Grotheer-Kelm scheme.

The 1983 reaction scheme of Dove and Warnatz [31] did not have an appropriate initiation reaction, for its original use was in studying steady state laminar flame propagation. For the purposes of this study, the DW83 mechanism was supplemented by two initiation reactions taken from the Gr92 reaction scheme. The original mechanism, supplemented in this way, which was validated by flame speed measurements and which by modern standards appears rudimentary, predicted the knock point to occur 3 degrees earlier than the

experimentally measured knock point for the indicated pressure trace.

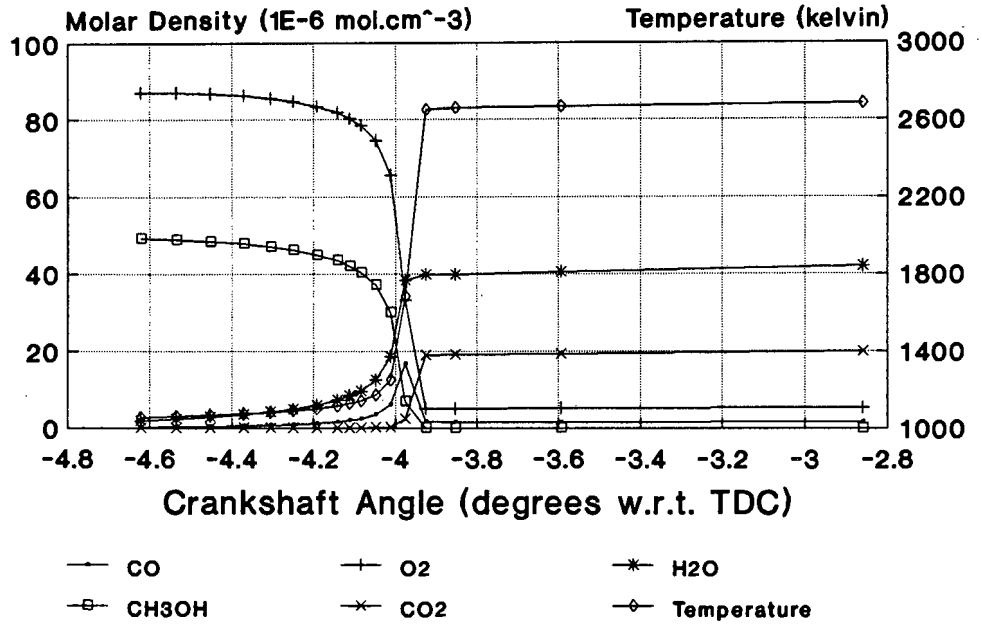

Figure 6.1: Major Species and Temperature Profile as a Function of Crankshaft Angle for the Gr92 Mechanism

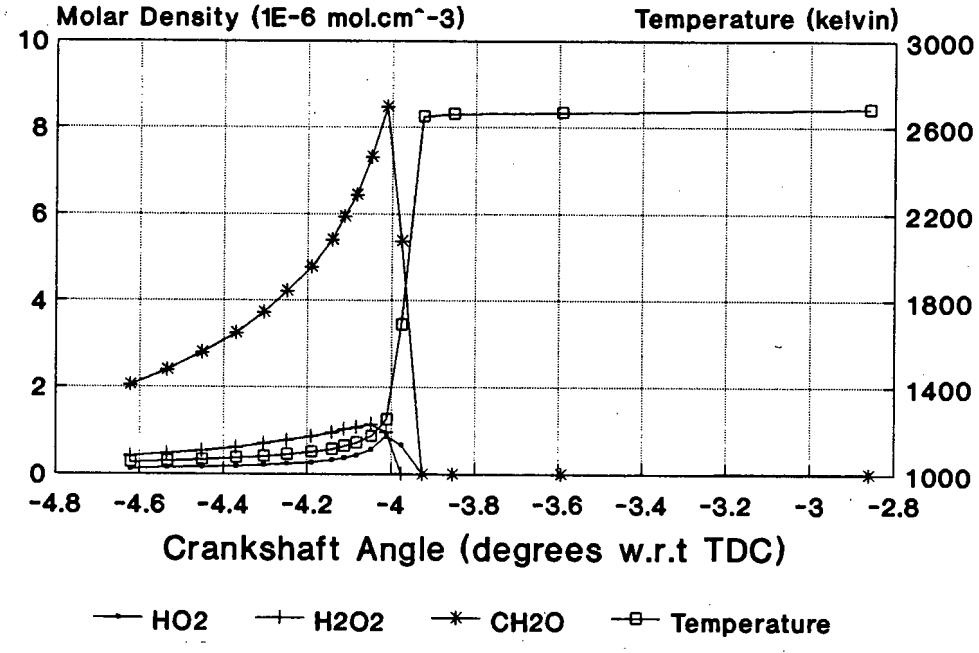

Figure 6.2: Intermediate Species and Temperature Profile as a Function of Crankshaft Angle for the Gr92 Mechanism

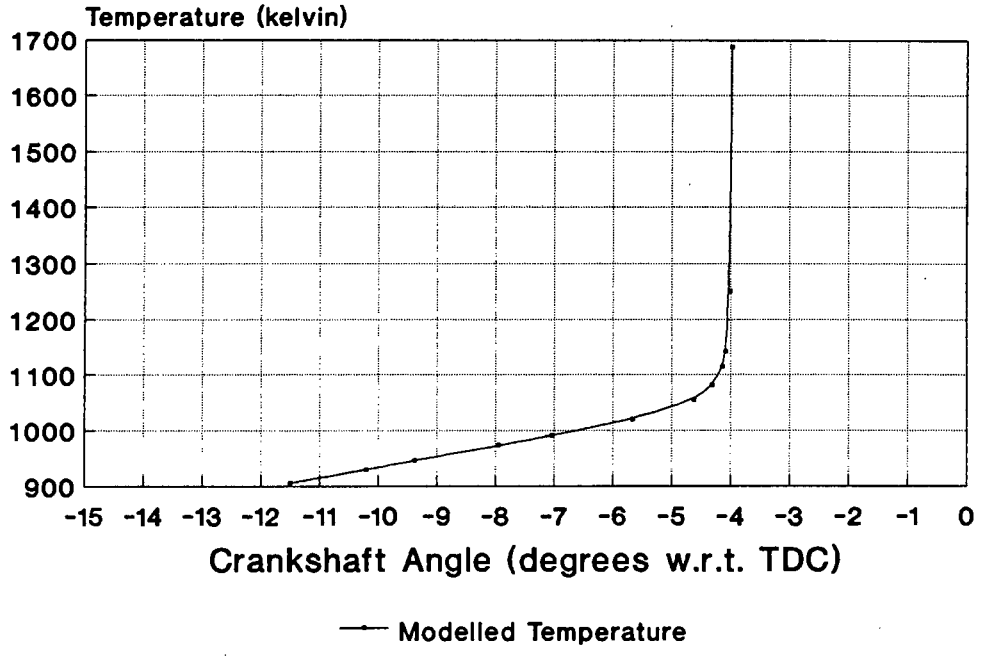

Figure 6.3: Temperature Profile as a Function of Crankshaft Angle for the Gr92 Mechanism

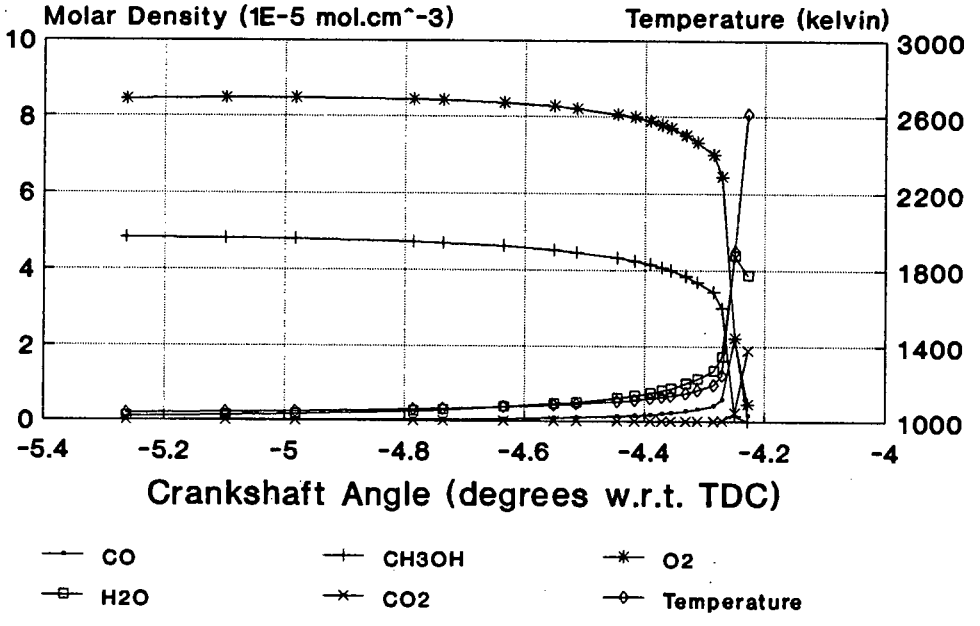

Figure 6.4: Major Species and Temperature Profile as a Function of Crankshaft Angle for the ND89 Mechanism

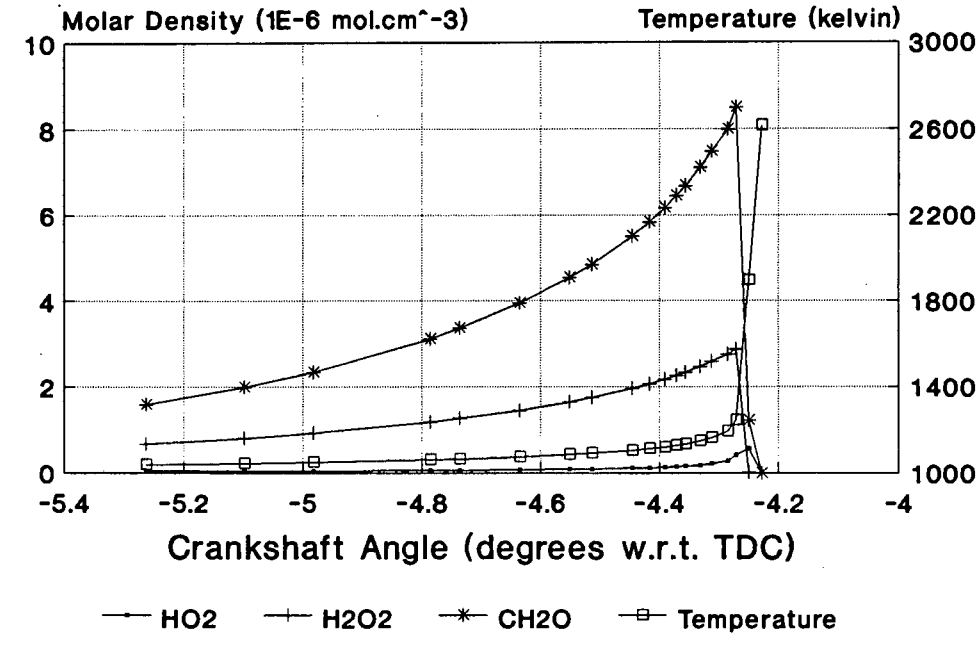

Figure 6.5: Intermediate Species and Temperature Profile as a Function of Crankshaft Angle for the ND89 Mechanism

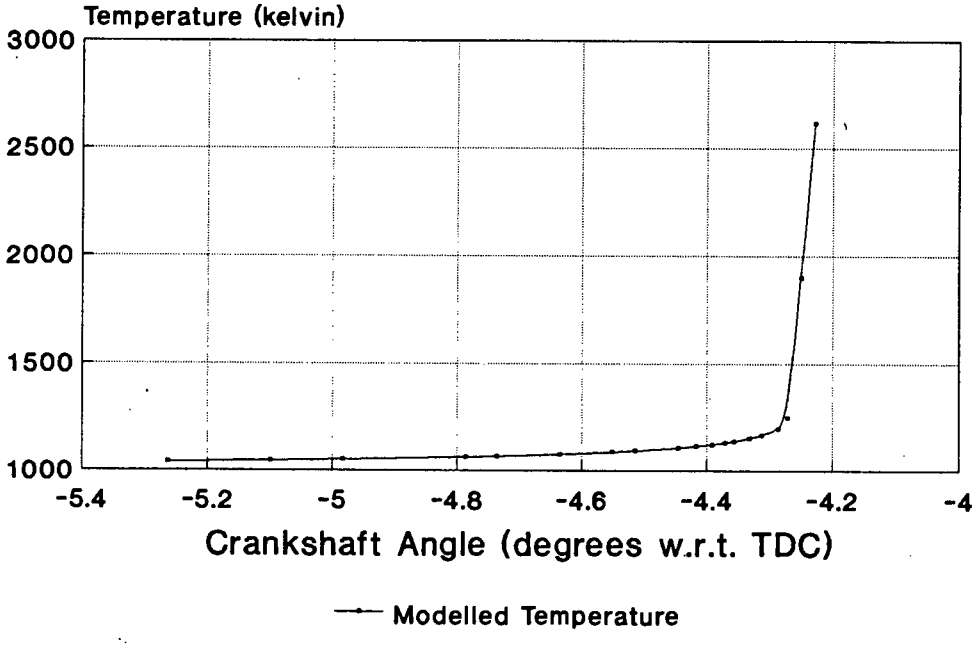

Figure 6.6: Temperature Profile as a Function of Crankshaft Angle for the ND89 Mechanism

6.3 Analysis of the Methanol Autoignition Mechanism

This section discusses the methanol autoignition mechanism in detail. The analysis is presented in four chemically separate stages. These stages of the autoignition cycle are the initiation, pre-ignition, autoignition, and high temperature combustion. The five published mechanisms describe the final three stages of the autoignition reaction in the same way at a qualitative level. The description differs quantitatively, as a consequence of the different rate coefficients specified in the mechanisms.

However, the initiation stage is described differently for the different mechanisms, and so the section on the initiation stage will consider the initiation reactions from the different mechanisms explicitly.

It should be noted that the DW83 mechanism uses the CH_2OH radical as indistinguishable from CH_3O, while the WE87 mechanism uses the CH_3O radical as indistinguishable from CH_2OH. The ND89 mechanism, the Gr89 mechanism, and the Gr92 mechanism all distinguish between CH_2OH and CH_3O.

6.3.1 Initiation: 550 K - 850 K, 3.5 bar - 14 bar

The Gr92/Gr89/ND89 Initiation Reaction Scheme

The initiation reaction at low temperatures involves a molecular oxygen attack on methanol, principally according to the reaction

$$CH_3OH + O_2 \rightarrow CH_2OH + HO_2. \tag{6.24}$$

This reaction provides an initial source of HO_2 radicals. Thermal decomposition of methanol does not appear to be significant as an initiation mechanism at engine temperatures.

The hydroperoxyl radical HO_2 is also produced in the reaction

$$CH_2OH + O_2 \rightarrow CH_2O + HO_2. \tag{6.25}$$

In the early stages of the reaction, the predominant attack on CH_3OH is by the HO_2 radical in the reaction

$$CH_3OH + HO_2 \rightarrow CH_2OH + H_2O_2, \tag{6.26}$$

and equations 6.25 and 6.26 describe a chain propagation sequence which results in the oxidation of methanol to formaldehyde and hydrogen peroxide. Hydrogen peroxide can also be formed by the disproportionation of HO_2 radical

$$HO_2 + HO_2 \rightarrow H_2O_2 + O_2, \tag{6.27}$$

but initially the HO_2 radical concentration is small, so that this reaction is not significant.

The only important reaction producing the highly reactive OH radical is the

thermal decomposition of hydrogen peroxide,

$$H_2O_2 + M' \rightarrow OH + OH + M'. \tag{6.28}$$

This reaction has a large activation energy, and only becomes significant at temperatures above 1000 K, whereupon its speed increases very rapidly with increasing temperature. (To all intents and purposes hydrogen peroxide is stable to thermal decomposition under engine conditions below 1000 K.) Reactions 6.26 and 6.28 together form a branching system, and thus play an important role in the overall combustion chemistry. However, during the initial low temperature stage, reaction 6.28 is very slow and the net branching ratio is small. Indeed, reaction 6.24 is principally responsible for branching during this phase.

At low temperatures reaction 6.27 is effectively a termination reaction, removing the HO_2 radical which is responsible for chain propagation. However, at much higher temperatures, when thermal dissociation of hydrogen peroxide into OH radicals takes place, the net effect of reactions 6.27 and 6.28 is to convert the relatively unreactive HO_2 radical produced in reaction 6.25 into the highly reactive OH radical.

The WE87 Initiation Reaction Scheme

The WE87 autoignition reaction is initiated by the thermal decomposition of methanol via the reaction

$$CH_3OH + M' \rightarrow CH_3 + OH + M'. \tag{6.29}$$

The hydroxyl radical OH subsequently reacts with methanol in the reaction

$$CH_3OH + OH \rightarrow CH_3O + H_2O. \tag{6.30}$$

Following the formation of the CH_3O radical is the fast reaction

$$CH_3O + O_2 \rightarrow CH_2O + HO_2. \tag{6.31}$$

The hydroperoxyl radical HO_2 then reacts with methanol in the important branching reaction

$$CH_3OH + HO_2 \rightarrow CH_3O + H_2O_2. \tag{6.32}$$

Equations 6.31 and 6.32 lead to the buildup of formaldehyde and hydrogen peroxide in the system, both of which are stable at temperatures below 1000 K. Both species are unstable at temperatures above 1000 K, and are known to accelerate autoignition.

The DW83 Initiation Reaction Scheme

The DW83 autoignition reaction does not have an initiation reaction explicitly, with only methanol, molecular oxygen and molecular nitrogen present. We therefore supplemented the DW83 mechanism with a molecular oxygen decomposition reaction, and the modern initiation reaction

$$O_2 + M' \rightarrow O + O + M' \tag{6.33}$$

$$CH_3OH + O_2 \rightarrow CH_2OH + HO_2. \tag{6.34}$$

These reactions initiate the methanol autoignition chemistry as laid out in the Gr89, ND89, Gr92 section.

6.3.2 Pre-autoignition: 900 K - 1200 K, 24 bar - 44 bar

This part of the reaction cycle is of great importance, for it is during this phase that a chemical explosion takes place (i.e., there is a rapid increase in the free radical pool without much heat being released), which prepares the system for the thermal explosion that occurs later.

During the early part of this phase (900 K < T < 1000 K), reaction 6.26 still serves as a propagation reaction, and the hydrogen peroxide concentration continues to increase. However, as the temperature increases beyond 1000 K, the thermal decomposition reaction 6.28 accelerates, causing the system to branch rapidly.

As the HO_2 radical concentration increases, the termination reaction

$$HO_2 + HO_2 \rightarrow H_2O_2 + O_2 \tag{6.35}$$

becomes progressively more important; however, it results in the further accumulation of hydrogen peroxide. The HO_2 concentration is sustained through

reaction 6.25, which is also responsible for the formation of formaldehyde. This is an extremely fast reaction. For temperatures below 1100 K the reaction between formaldehyde and HO_2 radical, which are both minor species, is relatively slow; and thus reaction 6.25 ensures the continued formation of large amounts of formaldehyde.

One may summarize the low temperature part of this pre-ignition phase succinctly as follows. The oxidation of methanol is principally by HO_2 radical attack and does not progress beyond formaldehyde, since the concentration of hydroxyl radicals is extremely small and the more abundant HO_2 radical is relatively unreactive. Hydrogen peroxide is stable at these temperatures. Thus, large amounts of hydrogen peroxide and formaldehyde accumulate in the end-gas during this phase. It is not until much higher temperatures are reached that the hydrogen peroxide and formaldehyde are able to react.

As the temperature rises above 1000 K, the reaction

$$CH_3OH + OH \rightarrow CH_2OH + H_2O \tag{6.36}$$

quickly dominates the attack on methanol, being responsible for 55% to 65% of the consumption of methanol at 1030 K. The HO_2 radical concentration has increased considerably, and reaction 6.27 is now the dominant source of hydrogen peroxide, being responsible for 55% to 65% of its formation. Reaction refreq:in3 still serves as a important propagation reaction (though it is no longer the dominant oxidation channel for methanol) and is responsible for about 30% of H_2O_2 formation. Reaction 6.25 remains the source of formaldehyde and HO_2.

As the end-gas temperature increases above 1075 K, a qualitative change can

be discerned. (In mathematical terms, the structure of the system of differential equations governing the chemical kinetics undergoes a bifurcation at this point, changing from a system governed by an unstable node to one governed by an unstable focus. This is discussed later in Chapter 8.) Reaction 6.28 accelerates gradually, and as the hydroxyl radical concentration increases, the system becomes generally more reactive.

In the new regime, the oxidation of methanol proceeds beyond formaldehyde, and carbon monoxide begins to be produced in appreciable quantities. Furthermore, the sequence of reactions which produces carbon monoxide also produces the degenerate branching agent hydrogen peroxide. In a sense, the sequences of reactions leading to CH_2O and to CO are mutually catalytic, since each sequence produces H_2O_2 which itself undergoes thermal decomposition to give OH radicals.

It is in this new regime that the methanol system begins self-heating. The reactions to formaldehyde are slightly exothermic, but most of the temperature rise of the system to this point is caused by isentropic compression of the core gas by the expanding flame front and burnt gases. However, now that the rate of oxidation of methanol to formaldehyde is large, the exothermic effects are noticeable in the system. Furthermore, the oxidation of formaldehyde to carbon(II) oxide begins, and this is accompanied by further heat release.

As the end-gas temperature reaches 1100 K and beyond, reaction 6.36 totally dominates the radical attack on methanol. Reaction 6.28 continues to accelerate, and by now 72% of the formation of hydrogen peroxide occurs via reaction 6.27. Reaction 6.26 accounts for 16% of the formation of H_2O_2, while the reaction

$$CH_2O + HO_2 \rightarrow CHO + H_2O_2 \tag{6.37}$$

accounts for the remaining 12% of its rate of formation. Formaldehyde is thus to some extent being oxidized by HO_2. However, the dominant formaldehyde reaction is

$$CH_2O + OH \rightarrow CHO + H_2O, \tag{6.38}$$

consuming 63% of the formaldehyde, while reaction 6.37 consumes 33%.

Reaction 6.37, taken together with reaction 6.28, adds a further branching path to the methanol autoignition chemistry, and is extremely important in preparing the transition from chemical branching to thermal explosion. It is interesting to observe, however, that at this stage the formaldehyde concentration is still increasing rapidly as a consequence of reaction 6.25.

CHO undergoes the very fast reactions

$$CHO + O_2 \rightarrow CO + HO_2 \tag{6.39}$$

$$CHO + M' \rightarrow CO + H + M' \tag{6.40}$$

to form carbon monoxide. The relative contribution of these reactions to the rate of CHO consumption is 60% and 40%, respectively. The reaction path from formaldehyde to carbon monoxide is substantially exothermic, and reaction heat release starts to affect the end-gas temperature profile significantly.

Up to this point the temperature rise of the end-gas is mainly the result of adiabatic compression.

It is appropriate at this point to compare the reactions of CH_2OH and CH_3O. CH_2OH is generally more reactive than CH_3O at low and intermediate temperatures. However, CH_3O undergoes thermal decomposition at high temperatures, and serves as an important source of hydrogen atoms from the reaction

$$CH_3O + M' \rightarrow CH_2O + H + M'. \tag{6.41}$$

CH_3O will also react with molecular oxygen as follows

$$CH_3O + O_2 \rightarrow CH_2O + HO_2. \tag{6.42}$$

The relative rates of consumption of CH_3O by reactions 6.41 and 6.42 at 1100 K are 60% and 33%, respectively.

6.3.3 Autoignition: T > 1200 K, P > 44 bar

As the temperature reaches 1200 K, the decomposition of hydrogen peroxide becomes very rapid (reaction 6.28). Large numbers of OH radicals are released into the system, resulting in fast exothermic reactions. Ultimately, the radical pool will start to decrease (indicated mathematically by a further bifurcation in the differential system, this time to a stable node singularity structure) and the heat generated by the exothermic chain sequence of methanol oxidation to formaldehyde, followed by formaldehyde oxidation to carbon monoxide, leads to a thermal explosion. The exothermic reactions forming water and carbon

monoxide release about 55% of the total heat of reaction. These reactions dominate during this stage of autoignition, and heat the system from 1200 K to 1800 K, at a rate of about 100 K per microsecond.

The attack on methanol is dominated by reaction 6.36 and by

$$CH_3OH + OH \rightarrow CH_3O + H_2O. \tag{6.43}$$

These reactions are responsible for the consumption of 70% and 12% of the methanol respectively. Other significant reactions in which methanol is consumed are reaction 6.27 and

$$CH_3OH + H \rightarrow CH_2OH + H_2. \tag{6.44}$$

The formation of formaldehyde occurs through reactions 6.25, 6.41 and 6.42 at the levels discussed earlier. Formaldehyde consumption is dominated by reaction 6.37, reaction 6.38 and

$$CH_2O + H \rightarrow CHO + H_2 \tag{6.45}$$

at the levels of 76%, 9% and 15% respectively. CHO is consumed to form carbon monoxide through reactions 6.39 and 6.40 at about equal rates.

6.3.4 High Temperature Combustion: T > 1800 K

As a result of this sequence of reactions the oxidation of the methanol-air mixture is carried a stage further, to carbon monoxide and water. The temperature rises extremely rapidly to about 1800 K, at a rate of about 100 degrees Celsius per microsecond, whereupon the wet combustion of carbon monoxide to form carbon dioxide becomes significant. This does not occur, however, until virtually all the fuel has been consumed. Oxidation of carbon monoxide is responsible for about 45% of the heat release of the methanol-air system, and a thermal explosion ensues.

The sequence of reactions is as follows. The carbon monoxide is consumed predominantly by the reaction

$$CO + OH \rightarrow CO_2 + H. \tag{6.46}$$

The H atoms freed by this reaction react with molecular oxygen in the endothermic branching reaction

$$H + O_2 \rightarrow OH + O. \tag{6.47}$$

Alternatively, the H atoms may (at sufficiently high pressures) be removed by the termolecular reaction

$$H + O_2 + M' \rightarrow HO_2 + M'. \tag{6.48}$$

The consumption of hydrogen at this stage is approximately 50% via reaction

6.47, and 50% via reaction 6.48.

The oxygen atoms produced by reaction 6.47 cannot react with fuel (since none is left), and therefore react with water in the branching reaction

$$H_2O + O \rightarrow OH + OH \tag{6.49}$$

The hydroxyl radicals produced by reactions 6.47 and 6.49 then attack CO according to reaction 6.46. The sequence of reactions is highly exothermic, so that the free radical branching and the increase in temperature both accelerate until all the carbon monoxide has been consumed. The temperature increase was calculated to be about 700 degrees Celsius in one microsecond.

6.4 A Local Sensitivity Analysis of the Gr92 Mechanism

A first-order normalised local sensitivity analysis was performed on the major methanol reactions as determined from the Gr92 mechanism study. The local sensitivities calculated using Warnatz's HOMCHEM code follow the definition of Yetter, Dryer and Rabitz [129], and are of the form

$$c_{ij} = \frac{d\log[N_i]}{d\log k_k}, \tag{6.50}$$

where c_{ij} is the first order sensitivity coefficient associated with reaction coefficient k_j, and $[N_i]$ is the concentration of the i'th species. The logarithms in equation 6.50 ensure that the sensitivity coefficient is normalised. Thus, the

sensitivity of the system, or a component of the system, to a given reaction, can be compared with other calculated sensitivities throughout the evolution of the system.

The first-order sensitivity coefficient gives the sensitivity of the required physical quantity (species concentration, temperature, flame velocity etc.) to changes in the specified reaction coefficient at a given point in time, or at a specified stage of the reaction conditions. Therefore, the sensitivity coefficients indicate which reactions are the most important in the system being studied, and which reactions in the combustion model require accurately known rate coefficients.

The reactions examined for system sensitivity were as follows:

$$H + O_2 \rightarrow OH + O \tag{6.51}$$

$$OH + O \rightarrow O_2 + H \tag{6.52}$$

$$H + O_2 + M' \rightleftharpoons HO_2 + M' \tag{6.53}$$

$$HO_2 + HO_2 \rightleftharpoons H_2O_2 + O_2 \tag{6.54}$$

$$HO_2 + OH \rightleftharpoons H_2O + O_2 \tag{6.55}$$

$$OH + OH + M' \rightleftharpoons H_2O_2 + M' \tag{6.56}$$

$$CH_3OH + O_2 \rightleftharpoons CH_2OH + HO_2 \tag{6.57}$$

$$CH_3OH + OH \rightleftharpoons CH_2OH + H_2O \tag{6.58}$$

$$CH_3OH + HO_2 \rightleftharpoons CH_2OH + H_2O_2 \tag{6.59}$$

$$CH_2OH + O_2 \rightleftharpoons CH_2O + HO_2 \tag{6.60}$$

$$CH_2OH + M' \rightleftharpoons CH_2O + H + M' \tag{6.61}$$

$$CH_2O + OH \rightleftharpoons CHO + H_2O \tag{6.62}$$

$$CH_2O + HO_2 \rightleftharpoons CHO + H_2O_2 \tag{6.63}$$

$$CHO + O_2 \rightleftharpoons CO + HO_2 \tag{6.64}$$

$$CHO + M' \rightleftharpoons CO + H + M' \tag{6.65}$$

$$CO + OH \rightleftharpoons CO_2 + H \tag{6.66}$$

$$CO + HO_2 \rightleftharpoons CO_2 + OH. \tag{6.67}$$

The above reactions were chosen as they play the most important role in the methanol combustion mechanism. Since the other reactions only play a minor role in the autoignition mechanism, it was not considered necessary to study the consequences of varying their rate coefficients. This can be seen from the analysis earlier in this chapter.

It was found that the methanol autoignition chemistry is most sensitive to the four reactions 6.54, 6.56, 6.59, and 6.60. Successful quantitative modelling of engine knock will depend critically on the accuracy of the rate coefficients available for these four reactions.

Figures 6.7 to 6.14 show the temperature profile of the first-order normalised sensitivities of the major species, the intermediate species, and the temperature of the system as a function of system temperature, with respect to normalised variations in the rates of the above reactions (Gr92 mechanism). It is interesting to note the low sensitivity of the reaction system and the temperature to reaction 6.51. This reaction plays a major role in methanol flame chemistry, and yet is relatively unimportant in autoignition chemistry. This is because flame chemistry takes place at high temperatures ($\sim$ 2300K), while autoignition chemistry takes place at intermediate temperatures ($\sim$ 1250K).

Reaction 6.54 serves as a termination reaction in the methanol/air oxidation system. The autoignition temperature-dependent sensitivities from this reaction are positive and increase monotonically for methanol and molecular

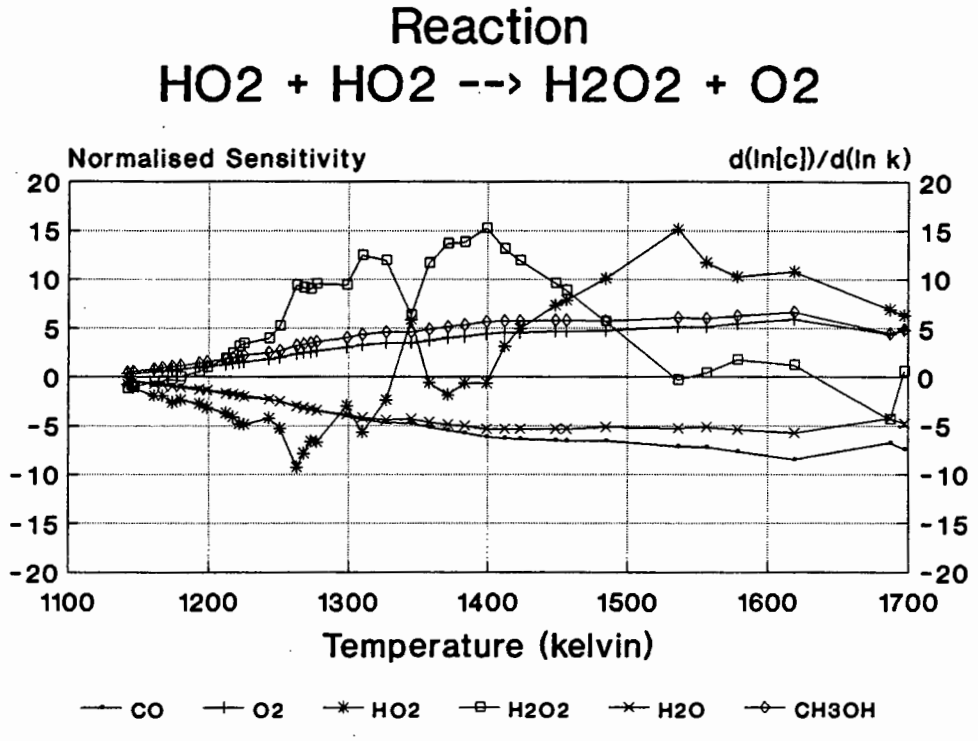

Figure 6.7: Major Species and Temperature Sensitivities as a Function of System Temperature.

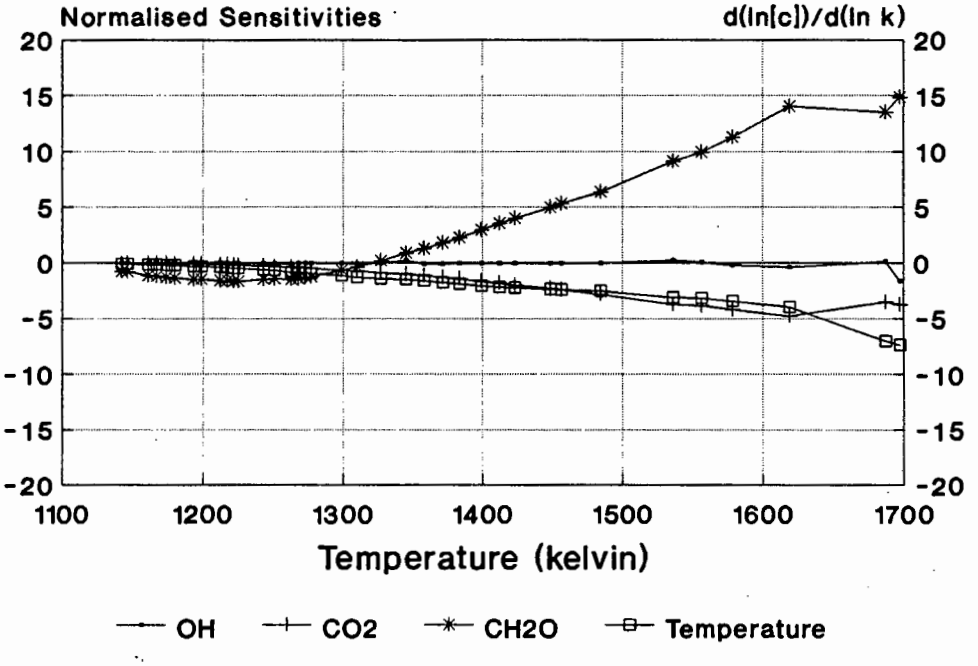

Figure 6.8: Intermediate Species and Temperature Sensitivities as a Function of System Temperature.

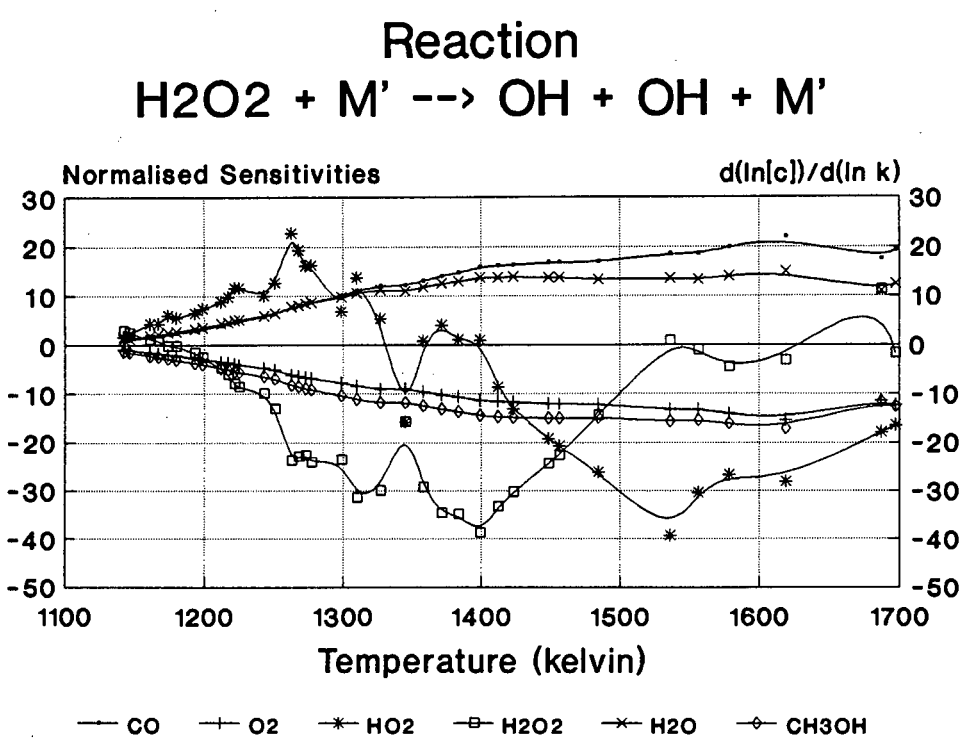

Figure 6.9: Major Species and Temperature Sensitivities as a Function of System Temperature.

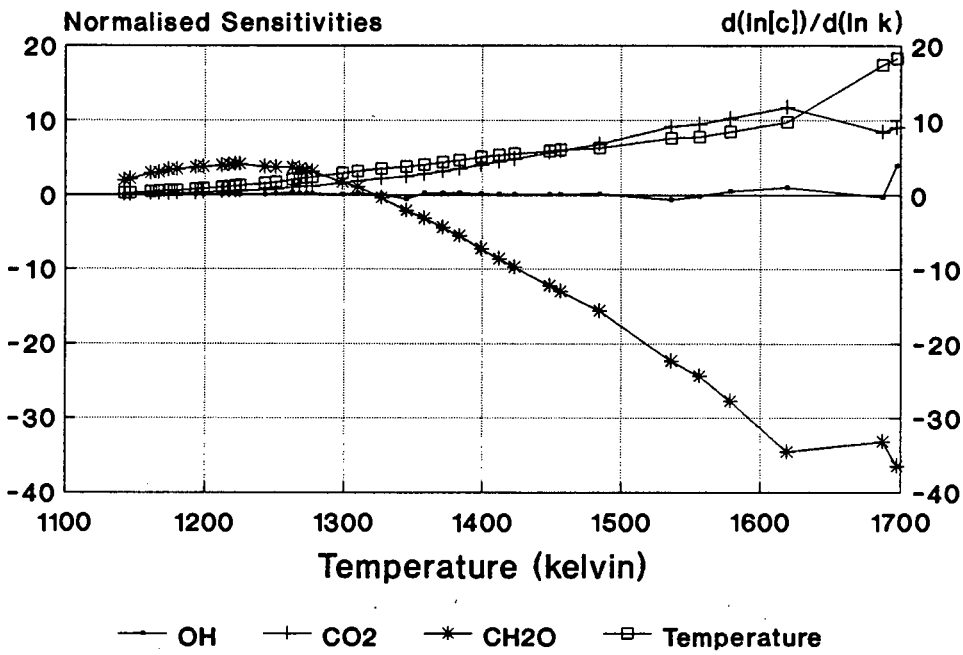

Figure 6.10: Intermediate Species and Temperature Sensitivities as a Function of System Temperature.

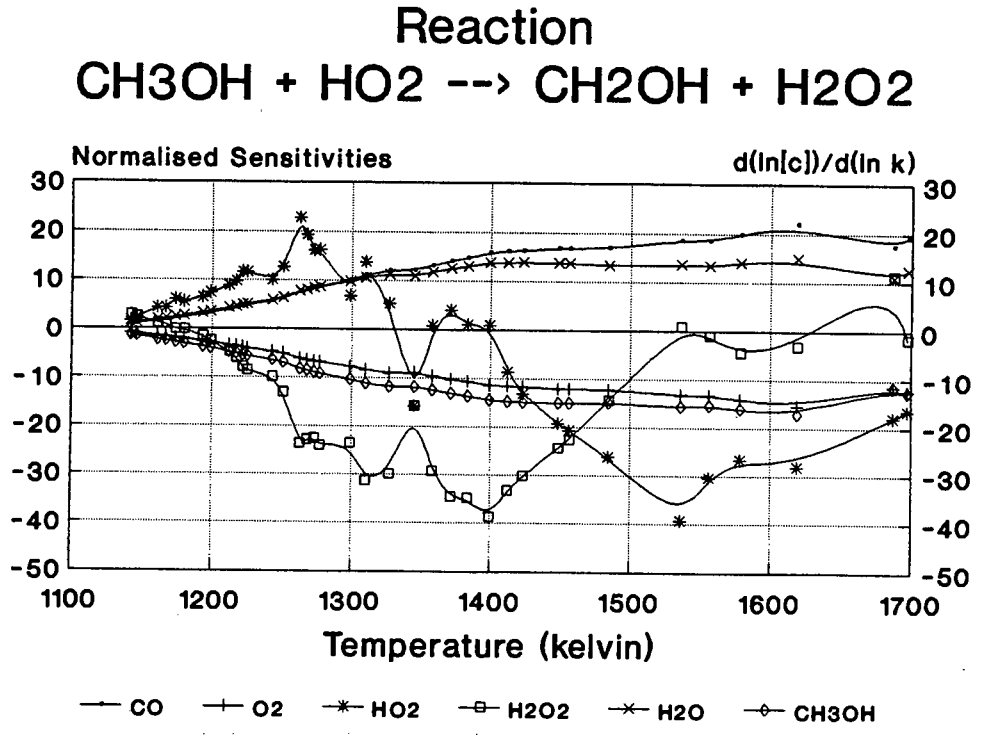

Figure 6.11: Major Species and Temperature Sensitivities as a Function of System Temperature.

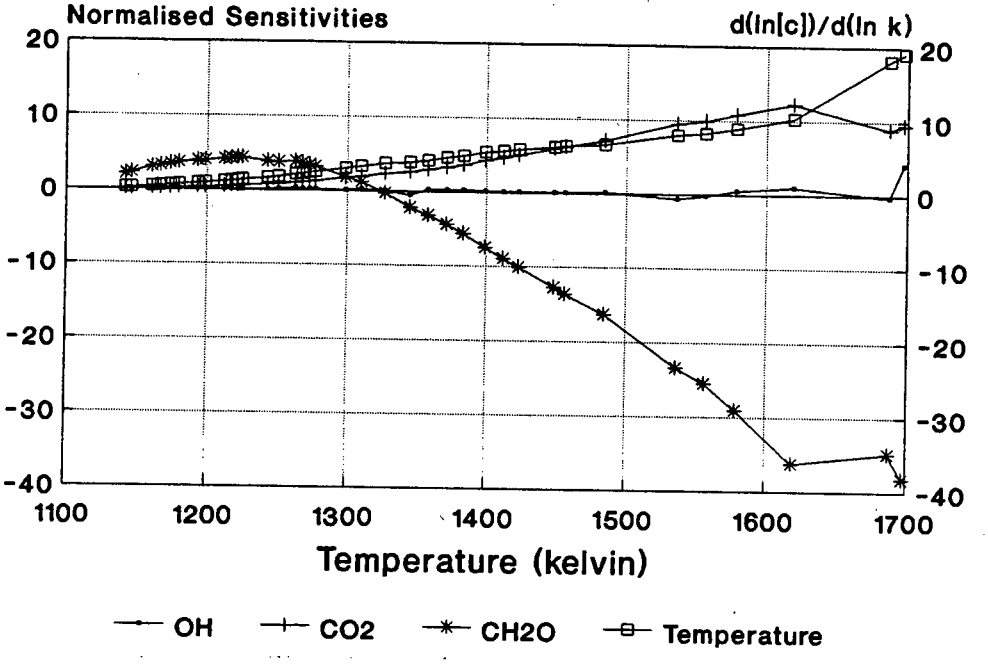

Figure 6.12: Intermediate Species and Temperature Sensitivities as a Function of System Temperature.

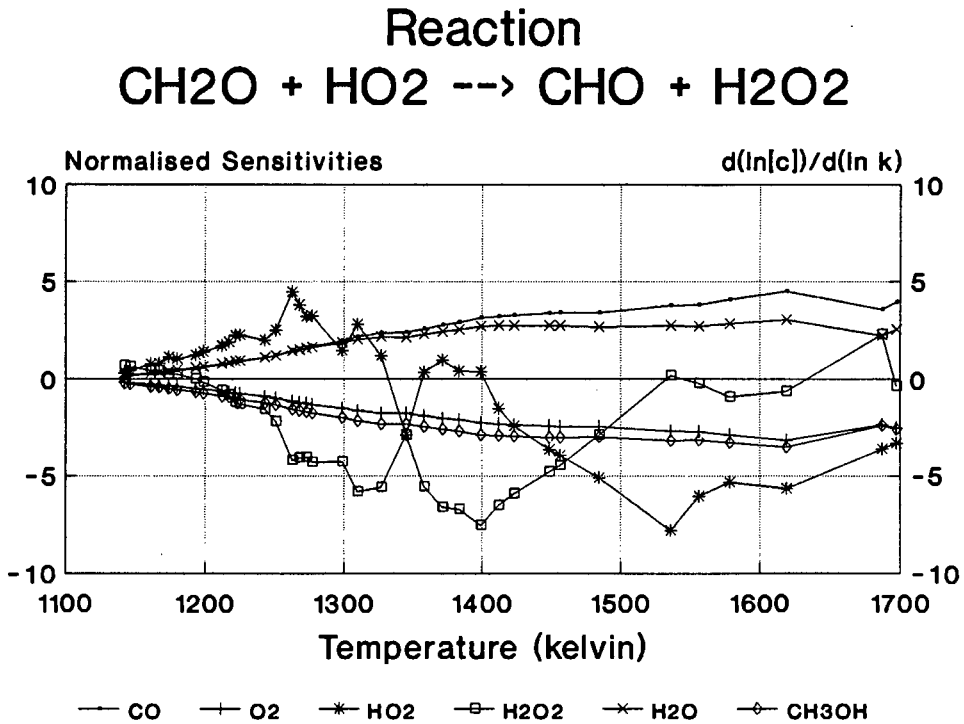

Figure 6.13: Major Species and Temperature Sensitivities as a Function of System Temperature.

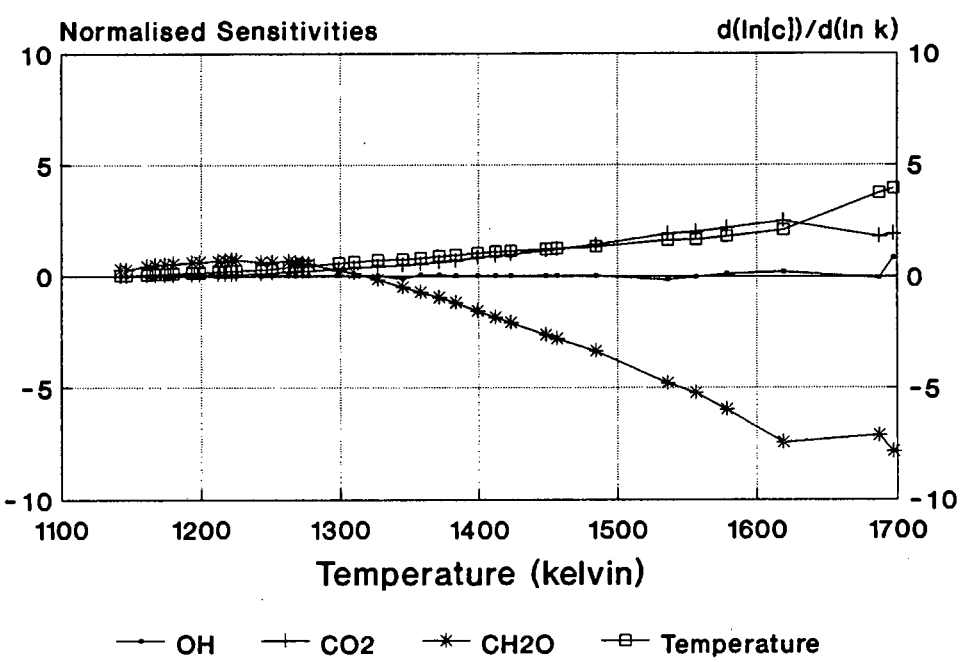

Figure 6.14: Intermediate Species and Temperature Sensitivities as a Function of System Temperature.

oxygen up to 1600K, and then begin to decrease (but remain positive) as the oxidation chemistry changes from methanol and formaldehyde oxidation to wet carbon monoxide oxidation. The temperature-dependent sensitivities for carbon monoxide, carbon dioxide, water and temperature are negative and decrease monotonically up to 1600K, and then begin to increase slightly (excluding the temperature sensitivity, which continues to decrease).

The sensitivities of the intermediate species to positive changes in the reaction 6.54 rate coefficient, is also a function of the progress of the autoignition reaction, and is therefore rather complex. The concentration of hydrogen peroxide would increase substantially through an increase of the above reaction rate coefficient, while the concentration of hydroxyl radicals would decrease in the temperature range below 1330K, and between 1360K and 1400K, and would increase for temperatures between 1330K and 1360K, and temperatures above 1400K.

The terminating nature of reaction 6.54 is most notable in the influence of an increment in this reaction rate coefficient on the concentration of formaldehyde. While formaldehyde is being formed from the oxidation of methanol, its temperature-dependent sensitivity is negative, but when formaldehyde begins to be oxidised to carbon monoxide, its sensitivity becomes positive.

The reverse reaction of reaction 6.56, which is the thermal decomposition of hydrogen peroxide to hydroxyl radicals, is the key branching reaction in the methanol/air oxidation system. An increase in this reverse reaction rate coefficient serves to increase concentrations of water, carbon monoxide, and carbon dioxide, and the temperature of the autoignition system; and decreases concentrations of molecular oxygen and methanol, for temperatures less than 1700K.

For temperatures lower than 1175K, an increase in this reaction rate coefficient serves to increase the amount of hydrogen peroxide in the system; while for temperatures in the range 1175K to 1600K, an increase in this reaction rate coefficient serves to lower the concentration of hydrogen peroxide in the system, and simultaneously enhances the reactivity of the system, through an increase in hydroxyl radical concentration. Hydroperoxyl radical concentration is raised by an increase in this rate coefficient, for temperatures less than 1330K, and in the temperature range 1360K to 1400K; and lowered by an increase in this reaction rate coefficient in the temperature range 1330K to 1360K, and for temperatures larger than 1400K.

The accelerating nature of this reaction is evident from the effect an increase in this reaction rate coefficient has on the concentration of formaldehyde. When formaldehyde is being formed from the oxidation of methanol, its concentration is raised by an increase in the rate coefficient, but when formaldehyde is being oxidised to form carbon monoxide, its concentration is lowered by an increase in the reaction rate coefficient.

Reaction 6.59 serves to accelerate methanol oxidation. Together with the reverse reaction of reaction 6.56, these reactions form a branching system. An increase in the reaction 6.59 rate constant increases the temperature of the autoignition system monotonically, and increases the concentrations of water, carbon monoxide, and carbon dioxide for temperatures less than 1700K. An increase in this reaction rate coefficient simultaneously causes a decrease in the concentrations of molecular oxygen and methanol.

An increase in this reaction rate coefficient increases the concentration of hydrogen peroxide for temperatures less than 1175K, and serves to decrease the concentration of hydrogen peroxide for temperatures in the range 1175K to 1650K (except for a small unstable region at about 1540K). Hydroperoxyl rad-

ical concentration is raised by an increase in this reaction rate coefficient for temperatures less than 1330K, and in the range 1360K to 1400K, and is lowered by an increase in this reaction rate coefficient in the temperature range 1330K to 1360K, and for temperatures larger than 1400K.

As in the case of the reverse reaction of reaction 6.56, the accelerating nature of this reaction is evident from the effect an increase in this reaction rate coefficient has on the concentration of formaldehyde. When formaldehyde is being formed from the oxidation of methanol, its concentration is raised by an increase in the rate coefficient, but when formaldehyde is being oxidised to form carbon monoxide, its concentration is lowered by an increase in the reaction rate coefficient.

Reaction 6.59 and the reverse branching reaction of reaction 6.56 both accelerate the reaction chemistry far more than reaction 6.54 impedes it. This can be seen from a comparison of the normalised scales of the respective sensitivities.

Finally, an increase in the reaction rate of reaction 6.63 also serves to increase the reactivity of the autoignition system, by increasing the temperature of the system, and increasing the concentrations of water, carbon monoxide, and carbon dioxide. An increase in this reaction rate coefficient simultaneously decreases the concentrations of methanol and molecular oxygen.

An increase in this reaction rate coefficient increases the concentration of hydrogen peroxide for temperatures less than 1190K, and serves to decrease the concentration of hydrogen peroxide for temperatures in the range 1190K to 1620K (except for a small unstable region at about 1540K). Hydroperoxyl radical concentration is raised by an increase in this reaction rate coefficient for temperatures less than 1330K, and in the range 1360K to 1400K, and is lowered by an increase in this reaction rate coefficient in the temperature range

1330K to 1360K, and for temperatures larger than 1400K.

Once again, the accelerating nature of this reaction is evident from the effect an increase in this reaction rate coefficient has on the concentration of formaldehyde. When formaldehyde is being formed from the oxidation of methanol, its concentration is raised by an increase in the rate coefficient, but when formaldehyde is being oxidised to form carbon monoxide, its concentration is lowered by an increase in the reaction rate coefficient.

Reaction 6.63 is of significance in the combustion of methane, and has been the subject of careful experimental studies. Tsang and Hampson's recommendation [109] is based on Walker's review [115]; the CEC recommendation is identical. Therefore, Grotheer et al [56], and Norton and Dryer [89], use the same value for this reaction coefficient.

Reaction 6.59 is somewhat controversial. It appears that no rate coefficients have ever been measured directly. Norton and Dryer [89], in their revision of Westbrook and Dryer's [119] pioneering work, have adjusted the Arrhenius factor for this reaction upwards by a factor of 6.2, following a suggestion by Cathonnet et al [21] in 1982. Grotheer et al [56] have preferred to retain the original value [119] which was also used by Dove and Warnatz [31].

The two reactions 6.54 and 6.56 are very well known in the context of H_2/O_2 oxidation. This does not, however, mean that the rate coefficients are uncontroversial.

By adopting the CEC recommendations for the reaction

$$OH + OH + M' \rightarrow H_2O_2 + M',$$

and calculating reverse rates by appeal to equilibrium thermodynamics, the following Arrhenius constants for the Gr92 mechanism [56], for the thermal decomposition of hydrogen peroxide, reaction 6.56 were obtained: $A = 1.20 \times 10^{17}$, $n = -2.0$, $E_a = 206.8$ (in $cm^3.mol^{-1}.s^{-1}$ and kJ/mol units).

The constants used by Norton and Dryer are $A = 1.20 \times 10^{17} cm^6.mol^{-2}.s-1$, $n = 0.0$, and $E_a = 190.4$kJ/mol respectively. The net effect is that between 650 K and 1500 K the reaction coefficient of H_2O_2 decomposition in Norton and Dryer's model is always smaller than the Gr92 model by a factor of between 0.4 and 0.5. However, the chaperon efficiencies are defined differently for the two groups. The CEC expression refers to $M' = H_2 + 0.4N_2 + \ldots$, while the Norton-Dryer group refers to $M' = N_2 + 2.5H_2 + \ldots$. Therefore the reaction rates for this reaction used by the two groups differ at most by 30% over this temperature range. This reaction is involved in all the branching mechanisms that have been studied here.

For reaction 6.54, the disproportionation of hydroperoxyl radical, Grotheer et al [56] adopts the CEC recommendations, viz. $A = 1.90 \times 10^{12} cm^3.mol^{-1}.s^{-1}$, $n = 0.0$, $E_a = 6.434$ kJ/mol. Norton and Dryer [89] use $A = 1.00 \times 10^{13} cm^3.mol^{-1}.s^{-1}$, $n = 0.0$, $E_a = 4.18$ kJ/mol. Between 650 K and 1500 K Norton and Dryer's hydroperoxyl radical recombination rates are therefore very much greater than Grotheer's, by a factor of between 6.3 and 8.0. However, this is an ambiguous reaction to classify: although it clearly represents a terminating reaction at low temperatures, at temperatures above 1000 K it is instrumental (together with 6.56) in the relatively unreactive HO_2 being converted into the highly reactive OH radical.

In these circumstances it is difficult to compare the Norton-Dryer model with Grotheer's solely on the basis of autoignition delay times. The interplay between the three sensitive reactions, for which there are conflicting data, is very

complicated. In Norton and Dryer's model, the most sensitive branching reaction 6.56 is roughly the same as Grotheer's, but the most sensitive termination reaction 6.54 is nearly an order of magnitude faster than in Grotheer's, both factors leading to decreased reactivity; but ND's sensitive propagation reaction 6.59 is much faster. The fairly close agreement between the calculated knock points obtained using the two sets of reaction rate data must surely be fortuitous. A careful independent evaluation of kinetic data for the three crucial sensitive reactions is necessary.

If the reaction coefficient for reaction 6.54 in the Gr92 mechanism is replaced by the corresponding rate coefficient contained in the ND89 mechanism, and the methanol autoignition model is re-tested on this basis, it is found that autoignition is predicted to occur one crankshaft degree before the experimentally measured autoignition point (the predicted autoignition time improves from 4^o BTDC to 1^o BTDC). This is a considerable improvement over the predicted results from the separate mechanisms, and it should be borne in mind that this reaction rate coefficient has to some extent been validated in this temperature and pressure range [89].

It is perfectly clear why the relatively simple 1989 mechanism of Grotheer and Kelm [55] (20 species, 171 reactions) gives autoignition delay times essentially identical to those obtained with the extensive mechanism of Grotheer et al [56] (43 species, 414 reactions). The rate coefficients for the sensitive reactions 6.56, 6.59, 6.63 are exactly the same; the only difference occurs in reaction 6.54. Lightfoot's 1988 expression [77] for the HO_2 recombination reaction, used by Grotheer and Kelm in their 1989 work [55], gives the same reaction rate as the recent CEC recommendation at a temperature of 980 K. At lower temperatures Lightfoot's expression decreases more rapidly. This has negligible consequences for the prediction of autoignition times using the two mechanisms, but does produce identifiable differences in the qualitative

behaviour of the rate equations (see chapter 7).

It is also easy to understand qualitatively why the 1987 mechanism of Esser and Warnatz predicts autoignition to occur significantly earlier than Grotheer's 1992 mechanism. The rate constants for the thermal decomposition of hydrogen peroxide (the branching reaction 6.56) are exactly the same in both models, but different expressions are used for the HO_2 recombination reaction (the terminating reaction 6.54). At temperatures below 700 K the termination reaction is faster in the Esser-Warnatz model, but this is not significant since H_2O_2 thermal decomposition is so slow at such temperatures. At 1050 K, the Esser-Warnatz reaction 6.54 rate is half as fast as the Gr92 rate; at 1150 K the ratio is 0.45, and at 1250 K it is 0.40. Clearly their net branching ratio accelerates far more rapidly than Gr92 as soon as the temperature reaches 700 K. Of course, their scheme was never intended for use at low temperatures.

In the 1983 scheme of Dove and Warnatz [31], the rate expression used for the H_2O_2 decomposition reaction is greater than Grotheer's at very low temperatures, but this is insignificant. Between 850 K and 1200 K it is slightly greater than Grotheer's (between 8% and 11% greater). However, their termination reaction 6.54 is very much faster than Grotheer's at all temperatures, by a factor of 2.9 at 750 K, 2.3 at 1000 K, and 2.0 at 1250 K. The net branching ratio will be less than in Grotheer's 1992 model at all temperatures.

Examining the sensitivity of the HO_2, CH_3OH, H_2O_2 and OH concentrations (and also of the temperature) to variations in the rate coefficient for reaction 6.59, shows clearly that this propagation reaction, in which HO_2 is consumed, participates in a branching sequence. The sensitivity of HO_2 concentration to this reaction rate is positive, indicating that an increase in overall HO_2 production would accompany an increase in reaction coefficient 6.59. Furthermore, the temperature would rise more rapidly if this reaction coefficient were

to be increased, from which it follows that the modelled autoignition point would occur earlier.

This is confirmed by modelling the end-gas autoignition using the extended Grotheer-Kelm mechanism, but with the rate constants for reaction 6.59 changed to the values adopted by Norton and Dryer [89]: i.e. by retaining the same activation energy but increasing the Arrhenius factor by a factor of 6.2. The calculated autoignition point now occurs at 7.5 degrees BTDC, as opposed to the 4 degree BTDC prediction of the Grotheer-Kelm mechanism. This is a much more serious discrepancy than before.

It must be emphasized that 6.59 is the only sensitive reaction (in the context of methanol autoignition) for which no carefully evaluated CEC recommendation exists. Adopting CEC reaction rate expressions systematically, but varying the Arrhenius factor of Westbrook and Dryer [119] for 6.59 in the direction suggested by Norton and Dryer [89] does not seem appropriate. If any adjustment to the 6.59 rate coefficient is necessary, the balance of evidence suggests that it should be downwards rather than upwards.

Tsang [109] presented an estimate of the uncertainty in the accuracy of the reaction 6.59 rate coefficient to be in the region of twenty. Taking this assessment into account, when the rate coefficient for this reaction in the Gr92 mechanism was reduced by a factor of ten, autoignition was predicted to occur at the correct crankshaft angle, in agreement with the experimentally measured knock point, within the limits of experimental error (the predicted autoignition time improved from 4° BTDC to TDC).

The interplay of reactions 6.56 and 6.54 is interesting. Reaction 6.54 is clearly a termination reaction; and figure 7.1 shows that even at 1250 K, when the H_2O_2 produced in the reaction is able to decay thermally at an appreciable rate, the

effect of an increase in the 6.54 rate coefficient would be to raise the H_2O_2 concentration and to lower the concentrations of all other product species (as well as to lower the concentration of the HO_2 which is consumed). Reaction 6.56 is a branching reaction; and figure 7.2 shows that at 1250 K a small increase in the reaction rate of 6.54 would produce a fifteen-fold greater relative increase in the HO_2 radical concentration. There is an evident conclusion to be drawn from this: in order to model methanol autoignition quantitatively it is essential to have very accurate kinetic information about the thermal decomposition of H_2O_2, over an extended temperature range.

Both the sensitivity analysis, and the survey of the results of autoignition calculations derived from the major published methanol combustion mechanisms, suggest that either or both of the rate coefficients that have been used for reactions 6.56 and 6.59, should be adjusted downward at intermediate temperatures; or alternatively that 6.54 should be adjusted upwards (which is the key to the apparent superiority of the early and rudimentary Dove-Warnatz model). The only other realistic possibility is that the CARS temperature measurements are significantly and systematically too high. This is unlikely, since the temperatures were deduced by direct comparison of CARS spectra recorded in the engine, and in an accurately calibrated HPHT optical cell using the same lasers, spectrometer and detector.

The measured temperature profile is in no way dependent on the uncertainties inherent in scaling law theories of motional narrowing in nitrogen Q-branch CARS spectra, or on the vagaries of non-linear least squares fitting routines applied to noisy (and highly correlated) CARS spectral data, for which it is impossible to make realistic error estimates. It is true that isentropic conditions have been assumed for the last part of the chemical kinetic modeling calculation, i.e. that no empirical heat loss correction has been applied, but this is generally believed to be a harmless procedure in the present context

[127] [22] [30].

It must be conceded, however, that throughout the compression stroke, the gas in the small region which was sampled in the centre of the combustion chamber, approximately 6mm below the cylinder head, may be slightly hotter than the gas at the extreme periphery, because of macroscopic heat loss effects during compression, and because of static temperature gradients in the engine itself. It is known from thermocouple measurements that the inner surface of the cylinder head may be as much as 200 degrees celcius hotter at the center than at the edges. Damage studies indicate that, in an engine with cylindrical combustion chamber geometry, the most severe abnormal combustion often occurs near the periphery of the piston crown closest to the exhaust valve, sometimes even in the small clearance zone between the upper wall of the piston above the first piston ring and the cylinder wall.

It cannot be claimed that realistic estimates of the end-gas temperature in such small crevices were obtained by performing CARS measurements and adiabatic heat release calculations in a representative sample of the bulk of the gas. The temperatures that have been measured and calculated may be systematically higher than end-gas temperatures in peripheral crevices. It is possible that part of the discrepancy between the observed and calculated autoignition times can be accounted for in this way, but it is unlikely that this could account for the entire discrepancies.

Chapter 7

A Linearised Eigenmode Analysis of the Reaction Equations

7.1 Introduction to Geometric Qualitative Theory of Ordinary Differential Equations

Consider a system of N coupled non-linear first order differential equations in time, described by

$$\frac{dy_1}{dt} = M_1 + a_1 y_1 + a_2 y_2 + \cdots + a_N y_N + F_1(y_1, y_2, \cdots)$$

$$\frac{dy_2}{dt} = M_2 + b_1 y_1 + b_2 y_2 + \cdots + b_N y_N + F_2(y_1, y_2, \cdots)$$

$$\frac{dy_3}{dt} = M_3 + c_1 y_1 + c_2 y_2 + \cdots + c_N y_N + F_3(y_1, y_2, \cdots)$$

$$\vdots$$

$$\frac{dy_N}{dt} = M_N + p_1 y_1 + p_2 y_2 + \cdots + p_N y_N + F_N(y_1, y_2, \cdots). \qquad (7.1)$$

The functions $F_i(y_1, y_2, \cdots)$ describe the non-linear part of the above system of non-linear differential equations. Equations of this sort, that are only implicitly dependent on the time, are called autonomous or time invariant equations, and the system described by the above equations is called a dynamical system. It turns out that there are important properties of the full non-linear system of equations that are shared by the simpler linear system. Therefore much can be learnt about the full non-linear system by studying the linear system.

The linear form of the above system of equations are

$$\begin{aligned}
\frac{dy_1}{dt} &= M_1 + a_1 y_1 + a_2 y_2 + \cdots + a_N y_N \\
\frac{dy_2}{dt} &= M_2 + b_1 y_1 + b_2 y_2 + \cdots + b_N y_N \\
\frac{dy_3}{dt} &= M_3 + c_1 y_1 + c_2 y_2 + \cdots + c_N y_N \\
&\vdots \\
\frac{dy_N}{dt} &= M_N + p_1 y_1 + p_2 y_2 + \cdots + p_N y_N. \qquad (7.2)
\end{aligned}$$

It proves useful to study the behaviour of the solutions of 7.2 in the space defined by the solutions y_i. This is an N-dimensional space, and is called the generalised phase space of the system. When the solutions of 7.2 are represented in the generalised phase space, the time t appears as a parameter in $y_i(t)$, and as t increases, so an N-dimensional manifold evolves in the generalised phase space, which describes the path of the system. The sense in which time increases along the path of the system is usually shown by arrows.

The system of equations 7.2 can be written in the simpler form,

$$\frac{dy_1}{dt} = G_1(y_1, y_2, \cdots, y_N)$$
$$\frac{dy_2}{dt} = G_2(y_1, y_2, \cdots, y_N)$$
$$\frac{dy_3}{dt} = G_3(y_1, y_2, \cdots, y_N)$$
$$\vdots$$
$$\frac{dy_N}{dt} = G_N(y_1, y_2, \cdots, y_N), \tag{7.3}$$

or even more simply

$$\frac{dy_i}{dt} = G_i(y_i)$$
$$= \sum_j K_{ij} y_j + M_i. \tag{7.4}$$

The time may always be eliminated from an autonomous system like 7.3 by dividing the equations to obtain the set of first order partial derivatives,

$$\frac{\partial y_i}{\partial y_j} = \frac{G_i}{G_j}. \tag{7.5}$$

The equilibrium (critical) points of the system occur when $G_i = 0$ for all i in the system, because then the direction fields associated with the partial derivatives 7.5 become indeterminate [6] [68]. There are four different types of equilibrium points in the generalised phase space; namely, centres, nodes, focii, and saddle points.

The general solution of the above set of linear equations is

$$y_i(t) = \sum_{jk} Q_{ij} e^{\gamma^d_{jk} t} C_k - \sum_{jkl} Q_{ij} (\gamma^d_{jk})^{-1} Q^{-1}_{kl} M_l, \tag{7.6}$$

where γ^d_{ij} is a diagonal matrix with matrix elements given by the eigenvalues of K_{ij}, Q_{ij} is the matrix of eigenvectors obtained from the diagonalisation of K_{ij}. C_i is a constant matrix, independent of time, and specified by the initial conditions of the system. This expression is derived in full detail later in this chapter. Another way of expressing the above solution is in the form

$$y_i(t) = \sum_j Q_{ij} c_j e^{\gamma_j t}. \tag{7.7}$$

It turns out that the full N-dimensional system can be expressed in terms of a direct product of one-dimensional and two dimensional systems [6], and so the solutions of the N-dimensional problem can be analysed in terms of the solutions of the one-dimensional and two-dimensional problem. Therefore a discussion of the properties of the manifold in the N-dimensional generalised phase space can be specialised to a discussion of the properties of one-dimensional and two-dimensional trajectories in the generalised two-dimensional phase plane.

Consider the homogeneous two-dimensional problem in the form

$$\begin{aligned} \frac{dy_1}{dt} &= ay_1 + by_2 \\ \frac{dy_2}{dt} &= cy_1 + dy_2. \end{aligned} \tag{7.8}$$

This equation can be written in the matrix form

$$\frac{dy_i}{dt} = \sum_j A_{ij} y_j \tag{7.9}$$

which has the formal solution

$$y_i(t) = \sum_j e^{A_{ij}t} y_j(0) + C_i, \tag{7.10}$$

where $\exp(A_{ij}t)$ is defined in one of the two following ways:

$$e^{A_{ij}t} = \delta_{ij} + A_{ij}t + \frac{(A_{ij}t)^2}{2} + \frac{(A_{ij}t)^3}{3!} + \cdots \tag{7.11}$$

or

$$e^{A_{ij}t} = \lim_{N\to\infty} (\delta_{ij} + \frac{A_{ij}t}{N})^N. \tag{7.12}$$

The solution of system 7.8 is

$$y_i(t) = c_1 \lambda_{1i} e^{\gamma_1 t} + c_2 \lambda_{2i} e^{\gamma_2 t}, \tag{7.13}$$

where γ_1 and γ_2 are the eigenvalues of the matrix A_{ij}, and λ_{1i} and λ_{2i} are the eigenvectors of A_{ij}. The characteristic equation of A_{ij} is

$$\det(A_{ij} - \gamma\delta_{ij}) = \gamma^2 - (a+d)\gamma + (ad - bc) = 0, \tag{7.14}$$

with eigenvalues

$$\gamma_{1,2} = \frac{(a+d) \pm \sqrt{(a+d)^2 - 4(ad-bc)}}{2}. \tag{7.15}$$

When both eigenvalues are real, and $c_2 = 0$, $y_1 = c_1\lambda_{11}\exp(\gamma_1 t)$, and $y_2 = c_1\lambda_{12}\exp(\gamma_1 t)$. Thus there is a degenerate straight line trajectory

$$y_2 = (\lambda_{12}/\lambda_{11})y_1$$

through the origin of the generalised phase plane. Similarly, when $c_1 = 0$, there is another degenerate straight line trajectory $y_2 = (\lambda_{22}/\lambda_{21})y_1$ through the origin.

When the eigenvalues are real and unequal, then the equilibrium point will be an improper node. This improper node will be stable and attractive when both eigenvalues are negative, and unstable when both eigenvalues are positive. In other words, the system converges towards the equilibrium point along the improper node trajectories when both eigenvalues are negative, and diverges from the equilibrium point along the improper node trajectories when both eigenvalues are positive. A proper node arises when A_{ij} has two linearly independent eigenvectors with the same eigenvalue.

If the eigenvalues have opposite signs, then the equilibrium point is a saddle point, which is inherently unstable.

When the eigenvalues are complex, the equilibrium point will be a focus. This focus will be stable if the real part of the eigenvalues is negative, and will be unstable if the real part is positive. This means that the system will converge towards the equilibrium point along an inward spiral if the real part of the eigenvalue is negative, and will diverge from the equilibrium point along an

outward spiral if the real part of the eigenvalue is positive. If the eigenvalue is purely imaginary, then the equilibrium point will be a centre.

Figure 7.1 shows the phase portraits associated with the system of equations 7.8 for the different eigenvalue conditions specified above.

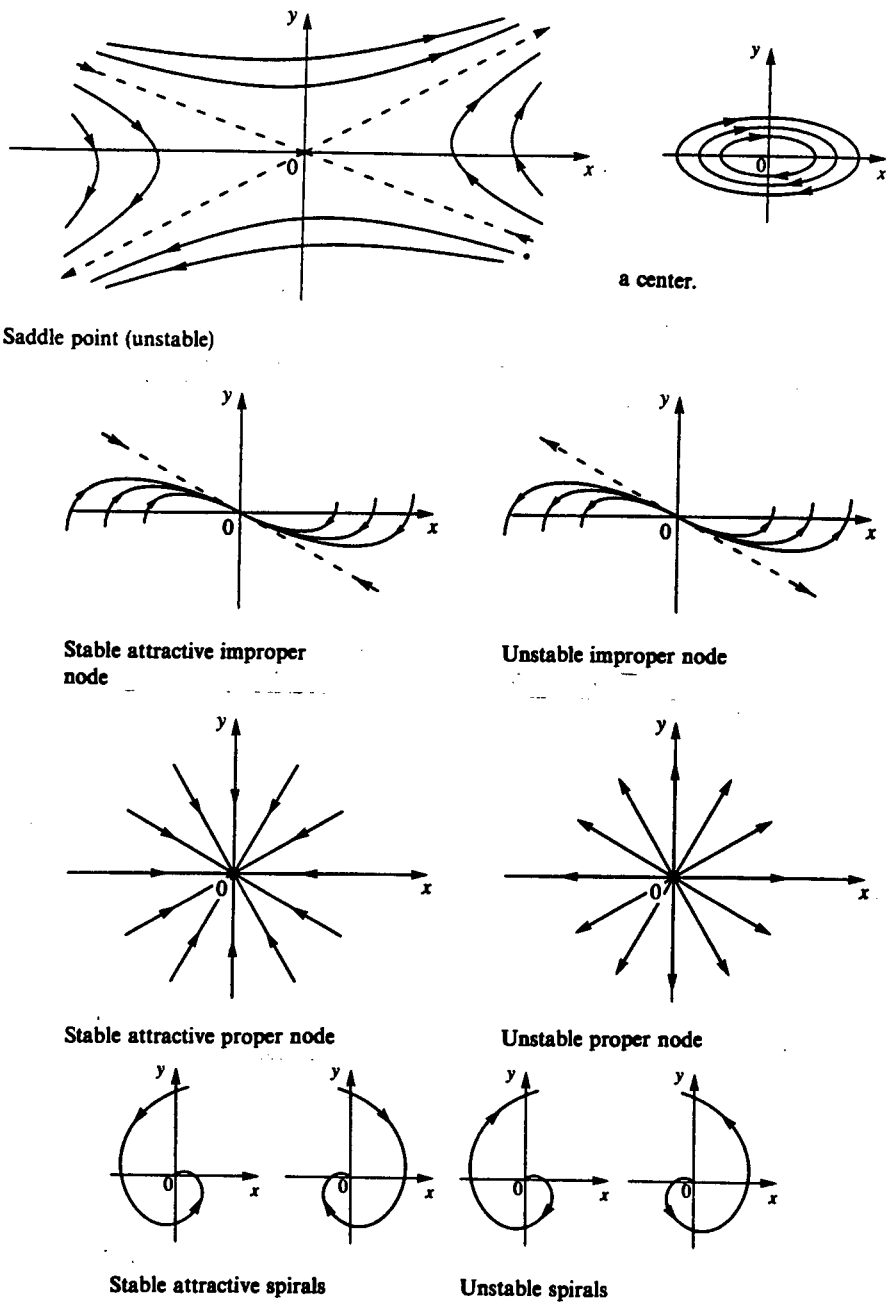

Figure 7.1: Phase Portraits in the Two-dimensional Generalised Phase Plane

The most important theorem in geometric qualitative theory of non-linear differential equations is the Linearisation Theorem. This theorem states that in the neighbourhood of a fixed point (equilibrium point), the N-dimensional manifold describing the evolution of an N-dimensional non-linear system in generalised phase space is topologically equivalent to the N-dimensional manifold describing the evolution of the N-dimensional linear system, as long as the linear part has no purely imaginary eigenvalue. In other words, as long as a fixed point (equilibrium point) in the manifold describing the linear system is not a centre, then that fixed point of the linear system is topologically equivalent to the same fixed point of the non-linear system.

Therefore the qualitative behaviour of the non-linear solution in a neighbourhood of an equilibrium point, is the same as the qualitative behaviour of the linear solution in the neighbourhood of the equilibrium point.

7.2 Derivation of the Linear Mode Analysis

7.2.1 General Comments

It is common practice in the study of non-linear differential equations to linearise the set of equations about different points in the solution space, and then solve for the linearised system. These linearised solutions are then first order approximations to the true solution of the problem, and are used to study the qualitative behaviour of the system at the specified points in the solution space.

Geometric qualitative studies of systems of non-linear differential equations have not been widely used in chemical kinetics. K. Chinnick et al [23] used a linearisation technique in studying oscillatory reaction behaviour in H_2/O_2

systems. This study was conducted analytically using a simplified H_2/O_2 mechanism. She was able to derive expressions defining the critical ignition boundary criteria and the conditions for oscillatory ignition.

More recently, Maas and Pope [79] used qualitative dynamical methods as a means of determining how a chemical kinetic system can be simplified. They showed that the linearised time development of a chemical system can be closely approximated by a subspace of the composition space, where the subspace is defined as that in which all movements of the chemistry correspond to slow time scales. This subspace is determined by finding the points in the composition space that are in equilibrium with respect to the fastest time scales of the chemical system. This linear approach was then generalised to the full non-linear problem. They were able to demonstrate the method successfully for a CO/H_2/air system, reducing the system to one and two dimensional manifolds in the reaction space, and comparing the results with conventional reduced mechanisms.

7.2.2 The Method of Linearisation

The system of reaction equations are linearised in the following way. The species concentration vector $y_i(t)$ evolves according to the system of equations

$$\frac{dy_i}{dt} = \sum_{j}^{N} A_{ij} y_j + \sum_{jk}^{N} B_{ijk} y_j y_k + \sum_{jkl}^{N} C_{ijkl} y_j y_k y_l. \qquad (7.16)$$

The first term corresponds to rates for unimolecular decomposition reactions. The second term corresponds to the rates for bimolecular reactions, and the third term corresponds to the rates for termolecular reactions. Now, if the solution is expanded about some point $y_i(t_0)$, then the displacement from

that point $x_i(t)$ can be defined as

$$x_i(t) = y_i(t) - y_i(t_0), \tag{7.17}$$

and the equation for $x_i(t)$ can be written

$$\frac{dx_i}{dt} = \sum_{j}^{N} A_{ij}(x_j(t) + y_j(t_0)) + \sum_{jk}^{N} B_{ijk}(x_j(t) + y_j(t_0))(x_k(t) + y_k(t_0))$$
$$+ \sum_{jkl}^{N} C_{ijkl}(x_j(t) + y_j(t_0))(x_k(t) + y_k(t_0))(x_l(t) + y_l(t_0)). \tag{7.18}$$

The non-linear terms in equation 7.18 involve products $x_j x_k$ and $x_j x_k x_l$. Equation 7.18 is linearised by ignoring terms that are quadratic and cubic in x_j. This yields the linearised equation

$$\dot{x_i} = \sum_{j}^{N} A_{ij} y_j(t_0) + \sum_{jk}^{N} B_{ijk} y_j(t_0) y_k(t_0) + \sum_{jkl}^{N} C_{ijkl} y_j(t_0) y_k(t_0) y_l(t_0)$$
$$+ \sum_{j}^{N} A_{ij} x_j(t) + \sum_{jk}^{N} [(B_{ijk} + B_{ikj}) y_k(t_0)] x_j(t)$$
$$+ \sum_{jkl}^{N} [(C_{ijkl} + C_{ikjl} + C_{ilkj}) y_k(t_0) y_l(t_0)] x_j(t). \tag{7.19}$$

Equation 7.19 can be written in the form

$$\dot{x_i} = \sum_{j=1}^{N} K_{ij} x_j + M_i. \tag{7.20}$$

Equation 7.20 defines a linear system of coupled first order differential equations, with

$$x_i(t_0) = 0. \tag{7.21}$$

The solution for equation 7.20 is obtained in the following way. The matrix K_{ij} is diagonalised through a similarity transformation

$$\gamma_{il}^d = \sum_{jk} Q_{ij}^{-1} K_{jk} Q_{kl}, \tag{7.22}$$

where Q_{ij} is the matrix of eigenvectors obtained from the matrix K_{ij}. γ_{ij}^d is a diagonal matrix with diagonal matrix elements given by the eigenvalues of K_{ij}. Equation 7.20 can be transformed to

$$\sum_j Q_{ij}^{-1} \dot{x_j} = \sum_{jkm} Q_{ij}^{-1} K_{jk} Q_{kl} Q_{lm}^{-1} x_m + \sum_j Q_{ij}^{-1} M_j, \tag{7.23}$$

by premultiplying equation 7.20 by Q_{ij}^{-1}. Equation 7.23 can be rewritten in the simplified form

$$\dot{X}_i = \sum_j \gamma_{ij}^d X_j + m_i, \tag{7.24}$$

where $X_i = \sum_j Q_{ij}^{-1} x_j$ and $m_i = \sum_j Q_{ij}^{-1} M_i$.

Equation 7.24 can now be written as

$$\dot{X}_i - \sum_j \gamma_{ij}^d X_j = m_i. \tag{7.25}$$

Premultiplying equation 7.24 by the matrix $\exp[-\gamma_{ij}^{d}(t-t_0)]$, which has the form

$$e^{-\gamma_{ij}^{d}(t-t_0)} = \begin{pmatrix} e^{-\gamma_1(t-t_0)} & 0 & 0 & \cdots \\ 0 & e^{-\gamma_2(t-t_0)} & 0 & \cdots \\ 0 & 0 & e^{-\gamma_3(t-t_0)} & \cdots \\ \vdots & \vdots & \vdots & \end{pmatrix} \tag{7.26}$$

gives

$$\sum_j e^{-\gamma_{ij}^{d}(t-t_0)}\dot{X}_j - \sum_{jk} e^{-\gamma_{ij}^{d}(t-t_0)}\gamma_{jk}^{d}X_k = \sum_j e^{-\gamma_{ij}^{d}(t-t_0)}m_j. \tag{7.27}$$

Equation 7.27 can be written as

$$\frac{d}{dt}\left(\sum_j e^{-\gamma_{ij}^{d}(t-t_0)}X_j\right) = \sum_j e^{-\gamma_{ij}^{d}(t-t_0)}m_j, \tag{7.28}$$

which can be integrated to

$$\sum_j e^{-\gamma_{ij}^{d}(t-t_0)}X_j = C_i - \sum_{jk} e^{-\gamma_{ij}^{d}(t-t_0)}(\gamma_{jk}^{d})^{-1}m_k. \tag{7.29}$$

C_i is a constant matrix independent of time, and $(\gamma_{ij}^{d})^{-1}$ is the inverse of γ_{ij}^{d}, containing only diagonal matrix elements that are of the form

$$(\gamma_{ij}^d)^{-1} = \begin{pmatrix} \frac{1}{\gamma_1} & 0 & 0 & \cdots \\ 0 & \frac{1}{\gamma_2} & 0 & \cdots \\ 0 & 0 & \frac{1}{\gamma_3} & \cdots \\ \vdots & \vdots & \vdots & \end{pmatrix}. \tag{7.30}$$

Premultiplying equation 7.29 by $\exp(\gamma_{ij}^d(t-t_0)$ yields the following expression for X_i,

$$X_i(t) = \sum_j e^{\gamma_{ij}^d(t-t_0)} C_j - \sum_j (\gamma_{ij}^d)^{-1} m_j. \tag{7.31}$$

$x_i(t)$ can now be obtained by premultiplying the above equation by Q_{ij}, and substituting $m_i = \sum_j Q_{ij}^{-1} M_j$ back into the equation to give

$$x_i(t) = \sum_{jk} Q_{ij} e^{\gamma_{jk}^d(t-t_0)} C_k - \sum_{jkl} Q_{ij} (\gamma_{jk}^d)^{-1} Q_{kl}^{-1} M_l. \tag{7.32}$$

Applying the initial conditions (equation 7.21) yields the solution

$$x_i(t) = \sum_{jklm} Q_{ij} [e^{\gamma_{jk}^d(t-t_0)} - \delta_{jk}] (\gamma_{kl}^d)^{-1} Q_{lm}^{-1} M_m. \tag{7.33}$$

The linearised solution for $x_i(t)$ is in the form of an eigenvalue-eigenvector decomposition of K_{ij}, and involving the vector M_i. For small times t, equation 7.33 behaves like

$$x_i(t) = M_i(t - t_0)$$

as expected.

In order to find the projection of the solution vector $x_i(t)$ onto the eigenvectors, we write

$$x_i(t) = \sum_j Q_{ij} a_j(t). \tag{7.34}$$

$a_i(t)$ is the time dependent projection of the solution vector $x_i(t)$ onto the eigenvectors, and Q_{ij} is the eigenvector matrix. $a_i(t)$ is found by premultiplying the above equation by Q_{ij}^{-1} to give

$$\sum_{jk} Q_{ij}^{-1} Q_{jk} a_k(t) = \sum_j Q_{ij}^{-1} x_j(t) \tag{7.35}$$

yielding

$$a_i(t) = \sum_j Q_{ij}^{-1} x_j(t). \tag{7.36}$$

$$a_i(t) = \sum_{jkl} [e^{\gamma_{ij}^d (t-t_0)} - \delta_{ij}](\gamma_{jk}^d)^{-1} Q_{kl}^{-1} M_l. \tag{7.37}$$

Mathematical systems of this sort are dynamic in the sense that the linearised solution derived above reflects not only the reaction chemistry, but also the response of the system to changes in the variables of state, such as changes in temperature, pressure and volume. A study of the evolution of the eigenvalues, eigenvectors and consequent solution vector therefore provides important information on the qualitative behaviour of the system.

The behaviour of the eigenmodes determine the concentration behaviour of the system. When analysing a mathematical system of this sort, the important components to look out for are the projections of the solution vector onto the eigenvectors, and the corresponding eigenvalues. The modes that dominate the system are those whose rates of production of species are largest. Clearly the eigenmodes i for which $c_i = \dot{a}_i(t_0)$ are largest dominate the system.

Once the dominant eigenmodes have been determined, then it becomes necessary to examine the corresponding eigenvalues. Those eigenvalues that are distinct, real, large and positive define the separate exponentially increasing modes of the chemical system. Exponentially increasing coupled oscillatory modes are also found, and exhibit themselves as eigenmodes with eigenvalues that are complex conjugates of each other, with the real part large and positive.

Evanescent, or decaying eigenmodes, both distinct and coupled oscillatory modes, are described by eigenvalues that are either separate and real, or coupled complex conjugate pairs, with the real part of the eigenvalue negative.

The expectation is that in a system where radical multiplication takes place, only a small number of independent modes will have eigenvalues with positive real parts. The process of branching, which is of central importance in understanding autoignition, can then be understood in terms of the development of these modes, rather than a large system of coupled reaction equations.

In mathematical systems of this kind, it may happen that at some point in the evolution of the system, the solution abruptly changes its analytic structure. The equilibrium point in the generalised phase space describing the system is then said to have undergone a bifurcation, and this change reveals a qualitative change in the evolution of the system. Bifurcations are identified as follows:

no functional mapping exists to map the form of the solution prior to the bifurcation to the solution after the bifurcation. Pseudo-bifurcations occur when the solutions change structure, but a functional mapping can be found to map the solution prior to the pseudo-bifurcation to the solution after the pseudo-bifurcation.

By examining closely the detailed mechanism around the bifurcation and pseudo-bifurcation points, the reasons for the bifurcations, and hence the source of the corresponding change in the chemistry, can be revealed.

7.3 Programming Features

A program called CHEMMODE was written to calculate numerical expressions for $x_i(t)$ and $a_i(t)$. The output of HOMINP and HOMCHEM includes local concentrations, temperatures, pressures, rate constants, and reaction stoichiometric coefficients. CHEMMODE reads in this data, prepares the matrix K_{ij} and the vector M_i, and then proceeds to diagonalise K_{ij}. The elements of K_{ij} are all real, with the consequence that the eigenvalues and eigenvector components must be real, or that the eigenvalues and eigenvectors must appear as complex conjugate pairs, in order that a real solution for $x_i(t)$ is able to be constructed. This requirement is a consequence of the characteristic equation for matrix K_{ij},

$$\det(K_{ij} - \gamma\delta_{ij}) = 0. \tag{7.38}$$

The above equation can be written in the form

$$\gamma^n + a_1\gamma^{n-1} + a_2\gamma^{n-2} + \cdots + a_n = 0 \tag{7.39}$$

which can be factored to

$$(\gamma_1 - b_1)(\gamma_2 - b_2)(\gamma_3 - b_3)\cdots(\gamma_n - b_n) = 0. \tag{7.40}$$

In order for expression 7.40 to be real and identically zero, the eigenvalues must either be real or appear in groups of two as complex conjugate pairs.

The similarity transformation of matrix K_{ij} must produce a diagonal matrix with matrix elements given by the eigenvalues of K_{ij}, which are either real, or appear as complex conjugate pairs. The real eigenvalues must have corresponding eigenvectors with real components, while the complex conjugate eigenvalues must have complex conjugate eigenvectors for a proper diagonalisation.

The diagonalisation subroutine must be able to identify the coupled complex conjugate terms in the characteristic equation, and appropriately reduce the matrix with complex diagonal matrix elements.

As the matrix K_{ij} is real and unsymmetric, there is no guarantee that a complete set of eigenvectors for K_{ij} exists. The diagonalisation subroutine used here finds all of the eigenvalues of K_{ij}, and then attempts to find a complete set of eigenvectors.

Numerical matrix methods of finding eigenvalues have errors that are generally proportional to the Euclidean norm of the matrix (the norm of a matrix is the square root of the sum of squares of the elements). The diagonalisation

subroutine first balances the matrix by using similarity transformations to make corresponding rows and columns have comparable norms, in order to reduce the overall norm of the matrix while leaving the eigenvalues unchanged.

Following this, the subroutine reduces the balanced matrix to upper Hessenberg form using a similarity transformation procedure analogous to Gaussian elimination with pivoting. (An upper Hessenberg matrix has zeros everywhere below the diagonal except for the subdiagonal row.) The similarity transformation is performed in stages. The i'th stage consists of first finding the element of maximum magnitude in the i'th column below the diagonal. If this element is in row k, then pivot the matrix by interchanging the k'th row of elements with the $i+1$'th row, and make a similarity transformation by interchanging the k'th column with the $i+1$'th column. This is followed by Gauss elimination of the i,k matrix element for $i = k+1, k+2, ..., N$, and addition of the product of the elimination multiplier and the elements of column i, to the elements of column $k+1$.

Now that the matrix is in Hessenberg form, the subroutine uses a QR algorithm with shifts to find the eigenvalues. If the Hessenberg matrix is H_{ij}, then the QR transformation involves factoring the matrix $H_{ij} - s_0\delta_{ij}$, where s_0 is a suitably chosen shift parameter, into a unitary matrix Q_{ij}, and an upper-triangular matrix R_{ij}, and then finding the similarity matrix $A^{(1)}_{il} = \sum_{jk} Q^{-1}_{ij} H_{jk} Q_{kl}$. This similarity transformation is repeated with $A^{(1)}_{il} - s_1\delta_{il}$ to give another similar matrix $A^{(2)}_{ij}$. This process is repeated k times until $A^{(k)}_{ij}$ converges to an upper-triangular matrix whose diagonal elements are just the eigenvalues of the original matrix K_{ij}. The subroutine then finds the eigenvectors of matrix K_{ij} using Gaussian elimination with pivoting.

Following the diagonalisation of matrix K_{ij}, CHEMMODE then calculates $x_i(t)$ and $a_i(t)$ for the output times specified by HOMCHEM and chosen by

the user. In this way the mechanism analysis is elucidated by a qualitative linear analysis of the analytic structure of the non-linear system of reaction equations.

7.4 Mode Analysis of Autoignition

This part of the thesis discusses the numerical linearised solutions to the different mechanisms examined in Chapter 5. Section 1 discusses the linearised solution of methanol autoignition in detail, using a stripped down version of the Gr92 mechanism, consisting of 188 reactions involving 21 species. This mechanism will be called the Gr92r mechanism, and is presented in Appendix (3). Section 2 compares this linearised solution of methanol autoignition with the linearised solution of autoignition using the Gr89 mechanism and the ND89 mechanism.

It must be realised that the eigenvector components do not give a realistic set of chemical reaction equations directly, but they do give the linearised rate of production and consumption of species associated with the given eigenmode.

In the following analysis, the γ_i represent the eigenvalues of the eigenmodes, and the c_i are the rates of production of species associated with the specified mode at time t_0, and is given by $c_i = \sum_j Q_{ij}^{-1} M_j$. The tables present the eigenvector components for the chemically important and distinguishing species, and omit the less important species.

The behaviour of the hydroxyl radical is omitted from the following eigenmode analysis. Its reactivity in the autoignition system is very high, with the consequence that the eigenvector elements for hydroxyl radicals are always very small. Furthermore, as autoignition progresses, other reaction pathways for

the formation of hydroxyl radicals develop, and so the hydroxyl radical concentration increases monotonically up to 2400K. Thus there is little to be gained by including the evolution of the hydroxyl radical concentration explicitly in the eigenmode analysis.

Figures 7.2(a), 7.2(b), and 7.2(c) represent the evolution of the major species concentrations, the intermediate species concentrations, and the temperature of the autoignition system. Figure 7.2(a) shows the full evolution of the temperature, while figures 7.2(b) and 7.2(c) show the temperature evolution truncated at 1442K, in order to concentrate on the detail of the temperature change and the time scale over which the autoignition system changes qualitatively.

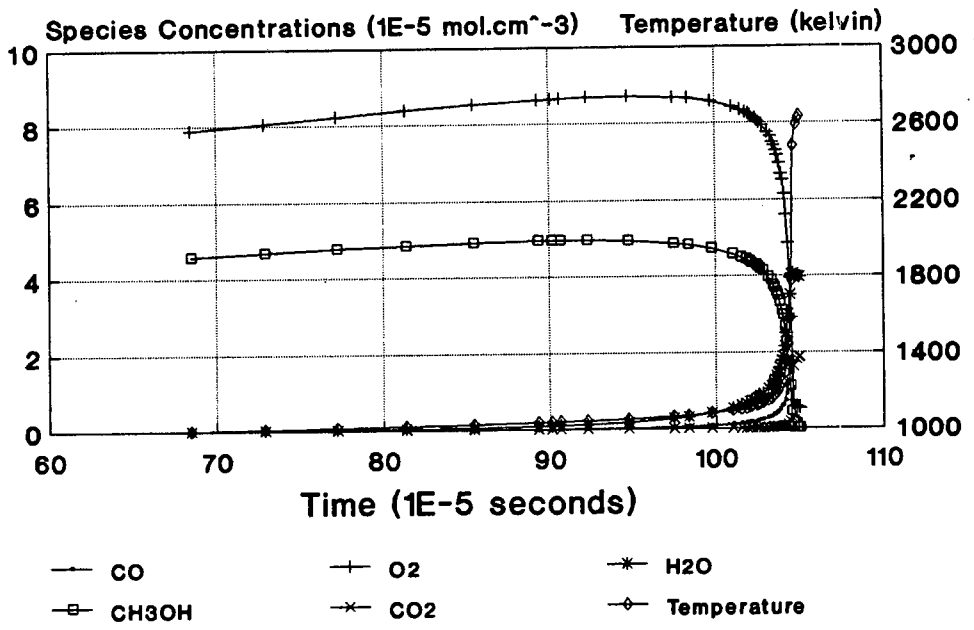

Figure 7.2(a): Major Species and Temperature Evolution as a Function of Time

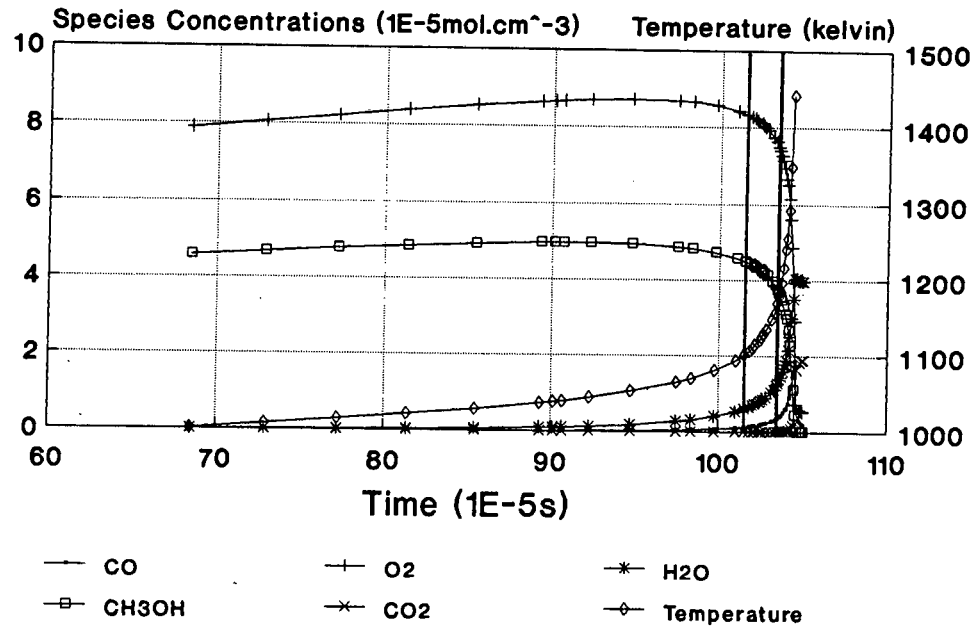

Figure 7.2(b): Major Species and Temperature Evolution (Temperature truncated at 1442K, qualitative changes shown by vertical lines)

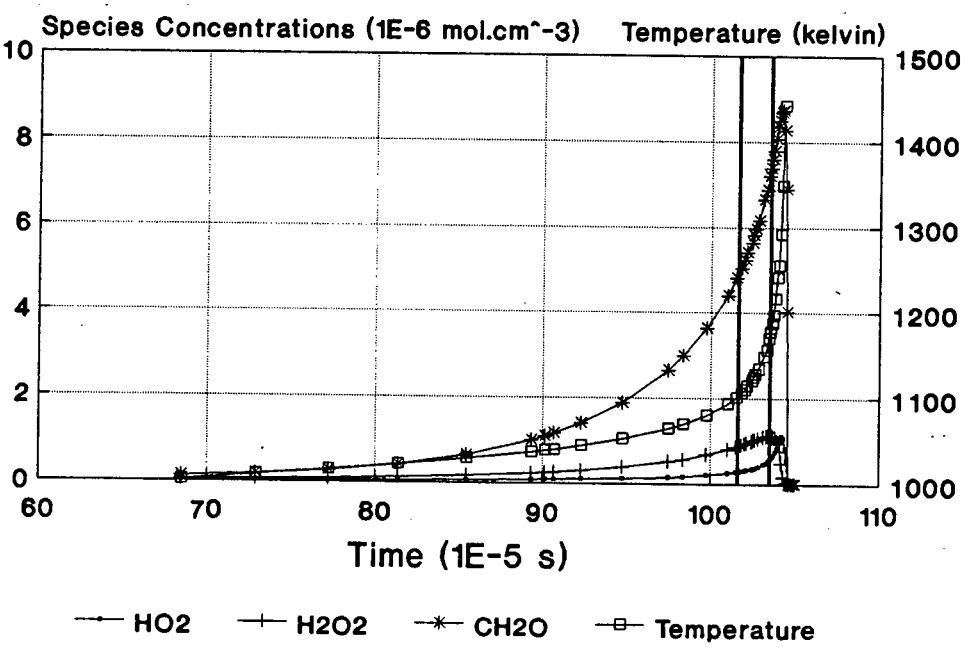

Figure 7.2(c): Intermediate Species and Temperature Evolution (Temperature truncated at 1442K, qualitative changes shown by vertical lines)

The behaviour of the linear solutions was qualitatively the same for the different mechanisms studied. There are three distinct regions to the linearised solution.

7.4.1 A Detailed Linear Mode Analysis of Methanol Autoignition using a Reduced Gr92 Mechanism

T < 1100K, P < 43.0bar

In the low temperature part of this regime (~980K), there are three eigenmodes dominating the local evolution of the concentration vector. Two of these eigenmodes have distinct, positive eigenvalues, denoting two explosive modes, and the third is an evanescent mode. The corresponding eigenvectors reflect the linearised rates of production and consumption of species.

t = 0.532 ms, T = 978K, P = 31.6bar

eigenvector 1: $\gamma_1 = 3965 s^{-1}$, $c_1 = 549.8 mol.m^{-3}s^{-1}$

CO	O_2	H_2	HO_2	H_2O_2	H_2O	CH_3OH	CO_2	CH_2O
.009	-.403	.011	.055	.149	.398	-.576	.000	.567

eigenvector 2: $\gamma_2 = -153.5 s^{-1}$, $c_2 = 132.0 mol.m^{-3}s^{-1}$

CO	O_2	H_2	HO_2	H_2O_2	H_2O	CH_3OH	CO_2	CH_2O
.219	.158	-.004	.002	.005	-.320	.528	-.008	-.739

eigenvector 3: $\gamma_3 = 1.84 s^{-1}$, $c_3 = -103.3 mol.m^{-3}s^{-1}$

CO	O_2	H_2	HO_2	H_2O_2	H_2O	CH_3OH	CO_2	CH_2O
.086	-.500	.013	.000	.000	.724	-.377	.276	.015

Eigenmode 1 dominates the system at this time, having both the largest rate of production, and the largest eigenvalue. The system is essentially one-dimensional, and the equilibrium point is an unstable node. The dominant eigenmode describes the oxidation of methanol by oxygen, forming water, formaldehyde, hydrogen peroxide, and small amounts of carbon monoxide and hydroperoxyl radical.

Eigenmode 2 is decaying rapidly, and will quickly die out. This mode describes a small correction to mode 1, which overstates formaldehyde production, and methanol and oxygen consumption, and understates carbon monoxide production.

Eigenmode 3 is slow at this stage, though it has a positive real eigenvalue. It competes weakly with mode 1.

As the temperature increases beyond 1000K, a fourth exponentally increasing mode appears, but this mode lasts only a very short time before its eigenvalue changes from positive to negative, and then dies out.

t = 0.685 ms, T = 1001K, P = 35.1bar

eigenvector 1: $\gamma_1 = 4557 s^{-1}$, $c_1 = 2682 mol.m^{-3}s^{-1}$

CO	O_2	H_2	HO_2	H_2O_2	H_2O	CH_3OH	CO_2	CH_2O
.026	-.371	.013	.030	.108	.465	-.575	.000	.550

eigenvector 2: $\gamma_2 = -627.5s^{-1}$, $c_2 = 634.2mol.m^{-3}s^{-1}$

CO	O_2	H_2	HO_2	H_2O_2	H_2O	CH_3OH	CO_2	CH_2O
.165	.180	-.006	.004	.012	-.386	.542	-.007	-.705

eigenvector 3: $\gamma_3 = 6.5s^{-1}$, $c_3 = -372.7mol.m^{-3}s^{-1}$

CO	O_2	H_2	HO_2	H_2O_2	H_2O	CH_3OH	CO_2	CH_2O
-.016	-.400	.009	.000	.000	.818	-.413	-.019	-.002

eigenvector 4: $\gamma_4 = 52.72s^{-1}$, $c_4 = -120.4mol.m^{-3}s^{-1}$

CO	O_2	H_2	HO_2	H_2O_2	H_2O	CH_3OH	CO_2	CH_2O
.787	-.276	.010	.000	.000	.267	-.276	.289	.272

Eigenmode 4 corrects the other modes by reducing carbon monoxide, carbon dioxide, and water concentrations, and increasing oxygen and methanol concentrations.

t = 0.854 ms, T = 1028K, P = 39.2bar

eigenvector 1: $\gamma_1 = 5800s^{-1}$, $c_1 = 16440mol.m^{-3}s^{-1}$

CO	O_2	H_2	HO_2	H_2O_2	H_2O	CH_3OH	CO_2	CH_2O
.088	-.372	.017	.015	.081	.550	-.565	.000	.475

eigenvector 3: $\gamma_3 = 46.2s^{-1}$, $c_3 = -2817mol.m^{-3}s^{-1}$

CO	O_2	H_2	HO_2	H_2O_2	H_2O	CH_3OH	CO_2	CH_2O
-.058	-.388	.008	.000	.001	.824	-.405	-.052	-.021

eigenvector 2: $\gamma_2 = -2894s^{-1}$, $c_2 = 1422mol.m^{-3}s^{-1}$

CO	O_2	H_2	HO_2	H_2O_2	H_2O	CH_3OH	CO_2	CH_2O
.152	.177	-.006	.006	.031	-.425	.542	-.003	-.686

eigenvector 4: $\gamma_4 = 144.2s^{-1}$, $c_4 = -1063mol.m^{-3}s^{-1}$

CO	O_2	H_2	HO_2	H_2O_2	H_2O	CH_3OH	CO_2	CH_2O
.726	-.313	.015	-.001	-.002	.295	-.299	.342	.283

The system remains dominated by eigenmode 1, which continues to describe the oxidation of methanol by molecular oxygen to form water, formaldehyde, and small amounts of hydroperoxyl radical, hydrogen peroxide and carbon monoxide. Note that eigenmode 3 from the previous page has taken over from eigenmode 2 in importance.

Eigenmode 4 continues to correct the other modes for the over-consumption of methanol and oxygen, and for the overproduction of formaldehyde, carbon monoxide, water, and carbon dioxide.

t = 0.948 ms, T = 1052K, P = 41.4bar

eigenvector 1: $\gamma_1 = 7682s^{-1}$, $c_1 = 61250mol.m^{-3}s^{-1}$

CO	O_2	H_2	HO_2	H_2O_2	H_2O	CH_3OH	CO_2	CH_2O
.174	-.395	.022	.011	.070	.623	-.540	.006	.359

eigenvector 3: $\gamma_3 = 249s^{-1}$, $c_3 = -18400mol.m^{-3}s^{-1}$

CO	O_2	H_2	HO_2	H_2O_2	H_2O	CH_3OH	CO_2	CH_2O
.188	-.465	.015	.000	.002	.746	-.397	.182	.025

eigenvector 4: $\gamma_4 = -224.8s^{-1}$, $c_4 = -4415mol.m^{-3}s^{-1}$

CO	O_2	H_2	HO_2	H_2O_2	H_2O	CH_3OH	CO_2	CH_2O
.631	.375	.008	.000	-.002	-.084	.046	-.673	.006

eigenvector 2: $\gamma_2 = -7176s^{-1}$, $c_2 = 1629mol.m^{-3}s^{-1}$

CO	O_2	H_2	HO_2	H_2O_2	H_2O	CH_3OH	CO_2	CH_2O
-.149	-.169	.005	-.007	-.046	.440	-.538	.005	.681

The first exponentially increasing mode still dominates the other modes, and therefore the chemistry, in this regime. The chemistry reflected by this mode involves the chemically explosive oxidation of methanol by oxygen and related radicals, to water and formaldehyde, with a net production of hydrogen peroxide, hydroperoxyl and hydroxyl radicals.

The second eigenmode (eigenvector 3) is growing in importance in terms of competition with mode 1, as its rate of production of species is negative, and the magnitude of rate of production is increasing rapidly relative to mode 1. It corrects mode 1 for the overproduction of water and carbon monoxide, and over-consumption of oxygen and methanol. This mode also serves to reduce the level of carbon dioxide produced in mode 3.

Note that the third eigenmode above (eigenvector 4) has taken over from the fourth eigenmode (eigenvector 2), and its eigenvalue has changed from being

real and positive, to real and negative. This mode describes the consumption of carbon monoxide and oxygen to form carbon dioxide.

As the temperature of the system approaches 1060K, the last two of the four dominant modes collapse, leaving the two exponentially increasing competitive modes to dominate the system until autoignition occurs. Ignoring the smaller modes, and concentrating on the dominant modes, the system is qualitatively described by a two mode solution, which is of the form

$$x_n(t) \approx (e^{\gamma_1(t-t_0)} - 1)\frac{c_1\lambda_{1n}}{\gamma_1} + (e^{\gamma_2(t-t_0)} - 1)\frac{c_2\lambda_{2n}}{\gamma_2}, \qquad (7.41)$$

for two real, independent eigenmodes, where λ_{mn} is the eigenvector corresponding to mode m with components defined by n, and c_m is the overall rate of production of species for the m'th mode.

Qualitatively, the system is two-dimensional in nature, but mostly dominated by the first mode discussed above. The equilibrium point is an unstable improper node, and the solution of both the linear system and the non-linear system diverge from the equilibrium point with time.

t = 0.984 ms, T = 1069K, P = 42.4bar

eigenvector 1: $\gamma_1 = 8637s^{-1}$, $c_1 = 1.426 \times 10^5 mol.m^{-3}s^{-1}$

CO	O_2	H_2	HO_2	H_2O_2	H_2O	CH_3OH	CO_2	CH_2O
.233	-.406	.026	.008	.058	.668	-.510	.013	.265

eigenvector 3: $\gamma_3 = 715.5s^{-1}$, $c_3 = -58480 mol.m^{-3}s^{-1}$

CO	O_2	H_2	HO_2	H_2O_2	H_2O	CH_3OH	CO_2	CH_2O
.232	-.448	.019	.000	.005	.749	-.404	.140	.030

eigenvector 4: $\gamma_4 = -406.8s^{-1}$, $c_4 = -9539mol.m^{-3}s^{-1}$

CO	O_2	H_2	HO_2	H_2O_2	H_2O	CH_3OH	CO_2	CH_2O
.641	.363	.004	-.000	-.002	-.061	.039	-.673	.005

eigenvector 2: $\gamma_2 = -11830s^{-1}$, $c_2 = 7580mol.m^{-3}s^{-1}$

CO	O_2	H_2	HO_2	H_2O_2	H_2O	CH_3OH	CO_2	CH_2O
-.146	-.166	.004	-.008	-.054	.450	-.536	.006	.676

t = 1.010 ms, T = 1093K, P = 43.0bar

eigenvector 1: $\gamma_1 = 7764s^{-1}$, $c_1 = 6.408 \times 10^5 mol.m^{-3}s^{-1}$

CO	O_2	H_2	HO_2	H_2O_2	H_2O	CH_3OH	CO_2	CH_2O
.290	-.413	.030	.005	.033	.717	-.459	.033	.135

eigenvector 2: $\gamma_2 = 3159s^{-1}$, $c_2 = -4.615 \times 10^5 mol.m^{-3}s^{-1}$

CO	O_2	H_2	HO_2	H_2O_2	H_2O	CH_3OH	CO_2	CH_2O
.286	-.424	.026	.002	.013	.742	-.421	.077	.056

The two competing exponentially increasing modes that dominate the qualitative behaviour of the system in this temperature regime are now of similar

importance, since the rates of production of species from the two dominant modes are of opposite sign, and approximately equal magnitude. Chemically, the dominant mode develops from the hydrogen abstraction reaction of the hydroperoxyl radical with methanol, to form hydrogen peroxide and CH_2OH, plus the hydrogen abstraction reaction of hydroperoxyl with formaldehyde, to form CHO and hydrogen peroxide, and the subsequent branching thermal decomposition of hydrogen peroxide to hydroxyl radicals.

The competitive second mode develops with the formation of large quantities of hydroperoxyl radical in the system. The hydroperoxyl radicals react with other hydroperoxyl radicals preferentially in a terminating reaction, to form O_2 and hydrogen peroxide. The hydrogen peroxide subsequently thermally decomposes to hydroxyl radicals.

The hydrogen abstraction reaction from methanol and formaldehyde, and the hydroperoxyl on hydroperoxyl reaction compete with each other for hydroperoxyl radicals, through the set of reactions

$$CH_3OH + HO_2 \rightarrow CH_2OH + H_2O_2 \tag{7.42}$$

$$CH_2O + HO_2 \rightarrow CHO + H_2O_2 \tag{7.43}$$

$$HO_2 + HO_2 \rightarrow H_2O_2 + O_2 \tag{7.44}$$

$$H_2O_2 + M' \rightarrow OH + OH + M'. \tag{7.45}$$

The linear modal solution of the chemical rate equations reflects this competition for hydroperoxyl radical in terms of the two competitive exponentially increasing modes shown above. These two dominant real modes converge as the coupled termination-branching reaction sequence 7.44 and 7.45 compete successfully for hydroperoxyl radicals against the coupled propagation-branching reaction sequence 7.42 7.43, and 7.45.

1100K < T < 1160K, 43.0bar < P < 43.6bar

This temperature regime sees the equilibrium point undergoing a bifurcation from an unstable improper node structure to an unstable focus, through the two competing real, positive exponential modes becoming complex conjugate pairs. The bifurcation of the equilibrium point in the generalised phase space of the chemical system marks the point where the two competitive modes become exponentially increasing, oscillatory modes.

The evolving coupled modes are related to the oxidation reactions of methanol to formaldehyde to carbon monoxide, and the heat from these reactions is now sufficient to heat the end-gas methanol/air mixture to autoignition.

The coupled second mode, which describes the competitive effect of the coupled termination-branching sequence 7.44 and 7.45 on the propagation-branching sequence 7.42, 7.43, and 7.45 causes the chemical system to change from one which is chemically explosive, to one which propagates. This change in the chemistry is reflected by the bifurcation in the equilibrium point from an unstable node to an unstable focus, and occurs at the inflection point of the evolution curve of the hydrogen peroxide concentration. In other words, the change in the structure of the chemical rate equations (the bifurcation of the equilibrium point) occurs when the second time derivative of the hydrogen

peroxide concentration is zero. The point in time when the bifurcation occurs is shown in figures 7.2 (a) and 7.2 (b) by the first vertical line along the time axis, occurring at time $t = 1.018$ ms. The unstable focus indicates that the chemical system diverges from the equilibrium point along an outward spiral.

In this temperature and pressure regime, only the two coupled modes are presented, for the complex strengths of these modes have magnitudes ten to twenty times larger than the next largest mode. Therefore, these two coupled modes dominate the linear solution space of the chemical system. If the eigenvalues of the coupled exponentially increasing, oscillatory modes are $\gamma + i\omega$ and $\gamma - i\omega$ respectively, the coupled two mode solution vector has the form

$$x_n(t) \approx a_1(t)\lambda_{1n} + a_2(t)\lambda_{2n} \tag{7.46}$$

$$= [e^{(\gamma+i\omega)t} - 1]\frac{(c_r + ic_i)(\lambda_{rn} + i\lambda_{in})}{\gamma + i\omega} + [e^{(\gamma-i\omega)t} - 1]\frac{(c_r - ic_i)(\lambda_{rn} - i\lambda_{in})}{\gamma - i\omega}, \tag{7.47}$$

where λ_{rn} and λ_{in} are the real and imaginary components of the eigenvector $\vec{\lambda}$, c_r and c_i are the time independent real and imaginary components of the strength coefficient $a_m(t)$. This equation finally becomes

$$x_n(t) = \frac{2(e^{\gamma t}\cos\omega t - 1)[\lambda_{rn}(c_r\gamma + c_i\omega) - \lambda_{in}(c_i\gamma - c_r\omega)]}{\gamma^2 + \omega^2}$$
$$- \frac{2e^{\gamma t}\sin\omega t[\lambda_{in}(c_r\gamma + c_i\omega) + \lambda_{rn}(c_i\gamma - c_r\omega)]}{\gamma^2 + \omega^2}. \tag{7.48}$$

The solution $x_n(t)$ increases exponentially with time dependence given by the real part γ, and simultaneously oscillates with frequency ω.

t = 1.018 ms, T = 1106K, P = 43.2bar

eigenvector 1: $\gamma_1 = 5601 + i4047 s^{-1}$, $c_1 = 2.535 \times 10^5 - i5.018 \times 10^5 mol.m^{-3}s^{-1}$

CO	O_2	H_2	HO_2	H_2O_2
.304-.070i	-.397+.104i	.031-.004i	.003+.001i	.021+.009i

H_2O	CH_3OH	CO_2	CH_2O
.709-.190i	-.423+.076i	.037-.039i	.081+.034i

eigenvector 2: $\gamma_2 = 5601 - i4047 s^{-1}$, $c_2 = -5.018 \times 10^5 + i2.535 \times 10^5 mol.m^{-3}s^{-1}$

CO	O_2	H_2	HO_2	H_2O_2
.070-.304i	-.104+.397i	.004-.031i	-.001-.003i	-.009-.021i

H_2O	CH_3OH	CO_2	CH_2O
.190-.709i	-.076+.423i	.039-.037i	-.034-.081i

t = 1.028 ms, T = 1134K, P = 43.5bar

eigenvector 1: $\gamma_1 = 5010 + i11930 s^{-1}$, $c_1 = 2.260 \times 10^5 - i5.403 \times 10^5 mol.m^{-3}s^{-1}$

CO	O_2	H_2	HO_2	H_2O_2
.350+.021i	-.392-.004i	.039+.009i	.001+.005i	.008+.024i

H_2O	CH_3OH	CO_2	CH_2O
.736-.001i	-.405-.062i	.029-.049i	.026+.091i

eigenvector 2: $\gamma_2 = 5010 - i11930 s^{-1}$, $c_2 = 5.403 \times 10^5 - i2.260 \times 10^5 mol.m^{-3}s^{-1}$

CO	O_2	H_2	HO_2	H_2O_2
.021+.350i	-.004-.392i	.009+.039i	.005+.001i	.024+.008i

H_2O	CH_3OH	CO_2	CH_2O
-.001+.736i	-.062-.405i	-.049+.029i	.091+.026i

t = 1.033 ms, T = 1156K, P = 43.6bar

eigenvector 1: $\gamma_1 = 2570+i20170s^{-1}$, $c_1 = -5.548\times10^5-i5.208\times10^5 mol.m^{-3}s^{-1}$

CO	O_2	H_2	HO_2	H_2O_2
.075+.370i	-.095-.365i	-.002+.047i	-.006+.002i	-.026+.008i

H_2O	CH_3OH	CO_2	CH_2O
.196+.709i	-.033-.394i	.058+.002i	-.102+.023i

eigenvector 2: $\gamma_2 = 2570-i20170s^{-1}$, $c_2 = 5.208\times10^5+i5.548\times10^5 mol.m^{-3}s^{-1}$

CO	O_2	H_2	HO_2	H_2O_2
.370+.075i	-.365-.094i	.047-.002i	.002-.006i	.008-.026i

H_2O	CH_3OH	CO_2	CH_2O
.709+.196i	-.394-.033i	.002+.058i	.023-.102i

Examining the evolution of the coupled complex eigenvalues reveals that the rate of exponential increase decreases with time, and the frequency of oscillation increases relative to the rate of exponential increase. The time scales defined by the dominant coupled eigenvalues and the evolution of the chemistry result in there not being enough time for the system to pass through

a single oscillation before a second qualitative transition takes place. Chemically, this means that the net rate of production of radicals in the methanol/air oxidation system begins to decrease.

T > 1160K, P > 43.6bar

This temperature and pressure region defines the autoignition regime. Mathematically, the equilibrium points of the linear and the non-linear system undergo a pseudo-bifurcation from an unstable focus to a centre, and then to a stable focus. These changes are a consequence of the sudden change of the coupled exponentially increasing, oscillatory modes to coupled, exponentially decaying, oscillatory modes. This means that the chemical system will now converge towards its equilibrium point, along an inward spiral. As this transition takes place, other real evanescent modes are introduced that are also important in the evolution of the system.

The pseudo-bifurcation of the equilibrium point from an unstable focus to a stable focus occurs when hydrogen peroxide reaches its maximum concentration, or in other words, when the first time derivative of the hydrogen peroxide concentration is zero. This is shown by the second vertical line along the time axis in figures 7.2 (a) and 7.2 (b). This point in time can be used to define the autoignition point.

Chemically, the system is now described in terms of the termination-branching reaction sequence 7.44 and 7.45. The intermediate chemical species (apart from hydrogen peroxide) quickly reach their maximum concentrations, followed by the collapse of the radical pool and simultaneous thermal explosion, through the rapid oxidation of methanol by hydroxyl radicals and molecular oxygen to formaldehyde and water, followed by the oxidation of formaldehyde

to carbon monoxide. The rapid release of heat into the end-gas mixture causes the temperature of the gas to rise far more rapidly than the rate of increase of the external pressure. Consequently, the gas expands rapidly, and the species concentrations decrease.

t = 1.035 ms, T = 1177K, P = 43.7bar

eigenvector 1: $\gamma_1 = -1656+i29750s^{-1}$, $c_1 = -8.579\times10^5-i5.082\times10^5 mol.m^{-3}s^{-1}$

CO	O_2	H_2	HO_2	H_2O_2
-.031+.397i	.010-.365i	-.020+.052i	-.007-.001i	-.027-.005i

H_2O	CH_3OH	CO_2	CH_2O
-.008+.734i	.084-.376i	.058+.008i	-.112-.029i

eigenvector 2: $\gamma_2 = -1656-i29750s^{-1}$, $c_2 = 5.208\times10^5+i5.548\times10^5 mol.m^{-3}s^{-1}$

CO	O_2	H_2	HO_2	H_2O_2
.397-.031i	-.365+.010i	.052-.020i	-.001-.007i	-.005-.027i

H_2O	CH_3OH	CO_2	CH_2O
.734+.008i	-.376+.084i	.008+.058i	-.029-.112i

eigenvector 3: $\gamma_3 = -97270s^{-1}$, $c_3 = 1.704\times10^5 mol.m^{-3}s^{-1}$

CO	O_2	H_2	HO_2	H_2O_2	H_2O	CH_3OH	CO_2	CH_2O
-.595	-.198	-.005	-.018	-.073	.571	-.534	.009	.584

eigenvector 4: $\gamma_4 = -4368s^{-1}$, $c_4 = 1.532\times10^5 mol.m^{-3}s^{-1}$

CO	O_2	H_2	HO_2	H_2O_2	H_2O	CH_3OH	CO_2	CH_2O
-.675	-.313	.013	.000	.003	-.033	-.004	.667	-.013

t = 1.039 ms, T = 1241K, P = 43.8bar

eigenvector 1: $\gamma_1 = -38220 + i71030 s^{-1}$, $c_1 = -1.703 \times 10^5 - i2.116 \times 10^6 mol.m^{-3}s^{-1}$

CO	O_2	H_2	HO_2	H_2O_2
.326+.319i	-.244-.221i	.036+.085i	-.011+.002i	-.026+.005i

H_2O	CH_3OH	CO_2	CH_2O
.539+.478i	-.194-.299i	.024-.050i	-.156+.031i

eigenvector 2: $\gamma_2 = -38220 - i71030 s^{-1}$, $c_2 = 2.116 \times 10^6 + i1.703 \times 10^5 mol.m^{-3}s^{-1}$

CO	O_2	H_2	HO_2	H_2O_2
.319+.326i	-.221-.244i	.085+.036i	.002-.011i	.005-.026i

H_2O	CH_3OH	CO_2	CH_2O
.478+.539i	-.299-.194i	-.050+.024i	.031-.156i

eigenvector 3: $\gamma_3 = -2.503 \times 10^5 s^{-1}$, $c_3 = 5.032 \times 10^5 mol.m^{-3}s^{-1}$

CO	O_2	H_2	HO_2	H_2O_2	H_2O	CH_3OH	CO_2	CH_2O
.052	-.231	.004	-.032	-.077	.672	-.522	.009	.461

eigenvector 4: $\gamma_4 = -11030 s^{-1}$, $c_4 = 4.059 \times 10^5 mol.m^{-3}s^{-1}$

CO	O_2	H_2	HO_2	H_2O_2	H_2O	CH_3OH	CO_2	CH_2O
-.686	-.294	.021	.001	.002	-.069	.010	.662	.002

t = 1.041 ms, T = 1292K, P = 43.8bar

eigenvector 1: $\gamma_1 = -1.025 \times 10^5 + i1.059 \times 10^5 s^{-1}$, $c_1 = -3.069 \times 10^6 - i1.654 \times 10^6 mol.m^{-3}s^{-1}$

CO	O_2	H_2	HO_2	H_2O_2
-.089+.496i	.039-.298i	-.080+.115i	-.006-.014i	-.010-.019i

H_2O	CH_3OH	CO_2	CH_2O
-.094+.685i	.147-.301i	.049-.023i	-.108-.173i

eigenvector 2: $\gamma_2 = -1.025 \times 10^5 - i1.059 \times 10^5 s^{-1}$, $c_2 = 1.654 \times 10^6 + i3.069 \times 10^6 mol.m^{-3}s^{-1}$

CO	O_2	H_2	HO_2	H_2O_2
.496-.089i	-.298+.039i	.115-.080i	-.014-.006i	-.019-.010i

H_2O	CH_3OH	CO_2	CH_2O
.685-.094i	-.301+.147i	-.023+.049i	-.173-.108i

eigenvector 3: $\gamma_3 = -4.942 \times 10^5 s^{-1}$, $c_3 = 1.034 \times 10^6 mol.m^{-3}s^{-1}$

CO	O_2	H_2	HO_2	H_2O_2	H_2O	CH_3OH	CO_2	CH_2O
.157	-.250	.023	-.050	-.075	.740	-.497	.010	.330

eigenvector 4: $\gamma_4 = -19620 s^{-1}$, $c_4 = 7.214 \times 10^5 mol.m^{-3}s^{-1}$

CO	O_2	H_2	HO_2	H_2O_2	H_2O	CH_3OH	CO_2	CH_2O
-.691	-.282	.026	.001	.002	-.089	.017	.659	.005

eigenvector 5: $\gamma_5 = -78850s^{-1}$, $c_5 = 6.692 \times 10^5 mol.m^{-3}s^{-1}$

CO	O_2	H_2	HO_2	H_2O_2	H_2O	CH_3OH	CO_2	CH_2O
-.233	-.276	-.779	.001	.003	.493	.100	.051	.081

t = 1.043 ms, T = 1442K, P = 43.9bar

eigenvector 1: $\gamma_1 = -3.079 \times 10^5 + i1.478 \times 10^5 s^{-1}$, $c_1 = -1.240 \times 10^6 - i1.054 \times 10^7 mol.m^{-3}s^{-1}$

CO	O_2	H_2	HO_2	H_2O_2
.412+.439i	-.190-.122i	.121+.318i	-.017-.012i	-.005-.003i

H_2O	CH_3OH	CO_2	CH_2O
.434+.330i	-.140-.256i	-.010-.057i	-.262-.126i

eigenvector 2: $\gamma_2 = -3.079 \times 10^5 - i1.478 \times 10^5 s^{-1}$, $c_2 = 1.054 \times 10^7 + i1.240 \times 10^6 mol.m^{-3}s^{-1}$

CO	O_2	H_2	HO_2	H_2O_2
.439+.412i	-.122-.190i	.318+.121i	-.012-.017i	-.003-.005i

H_2O	CH_3OH	CO_2	CH_2O
.330+.434i	-.256-.140i	-.057-.010i	-.126-.262i

eigenvector 5: $\gamma_5 = -2.409 \times 10^5 s^{-1}$, $c_5 = 7.305 \times 10^6 mol.m^{-3}s^{-1}$

CO	O_2	H_2	HO_2	H_2O_2	H_2O	CH_3OH	CO_2	CH_2O
-.565	-.701	-.744	.014	.004	.019	.235	.086	.242

eigenvector 4: $\gamma_4 = -52100 s^{-1}$, $c_4 = 1.654 \times 10^6 mol.m^{-3}s^{-1}$

CO	O_2	H_2	HO_2	H_2O_2	H_2O	CH_3OH	CO_2	CH_2O
-.698	-.261	.048	.003	.000	-.131	.029	.652	.011

eigenvector 3: $\gamma_3 = -1.849 \times 10^6 s^{-1}$, $c_3 = 1.556 \times 10^6 mol.m^{-3}s^{-1}$

CO	O_2	H_2	HO_2	H_2O_2	H_2O	CH_3OH	CO_2	CH_2O
.315	-.254	.072	-.121	-.034	.792	-.425	.030	.082

Note that eigenvector 5 (mode 3) and eigenvector 4 (mode 4) have displaced eigenvector 3 (mode 5) above, in comparison with the rates of production of the eigenmodes presented earlier in this section. Mode 3 and mode 4 above both describe the formation of carbon dioxide from oxygen and carbon monoxide. Mode 3 also describes a considerable decrease in molecular hydrogen concentration and an increase of formaldehyde concentration.

Mode 5 above describes a reduction in concentrations of methanol and oxygen, and an increase in concentrations of carbon monoxide and water, and to a lesser extent reductions of hydroperoxyl radical and hydrogen peroxide, and increases in carbon dioxide and formaldehyde.

The exponentially decaying oscillatory modes reflect the thermally explosive condition of the methanol/air oxidation system as explained earlier. The dominant coupled complex modes explain the exothermic chemistry in terms of the oxidation reactions of methanol to formaldehyde, followed by the oxidation

reactions of formaldehyde to carbon monoxide. The dominance of these two coupled modes continues to about 1800 K, at which time mode 4 above begins to dominate. This mode reflects the wet oxidation of carbon monoxide to carbon dioxide, and dominates the system in the thermally explosive regime 1800K to 2500K.

7.4.2 A Comparison of the Linear Mode Analysis of the Gr92r Mechanism with the Gr89 Mechanism and the ND89 Mechanism

The Gr89 Mechanism

It was stated earlier in this chapter that the eigenmode structure in the linear solution space of the chemical rate equations has the same form for the three mechanisms studied. There are subtle differences though, relating to the differences in the detailed chemistry described by the three mechanisms.

Performing the mode analysis on the dynamical evolution of the methanol/air autoignition system using the Gr89 mechanism, and comparing the results of this study with the results presented above, reveals that the Gr89 mechanism produces a larger branching ratio than the Gr92r mechanism. This can be deduced from the fact that the evolving explosive modes from the Gr89 mechanism are larger than the evolving explosive modes from the Gr92r mechanism. Coupled to this is the observation that the Gr89 mechanism predicts a greater rate of hydroperoxyl, hydrogen peroxide, and hydroxyl radical formation prior to, and in the region of autoignition.

A consequence of the larger predicted rate of formation of hydrogen peroxide in the Gr89 system than the Gr92r system is the prediction of storage of larger

amounts of hydrogen peroxide in the Gr89 system. Thus when thermal decomposition of hydrogen peroxide develops, the branching ratio for the Gr89 system is higher than that for the Gr92r system. Furthermore, the formaldehyde formed from the oxidation of methanol is marginally more stable in the Gr89 mechanism than in the Gr92r mechanism, with the consequence that more formaldehyde is stored in the Gr89 system than in the Gr92r system. Branching from formaldehyde occurs at slightly higher temperatures in the Gr89 mechanism, with a larger branching ratio.

The bifurcation of the equilibrium point of the system from an unstable node structure to an unstable focus develops slightly later in the Gr89 mechanism than the Gr92r mechanism, occurring at a temperature and pressure of 1130K, and 43.7bar respectively. The unstable node structure develops for about a 90K change in temperature, to a temperature and pressure of 1220K and 43.9bar respectively, before undergoing a pseudo-bifurcation to a stable node structure. Furthermore, when autoignition takes place, the Gr89 mechanism predicts a greater rate of heat release than the Gr92r mechanism.

The ND89 Mechanism

The rate coefficients for the termination hydroperoxyl recombination reaction forming hydrogen peroxide and molecular oxygen is larger in the ND89 mechanism than the Gr92 mechanism, while the rate coefficients for the propagation reaction of methanol with hydroperoxyl to form hydrogen peroxide and CH_2OH is smaller in the ND89 mechanism than the Gr92 mechanism (see chapter 6). This has the consequence that the branching ratio is smaller in the ND89 mechanism than the Gr92r mechanism.

The linear mode analysis reveals this lower branching ratio in the ND89 mecha-

nism through the eigenvalues of the explosive modes being smaller in the ND89 mode analysis than the Gr92r mode analysis. Smaller amounts of hydrogen peroxide are formed through the propagation path than the termination path when comparing the two mechanisms, and so when the thermal decomposition of hydrogen peroxide develops in the end-gas, and the system branches, rates of reaction and heat release are lower.

The equilibrium point of the system changes from an unstable node structure to an unstable focus at a temperature and pressure of 1070K and 41.6bar respectively, using the ND89 mechanism. This is about 30K lower in temperature than the corresponding bifurcation predicted from the Gr92r mechanism. The unstable focus structure lasts through a temperature change of about 110K, before changing to a stable focus at a temperature and pressure of 1180K and 42.9bar respectively.

7.5 General Discussion

Bowman's [16] experimental measurements of methanol oxidation in the temperature range 1545K to 2180K behind reflected shock waves was described as proceeding through two distinct phases. The first phase was an induction period, in which the concentrations of radical species and water increased rapidly, with little change in temperature. The second phase was the exothermic period, where it was observed that the concentration of radical species and water approached equilibrium values.

This description of methanol oxidation is well described by the linear mode analysis of methanol autoignition. The induction period defined above is well represented by the first two stages in the mode analysis; the unstable node structure and the unstable focus structure of the equilibrium points result in

a rapid production of water, radicals and other intermediates with a small degree of exothermicity, while the second strongly exothermic period is represented by a change in the equilibrium point of the system from an unstable focus to a stable focus. The concentrations of radicals and other intermediates converge towards the equilibrium along an inward spiral, as the system explodes thermally.

In Norton and Dryer's paper [89] of 1989, the authors report results of methanol oxidation in a turbulent flow reactor that have not been seen before; namely, a kinetic deceleration (or plateau) in the temperature and species profiles. There may be a relationship between this reported kinetic deceleration and the unstable focus behaviour in the linear mode analysis of methanol/air autoignition. Certainly the temperature regime is of the right order (1070K - 1170K), and the two coupled complex modes describe a deceleration of branching and simultaneous oscillation.

Chapter 8

Summary and Conclusion

8.1 Summary

Chapter 2 presented the cross-covariance (or cross-correlation) function as a method of fitting CARS spectra. The cross-covariance function used in this way is a reformulation of the method of non-linear least squares, and has not been used explicitly in the CARS context before. The method is computationally simple, linear and provides an objective measure of goodness of fit. Convergence to the coefficient of maximum cross-covariance is straightforward.

The method of cross-covariance can be used for fitting theoretical CARS spectra to experimental spectra, and for fitting experimental spectra against each other. Fitting of experimental spectra against each other requires a considerable degree of shot-to-shot stability. The shape of experimental CARS spectra is determined by the convolution of the modulus of the non-linear susceptibility squared, with the normalised response function of the spectrometer-detector system, and the normalised spectral density functions of the pump and Stokes

lasers. The normalised response function of the spectrometer-detector system depends on the focussing of the CARS signal at the detector, and in practice, is often different from experiment to experiment.

An empirical method was developed to match the focussing conditions of two experiments in order that experimental CARS spectra from two different experiments can be compared with each other. This method involved broadening or narrowing the spectrometer-detector response function from the one experiment to match the spectrometer-detector response function for the second experiment by convolving the response function with a suitably chosen Gaussian profile.

In chapter 3, CARS spectra obtained from a calibrated high pressure high temperature (HPHT) cell were presented, and used to evaluate two standard theoretical CARS models, namely the ONERA hard collision model [104], and Hall's EGL model [60]. It was found that the ONERA hard collision model predicted temperatures reasonably accurately in the temperature and pressure range 300K to 900K, and 1.0 bar to 12.0 bar respectively, but under-estimated temperatures considerably in the pressure range 14.0 bar to 18.0 bar. Hall's EGL model predicted temperatures very accurately at 1.0 bar, but progressively deteriorated as the HPHT cell pressure increased. The EGL model over-emphasized pressure narrowing effects on CARS spectra obtained at high pressures, and therefore consistently over-estimated HPHT cell temperatures.

CARS spectra in the pressure range 8.0 bar to 9.5 bar were observed to undergo substantial pressure related changes not reflected in the standard theoretical models evaluated. These changes in the CARS spectra were identified by a significant change in the trend of predicted temperatures by both models in this pressure range. The ONERA hard collision model over-estimated HPHT cell temperatures by about 30K at 8.0 bar, and then under-estimated HPHT

cell temperatures by about 40K at 9.5 bar. The EGL model over-estimated HPHT cell temperatures by about 150K at 8.0 bar, and over-estimated HPHT cell temperatures by about 70K to 100K at 9.5bar

Maximum shot-to-shot cross-covariances obtained from comparing experimental HPHT cell spectra, ONERA hard collision model spectra, and EGL model spectra with experimental HPHT spectra obtained in a different experimental environment were compared, in order to determine which gave the best fit. Maximum cross-covariances obtained from fitting the two sets of HPHT data against each other were the highest, followed by the EGL model, and then the ONERA hard collision model. However, the EGL model over-estimated the HPHT cell temperature considerably.

In chapter 4, the method of obtaining in-cylinder CARS temperature measurements and transducer pressure measurements from a knocking, methanol fuelled, Ricardo E6 research engine was described, and the temperature and pressure results presented. The in-cylinder temperatures were deduced by fitting the engine spectra against a database of HPHT spectra, using the empirical broadening method as outlined in chapter 2. Shot-to-shot maximum cross-covariances, and related CARS data statistics for two different crankshaft angles were presented as typical CARS data sets obtained from the running engine.

Chapter 5 presented a review of recent research into methanol ignition chemistry, focussing on the development of comprehensive methanol/air oxidation mechanisms, and a review of research into engine knock, focussing on the development of relevant chemical mechanisms underlying end-gas autoignition.

Chapter 6 presented a comprehensive zero-dimensional chemical kinetic modelling study of methanol/air autoignition in the end-gas, using five published

mechanisms. The model imposed the measured temperatures and pressures on a homogeneous methanol/air mixture up to the last measured temperature, and then assumed that the methanol/air mixture was isentropically compressed by the piston, the advancing flame front and the burnt gases. Thus the pressure measurements were used to calculate the isentropic temperature of the end-gas mixture up to the crankshaft angle where autoignition occurred.

The best prediction of the autoignition point came from the simplified Dove-Warnatz mechanism [31], followed by the two Grotheer mechanisms [55] [56], followed by the Norton-Dryer mechanism [89], and lastly, the Esser-Warnatz mechanism [41]. The methanol/air autoignition chemistry was qualitatively the same for all of the mechanisms studied. The evolution of the autoignition chemistry was explained in terms of the production of hydrogen peroxide and formaldehyde in the end-gas, formed from a series of propagation reactions. This is followed by thermal decomposition of hydrogen peroxide to hydroxyl radicals. The formation of hydrogen peroxide by hydrogen abstraction from methanol, and hydrogen abstraction from formaldehyde by hydroperoxyl radicals, followed by thermal decomposition of hydrogen peroxide provides two branching sequences in the autoignition system. The rapid production of hydroxyl radicals in the system results in autoignition.

A first order local sensitivity analysis was performed on the system, and four reactions were found to dominate the autoignition chemistry and the temperature evolution. These were the hydroperoxyl recombination reaction to form hydrogen peroxide and molecular oxygen, the thermal decomposition of hydrogen peroxide to form hydroxyl radicals, the hydrogen abstraction reaction from methanol by hydroperoxyl radicals to form CH_2OH and hydrogen peroxide, and the hydrogen abstraction reaction from formaldehyde by hydroperoxyl radicals to form CHO and hydrogen peroxide. The origin of the

rate coefficients for these reactions in the five mechanisms used in the autoignition modelling was established, and the relationship between the rate coefficients and the predicted autoignition times was discussed.

It was found that the rate coefficient for the most sensitive reaction in the methanol/air autoignition system, the hydrogen abstraction from methanol by hydroperoxyl radicals, to form hydrogen peroxide and CH_2OH, has never been directly measured, and the published value has an uncertainty of about twenty. When the value used in Grotheer's mechanisms was reduced by a factor of ten, the predicted autoignition time agreed with the experimentally measured knock point within experimental error.

When the rate coefficient for the hydroperoxyl recombination reaction in the Grotheer mechanisms was replaced by the value published in the Norton-Dryer mechanism, the predicted autoignition point improved from 4^o BTDC to 1^o BTDC, an error of one crankshaft angle degree.

In chapter 7, a linear mode analysis of the reaction rate equations was presented in detail for a reduced version of the 1992 Grotheer mechanism. This is the first time a linear mode analysis has been performed on such a comprehensively described autoignition system, using methods from the geometric qualitative theory of differential equations. It was found that the chemical rate equations passed through three mathematically well defined regions as a function of time.

The qualitative behaviour of the chemical rate equations were represented in generalised phase space, in terms of the structure of the equilibrium points of the system. The equilibrium points took the form of unstable improper nodes in the first region, unstable focii in the second region, and stable focii in the third region. The bifurcation of the equilibrium point from an unstable node

structure to an unstable focus was defined by a point of inflection (second time derivative equals zero) in the concentration history of hydrogen peroxide. The oxidation of methanol to formaldehyde and carbon monoxide begins to release substantial amounts of heat at this time.

The evolving competition between the two dominant exponentially increasing eigenmodes was explained in terms of the competition for hydroperoxyl radicals between the hydrogen-abstraction propagation reactions

$$CH_3OH + HO_2 \rightarrow CH_2OH + H_2O_2 \tag{8.1}$$

$$CH_2O + HO_2 \rightarrow CHO + H_2O_2, \tag{8.2}$$

and the hydroperoxyl termination reaction

$$HO_2 + HO_2 \rightarrow H_2O_2 + O_2. \tag{8.3}$$

The above propagation reactions are two-stage reactions, proceeding through the first stage via hydroperoxyl radical. In other words they are catalysed by the hydroperoxyl radical. However, the competing hydroperoxyl disproportionation reaction serves to anti-catalyse the above propagation reactions.

The chemical system therefore changes from a branching system to a propagating system, and this change is reflected qualitatively through the bifurcation of the equilibrium point from the unstable node structure to an unstable focus.

The pseudo-bifurcation of the equilibrium point from an unstable focus to a

stable focus was defined by the point of maximum hydrogen peroxide concentration, or in other words, the point at which the first time derivative of the hydrogen peroxide concentration was zero. This point in time marked the beginning of the autoignition reaction.

The linear mode analysis was also performed on the rate equations using both the 1989 Grotheer mechanism, and the 1989 Norton-Dryer mechanism, and it was found that the rate equations had the same qualitative structure for all three mechanisms. There were some differences though, and these related to differences in the rate coefficients of the most sensitive reactions in the three mechanisms mentioned earlier. It was noted that the modal description of methanol autoignition was very similar to the description of methanol ignition behind shock waves as measured and reported by Bowman [16].

8.2 Further Work suggested by this Thesis

The modern scaling laws for calculating rotationally inelastic collision rates require more experimental evaluation in terms of the resultant theoretical CARS spectra produced as a function of temperature and pressure. Important evaluation work has been performed by Brüggeman et al [19] and Bouché et al [15] on the MEG law, and by Woyde and Stricker [125] on the XMEG law. However, more detailed and comprehensive temperature calibration studies as a function of pressure need to be performed on the theoretical CARS spectra calculated from the two scaling laws mentioned above.

To date, there has been only one set of reliable CARS temperature measurements performed in the end-gas region at autoignition reported. This is the set of measurements reported by Brüggeman et al [19], using the MEG law. The CARS temperature measurements performed by Lucht et al [78] involved

the use of the rotational diffusion model. The accuracy of the rotational diffusion model has not been adequately studied, and has now been superseded by the more reliable MEG law. Any systematic errors in the rotational diffusion model will be projected onto the predicted end-gas temperatures.

Brüggemann et al have followed a more rigorous route. They tested the MEG law in a high pressure high temperature cell, and found that the predicted CARS temperatures deviated from thermocouple measurements by less than 30K over the full range of temperatures and pressures 300K to 1300K, and 1 bar to 50 bar respectively. They then used the same code for the measurement of temperatures inside the engine.

Further temperature measurements in the end-gas region just prior to autoignition need to be performed with a variety of fuels, including methanol, in order to establish experimentally autoignition temperatures for different automotive fuels.

The validation of a comprehensive methanol/oxidation mechanism at engine autoignition temperatures requires careful measurement of the rate coefficients for the following three reactions in particular:

$$HO_2 + HO_2 \rightarrow H_2O_2 + O_2$$

$$H_2O_2 + M' \rightarrow OH + OH + M'$$

$$CH_3OH + HO_2 \rightarrow CH_2OH + H_2O_2.$$

Most important of these will be the measurement of the rate coefficient for the hydrogen abstraction reaction from methanol by the hydroperoxyl radical to form CH_2OH and hydrogen peroxide.

It will soon be appropriate to combine fluid flow and chemical reaction processes in order to understand autoignition more fully. This approach will develop after rigorous validation of comprehensive fuel oxidation mechanisms. Even now, researchers have begun to publish in this area [80].

8.3 General Discussion

From a fundamental point of view, the great interest of methanol is that it is easy to run a methanol-fuelled internal combustion engine under knocking conditions, yet the chemistry of the end-gas autoignition is sufficiently simple for an exhaustive analytical treatment to be possible.

The theoretical analysis can, however, be translated into practical advice for the engineer, of a rather general nature.

It has been shown above that the mechanism responsible for autoignition in a methanol-fuelled engine involves the formation first of HO_2 radicals, and then of hydrogen peroxide. Accumulation of hydrogen peroxide in the end-gas is inevitable; but this only has pernicious consequences when the end-gas temperature is allowed to rise above 1050 K. To avoid knock, the engine should be designed to run as cool as possible, consistent with the need to maximize thermodynamic efficiency.

In this respect it may be possible for the engineer to exploit the very high latent heat of vaporization of methanol, so as to keep the air-fuel charge cool when the engine is running at high speed and under full load. Any preheating of the inlet air or of the fuel, which may be necessary either for cold starting or to improve driveability under partial load conditions, should definitely be discontinued when the engine is operating under full load.

If non-toxic antiknock additives are required for methanol fuels, a systematic search should be made for compounds which promote the conversion of HO_2 radical and/or hydrogen peroxide into stable products at low temperatures.

Bibliography

[1] R. Ackrich, C. Vovelle, and R. Delbourgo. Combustion and Flame 32, 171, 1978.

[2] H. Adelman, L. Browning, and R. Pefley. AIAA Journal 14, p793, 1976.

[3] J. Agnew. SAE 670125, 1967.

[4] G. Alessandretti and P. Violino. Journal of Physics D: Applied Physics 16, p1583, 1983.

[5] C. Amann. Progress in Energy and Combustion Science 9, p239, 1983.

[6] V.I. Arnold. **Ordinary Differential Equations**, chapter Systems of Linear Differential Equations, page 545. MIT Press, 1987.

[7] D. Aronowitz, D. Naegeli, and I. Glassman. The Journal of Physical Chemistry v81, no.25, p2555, 1977.

[8] D. Aronowitz, R. Santoro, and I. Glassman F. Dryer. Kinetics of the oxidation of methanol: Experimental results, semi-global modelling and mechanistic concepts. In **Seventeenth Symposium (International) on Combustion**, page 633, 1978.

[9] D. Ball and G. Robertson. C.a.r.s. measurements in a static environment at high temperature and pressure. SAIP 35th Annual Conference: Paper D.04, 1990.

[10] J. Barnard and B. Harwood. Combustion and Flame 21, p141, 1973.

[11] J. Barnard and B. Harwood. Combustion and Flame 21, p345, 1973.

[12] H. Bekker, P. Monkhouse, and J. Wolfrum. Applied Physics B 50, p473, 1990.

[13] S. Benson. **The Foundations of Chemical Kinetics**, page 66. McGraw Hill, 1967.

[14] S. Benson. Progress in Energy and Combustion Science 7, p125, 1981.

[15] T. Bouche, T. Dryer, B. Lange, J. Wolfrum, E. Franck, and W. Schilling. Applied Physics B 50, p527, 1990.

[16] C. Bowman. Combustion and Flame 25, p343, 1975.

[17] D. Bradley, G. Dixon-Lewis, S. El-Din Habik, L. Kwa, and S. El-Sherif. Combustion and Flame 85, p105, 1991.

[18] K. Brezinsky and F. Dryer. SAE 872109, 1987.

[19] D. Brüggemann, B. Wies, and X. Zhang. Measurements in a knocking spark-ignition engine by C.A.R.S. spectroscopy. Joint Meeting of the Italian and German Sections of the Combustion Institute, September 1989.

[20] A. Burcat and K. Scheller. Combustion and Flame 16, p29, 1971.

[21] M. Cathonnet, J. Boettner, and H. James. Journal de Chimie Physique 79, p475, 1982.

[22] N. Cernansky, R. Green, W. Pitz, and C. Westbrook. Combustion Science and Technology 50, p3, 1986.

[23] K. Chinnick, C. Gibson, J. Griffiths, and W. Kordylewski. Proceedings of the Royal Society of London A, v405, p117, 1986.

[24] C. Coats and A. Williams. Investigation of the ignition and combustion of n-heptane-oxygen mixtures. In **Seventeenth Symposium (International) on Combustion**, page 611, 1979.

[25] R. Cox and J. Cole. Combustion and Flame 60, p109, 1985.

[26] P. Cribb, J. Dove, and S. Yamazaki. Combustion and Flame 88, p169, 1992.

[27] P. Cribb, J. Dove, and S. Yamazaki. Combustion and Flame 88, p186, 1992.

[28] W. Daniel. Flame quenching at the walls of an internal combustion engine. In **Sixth Symposium (International) on Combustion**, 1956.

[29] P. Deuflhard and U. Nowak. University of Heidelberg: Technical Report 332, 1985.

[30] P. Dimpelfeld and D. Foster. SAE 841337, 1984.

[31] J. Dove and J. Warnatz. Berichte der Bunsen-Gesellschaft fur physikalische Chemie 87, p1040, 1983.

[32] D. Downs, S. Griffiths, and R. Wheeler. Journal of the Institute of Petroleum v49, no.469, p8, 1963.

[33] D. Downs, A. Walsh, and R. Wheeler. Philisophical Transactions of the Royal Society A243, p463, 1951.

[34] S. Driver, R. Hutcheon, R. Lockett, G. Robertson, H. Grotheer, and S. Kelm. Berichte der Bunsen-Gesellschaft fur physikalische Chemie, in press, 1992.

[35] S. Druet and J. Taran. C.a.r.s. spectroscopy. Progress in Quantum Electronics 7, p1, 1981.

[36] F. Dryer and K. Brezinsky. Combustion Science and Technolody 45, p199, 1986.

[37] A. Eckbreth. Journal of Quantitative Spectroscopy and Radiation Transfer 40, p369, 1988.

[38] A. Eckbreth. **Laser Diagnostics for Combustion Temperature and Species**, chapter Coherent Anti-Stokes Raman Spectroscopy (C.A.R.S.). Abacus Press, 1988.

[39] A. Egerton, F. Smith, and A. Ubbelohde. Philisophical Transactions of the Royal Society A234, p433, 1935.

[40] C. Esser, U. Maas, and J. Warnatz. Chemistry of the auto-ignition in hydrocarbon-air mixtures up to octane and its relation to engine knock. In **Proceedings of the International Symposium on Diagnostics and Modeling of Combustion in Reciprocating Engines**, page 335, 1985.

[41] C. Esser and J. Warnatz. Private Communication, 1987.

[42] C. Ferguson. **Internal Combustion Engines - Applied Thermosciences**. John Wiley and Sons, 1986.

[43] C. Ferguson, R. Green, and R. Lucht. Combustion Science and Technology 55, p63, 1987.

[44] W. Gardiner, editor. **Combustion Chemistry**, chapter Rate Coefficients in the C/H/O System, page 197. Springer-Verlag, 1984.

[45] W. Gardiner, editor. **Combustion Chemistry**, chapter Bimolecular Reaction Rate Coefficients, page 130. Springer-Verlag, 1984.

[46] C. Gear. Communications of the ACM v14, no.3, p176, 1971.

[47] C. Gibbs and H. Calcote. Journal of Chemical Engineering Data 4, p226, 1959.

[48] I. Glassman. **Combustion**. Academic Press, second edition, 1987.

[49] R. Gordon. The Journal of Chemical Physics v45, no.5, p1649, 1966.

[50] R. Gordon. The Journal of Chemical Physics v44, no.8, p3083, 1966.

[51] C. Gray and J. Alson. The case for methanol. Scientific American, November 1989.

[52] R. Green, C. Parker, W. Pitz, and C. Westbrook. SAE no. 870169, 1987.

[53] D. Greenhalgh. Quantitative c.a.r.s. spectroscopy. Chapter 5:- Advances in Non-linear Spectroscopy, p193, 1988.

[54] D. Greenhalgh, F. Porter, and S. Barton. Journal of Quantitative Spectroscopy and Radiation Transfer v34, no.1, p95, 1985.

[55] H. Grotheer and S. Kelm. Presented at the Third International Seminar on Flame Structure, USSR, 1989.

[56] H.H. Grotheer, S. Kelm, S. Driver, R. Hutcheon, R. Lockett, and G. Robertson. Berichte der Bunsen-Gesellschaft fur physikalische Chemie, in press, 1992.

[57] O. Gulder. Laminar burning velocities of methanol, ethanol and isooctane mixtures. In **Nineteenth Symposium (International) on Combustion**, page 275, 1983.

[58] D. Hagen. SAE 770792, 1979.

[59] R. Hall and D. Greenhalgh. Optics Communications v40, no.6, p417, 1982.

[60] R. Hall, J. Verdieck, and A. Eckbreth. Optics Communications v35, no.1, p69, 1980.

[61] M. Halstead, L. Kirsch, A. Prothero, and C. Quinn. Proceedings of the Royal Society of London A346, p515, 1975.

[62] M. Halstead, L. Kirsch, and C. Quinn. Combustion and Flame 30, p45, 1977.

[63] T. Hayashi, M. Taki, S. Kojima, and T. Kondo. SAE 841336, 1984.

[64] S. Hirst and L. Kirsch. The application of a hydrocarbon autoignition model in simulating knock and other engine combustion phenomena. In J. Mattavi and C. Amann, editors, **Combustion Modeling in Reciprocating Engines**, page 193. Plenum Publishing Corporation, 1980.

[65] J. Horrell, R. Hutcheon, and G. Robertson. Comparitive evaluation of dyes for stokes laser in c.a.r.s. system. SAIP 36th Annual Conference: Paper D.18, 1991.

[66] H. Hu and J. Keck. SAE 872110, 1987.

[67] K. Ito, T. Yano, and R. Nagasaka. Bulletin of the Japanese Society of Mechanical Engineers v25, no.10, p210, 1982.

[68] A. Jeffrey. **Linear Algebra and Ordinary Differential Equations**, chapter Linear Systems. Blackwell Scientific Publications, 1990.

[69] H. Kataoka, S Maeda, C. Hirose, and K. Kajiyama. Applied Spectroscopy v37, no.6, p508, 1983.

[70] L. Kirsch and C. Quinn. Journal de Chimie Physique v82, no.5, p459, 1985.

[71] D. Klick, K. Marko, and L. Rimai. Applied Optics v20, no.7, p1178, 1981.

[72] G. Konig, R. Maly, D. Bradley, A. Lau, and C. Sheppard. SAE 902136, 1990.

[73] M. Koszykowski, R. Farrow, and R. Palmer. Optics Letters v10, no.10, p478, 1985.

[74] M. Koszykowski, L. Rahn, R. Palmer, and M. Coltrin. The Journal of Physical Chemistry v91, no.1, p41, 1987.

[75] K. Laidler. **Chemical Kinetics**, page 50. McGraw-Hill, 1965.

[76] W. Leppard. Combustion Science and Technology 43, p1, 1985.

[77] P. Lightfoot, B. Veyret, and R. Lesclaux. Chemical Physics Letters 150, p120, 1988.

[78] R. Lucht, R. Teets, R. Green, and C. Ferguson R. Palmer. Combustion Science and Technology 55, p41, 1987.

[79] U. Maas and S. Pope. Combustion and Flame 88, p239, 1992.

[80] U. Maas and J. Warnatz. Progress in Astronautics and Aeronautics 131, p3, 1991.

[81] R. Maly, R. Klein, N. Peters, and G. Konig. SAE 900025, 1990.

[82] R. Maly and G. Ziegler. SAE 820758, 1982.

[83] J. Marie, P. Dlsgroun, and M. Cottereau. IX International Symposium on Combustion Processes, 1985.

[84] M. Metghalchi and J. Keck. Combustion and Flame 48, p191, 1982.

[85] C. Miller. Transactions of the SAE v1, no.1, p98, 1947.

[86] C. Morley. Combustion Science and Technology 55, p115, 1987.

[87] B. Mullins. Fuel 32, p467, 1953.

[88] K. Natarajan and K. Bhaskaran. Combustion and Flame 43, p35, 1981.

[89] T. Norton and F. Dryer. Combustion Science and Technology 63, p107, 1989.

[90] T. Norton and F. Dryer. International Journal of Chemical Kinetics 22, p219, 1990.

[91] J. Olssen, L. Karlsson, and L. Anderson. Journal of Physical Chemistry 90, p1458, 1986.

[92] J. Olssen, I. Olssen, and L. Anderson. Journal of Physical Chemistry 91, p4160, 1987.

[93] J. Pauwels, M. Carlier, P. Devolder, and L. Sochet. Combustion Science and Technology 64, p97, 1989.

[94] J. Pauwels, M. Carlier, P. Devolder, and L. Sochet. Combustion and Flame 82, p163, 1990.

[95] M. Pealat, P. Bouchardy, M. Lefebvre, and J. Taran. Applied Optics 24, p1012, 1985.

[96] W. Pitz and C. Westbrook. Combustion and Flame 63, p113, 1986.

[97] W. Pitz, C. Westbrook, W. Proscia, and F. Dryer. A comprehensive chemical kinetic reaction mechanism for the oxidation of n-butane. In **Twentieth Symposium (International) on Combustion**, page 831, 1984.

[98] F. Porter. **A Study of Temperature Measurement using Coherent Anti-Stokes Raman Spectroscopy**. PhD thesis, University of Surrey, 1985.

[99] L. Rahn, A. Owyoung, M. Cotton, and M. Kosykowski. Proceedings of the 7th International Raman Conference, p694, 1980.

[100] L. Rahn and R. Palmer. Journal of the Optical Society of America B: v3, no.9, p1164, 1986.

[101] L. Rahn, R. Palmer, M. Koszykowski, and D. Greenhalgh. Chemical Physics Letters v133, no.6, p513, 1987.

[102] G. Robertson and A. Roblin. Analysis of c.a.r.s. spectra using fourier transform techniques. In E. Castellucci, editor, **Coherent Raman**

Spectroscopy: Applications and New Developments: in press. World Scientific, 1992.

[103] G. Rosasco, W. Lempert, and W. Hurst. Chemical Physics Letters 97, p417, 1983.

[104] J. Sala, J. Bonamy, D. Robert, G. Millot B. Lavorel, and H. Berger. Chemical Physics 106, p427, 1986.

[105] J. Smith, R. Green, C. Westbrook, and W. Pitz. An experimental and modeling study of engine knock. In **Twentieth Symposium (International) on Combustion**, page 91, 1984.

[106] I. Stenhouse, D. Williams, J. Cole, and M. Swords. Applied Optics v18, no.22, p3819, 1979.

[107] R. Toepel, J. Bennethum, and R. Heruth. SAE 831744, 1983.

[108] D. Trumpy, O. Uyehara, and P. Myers. SAE Transactions 78, p1849, 1969.

[109] W. Tsang and R. Hampson. Journal of Physical Chemistry Reference Data 15, p1087, 1986.

[110] T. Tsuboi and K. Hashimoto. Combustion and Flame 42, p61, 1981.

[111] T. Tsuboi, M. Katoh, S. Kikuchi, and K. Hashimoto. Japanese Journal of Applied Physics v20, no.5, p985, 1981.

[112] J. Vandooren and P. van Tiggelen L. Oldenhove de Guertechin. Combustion and Flame 64, p127, 1986.

[113] J. Vandooren and P. Van Tiggelen. Eighteenth Symposium (International) on Combustion, p473, 1981.

[114] M. Vermeersch, T. Held, Y. Stein, and F. Dryer. 1991 SAE Fuels and Lubricants Meeting, Toronto, Ontario, 1991.

[115] R. Walker. Reaction Kinetics, a Specialist Periodical Report, Chemical Society, London, v1, p161, 1977.

[116] J. Warnatz and W. Jager, editors. **Complex Chemical Reaction Systems, Mathematical Modelling and Simulation.** Springer-Verlag, 1986.

[117] C. Westbrook. Combustion Science and Technology 23, p191, 1980.

[118] C. Westbrook, A. Adamczyk, and G. Lavoie. Combustion and Flame 40, p81, 1981.

[119] C. Westbrook and F. Dryer. Combustion Science and Technology 20, p125, 1979.

[120] C. Westbrook and F. Dryer. Combustion and Flame 37, p171, 1980.

[121] C. Westbrook and F. Dryer. Progress in Energy and Combustion Science 10, p1, 1984.

[122] C. Westbrook, F. Dryer, and K. Schug. A comprehensive mechanism for the pyrolysis and oxidation of ethylene. In **Nineteenth Symposium (International) on Combustion**, page 153, 1983.

[123] C. Westbrook and W. Pitz. Chemical kinetics modeling of the influence of molecular structure on shock tube ignition delay. In **International Symposium on Shock Waves and Shock Tubes (15th: 1985, Berkeley, California)**, page 287, 1986.

[124] C. Westbrook, J. Warnatz, and W. Pitz. A detailed chemical kinetic reaction mechanism for the oxidation of iso-octane and n-heptane over an extended temperature range and its application to engine knock. In **Twenty-second Symposium (International) on Combustion**, page 893, 1988.

[125] M. Woyde and W. Stricker. Applied Physics B: v50, p519, 1990.

[126] T. Yano and K. Ito. Bulletin of the Japanese Society of Mechanical Engineers v26, no.211, p94, 1983.

[127] A. Yates. **Abnormal Combustion: Methanol versus Gasoline.** PhD thesis, University of Cape Town, 1988.

[128] A. Yates. Private Communication, Department of Mechanical Engineering, U.C.T., 1992.

[129] R. Yetter, F. Dryer, and H. Rabitz. Combustion and Flame 59, p107, 1985.

[130] J. Zaslonko, Y. Mukoseyev, and A. Tyurin. Kinetics and Catalysis 29, p66, 1988.

Appendix (1): General Properties of Methanol

General Physical Properties

Vapour Pressure: P

$$\log(P/kPa) = 15.76129944 - \frac{2.845920984 \times 10^3}{T} - \frac{3.743415457 \times 10^5}{T^2} + \frac{2.188669828 \times 10^7}{T^3}$$

This expression is accurate to ± 1Pa over the range 288.15K to 337.65K.

Molecular Weight: 32.042g.mol^{-1}

Density (@STP): $\rho = 0.8100 \text{kg.m}^{-3}$

Boiling Point: $T_b = 337.664K \pm 0.002K$, 64.514^oC

Melting Point (Triple Point): $T_f = -97.56 \pm 0.02^oC$

Critical Temperature: $T_c = 239.43^oC$

Critical Pressure: $P_c = 8096kPa$

Critical Density: $\rho_c = 0.272 \text{g.cm}^{-3}$

Heat of Fusion: $\Delta H = 32.13 \pm 0.05 \text{kJ.mol}^{-1}$

Heat of Vaporisation (@64.7^oC, 760mm Hg) : $\Delta H_v = 34.48 \pm 0.04 \text{kJ.mol}^{-1}$

Heat of Vaporisation (@25.0^oC, 125.45mm Hg) : $\Delta H_v = 37.40 \pm 0.15 \text{kJ.mol}^{-1}$

Thermodynamic Functions of Methanol Gas at One Atmosphere

Standard Entropy @298.15K: $S^0 = 239.7\text{J.K}^{-1}\text{.mol}^{-1}$

Specific Heat @298.15K: $C_p = 43.89\text{J.K}^{-1}\text{.mol}^{-1}$

Heat of Formation @298.15K: $\Delta H_f = -201.08\text{kJ.mol}^{-1}$

Gibbs Energy of Formation @298.15K: $\Delta G_f = -162.42\text{kJ.mol}^{-1}$

Thermodynamic Functions of Methanol Liquid at One Atmosphere

Standard Entropy @298.15: $S^0 = 127.24\text{J.K}^{-1}\text{.mol}^{-1}$

Specific Heat @298.15K: $C_p = 81.17\text{J.K}^{-1}\text{.mol}^{-1}$

Heat of Formation @298.15K: $\Delta H_f = -239.03\text{kJ.mol}^{-1}$

Gibbs Energy of Formation @298.15K: $\Delta G_f = -166.82\text{kJ.mol}^{-1}$

The above information was obtained from the SAE paper by D. Hagen, entitled "Methanol as a Fuel: A Review with Bibliography".

Appendix (2): Ricardo E6 Research Engine Conditions during Knock Tests

800 rpm Data

Water Coolant Temperature: $130^{o}C$

Inlet Air Temperature: $156^{o}C$

Air Mass Flow Rate: $190 \pm 5 g.min^{-1}$

Methanol Mass Flow Rate: $28.1 \pm 1.4 g.min^{-1}$

Air/fuel Ratio: $6.8 \pm 0.3 : 1$

Engine Speed: 800 ± 20 rpm

Spark Ignition Timing during Knocking: 34^{o} BTDC

1000 rpm Data

Water Coolant Temperature: $164^{o}C$

Inlet Air Temperature: $161^{o}C$

Air Mass Flow Rate: $227 \pm 5 g.min^{-1}$

Methanol Mass Flow Rate: $32.7 \pm 1.1 g.min^{-1}$

Air/fuel Ratio: $6.9 \pm 0.3 : 1$

Engine Speed: 1000 ± 20 rpm

Spark Ignition Timing during Knocking: 34^o BTDC

1200 rpm Data

Water Coolant Temperature: not available

Inlet Air Temperature: 153^oC

Air Mass Flow Rate: $260 \pm 5 g.min^{-1}$

Methanol Mass Flow Rate: $32.3 \pm 1.2 g.min^{-1}$

Air/fuel Ratio: $8.0 \pm 0.3 : 1$

Engine Speed: 1200 ± 20 rpm

Spark Ignition Timing during Knocking: 34^o BTDC

1400 rpm Data

Water Coolant Temperature: not available

Inlet Air Temperature: 141^oC

Air Mass Flow Rate: $284 \pm 6 g.min^{-1}$

Methanol Mass Flow Rate: $33.6 \pm 1.3 g.min^{-1}$

Air/fuel Ratio: $8.5 \pm 0.3 : 1$

Engine Speed: 1400 ± 20 rpm

Spark Ignition Timing during Knocking: 34^o BTDC

2000 rpm Data

Water Coolant Temperature: not available

Inlet Air Temperature: 127^oC

Air Mass Flow Rate: $317 \pm 6 g.min^{-1}$

Methanol Mass Flow Rate: $51.1 \pm 1.3 g.min^{-1}$

Air/fuel Ratio: $6.2 \pm 0.3 : 1$

Engine Speed: 2000 ± 20 rpm

Spark Ignition Timing during Knocking: N/A

Appendix (3): Grotheer 1992 Reduced Mechanism

Reaction	A	b	E_a
$O2 + H \rightarrow OH + O$	9.36E+13	0.00	61.10
$OH + O \rightarrow O2 + H$	2.58E+11	0.40	-10.71
$H2 + O \rightarrow OH + H$	5.10E+04	2.67	26.30
$OH + H \rightarrow H2 + O$	2.26E+04	2.67	18.44
$H2 + O \rightarrow H2O + H$	1.30E+08	1.80	13.80
$H2O + H \rightarrow H2 + OH$	5.79E+08	1.80	77.13
$OH + O \rightarrow H2O + O$	1.50E+09	1.14	0.42
$H2O + O \rightarrow OH + OH$	1.51E+10	1.14	71.61
$H + H + M' \rightarrow H2 + M'$	1.80E+18	-1.00	0.00
$H2 + M' \rightarrow H + H + M'$	6.99E+18	-1.00	436.03
$H + OH + M' \rightarrow H2O + M'$	2.20E+22	-2.00	0.00
$H2O + M' \rightarrow H + OH + M'$	3.80E+23	-2.00	499.36
$O + O + M' \rightarrow O2 + M'$	2.90E+17	-1.00	0.00
$O2 + M' \rightarrow O + O + M'$	6.82E+18	-1.00	496.40
$H + O2 + M' \rightarrow HO2 + M'$	2.30E+18	-0.80	0.00
$HO2 + M' \rightarrow H + O2 + M'$	3.26E+18	-0.80	195.86
$HO2 + H \rightarrow OH + OH$	1.70E+14	0.00	3.66
$OH + OH \rightarrow HO2 + H$	1.50E+13	0.00	167.72
$HO2 + H \rightarrow H2 + O2$	4.30E+13	0.00	5.90

Reaction	A	b	E_a
$H2 + O2 \rightarrow HO2 + H$	1.18E+14	0.00	246.07
$HO2 + H \rightarrow H2O + O$	3.00E+13	0.00	7.20
$H2O + O \rightarrow HO2 + H$	2.67E+13	0.00	242.45
$HO2 + O \rightarrow OH + O2$	3.20E+13	0.00	0.00
$OH + O2 \rightarrow HO2 + O$	3.87E+13	0.00	232.30
$HO2 + OH \rightarrow H2O + O2$	2.90E+13	0.00	-2.08
$H2O + O2 \rightarrow HO2 + OH$	3.53E+14	0.00	301.41
$HO2 + HO2 \rightarrow H2O2 + O2$	1.90E+12	0.00	6.44
$H2O2 + O2 \rightarrow HO2 + HO2$	7.67E+12	0.00	181.46
$OH + OH + M' \rightarrow H2O2 + M'$	3.25E+22	-2.00	0.00
$H2O2 + M' \rightarrow OH + OH + M'$	2.10E+24	-2.00	206.82
$H2O2 + H \rightarrow H2 + HO2$	1.70E+12	0.00	15.73
$H2 + HO2 \rightarrow H2O2 + H$	1.15E+12	0.00	80.88
$H2O2 + H \rightarrow H2O + OH$	1.00E+13	0.00	15.02
$H2O + OH \rightarrow H2O2 + H$	2.67E+12	0.00	307.56
$H2O2 + O \rightarrow OH + HO2$	2.80E+13	0.00	26.82
$OH + HO2 \rightarrow H2O2 + O$	8.40E+12	0.00	84.11
$H2O2 + OH \rightarrow H2O + HO2$	7.80E+12	0.00	5.57
$H2O + HO2 \rightarrow H2O2 + OH$	2.36E+13	0.00	134.05
$CO + OH \rightarrow CO2 + H$	6.30E+06	1.50	-2.08
$CO2 + H \rightarrow CO + OH$	8.77E+08	1.50	95.11
$CO + HO2 \rightarrow CO2 + OH$	1.50E+14	0.00	98.70
$CO2 + OH \rightarrow CO + HO2$	1.85E+15	0.00	359.95
$CO + O + M' \rightarrow CO2 + M'$	5.30E+13	0.00	-19.00
$CO2 + M' \rightarrow CO + O + M'$	1.27E+16	0.00	506.35
$CO2 + O \rightarrow CO + O2$	1.70E+13	0.00	220.00

Reaction	A	b	E_a
$CO + O2 \rightarrow CO2 + O$	1.67E+12	0.00	191.05
$CH3OH + H \rightarrow CH2OH + H2$	4.00E+13	0.00	25.50
$CH2OH + H2 \rightarrow CH3OH + H$	3.38E+12	0.00	58.80
$CH3OH + H \rightarrow CH3O + H2$	4.00E+12	0.00	25.50
$CH3O + H2 \rightarrow CH3OH + H$	2.48E+12	0.00	26.75
$CH3OH + O \rightarrow CH2OH + OH$	3.88E+05	2.50	12.89
$CH2OH + OH \rightarrow CH3OH + O$	1.45E+04	2.50	38.32
$CH3OH + O2 \rightarrow CH2OH + HO2$	2.00E+13	0.00	188.00
$CH2OH + HO2 \rightarrow CH3OH + O2$	6.18E+11	0.00	-18.87
$CH3OH + OH \rightarrow CH2OH + H2O$	3.00E+04	2.65	-3.70
$CH2OH + H2O \rightarrow CH3OH + OH$	1.13E+04	2.65	92.92
$CH3OH + OH \rightarrow CH3O + H2O$	5.30E+03	2.65	-3.70
$CH3O + H2O \rightarrow CH3OH + OH$	1.46E+04	2.65	60.88
$CH3OH + HO2 \rightarrow CH2OH + H2O2$	6.31E+12	0.00	81.20
$CH2OH + H2O2 \rightarrow CH3OH + HO2$	7.87E+11	0.00	49.35
$CH2OH + H \rightarrow CH2O + H2$	6.20E+13	0.00	2.50
$CH2O + H2 \rightarrow CH2OH + H$	3.34E+14	0.00	323.15
$CH2OH + OH \rightarrow CH2O + H2O$	2.40E+13	0.00	0.00
$CH2O + H2O \rightarrow CH2OH + OH$	5.76E+14	0.00	383.97
$CH2OH + O \rightarrow CH2O + OH$	9.00E+13	0.00	0.00
$CH2O + OH \rightarrow CH2OH + O$	2.15E+14	0.00	312.78
$CH2OH + O2 \rightarrow CH2O + HO2$	1.00E+14	0.00	21.00
$CH2O + HO2 \rightarrow CH2OH + O2$	1.97E+14	0.00	101.48
$CH2OH + HO2 \rightarrow CH2O + H2O2$	1.20E+13	0.00	0.00
$CH2O + H2O2 \rightarrow CH2OH + HO2$	9.54E+13	0.00	255.49
$CH2OH + M' \rightarrow CH2O + H + M'$	8.10E+27	-4.00	133.45
$CH2O + H + M' \rightarrow CH2OH + M'$	1.12E+28	-4.00	18.07
$CH2OH + CH3O \rightarrow CH3OH + CH2O$	2.40E+13	0.00	0.00

Reaction	A	b	E_a
$CH3OH + CH2O \rightarrow CH2OH + CH3O$	2.09E+14	0.00	319.39
$CH2OH + CH2OH \rightarrow CH2O + CH2O + H2$	1.00E+15	-0.70	0.00
$CH2O + CH2O + H2 \rightarrow CH2OH + CH2OH$	7.48E+15	-0.70	205.26
$CH3O + O2 \rightarrow CH2O + HO2$	4.28E-13	7.60	-14.80
$CH2O + HO2 \rightarrow CH3O + O2$	1.15E-13	7.60	97.72
$CH3O + CH4 \rightarrow CH3OH + CH3$	1.32E+14	0.00	63.08
$CH3OH + CH3 \rightarrow CH3O + CH4$	7.43E+12	0.00	56.77
$CH3O + CO \rightarrow CH3 + CO2$	1.56E+13	0.00	49.40
$CH3 + CO2 \rightarrow CH3O + CO$	5.09E+13	0.00	197.79
$CH3O + HO2 \rightarrow CH2O + H2O2$	2.70E+12	0.00	0.00
$CH2O + H2O2 \rightarrow CH3O + HO2$	2.93E+12	0.00	287.54
$CH3O + HO2 \rightarrow CH3OH + O2$	4.92E+12	0.00	0.00
$CH3OH + O2 \rightarrow CH3O + HO2$	2.17E+13	0.00	238.91
$CH3O + H \rightarrow CH2O + H2$	2.00E+13	0.00	0.00
$CH2O + H2 \rightarrow CH3O + H$	1.47E+13	0.00	352.69
$CH3O + O \rightarrow CH2O + OH$	3.00E+12	0.00	0.00
$CH2O + OH \rightarrow CH3O + O$	9.78E+11	0.00	344.83
$CH3O + OH \rightarrow CH2O + H2O$	1.80E+13	0.00	0.00
$CH2O + H2O \rightarrow CH3O + OH$	5.90E+13	0.00	416.02
$CH3O + M' \rightarrow CH2O + H + M'$	5.45E+13	0.00	56.50
$CH2O + H + M' \rightarrow CH3O + M'$	1.03E+13	0.00	-26.84
$CH3O + CH3O \rightarrow CH3OH + CH2O$	4.20E+12	0.00	0.00
$CH3OH + CH2O \rightarrow CH3O + CH3O$	5.00E+12	0.00	351.44
$CH3O + CH3OH \rightarrow CH3OH + CH2OH$	3.00E+11	0.00	17.05
$CH3OH + CH2OH \rightarrow CH3O + CH3OH$	4.10E+10	0.00	49.09
$CHO + H \rightarrow CO + H2$	9.00E+13	0.00	0.00
$CO + H2 \rightarrow CHO + H$	5.28E+14	0.00	374.37
$CHO + O \rightarrow CO + OH$	3.00E+13	0.00	0.00

Reaction	A	b	E_a
$CO + OH \rightarrow CHO + O$	7.78E+13	0.00	366.51
$CHO + O \rightarrow CO2 + H$	3.00E+13	0.00	0.00
$CO2 + H \rightarrow CHO + O$	1.08E+16	0.00	463.69
$CHO + OH \rightarrow CO + H2O$	1.00E+14	0.00	0.00
$CO + H2O \rightarrow CHO + OH$	2.61E+15	0.00	437.70
$CHO + O2 \rightarrow CO + HO2$	3.00E+12	0.00	0.00
$CO + HO2 \rightarrow CHO + O2$	6.43E+12	0.00	134.20
$CHO + M' \rightarrow CO + H + M'$	4.61E+17	-1.00	71.15
$CO + H + M' \rightarrow CHO + M'$	6.96E+17	-1.00	9.49
$CHO + CH3 \rightarrow CO + CH4$	1.20E+14	0.00	0.00
$CO + CH4 \rightarrow CHO + CH3$	2.02E+16	0.00	379.42
$CH2O + H \rightarrow CHO + H2$	2.26E+10	1.05	13.72
$CHO + H2 \rightarrow CH2O + H$	1.62E+09	1.05	72.94
$CH2O + O \rightarrow CHO + OH$	4.11E+11	0.57	11.56
$CHO + OH \rightarrow CH2O + O$	1.31E+10	0.57	62.92
$CH2O + OH \rightarrow CHO + H2O$	3.42E+09	1.18	-1.87
$CHO + H2O \rightarrow CH2O + OH$	1.09E+09	1.18	120.68
$CH2O + HO2 \rightarrow CHO + H2O2$	2.00E+12	0.00	48.80
$CHO + H2O2 \rightarrow CH2O + HO2$	2.12E+11	0.00	42.87
$CH2O + CH3 \rightarrow CHO + CH4$	4.10E+12	0.00	37.00
$CHO + CH4 \rightarrow CH2O + CH3$	8.46E+12	0.00	101.27
$CH2O + M' \rightarrow CHO + H + M'$	6.30E+16	0.00	325.90
$CHO + H + M' \rightarrow CH2O + M'$	1.17E+15	0.00	-50.91
$CH3 + H \rightarrow CH4$	4.60E+33	-6.47	23.19
$CH4 \rightarrow CH3 + H$	5.13E+35	-6.47	464.27
$CH3 + H \rightarrow CH2 + H2$	4.00E+13	0.00	66.53
$CH2 + H2 \rightarrow CH3 + H$	7.43E+12	0.00	46.32
$CH3 + O \rightarrow CH2O + H$	7.00E+13	0.00	0.00

Reaction	A	b	E_a
$CH2O + H \rightarrow CH3 + O$	9.73E+14	0.00	293.62
$CH3 + O + M' \rightarrow CH3O + M'$	7.00E+14	0.00	0.00
$CH3O + M' \rightarrow CH3 + O + M'$	5.13E+16	0.00	376.96
$CH3 + OH \rightarrow CH2OH + H$	9.00E+14	0.00	61.54
$CH2OH + H \rightarrow CH3 + OH$	5.24E+15	0.00	42.38
$CH3 + OH \rightarrow CH3OH$	3.40E+36	-7.33	33.30
$CH3OH \rightarrow CH3 + OH$	9.09E+38	-7.33	416.87
$CH3 + O2 \rightarrow CH3O + O$	5.78E+18	-1.58	133.63
$CH3O + O \rightarrow CH3 + O2$	1.80E+19	-1.58	14.18
$CH3 + O2 \rightarrow CH2O + OH$	5.20E+13	0.00	144.85
$CH2O + OH \rightarrow CH3 + O2$	5.28E+13	0.00	370.23
$CH3 + M' \rightarrow CH2 + H + M'$	6.10E+15	0.00	373.39
$CH2 + H + M' \rightarrow CH3 + M'$	2.92E+14	0.00	-82.85
$CH + O \rightarrow CO + H$	6.00E+13	0.00	0.00
$CO + H \rightarrow CH + O$	2.88E+15	0.00	736.05
$CH + OH \rightarrow CHO + H$	3.00E+13	0.00	0.00
$CHO + H \rightarrow CH + OH$	5.56E+14	0.00	369.54
$CH + O2 \rightarrow CO + OH$	3.60E+13	0.00	0.00
$CO + OH \rightarrow CH + O2$	1.26E+14	0.00	667.81
$CH + O2 \rightarrow CHO + O$	3.00E+13	0.00	0.00
$CHO + O \rightarrow CH + O2$	4.06E+13	0.00	301.30
$CH + CO2 \rightarrow CHO + CO$	3.00E+12	0.00	0.00
$CHO + CO \rightarrow CH + CO2$	3.99E+11	0.00	272.35
$CH + H2O \rightarrow CH2O + H$	3.00E+12	0.00	0.00
$CH2O + H \rightarrow CH + H2O$	1.74E+14	0.00	246.99
$CH2 + H \rightarrow CH + H2$	1.17E+13	-0.13	-8.38
$CH + H2 \rightarrow CH2 + H$	7.68E+12	-0.13	2.99
$CH2 + OH \rightarrow CH + H2O$	2.00E+13	0.00	20.79

Reaction	A	b	E_a
$CH2O + H \rightarrow CH3 + O$	9.73E+14	0.00	293.62
$CH3 + O + M' \rightarrow CH3O + M'$	7.00E+14	0.00	0.00
$CH3O + M' \rightarrow CH3 + O + M'$	5.13E+16	0.00	376.96
$CH3 + OH \rightarrow CH2OH + H$	9.00E+14	0.00	61.54
$CH2OH + H \rightarrow CH3 + OH$	5.24E+15	0.00	42.38
$CH3 + OH \rightarrow CH3OH$	3.40E+36	-7.33	33.30
$CH3OH \rightarrow CH3 + OH$	9.09E+38	-7.33	416.87
$CH3 + O2 \rightarrow CH3O + O$	5.78E+18	-1.58	133.63
$CH3O + O \rightarrow CH3 + O2$	1.80E+19	-1.58	14.18
$CH3 + O2 \rightarrow CH2O + OH$	5.20E+13	0.00	144.85
$CH2O + OH \rightarrow CH3 + O2$	5.28E+13	0.00	370.23
$CH3 + M' \rightarrow CH2 + H + M'$	6.10E+15	0.00	373.39
$CH2 + H + M' \rightarrow CH3 + M'$	2.92E+14	0.00	-82.85
$CH + O \rightarrow CO + H$	6.00E+13	0.00	0.00
$CO + H \rightarrow CH + O$	2.88E+15	0.00	736.05
$CH + OH \rightarrow CHO + H$	3.00E+13	0.00	0.00
$CHO + H \rightarrow CH + OH$	5.56E+14	0.00	369.54
$CH + O2 \rightarrow CO + OH$	3.60E+13	0.00	0.00
$CO + OH \rightarrow CH + O2$	1.26E+14	0.00	667.81
$CH + O2 \rightarrow CHO + O$	3.00E+13	0.00	0.00
O $CHO + \quad \rightarrow CH + O2$	4.06E+13	0.00	301.30
$CH + CO2 \rightarrow CHO + CO$	3.00E+12	0.00	0.00
$CHO + CO \rightarrow CH + CO2$	3.99E+11	0.00	272.35
$CH + H2O \rightarrow CH2O + H$	3.00E+12	0.00	0.00
$CH2O + H \rightarrow CH + H2O$	1.74E+14	0.00	246.99
$CH2 + H \rightarrow CH + H2$	1.17E+13	-0.13	-8.38
$CH + H2 \rightarrow CH2 + H$	7.68E+12	-0.13	2.99
$CH2 + OH \rightarrow CH + H2O$	2.00E+13	0.00	20.79

Reaction	A	b	E_a
$CH + H2O \rightarrow CH2 + OH$	5.84E+13	0.00	95.49
$CH2 + O \rightarrow CHO + H$	8.00E+13	0.00	0.00
$CHO + H \rightarrow CH2 + O$	4.30E+14	0.00	373.05
$CH2 + O \rightarrow CO + H2$	4.00E+13	0.00	0.00
$CO + H2 \rightarrow CH2 + O$	1.26E+15	0.00	747.42
$CH2 + O2 \rightarrow CHO + OH$	2.00E+13	0.00	0.00
$CHO + OH \rightarrow CH2 + O2$	7.86E+12	0.00	304.81
$CH2 + O2 \rightarrow CH2O + O$	2.00E+13	0.00	0.00
$CH2O + O \rightarrow CH2 + O2$	2.47E+14	0.00	253.45
$CH2 + O2 \rightarrow CO2 + H + H$	1.00E+13	0.00	0.00
$CO2 + H + H \rightarrow CH2 + O2$	8.26E+14	0.00	340.33
$H + CH \rightarrow C + H2$	6.00E+13	0.00	0.00
$C + H2 \rightarrow H + CH$	2.30E+14	0.00	96.73
$C + OH \rightarrow CO + H$	5.00E+13	0.00	0.00
$CO + H \rightarrow C + OH$	1.42E+15	0.00	647.18
$C + O \rightarrow CO$	5.00E+13	0.00	0.00
$CO \rightarrow C + O$	2.44E+15	0.00	1075.35
$C + O2 \rightarrow CO + O$	2.00E+13	0.00	0.00
$CO + O \rightarrow C + O2$	4.14E+13	0.00	578.94
$C + CO2 \rightarrow CO + CO$	6.00E+08	0.00	0.00
$CO + CO \rightarrow C + CO2$	1.22E+08	0.00	550.00
$C + H2O \rightarrow CHO + H$	2.00E+13	0.00	0.00
$CHO + H \rightarrow C + H2O$	2.17E+13	0.00	209.49
$CH4 + H \rightarrow H2 + CH3$	2.20E+04	3.00	36.65
$H2 + CH3 \rightarrow CH4 + H$	7.66E+02	3.00	31.60

Reaction	A	b	E_a
$CH4 + O \rightarrow OH + CH3$	1.20E+07	2.10	31.93
$OH + CH3 \rightarrow CH4 + O$	1.85E+05	2.10	19.01
$CH4 + OH \rightarrow H2O + CH3$	1.66E+06	2.10	10.67
$H2O + CH3 \rightarrow CH4 + OH$	2.57E+05	2.10	68.94
$CH4 + CH2 \rightarrow CH3 + CH3$	4.30E+12	0.00	42.01
$CH3 + CH3 \rightarrow CH4 + CH2$	8.06E+11	0.00	57.17

Inert species : N2

NM = 1 additional third bodies defined (besides M) :

M' = 1.00 H2 + 6.50 H2O + 0.40 O2 + 0.40 N2 + 3.00 CH3OH+ 0.75 CO + 1.50 CO2